Instrumentation to handle thermal polarized neutron beams

Instrumentation to handle thermal polarized neutron beams

PROEFSCHRIFT

ter verkrijging van de graad van doctor
aan de Technische Universiteit Delft,
op gezag van de Rector Magnificus Prof.dr.ir. J.T. Fokkema,
voorzitter van het College voor Promoties
in het openbaar te verdedigen op maandag 22 november 2004 om 10.30 uur

door

Wicher Hooite KRAAN

doctorandus in de natuurkunde
geboren te 's-Gravenhage

Dit proefschrift is goedgekeurd door de promotor:
Prof. dr. I.M. de Schepper

Samenstelling promotiecommissie:

Rector Magnificus	voorzitter
Prof.dr. I.M. de Schepper	Technische Universiteit Delft, promotor
Prof.dr. G.J. Kearley	Technische Universiteit Delft
Prof.dr.ir. P. Kruit	Technische Universiteit Delft
Prof.dr.ir. C.W.E. van Eijk	Technische Universiteit Delft
Univ.-Prof. dipl.ing.	
Dr. G. Badurek	Technische Universität Wien
Dr. S.V. Grigoriev	Petersburg Nuclear Physics Institute Gatchina, Russia
Dr. M.Th. Rekveldt	Interfacultair Reactor Instituut, Delft

Published and distributed by: DUP Science
DUP Science is an imprint of
Delft University Press
P.O. Box 98
2600 MG Delft
The Netherlands
Telephone: +31 15 27 85 678
Telefax: +31 15 27 85 706
E-mail: DUP@Library.TUDelft.nl

ISBN 90-407-2527-6

Keywords: neutron spin, spinor, Larmor precession, spin flippers

Printed in the Netherlands

Contents

πολλων δ'ανθρωπων 'ιδεν 'αστεα
και νοον 'εγνω

of many people he beheld the cities
and he tried to understand their minds

Chapter 1

Introduction

Very soon after the discovery of the neutron in 1932 [1] it was recognized that this elementary particle has a magnetic moment, in spite of the fact that it has no net electric charge. The magnetic moments of the neutrons in a beam tend to orient themselves either parallel or antiparallel to any chosen direction, in particular the direction of an external magnetic field. This is due to the fact that the magnetic moment is coupled with the neutron's angular moment (spin), equal to 1/2 elementary unit of angular moment. Let the number of neutrons with moment parallel to the field be n_+ and the number with antiparallel moment n_-. Then the degree of polarization is defined as

$$p = \frac{n_+ - n_-}{n_+ + n_-}.$$

If no special measures are taken, we will find $p = 0$. After a beam is transmitted through a so-called "polarizer", one state will occur preferably and we have a "polarized beam" with $p = 1$ (or $p = -1$) at most.
This thesis is a compilation of 6 articles on polarized neutron beams which appeared over a time period of nearly 15 years. The common theme is how to handle the spins in beams of neutrons and how such beams can be used to investigate the properties of matter.
The earliest method to create such a polarized beam was by transmission through a ferromagnetic material (iron) magnetized to saturation [2][3]. Soon it was found that the degree of polarization can be determined by using the double transmission effect, i.e. transmitting the beam through a second block of iron, acting as the "analyzer" and taking two intensity measurements: one with a thin unmagnetized slab of iron and one without this slab on the pathway between polarizer and analyzer. This way of determining the degree of polarization with a polarizer and an analyzer is used up to the present day.
A principal method to polarize a neutron beam is to pass an unpolarized beam

through a strong magnetic gradient field. Neutrons with magnetic moment parallel to the field will be deviated slightly into the field, whereas neutrons with opposite magnetic moment will be deviated away from the field. Thus, the initial unpolarized neutron beam splits into 2 fully polarized ($p = 1$) sub-beams running in slightly different directions [4]. All polarizers in practical use are based upon the interaction process of the neutron's magnetic moment with the atomic magnetic moments (as in the iron blocks just mentioned) or with the nuclear magnetic moments of the material inside the polarizer.

In the past decades more efficient ways to obtain a polarized neutron beam have been developed. First, diffraction of a beam in the lattice planes of a ferromagnetic crystal [5], which gives *monochromatic* beams with polarization p up to 0.98. In the seventies and eighties reflection from a magnetized mirror has become very successful, because they can provide intense poly-chromatic polarized beams [6]. Both of these techniques have the disadvantage of accepting neutron beams of very limited divergence (less than $1°$). This does not apply to the polarizers based on the interaction with nuclear moments: polarizers consisting of oriented protons [7] and ^{3}He nuclei [8].

An experiment with a polarized neutron beam requires that loss of polarization (which is a vector in 3D space) be minimized all the way to the analyzer (apart from the loss of polarization in a sample being studied - which might be the goal of the experiment). This is the purpose of "guide fields" produced by magnetic devices along the neutron beam path.

To determine the degree of polarization of a beam in an experiment it is necessary to take a measurement with the polarization reversed relative to the field. This calls for devices called "spin flippers".

In many applications the polarization must be oriented at an angle (in practice perpendicular) to the magnetic field through which the beam is transmitted. A device which does this, is called $\pi/2$-rotator.
Part of the present work is devoted to building and investigation of these devices as such.

As soon as the polarization vector is oriented at an angle to the local magnetic field, it rotates around the field direction, so called Larmor precession. This is the subject of a major part of this thesis. Since the seventies it has become popular to do neutron scattering experiments in the so-called "spin-echo" mode [9]. Before the sample to be investigated we let the polarization of a neutron beam precess over a fixed large angle; interaction with the sample takes place; next we let the polarization precess in an identical device but in opposite sense. In absence of the sample we have "spin-echo", i.e. the net precession angle is zero. When the sample is present, the "spin-echo" condition is disturbed which gives rise to loss of polarization. Very subtle interactions in the sample can thus be observed, if the precession angle can be pushed to very high values: 1000-10000 revolutions. In this thesis this technique is applied in several chapters.

This thesis starts with Chapter 2 containing a review of the theory for the behaviour of neutron polarization in space and time. Chapter 3 contains an explanation of the installations and technology of the methods to collect the knowledge about specific devices (polarizers, flippers, rotators, precession devices) which are the subject of subsequent chapters. Chapter 4 is an extended discussion how to find neutron spectra with polarization precession methods and, as an application, to determine the transmission of a sample, in particular for a multichannel neutron polarizer.

Chapter 5 deals with "adiabatic spin rotators" which are static devices (containing time independent magnetic fields) and are used for the technique of three-dimensional neutron polarization analysis. In Chapter 6 the "time of flight method" is applied to test the efficiencies of 2 types of adiabatic spin flippers: static and dynamic (containing static and time dependent radio frequency (RF) fields). In Chapter 7 we investigate the phenomenon of "zero field precession" which occurs between 2 dynamic RF flippers. In between the polarization behaves as if precession takes place in zero field. Chapter 8 deals with a **S**pin-**E**cho experiment in which the sample scatters mainly into a narrow cone around the direction of the incident beam: **S**mall **A**ngle **N**eutron **S**cattering (SESANS). In these experiments zero field precession - in opposite directions - is taking place before and after the sample. To illustrate the interplay between fundamental science and technology, Chapter 9 is devoted to a quantum mechanical aspect of the precession of a "spin-1/2-particle" which the neutron in fact is.

The reader will find slight inconsistencies in notation and interpretation in the published papers (Chapters 4-9). The two introductory Chapters (2 and 3) and the Summary give the present views.

Chapter 2

Basic theory for the neutron spin

In this chapter we discuss the basic theories needed to describe beams of neutrons running through space, in which, in general, magnetic fields $\vec{B}(\vec{r},t)$ are present which depend on position in space ($\vec{r}$) and time (t). We start with the neutron itself.
The particle "neutron" possesses a mass $m = 1.6723 \times 10^{-27}$ kg and a magnetic moment $|\mu_n|$ (equal to 1.913 nuclear magneton, i.e. 9.66×10^{-27} J/T $= 6.030 \times 10^{-5}$ meV/T) coupled to its spin of $(1/2)\hbar$ (equal to 0.526×10^{-34} Js), hence its gyromagnetic ratio $\gamma \equiv \mu_n/(\hbar/2) = 1.8301 \times 10^8$ (T sec)$^{-1}$. The magnetic moment operator for such a particle is

$$\vec{\mu} = \frac{1}{2}\gamma\,\hbar\vec{\sigma}. \tag{2.1}$$

The vector operator $\vec{\sigma} \equiv (\sigma_x, \sigma_y, \sigma_z)$ consists of 3 operators known as the Pauli spin matrices:

$$\sigma_x = \begin{pmatrix} 0 & 1 \\ 1 & 0 \end{pmatrix}; \quad \sigma_y = \begin{pmatrix} 0 & -i \\ i & 0 \end{pmatrix}; \quad \sigma_z = \begin{pmatrix} 1 & 0 \\ 0 & -1 \end{pmatrix}. \tag{2.2}$$

The interaction of the neutron spin with magnetic fields is described by the Hamiltonean

$$\mathcal{H}_{mag} = -\vec{\mu}\cdot\vec{B}(\vec{r},t) = -\frac{1}{2}\,\hbar\gamma\;\vec{\sigma}\cdot\vec{B}(\vec{r},t). \tag{2.3}$$

2.1 The Schrödinger equation

The behaviour of a neutron beam is most generally described by the time-dependent Schrödinger equation:

$$i\hbar\frac{\partial}{\partial t}\psi(\vec{r},t) \;=\; \mathcal{H}\;\psi(\vec{r},t), \tag{2.4}$$

with $\mathcal{H}$ the Hamiltonean operator and

$$\psi(\vec{r},t) = \begin{pmatrix} \psi^{+}(\vec{r},t) \\ \psi^{-}(\vec{r},t) \end{pmatrix}$$

the two component space and time dependent "spinor" which determines all physical properties of the neutron beam. In our experiments we make sure that the neutrons do not interact (measurably)with surrounding matter: there is no scattering. The neutrons only see the field $\vec{B}(\vec{r},t)$. Therefore the Hamiltonean is given by

$$\mathcal{H} = \frac{\vec{p}^{\,2}}{2m} - \frac{1}{2}\,\hbar\gamma\;\vec{\sigma}\cdot\vec{B}(\vec{r},t). \tag{2.5}$$

The first term represents the kinetic energy of the neutron, where $\vec{p} = -i\hbar\vec{\nabla}$ is the momentum operator and the second term is the magnetic energy interaction given by Eq.(2.3). From the spinor $\psi(\vec{r},t)$ (2-dimensional) we derive the experimentally observable spin $\vec{S}(\vec{r},t)$ given by the expectation value

$$\vec{S}(\vec{r},t) \equiv \langle\vec{\sigma}\rangle \equiv \langle\psi(\vec{r},t)\mid\vec{\sigma}\mid\psi(\vec{r},t)\rangle, \tag{2.6}$$

or

$$\vec{S}(\vec{r},t) \equiv \begin{pmatrix} \psi^{+}(\vec{r},t)^{*} \\ \psi^{-}(\vec{r},t)^{*} \end{pmatrix} \vec{\sigma} \begin{pmatrix} \psi^{+}(\vec{r},t) \\ \psi^{-}(\vec{r},t) \end{pmatrix} \tag{2.7}$$

which is a 3-dimensional vector. The left hand side $\vec{S}(\vec{r},t)$ is, what is measured experimentally. The right hand side is the theoretical prediction from the Schrödinger equation.
In the following we need the special spinors $|\chi_\alpha^+\rangle$ (with $\alpha = x, y, z$):

$$|\chi_x^+\rangle = \frac{1}{\sqrt{2}}\begin{pmatrix} 1 \\ 1 \end{pmatrix}; \quad |\chi_y^+\rangle = \frac{1}{\sqrt{2}}\begin{pmatrix} 1 \\ i \end{pmatrix}; \quad |\chi_z^+\rangle = \begin{pmatrix} 1 \\ 0 \end{pmatrix} \tag{2.8a}$$

and their counterparts $|\chi_\alpha^-\rangle$:

$$|\chi_x^-\rangle = \frac{1}{\sqrt{2}}\begin{pmatrix} 1 \\ -1 \end{pmatrix}; \quad |\chi_y^-\rangle = \frac{1}{\sqrt{2}}\begin{pmatrix} 1 \\ -i \end{pmatrix}; \quad |\chi_z^-\rangle = \begin{pmatrix} 0 \\ 1 \end{pmatrix}. \tag{2.8b}$$

We note the obvious properties

$$\langle\chi_\alpha^+|\chi_\alpha^+\rangle = 1, \quad \langle\chi_\alpha^-|\chi_\alpha^-\rangle = 1,$$

so all these six spinors are normalized and

$$\langle\chi_\alpha^+|\chi_\alpha^-\rangle = 0.$$

Therefore any pair $\chi_\alpha^+, \chi_\alpha^-$ is orthonormal and forms a basis in 2D spinor space. Furthermore

$$\sigma_\alpha |\chi_\alpha^+\rangle = |\chi_\alpha^+\rangle; \quad \sigma_\alpha |\chi_\alpha^-\rangle = -|\chi_\alpha^-\rangle.$$

Thus, the two $|\chi_\alpha^+\rangle$ and $|\chi_\alpha^-\rangle$ are the eigenspinors of σ_α with eigenvalues $+1$ and -1, respectively.
For the observed "macroscopic" spin, i.e. the expectation value, one finds directly

$$\langle \chi_\alpha^+ |\vec{\sigma}| \chi_\alpha^+\rangle = \hat{\alpha}; \quad \langle \chi_\alpha^- |\vec{\sigma}| \chi_\alpha^-\rangle = -\hat{\alpha} \tag{2.9}$$

with $\hat{\alpha}$ the unit vector in the direction $\alpha = x, y, z$. Therefore the spinors $|\chi_\alpha^\pm\rangle$ describe macroscopic spins in the $\pm\alpha$ direction. Any spinor pair $\chi_\alpha^+, \chi_\alpha^-$ can be expressed in any other pair $\chi_\beta^+, \chi_\beta^-$ according to

$$|\chi_\alpha^+\rangle = |\chi_\beta^+\rangle \langle \chi_\beta^+ | \chi_\alpha^+\rangle + |\chi_\beta^-\rangle \langle \chi_\beta^- | \chi_\alpha^+\rangle; \tag{2.10a}$$
$$|\chi_\alpha^-\rangle = |\chi_\beta^+\rangle \langle \chi_\beta^+ | \chi_\alpha^-\rangle + |\chi_\beta^-\rangle \langle \chi_\beta^- | \chi_\alpha^-\rangle \tag{2.10b}$$

and the coefficients $\langle \chi_\alpha^\pm | \chi_\beta^\mp\rangle$ are directly read off from Eqs.(2.8).

2.2 Time dependent fields

2.2.1 Larmor equations for 2D spinors and 3D spins

First we consider magnetic fields $\vec{B}(\vec{r}, t) \equiv \vec{B}(t)$ which do **not** depend on $\vec{r}$, i.e. at each time they are homogeneous over all space. Then the solution of the Schrödinger equation (2.4) can be written as

$$\psi(\vec{r}, t) = e^{i\vec{k}\cdot\vec{r} - i\omega t}\, |\chi(t)\rangle,$$

where the exponential factor corresponds to a neutron moving in the direction $\vec{k}$ with momentum $\langle \vec{p}\rangle = \hbar\vec{k} = m\vec{v}$ with $\vec{v}$ its velocity and kinetic energy

$$E = \hbar\omega = \frac{\hbar^2 k^2}{2m} = \frac{1}{2} m v^2.$$

The spinor $|\chi(t)\rangle$ in this solution does not depend on $\vec{r}$. As follows by substitution into the Schrödinger equation, taking Eq.(2.5) for the Hamiltonean, $|\chi(t)\rangle$ satisfies the so-called **Larmor equation for spinors**:

$$\frac{d}{dt}|\chi(t)\rangle = \frac{1}{2}\, i\, \vec{\sigma} \cdot \gamma \vec{B}(t)\, |\chi(t)\rangle. \tag{2.11}$$

The corresponding macroscopic 3D spin expectation is

$$\vec{S}(t) = \langle \chi(t)|\, \vec{\sigma}\, |\chi(t)\rangle$$

and its derivative

$$\frac{d}{dt}\vec{S}(t) = \langle\frac{d\chi(t)}{dt} \mid \vec{\sigma} \mid \chi(t)\rangle \ + \ \langle\chi(t) \mid \vec{\sigma} \mid \frac{d\chi(t)}{dt}\rangle,$$

so that with Eq.(2.11) we derive

$$\frac{d}{dt}\vec{S}(t) = \frac{1}{2}i\gamma\langle\chi(t)|\ [\vec{\sigma}, \vec{\sigma}\cdot\vec{B}(t)]\ |\chi(t)\rangle,$$

where $[A,B] \equiv AB - BA$ is the commutator of two operators. Now we use

$$[\sigma_\alpha, \sigma_\beta] = 2i\ \sum_\gamma \epsilon_{\alpha\beta\gamma}\ \sigma_\gamma$$

with $\epsilon_{\alpha\beta\gamma}$ the Levi-Civita symbol which describes the cross product of any two 3D vectors $\vec{a}$ and $\vec{b}$ as

$$(\vec{a}\times\vec{b})_\alpha = \sum_{\beta,\gamma}\epsilon_{\alpha\beta\gamma}\ a_\beta b_\gamma.$$

Thus one finds directly:

$$[\vec{\sigma}, \vec{\sigma}\cdot\vec{B}(t)] = 2i\ \vec{B}(t)\times\vec{\sigma}$$

and we arrive at the famous **Larmor equation for macroscopic 3D spins**:

$$\frac{d}{dt}\vec{S}(t) = \gamma\ \vec{S}(t)\times\vec{B}(t). \tag{2.12}$$

Geometrically, this means that at any time t an infinitesimal vector $\vec{dS}$ is added to the vector $\vec{S}(t)$ which is perpendicular both to $\vec{S}(t)$ and to $\vec{B}(t)$, i.e. the vector $\vec{S}(t)$ is rolling an infinitesimal amount over a cone with $\vec{B}(t)$ as axis.
Since cross products are mathematically inconvenient to handle we rewrite this equation with the help of the three "Angular Momentum Operators"

$$\vec{L} = (L_x, L_y, L_z),$$

which are the 3×3 matrices

$$L_x = \begin{pmatrix} 0 & 0 & 0 \\ 0 & 0 & -i \\ 0 & i & 0 \end{pmatrix};\ L_y = \begin{pmatrix} 0 & 0 & i \\ 0 & 0 & 0 \\ -i & 0 & 0 \end{pmatrix};\ L_z = \begin{pmatrix} 0 & -i & 0 \\ i & 0 & 0 \\ 0 & 0 & 0 \end{pmatrix}.$$

It is then easy to see that any cross product can be written as $\vec{a}\times\vec{b} = i(\vec{L}\cdot\vec{b})\vec{a}$. Therefore we can rewrite the **Larmor equation for macroscopic 3D spins:**

$$\frac{d}{dt}\vec{S}(t) = i\ \vec{L}\cdot\gamma\vec{B}(t)\ \ \vec{S}(t) \tag{2.13}$$

and one observes a close analogy with the Larmor equation (2.11) for the **spinors** which we exploit heavily. In fact Eqs.(2.11) and (2.13) are the same under the replacement $\vec{L} \Longleftrightarrow \vec{\sigma}/2$.

2.2.2 General solutions of the Larmor Equations

Standard solutions of the Larmor equations are often obtained by writing $\vec{B}(t)$ as a stepwise constant function. This means that we write $\vec{B}_1 = B_1\hat{B}_1$ for $0 \leq t \leq t_1$ and $\vec{B}_2 = B_2\hat{B}_2$ for $t > t_1$, ... as illustrated in Fig. 2.1.

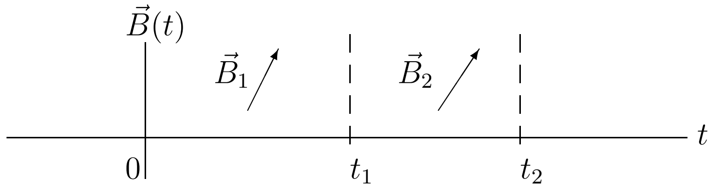

Figure 2.1: Sequence in time of magnetic fields representing a time dependent field $\vec{B}(t)$.

Here $\hat{B}_1$, $\hat{B}_2$... are unit vectors in the direction of $\vec{B}_1$, $\vec{B}_2$... respectively. By choosing the time intervals t_1, $t_2 - t_1$,... small enough, any time dependent field $\vec{B}(t)$ can be represented in this manner. The solutions of Eqs.(2.11) and (2.13) then read for $t \geq t_1$

$$|\chi(t)\rangle \;=\; \mathcal{T}^{-1}_{\hat{B}_2}(\gamma B_2(t-t_1))\;\; \mathcal{T}^{-1}_{\hat{B}_1}(\gamma B_1 t_1)\;\; |\chi(0)\rangle, \tag{2.14a}$$

$$\vec{S}(t) \;=\; \mathcal{R}^{-1}_{\hat{B}_2}(\gamma B_2(t-t_1))\;\; \mathcal{R}^{-1}_{\hat{B}_1}(\gamma B_1 t_1)\;\; \vec{S}(0), \tag{2.14b}$$

where for any unit vector $\vec{n}$ the transformations $\mathcal{T}_{\vec{n}}(\tau)$ and $\mathcal{R}_{\vec{n}}(\tau)$ are given by

$$\mathcal{T}_{\vec{n}}(\tau) = \exp\,(-\frac{1}{2}i\vec{\sigma}\cdot\vec{n}\tau); \qquad \mathcal{T}^{-1}_{\vec{n}}(\tau) = \mathcal{T}_{\vec{n}}(-\tau) = \exp\,(\frac{1}{2}i\vec{\sigma}\cdot\vec{n}\tau). \tag{2.15a}$$

$$\mathcal{R}_{\vec{n}}(\tau) = \exp\,(-i\vec{L}\cdot\vec{n}\tau); \qquad \mathcal{R}^{-1}_{\vec{n}}(\tau) = \mathcal{R}_{\vec{n}}(-\tau) = \exp\,(i\vec{L}\cdot\vec{n}\tau). \tag{2.15b}$$

Remembering that for an arbitrary operator $\mathcal{O}$ and vector $\vec{V}(t)$ one has in any dimension:

$$\frac{\partial}{\partial t}\vec{V}(t) = \mathcal{O}\vec{V}(t) \Longleftrightarrow \vec{V}(t) = e^{\mathcal{O}t}\vec{V}(0),$$

it is understood that the 2D-'streaming' operators $\mathcal{T}_{\vec{n}}(\tau)$ and the 3D-rotation operators $\mathcal{R}_{\vec{n}}(\tau)$ are the solutions of the Larmor equations for constant fields in the $\vec{n}$-direction.

The expression for $\mathcal{T}_{\vec{n}}(\tau)$ can be further evaluated by writing $\exp\,(-\frac{1}{2}i\vec{\sigma}\cdot\vec{n}\tau)$ as an infinite Taylor series. We use:

$$(\vec{\sigma}\cdot\vec{n})^2 = \mathcal{I}; \quad (\vec{\sigma}\cdot\vec{n})^3 = \vec{\sigma}\cdot\vec{n}; \quad (\vec{\sigma}\cdot\vec{n})^4 = \mathcal{I}; \quad ...$$

where $\mathcal{I}$ is the 2×2 identity matrix. Collecting the odd and even powers separately yields

$$\mathcal{T}_{\vec{n}}(\tau) = \cos(\tau/2)\mathcal{I} - i\vec{\sigma}\cdot\vec{n}\;\sin(\tau/2). \tag{2.16}$$

This result contains the three special solutions of the Larmor Equation for fields in the x, y, z directions respectively:

$$\mathcal{T}_x(\tau) = \begin{pmatrix} \cos\frac{\tau}{2} & -i\sin\frac{\tau}{2} \\ -i\sin\frac{\tau}{2} & \cos\frac{\tau}{2} \end{pmatrix}, \tag{2.17a}$$

$$\mathcal{T}_y(\tau) = \begin{pmatrix} \cos\frac{\tau}{2} & -\sin\frac{\tau}{2} \\ \sin\frac{\tau}{2} & \cos\frac{\tau}{2} \end{pmatrix}, \tag{2.17b}$$

$$\mathcal{T}_z(\tau) = \begin{pmatrix} e^{-i\tau/2} & 0 \\ 0 & e^{i\tau/2} \end{pmatrix}. \tag{2.17c}$$

Similarly, we expand $\mathcal{R}_{\vec{n}}(\tau) = \exp\left(-i\vec{L}\cdot\vec{n}\tau\right)$ in a Taylor series and use

$$(\vec{L}\cdot\vec{n})^3 = \vec{L}\cdot\vec{n}; \quad (\vec{L}\cdot\vec{n})^4 = (\vec{L}\cdot\vec{n})^2; \quad (\vec{L}\cdot\vec{n})^5 = \vec{L}\cdot\vec{n}; \quad ...$$

Collecting the odd and even powers yields

$$\mathcal{R}_{\vec{n}}(\tau) = \mathcal{I} + (\cos\tau - 1)(\vec{L}\cdot\vec{n})^2 - i\ \sin\tau\ \vec{L}\cdot\vec{n}, \tag{2.18}$$

where in this case $\mathcal{I}$ is the 3×3 identity matrix. We derive the three special solutions for magnetic fields in the x, y, z-direction respectively:

$$\mathcal{R}_x(\tau) = \begin{pmatrix} 1 & 0 & 0 \\ 0 & \cos\tau & -\sin\tau \\ 0 & \sin\tau & \cos\tau \end{pmatrix}, \tag{2.19a}$$

$$\mathcal{R}_y(\tau) = \begin{pmatrix} \cos\tau & 0 & \sin\tau \\ 0 & 1 & 0 \\ -\sin\tau & 0 & \cos\tau \end{pmatrix}, \tag{2.19b}$$

$$\mathcal{R}_z(\tau) = \begin{pmatrix} \cos\tau & -\sin\tau & 0 \\ \sin\tau & \cos\tau & 0 \\ 0 & 0 & 1 \end{pmatrix}. \tag{2.19c}$$

These are ordinary 3D-rotations over angles τ around the x, y, z-axes, respectively (to the "left" when $\tau > 0$). More generally, $\mathcal{R}_{\vec{n}}(\tau)$ is a rotation to the left over an angle τ around the $\vec{n}$-axis.
Thus we have found the solutions of the Larmor Equation for magnetic fields $\vec{B}(t)$ represented by a series of constant fields $\vec{B}_1, \vec{B}_2, ...$ in subsequent time intervals.

2.2.3 Solution for constant field in arbitrary direction

The above modelling of a time dependent field contains the general solution for a constant field in an arbitrary direction $\vec{B} = B\vec{n}$. Then the solutions given in

Eqs.(2.14) reduce to

$$
\begin{aligned}
|\chi(t)\rangle &= \mathcal{T}_{\vec{n}}^{-1}(\gamma B t)\;\; |\chi(0)\rangle && (2.20a)\\
\vec{S}(t) &= \mathcal{R}_{\vec{n}}^{-1}(\gamma B t)\; \vec{S}(0), && (2.20b)
\end{aligned}
$$

where the unit vector $\vec{n}$ can be written in polar coordinates as (cf. Fig. 2.2)

$$
\vec{n} = \mathcal{R}_z(\phi)\; \mathcal{R}_y(\theta)\; \hat{z} = \begin{pmatrix} \cos\phi\ \sin\theta \\ \sin\phi\ \sin\theta \\ \cos\theta \end{pmatrix}.
$$

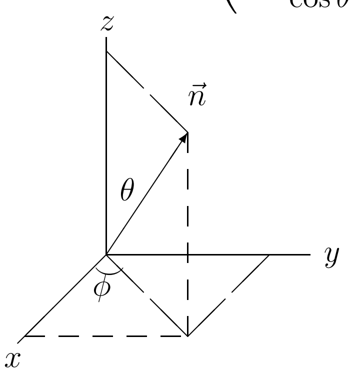

Figure 2.2: Definition of angles θ and ϕ for general $\vec{B} = B\vec{n}$

We want to write these solutions in terms of the basic matrices $\mathcal{T}_\alpha(\tau)$ and $\mathcal{R}_\alpha(\tau)$ given in (2.17) and (2.19), with $\alpha = x, y, z$. Therefore we need the fundamental relations:

$$
\begin{aligned}
\vec{\sigma} \cdot \mathcal{R}_{\vec{n}}(\tau)\vec{B} &= \mathcal{T}_{\vec{n}}(\tau)\; \vec{\sigma} \cdot \vec{B}\; \mathcal{T}_{\vec{n}}^{-1}(\tau); && (2.21a)\\
\vec{L} \cdot \mathcal{R}_{\vec{n}}(\tau)\vec{B} &= \mathcal{R}_{\vec{n}}(\tau)\; \vec{L} \cdot \vec{B}\; \mathcal{R}_{\vec{n}}^{-1}(\tau). && (2.21b)
\end{aligned}
$$

The proof is straightforward from Eqs.(2.16) and (2.18), by evaluating both sides term by term. From these relations one has, by exponentiating:

$$
\begin{aligned}
\mathcal{T}_{\mathcal{R}_{\vec{n}}(\tau)\vec{m}}(\phi) &= \mathcal{T}_{\vec{n}}(\tau)\; \mathcal{T}_{\vec{m}}(\phi)\; \mathcal{T}_{\vec{n}}^{-1}(\tau) && (2.22a)\\
\mathcal{R}_{\mathcal{R}_{\vec{n}}(\tau)\vec{m}}(\phi) &= \mathcal{R}_{\vec{n}}(\tau)\; \mathcal{R}_{\vec{m}}(\phi)\; \mathcal{R}_{\vec{n}}^{-1}(\tau). && (2.22b)
\end{aligned}
$$

Applying this relation successively to a rotation over ϕ around $\hat{z}$ and over θ around $\hat{y}$, yields:

Solution Larmor equation for a constant field $\vec{B} = B\vec{n}$:

$$
\begin{aligned}
|\chi(t)\rangle &= \mathcal{T}_z(\phi)\; \mathcal{T}_y(\theta)\;\; \mathcal{T}_z^{-1}(\gamma B t)\;\; \mathcal{T}_y^{-1}(\theta)\; \mathcal{T}_z^{-1}(\phi)\;\; |\chi(0)\rangle; && (2.23a)\\
\vec{S}(t) &= \mathcal{R}_z(\phi)\; \mathcal{R}_y(\theta)\;\; \mathcal{R}_z^{-1}(\gamma B t)\;\; \mathcal{R}_y^{-1}(\theta)\; \mathcal{R}_z^{-1}(\phi)\;\; \vec{S}(0). && (2.23b)
\end{aligned}
$$

In these equations only the basic matrices $\mathcal{T}_\alpha(\tau)$ and $\mathcal{R}_\alpha(\tau)$ occur, with $\alpha = x, y, z$.
One observes the "general rule" that **any $\mathcal{T}$-operator for spinors corresponds to a rotation operator $\mathcal{R}$ for the spin and that they occur in the same order with the same arguments.** This rule also holds for time dependent fields $\vec{B}(t)$ as can be seen from Eqs.(2.14).

2.2.4 Solution for a rotating field

Here we discuss the very important case of a rotating magnetic field as sketched in Fig. 2.3

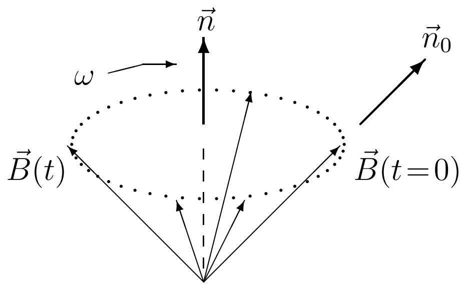

Figure 2.3: Rotating field $\vec{B}(t)$ around the $\vec{n}$-axis with frequency ω

and given by

$$\vec{B}(t) = B\mathcal{R}_{\vec{n}}^{-1}(\omega t)\,\vec{n}_0, \tag{2.24}$$

where the unit vector $\vec{n}$ is the rotation axis, the unit vector $\vec{n}_0$ is the direction of $\vec{B}(t=0)$, $B = |\vec{B}(t)|$ is the length of $\vec{B}(t)$ and ω is the rotation frequency. Such fields are highly interesting due to their curious consequences discussed in this thesis, which are similar to those seen in nuclear magnetic resonance (NMR). Furthermore, the corresponding Larmor equations: (cf. Eqs.(2.11) and (2.13))

$$\begin{aligned}
\frac{d}{dt}|\chi(t)\rangle &= \frac{1}{2}\, i\,\vec{\sigma}\cdot\gamma B\mathcal{R}_{\vec{n}}^{-1}(\omega t)\,\vec{n}_0\,|\chi(t)\rangle; \\
\frac{d}{dt}\vec{S}(t) &= i\,\vec{L}\cdot\gamma B\mathcal{R}_{\vec{n}}^{-1}(\omega t)\,\vec{n}_0\,\vec{S}(t).
\end{aligned}$$

can be solved exactly as we show here.
For this purpose we define the "rotated" spinor and spin

$$|\chi_r(t)\rangle \equiv \mathcal{T}_{\vec{n}}(\omega t)\,|\chi(t)\rangle \quad \text{and} \quad \vec{S}_r(t) \equiv \mathcal{R}_{\vec{n}}(\omega t)\,\vec{S}(t),$$

so that, inversely

$$|\chi(t)\rangle = \mathcal{T}_{\vec{n}}^{-1}(\omega t)\,|\chi_r(t)\rangle \quad \text{and} \quad \vec{S}(t) = \mathcal{R}_{\vec{n}}^{-1}(\omega t)\,\vec{S}_r(t).$$

Upon substitution, we get, with Eqs.(2.21):

$$\begin{aligned}
\mathcal{T}_{\vec{n}}(\omega t)\frac{d}{dt}\,\mathcal{T}_{\vec{n}}^{-1}(\omega t)|\chi_r(t)\rangle &= \frac{1}{2}\,i\,\vec{\sigma}\cdot\gamma B\vec{n}_0\ \ |\chi_r(t)\rangle \\
\mathcal{R}_{\vec{n}}(\omega t)\frac{d}{dt}\,\mathcal{R}_{\vec{n}}^{-1}(\omega t)\vec{S}_r(t) &= i\,\vec{L}\cdot\gamma B\vec{n}_0\ \ \vec{S}_r(t).
\end{aligned}$$

The time derivatives of $\mathcal{T}_{\vec{n}}^{-1}(\omega t)$ and $\mathcal{R}_{\vec{n}}^{-1}(\omega t)$ follow from the definitions Eqs.(2.15), so that

$$\frac{d}{dt}|\chi_r(t)\rangle = \frac{1}{2}\,i\,\vec{\sigma}\cdot[\gamma B\vec{n}_0-\omega\vec{n}]\ |\chi_r(t)\rangle; \tag{2.25a}$$

$$\frac{d}{dt}\vec{S}_r(t) = i\,\vec{L}\cdot[\gamma B\vec{n}_0-\omega\vec{n}]\ \vec{S}_r(t). \tag{2.25b}$$

These equations are formally identical with (2.11) and (2.13). So, in this "rotating frame" the neutron sees a **time-independent** effective field

$$\Omega\vec{m}\equiv\gamma B\vec{n}_0-\omega\vec{n},$$

i.e. the sum of the real field $\gamma B\vec{n}_0$ and a virtual component $-\omega\vec{n}$ along the rotation axis. The effective frequency Ω and the unit vector $\vec{m}$ are explicitly given in Eqs.(2.27d) and (2.27e) below. The vector diagram is shown in Fig. 2.4.

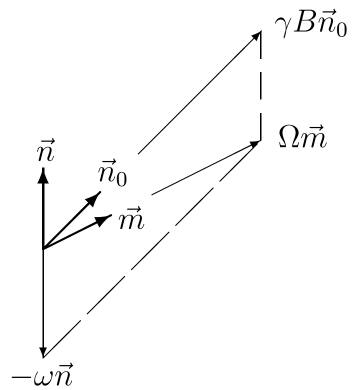

Figure 2.4: Diagram of the effective field $\Omega\vec{m}$ in the rotating frame.

The solution can be written down as in Eqs.(2.20):

$$\begin{aligned}
|\chi_r(t)\rangle &= \mathcal{T}_{\vec{m}}^{-1}(\Omega t)\ \ |\chi_r(0)\rangle \\
\vec{S}_r(t) &= \mathcal{R}_{\vec{m}}^{-1}(\Omega t)\ \vec{S}_r(0).
\end{aligned} \tag{2.26}$$

Using $|\chi_r(0)\rangle=|\chi(0)\rangle$ and $\vec{S}_r(0)=\vec{S}(0)$ and including the definitions of $|\chi_r(t)\rangle$ and $\vec{S}_r(t)$ yields the final result in the laboratory system which is summarized here:

The solution of the Larmor equation for a rotating magnetic field:

$$\vec{B}(t) \quad = \quad B\mathcal{R}_{\vec{n}}^{-1}(\omega t)\,\vec{n}_0 \tag{2.27a}$$

reads

$$|\chi(t)\rangle \quad = \quad \mathcal{T}_{\vec{n}}^{-1}(\omega t)\mathcal{T}_{\vec{m}}^{-1}(\Omega t)\ \ |\chi(0)\rangle \tag{2.27b}$$

$$\vec{S}(t) \quad = \quad \mathcal{R}_{\vec{n}}^{-1}(\omega t)\mathcal{R}_{\vec{m}}^{-1}(\Omega t)\ \ \vec{S}(0), \tag{2.27c}$$

where

$$\Omega \quad = \quad \sqrt{(\gamma B)^2 + \omega^2 - 2\omega\gamma B\vec{n}\cdot\vec{n}_0} \tag{2.27d}$$

$$\vec{m} \quad = \quad (\gamma B/\Omega)\vec{n}_0 - (\omega/\Omega)\vec{n}. \tag{2.27e}$$

In the next two paragraphs we discuss the consequences for two special cases.

2.2.5 Adiabatic spin flipper in time

First, we consider a planar magnetic field of the form

$$\vec{B}(t) = B\ (0,\ \sin\omega t,\ \cos\omega t) \equiv B\ \mathcal{R}_{\hat{x}}^{-1}(\omega t)\hat{z} \tag{2.28}$$

which rotates in the y,z-plane. Such a field is used for adiabatic spin flippers in time. The vector diagram takes the shape of Fig. 2.5.

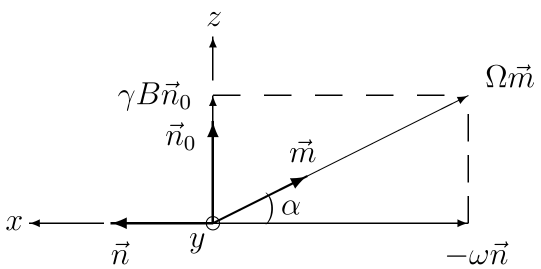

Figure 2.5: Diagram of the effective field $\Omega\vec{m}$ for a planar field rotating in the y,z-plane.

According to Eq.(2.27c) the spin at time t is

$$\vec{S}(t) = \mathcal{R}_{\hat{x}}^{-1}(\omega t)\ \mathcal{R}_{\vec{m}}^{-1}(\Omega t)\ \ \vec{S}(0) \tag{2.29}$$

with

$$\Omega = \sqrt{(\gamma B)^2 + \omega^2}; \tag{2.30a}$$

$$\vec{m} = (-\cos\alpha,\ 0,\ \sin\alpha) \equiv -\mathcal{R}_y(\alpha)\ \hat{x}; \quad \cos\alpha = \frac{\omega}{\Omega}; \quad \sin\alpha = \frac{\gamma B}{\Omega}, \tag{2.30b}$$

as illustrated in Fig. 2.5. Applying (2.22) the spin becomes:

$$\vec{S}(t) = \mathcal{R}_x^{-1}(\omega t)\ \mathcal{R}_y(\alpha)\ \mathcal{R}_x(\Omega t)\ \mathcal{R}_y^{-1}(\alpha)\ \ \vec{S}(0). \tag{2.30c}$$

Now we ask: In how far does the macroscopic spin $\vec{S}(t)$ follow the field $\vec{B}(t)$ in time? We start at $t = 0$ with spin $\vec{S}(0)$ in the direction of $\vec{B}(0)$, so that $\vec{S}(0) = \hat{z}$. At time t, the field has the direction $\hat{B}(t) = \mathcal{R}_x^{-1}(\omega t)\hat{z}$. The component of $\vec{S}(t)$ in the direction of $\vec{B}(t)$ is equal to the dot product

$$\vec{S}(t) \cdot \hat{B}(t) = \hat{z} \cdot \mathcal{R}_y(\alpha)\ \mathcal{R}_x(\Omega t)\ \mathcal{R}_y^{-1}(\alpha)\ \ \hat{z}$$

which gives the textbook result [10]

$$\vec{S}(t) \cdot \hat{B}(t) = 1 - \frac{2}{1+k^2} \sin^2\left(\frac{\omega t}{2}\sqrt{1+k^2}\right) \tag{2.31}$$

where k is the so called adiabaticity parameter

$$k \equiv \frac{\gamma B}{\omega}, \tag{2.32}$$

i.e. the ratio between the Larmor precession frequency γB and the frequency ω at which the field rotates. One sees that for $k \gg 1$, $\vec{S}(t) \cdot \hat{B}(t) \simeq 1$ for all times. This means: the spin $\vec{S}(t)$ "follows" the field (with small oscillations). There is an "adiabatic" region of frequencies $0 < \omega \ll \gamma B$ for which $k \gg 1$ and $\vec{S}(t) \cdot \hat{B}(t) \simeq 1$ for all times. In this way we manipulate spins "adiabatically".
Adiabatic spin flippers are well known from daily life. Consider a small magnet (compass needle) which is free to rotate and has some direction $\vec{S}(t=0)$. Take a second, strong, magnet and make sure that its field is parallel to $\vec{S}(0)$. Then, rotate the strong magnet (slowly!). The small magnet will follow, with tiny oscillations like in Fig. 2.6a. and k=2.5

A remarkable effect occurs when we rotate the field quickly: $\omega \gg \gamma B$ or $k \ll 1$. Then one has from Eqs.(2.30) and for $\omega \to \infty$:

$$\Omega = \omega\ [1 + \frac{1}{2}\left(\frac{\gamma B}{\omega}\right)^2 + ...\ ] \qquad \text{and} \qquad \alpha = \frac{\gamma B}{\omega} \to 0.$$

In Eq.(2.30c) we substitute $\mathcal{R}_y(\alpha) = \mathcal{I} + \mathcal{O}(\alpha)$, so that for $\omega \to \infty$

$$\vec{S}(t) = \mathcal{R}_x\left(\frac{\gamma^2 B^2}{2\omega} t\right) \vec{S}(0). \tag{2.33}$$

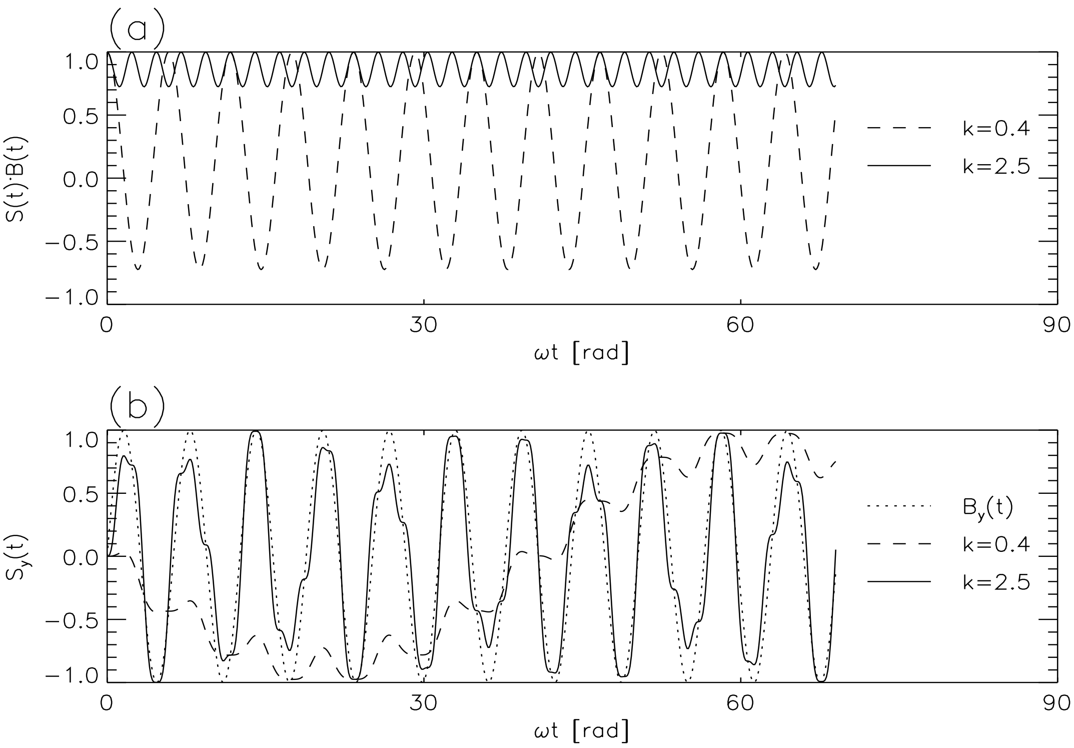

Figure 2.6: (a): $\vec{S}(t)\cdot\hat{B}(t)$ (Eq. (2.31)) for 2 values of the adiabaticity parameter k and $\vec{S}(0) = \hat{z}$. The minima are $1 - 2/(1 + k^2)$. (b): $\vec{S}(t)\cdot\hat{y}$ with $\vec{S}(0) = \hat{x}$ of Eq.(2.30c). For k=0.4, $\vec{S}(t)$ rotates slowly in the opposite sense as $\vec{B}(t)$. For k=2.5, $\vec{S}(t)$ closely follows $\vec{B}(t)$.

Thus, while the field rapidly rotates as $\vec{B}(t) = B\,\mathcal{R}_{\hat{x}}^{-1}(\omega t)\hat{z}$, the macroscopic spin $\vec{S}(t)$ rotates slowly in the **opposite** direction. This is illustrated in Fig. 2.6b for k=0.4.

In general one has the rule of thumb that $\vec{S}(t)$ remains $\simeq \vec{S}(0)$ for $\omega \gg \gamma B$ and finite times $t \ll 2\omega/(\gamma B)^2$. Physically this means that the spins cannot follow the field. They stay virtually constant in time. If we let the field quickly rotate over exactly π, this means that the spin initially parallel to the field, finds itself anti-parallel to the field: it has "flipped" relative to the field.

To estimate numerically the effect of a rapidly rotating field with zero time average for all times t we employ the replacement rule for $\omega \gg \gamma B$:

$$\vec{B}(t) \equiv B\,\mathcal{R}_{\vec{n}}(\omega t)\vec{n}_0 \quad \Rightarrow \quad \vec{B}_{eff} = \frac{\gamma B}{2\omega} B\,\vec{n}. \tag{2.34a}$$

This means that a rapidly rotating field $\vec{B}(t)$ around the $\hat{n}$-axis can be replaced by an effective constant field $\vec{B}_{eff}$ in the $\vec{n}$-direction as sketched in Fig. 2.7. We

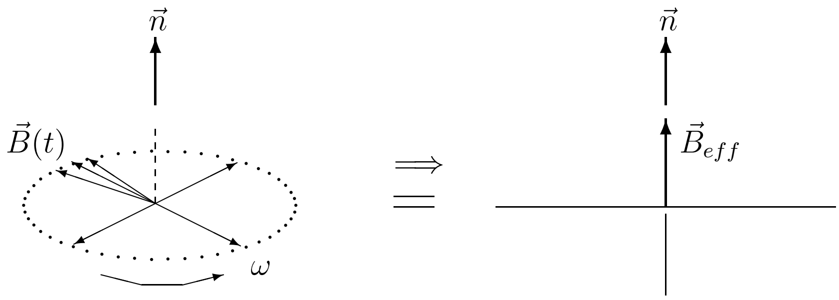

Figure 2.7: A planar rotating field around the $\vec{n}$-axis is replaced by a constant field $\vec{B}_{eff}$ in the $\vec{n}$ direction for high frequencies $\omega \gg \gamma B$.

have derived this rule in Eq.(2.33) where we showed that the initial phase $\vec{n}_0$ of $\vec{B}(t)$ is irrelevant.
We generalize this replacement rule for $\omega \gg \gamma B$ to

$$\vec{B}(t) = B\mathcal{R}_{\vec{n}(t)}(\omega t)\ \vec{n}_0(t) \quad \Rightarrow \quad \frac{\gamma B}{2\omega} B\ \vec{n}(t) \tag{2.34b}$$

where $\vec{n}(t)$ and $\vec{n}_0(t)$ are slowly varying in time, as compared with the fast rotation ωt. This can be derived by considering $\vec{n}(t)$ and $\vec{n}_0(t)$ in subsequent time intervals where they are constant. Then in each time interval one uses (2.34a). Again one observes that the initial phase $\vec{n}_0(t)$ of the rapidly rotating field vanishes in the replacement.

2.2.6 Resonance RF Spin Flipper in time

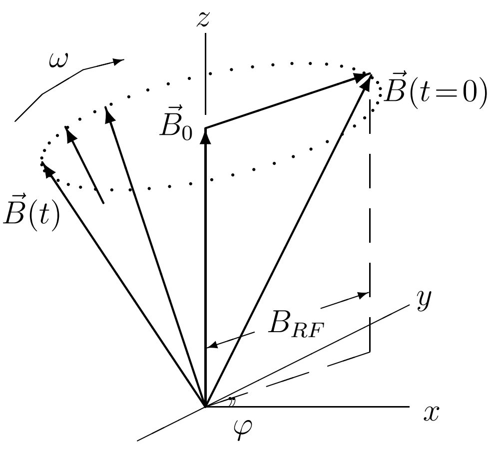

Figure 2.8: $\vec{B}(t)$ for a Resonance Flipper

In the second example, we consider a magnetic field of the form

$$\vec{B}(t) = B_0\hat{z} + B_{RF}(\cos(\omega t + \varphi),\ -\sin(\omega t + \varphi),\ 0). \tag{2.35}$$

The first term is a (strong) static field B_0 in the z-direction. In the technology of NMR it can be as high as several T; in our experimental setup (Chapter 7) it does not exceed 0.1 T. The second term is a "RF field" rotating around the z-axis with a frequency in the radio-frequency (RF) domain. In practice the amplitude B_{RF} of the latter is much smaller than the value B_0 of the static field. The phase φ is the initial phase of the RF field. In general such weak RF fields ($B_{RF} \ll B_0$) have no effect on the macroscopic spin $\vec{S}(t)$ and can be neglected: the vector $\vec{S}$ rotates (precesses) around the z-axis as due to the static field alone. Hence, the component $\vec{S}(t)\cdot\hat{z}$ is virtually constant in time. However, crucial exceptions occur for a narrow range of frequencies $|\omega| \simeq |\gamma B_0|$, which is the so-called "resonance condition". Here we show this explicitly.
We rewrite the field in the form $\vec{B}(t) = \mathcal{R}_z^{-1}(\omega t+\varphi)\ (B_{RF}, 0, B_0)$, or, equivalently, conform Eq.(2.24):

$$\vec{B}(t) = B\mathcal{R}_{\hat{z}}^{-1}(\omega t)\ \vec{n}_0,$$

where

$$B = \sqrt{B_0^2 + B_{RF}^2} \tag{2.36a}$$

$$\vec{n}_0 = \tfrac{1}{B}(B_{RF}\cos\varphi,\ -B_{RF}\sin\varphi,\ B_0). \tag{2.36b}$$

According to Eq.(2.27c) the solution for the macroscopic spin $\vec{S}(t)$ reads

$$\vec{S}(t) = \mathcal{R}_z^{-1}(\omega t)\ R_{\vec{m}}^{-1}(\Omega t)\ \ \vec{S}(0) \tag{2.37a}$$

with

$$\Omega = \sqrt{(\omega - \gamma B_0)^2 + (\gamma B_{RF})^2} \tag{2.37b}$$

$$\vec{m} = \tfrac{1}{\Omega}(\gamma B_{RF}\cos\varphi,\ -\gamma B_{RF}\sin\varphi,\ \gamma B_0 - \omega). \tag{2.37c}$$

The corresponding vector diagram is sketched in Fig. 2.9.

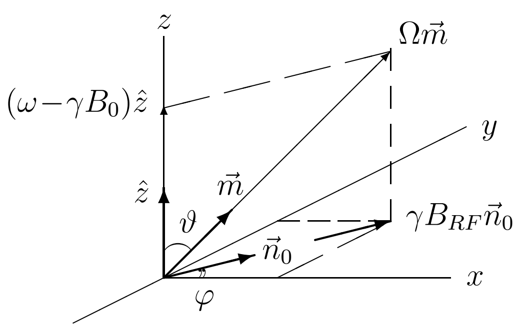

Figure 2.9: Diagram of the vectors $\vec{n}_0$ and $\vec{m}$ for the resonance flipper showing the angles ϑ and φ.

We define the angle ϑ through

$$\cos\vartheta = \frac{\gamma B_0 - \omega}{\Omega}; \quad \sin\vartheta = \frac{\gamma B_{RF}}{\Omega},$$

so that $\vec{m} = \mathcal{R}_z^{-1}(\varphi)\mathcal{R}_y(\vartheta)\,\hat{z}$ and we get the final result

$$\vec{S}(t) = \mathcal{R}_z^{-1}(\omega t + \varphi)\,\mathcal{R}_y(\vartheta)\,\mathcal{R}_z^{-1}(\Omega t)\,\mathcal{R}_y^{-1}(\vartheta)\,\mathcal{R}_z(\varphi)\;\vec{S}(0). \tag{2.38}$$

Now we consider the question: If one starts with spin in the direction of the (strong) static field $\vec{S}(0) = \hat{z}$, can we "flip" this spin to the opposite direction with the help of a weak RF-field? So again we calculate the dot product

$$\vec{S}(t)\cdot\hat{z} = \hat{z}\cdot\mathcal{R}_y(\vartheta)\,\mathcal{R}_z^{-1}(\Omega t)\,\mathcal{R}_y^{-1}(\vartheta)\;\hat{z}$$

which yields (cf. Eq.2.31):

$$\vec{S}(t)\cdot\hat{z} = 1 - \frac{2}{1+k^2}\sin^2\left(\frac{\gamma B_{RF} t}{2}\sqrt{1+k^2}\right) \tag{2.39}$$

where in this case the adiabaticity parameter k is defined as

$$k \equiv \frac{\gamma B_0 - \omega}{\gamma B_{RF}}. \tag{2.40}$$

Since $B_0 \gg B_{RF}$ the parameter k is in general $\gg 1$. Therefore $\vec{S}(t)\cdot\hat{z} \simeq 1$ (with small oscillations) and the spin will not flip. The important exception is $\omega = \gamma B_0$, i.e. the resonance condition for which $k = 0$. Then one has:

$$\vec{S}(t)\cdot\hat{z} = 1 - 2\sin^2\frac{\gamma B_{RF}\,t}{2}. \tag{2.41}$$

One sees that the spins oscillate between the direction parallel/antiparallel to $\hat{z}$ with a period $2\pi/(\gamma B_{RF})$. So, spins can be flipped in a strong static field B_0 with a weak RF-field in resonance condition $\omega = \gamma B_0$.
Finally we note the effect of the field of Eq.(2.35) on an arbitrary initial spin $\vec{S}(0)$ or spinor $|\chi(0)\rangle$. For $\omega = \gamma B$ one has in Eq.(2.38) that $\vartheta = \pi/2$, so

$$\begin{aligned} \vec{S}(t) &= \mathcal{R}_z^{-1}(\omega t + \varphi)\,\mathcal{R}_x^{-1}(\gamma B_{RF} t)\,\mathcal{R}_z(\varphi)\;\vec{S}(0) \\ |\chi(t)\rangle &= \mathcal{T}_z^{-1}(\omega t + \varphi)\,\mathcal{T}_x^{-1}(\gamma B_{RF} t)\,\mathcal{T}_z(\varphi)\;|\chi(0)\rangle, \end{aligned} \tag{2.42}$$

where for $|\chi(t)\rangle$ we applied the "general rule" given below Eqs.(2.23). For the special RF application time $t_{RF} = \pi/\gamma B_{RF}$ one finds

$$\begin{aligned} \vec{S}(t_{RF}) &= \mathcal{R}_z^{-1}(\omega t_{RF} + \varphi)\,\mathcal{R}_x^{-1}(\pi)\,\mathcal{R}_z(\varphi)\;\vec{S}(0) \\ |\chi(t_{RF})\rangle &= \mathcal{T}_z^{-1}(\omega t_{RF} + \varphi)\,\mathcal{T}_x^{-1}(\pi)\,\mathcal{T}_z(\varphi)\;|\chi(0)\rangle. \end{aligned}$$

We apply the relations which follow from Eqs.(2.22):

$$\mathcal{R}_x^{-1}(\pi)\,\mathcal{R}_z(\varphi) = \mathcal{R}_z^{-1}(\varphi)\,\mathcal{R}_x^{-1}(\pi) \tag{2.43a}$$
$$\mathcal{T}_x^{-1}(\pi)\,\mathcal{T}_z(\varphi) = \mathcal{T}_z^{-1}(\varphi)\,\mathcal{T}_x^{-1}(\pi). \tag{2.43b}$$

Because of its importance we summarize the final result in the following set of self-contained equations.

The solution of the Larmor equation for a spin flipper with rotating RF field

$$\vec{B}(t) = (B_{RF}\cos(\omega t+\varphi),\ -B_{RF}\sin(\omega t+\varphi),\ B_0) \tag{2.44a}$$
$$\text{with} \qquad \omega = \gamma B_0; \qquad t_{RF} = \pi/\gamma B_{RF} \tag{2.44b}$$

reads

$$\vec{S}(t_{RF}) = \mathcal{R}_z^{-1}(\gamma B_0 t_{RF} + 2\varphi)\,\mathcal{R}_x^{-1}(\pi)\ \ \vec{S}(0) \tag{2.44c}$$
$$|\chi(t_{RF})\rangle = \mathcal{T}_z^{-1}(\gamma B_0 t_{RF} + 2\varphi)\mathcal{T}_x^{-1}(\pi)\ \ |\chi(0)\rangle. \tag{2.44d}$$

One sees clearly: if $\vec{S}(0) = \hat{z}$ then $\vec{S}(t_{RF}) = -\hat{z}$ and if $\vec{S}(0) = -\hat{z}$ then $\vec{S}(t_{RF}) = \hat{z}$. Therefore it is a spin flipper for any phase angle φ.
For initial spin $\vec{S}(0)$ in general, the final spin $\vec{S}(t_{RF})$ will depend on the phase φ of the RF-field. Note that $\gamma B_0 t_{RF} = \pi B_0/B_{RF} \gg 1$ is very large so that the spin rotates many times.

2.2.7 Zero field precession in time

Now we discuss the basics of the remarkable and important phenomenon of "zero-field-precession", that is "as if" spins rotate in a region with $\vec{B} = 0$: no field present. We take the field as in the resonance flipper, Eqs.(2.44). We apply the field from $t = 0$ to $t = t_{RF}$ and switch it off. After an arbitrarily long "waiting time" T we switch it on again from $t = T$ to $t = T + t_{RF}$, as sketched in Fig. 2.10.

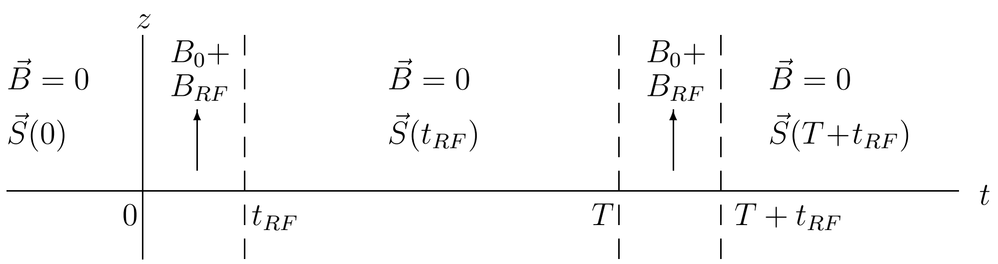

Figure 2.10: Sequence of two resonance flipping processes

As we have seen in Eqs.(2.44) the spin after one flipper is:

$$\vec{S}(t_{RF}) = \mathcal{R}_z^{-1}(\gamma B_0 t_{RF} + 2\varphi)\ \mathcal{R}_x^{-1}(\pi)\ \ \vec{S}(0).$$

At time T the phase of the magnetic field $\vec{B}(t)$ is $\varphi^* = \omega T + \varphi$. Therefore the spin after two flippers is $\vec{S}(T + t_{RF}) = \mathcal{R}_z^{-1}(\gamma B_0 t_{RF} + 2\varphi^*)\ \mathcal{R}_x^{-1}(\pi)\ \ \vec{S}(t_{RF})$. Substitution of $\vec{S}(t_{RF})$ yields

$$\vec{S}(T + t_{RF}) = \mathcal{R}_z^{-1}(2(\varphi^* - \varphi))\ \vec{S}(0). \tag{2.45}$$

Here we used Eq.(2.43). We note that the large term $\gamma B_0 t_{RF}$ in the argument of $\mathcal{R}_z^{-1}$ cancels. Substitution of the phase φ^* yields with $\omega = \gamma B_0$

$$\vec{S}(T + t_{RF}) = \mathcal{R}_z^{-1}(2\gamma B_0 T)\ \vec{S}(0). \tag{2.46}$$

This result is the same as for a constant field $2B_0\hat{z}$ present all the time from $t = 0$ up to T. Hence the name "zero-field precession" for two RF flippers separated by a time T and field zero in the time between.

2.2.8 Time dependent field in one direction

The Larmor Equation can be solved for time dependent magnetic fields $\vec{B}(t)$ with a fixed direction $\hat{B}$, but with an amplitude $B(t)$ which depends in an arbitrary way on t, i.e. $\vec{B}(t) = B(t)\hat{B}$. The exact solutions are immediately obtained from Eqs.(2.20):

$$|\chi(t)\rangle = \mathcal{T}_{\hat{B}}^{-1}(\phi(t))\ \ |\chi(0)\rangle \tag{2.47a}$$

$$\vec{S}(t) = \mathcal{R}_{\hat{B}}^{-1}(\phi(t))\ \vec{S}(0), \tag{2.47b}$$

where the rotation angle $\phi(t)$ is given by

$$\phi(t) = \gamma \int_0^t dt'\ B(t'). \tag{2.47c}$$

Physically this means that the spin $\vec{S}(t)$ rotates around the $\hat{B}$-axis over an angle which is the integral of the field $B(t')$ it has experienced up to time t.
For comparison with the Resonance Spin Flipper we consider in particular

$$\vec{B}(t) = (B_0 + B_{RF}\cos\omega t)\hat{B},$$

so that $\phi(t) = \gamma B_0 t + \frac{\gamma B_{RF}}{\omega}\sin\omega t$.
When $B_{RF} \ll B_0$ one finds that $\phi(t) \simeq \gamma B_0 t$ for all times t and all ω. There is no "resonance condition" for such a field. So, linearly polarized RF-fields in the **same** direction as the strong field B_0 have no (systematic) effect on the spin and can always be neglected.

2.2.9 Equivalence of Linearly and Circularly polarized field

Instead of the circularly polarized field as defined in Eq.(2.35), one uses in practice a linearly polarized RF-field orthogonal to the strong constant field $\vec{B}_0$. Here we show that both are equivalent. So we study the effect of a field

$$\vec{B}(t) = (2B_{RF}\cos(\omega t+\varphi),\ 0,\ B_0) \tag{2.48}$$

where $B_0\hat{z}$ is the strong static field as sketched in Fig. 2.11.

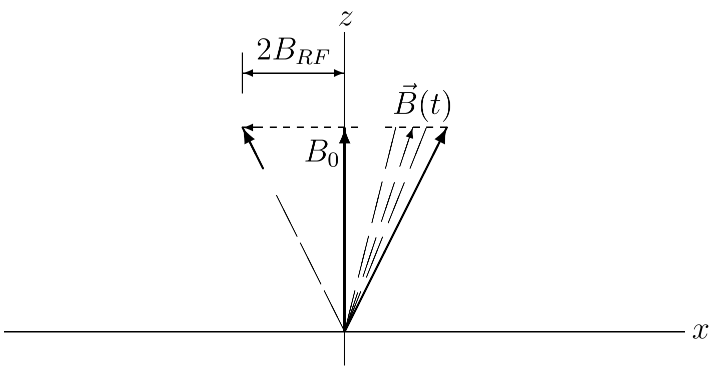

Figure 2.11: Linearly polarized RF field in the x-direction

We consider the resonance condition $\omega = \gamma B_0$ and small amplitudes $2B_{RF} \ll B_0$ or, equivalently, high frequencies $\omega \gg 2\gamma B_{RF}$. We rewrite the RF field as

$$\vec{B}(t) = B_0\hat{z} + B_{RF}\mathcal{R}_z^{-1}(\omega t+\varphi)\ \hat{x} + B_{RF}\mathcal{R}_z(\omega t+\varphi)\ \hat{x}, \tag{2.49}$$

so it is written as the sum of two circularly polarized fields rotating in opposite directions. The Larmor equation reads (cf. Eq.2.13)

$$\frac{d}{dt}\vec{S}(t) = i\ \vec{L}\cdot\gamma\vec{B}(t)\ \ \vec{S}(t).$$

Now we define a frame rotating at frequency ω around $\hat{z}$. In this frame the spin is $\vec{S}_r(t) = \mathcal{R}_z(\omega t+\varphi)\ \vec{S}(t)$, so that the Larmor equation becomes:

$$\frac{d}{dt}\vec{S}_r(t) = i\ \vec{L}\cdot\gamma\vec{B}_r(t)\ \ \vec{S}_r(t),$$

with the field in this frame given by

$$\vec{B}_r(t) = B_{RF}\hat{x} + B_{RF}\mathcal{R}_z(2\omega t+2\varphi)\ \hat{x}.$$

Note that the strong field $\vec{B}_0$ has been transformed away and one of the circularly polarized fields has become a weak constant field $B_{RF}\hat{x}$. It is transformed away by defining the spin in the doubly rotating frame (with frequency γB_{RF} around $\hat{x}$ of the previous rotating frame) as

$$\vec{S}_{rr}(t) \equiv \mathcal{R}_x(\gamma B_{RF} t)\ \vec{S}_r(t).$$

The corresponding Larmor equation becomes

$$\frac{d}{dt}\vec{S}_{rr}(t) = i\ \vec{L}\cdot\gamma\vec{B}_{rr}(t)\ \ \vec{S}_{rr}(t),$$

where now

$$\vec{B}_{rr}(t) = B_{RF}\mathcal{R}_x(\gamma B_{RF} t)\mathcal{R}_z(2\omega t + 2\varphi)\hat{x}.$$

We are left with a field $B_{rr}(t)$ which is quickly rotating with a zero time average. Such fields have only minor effects on the spins as we show here.
We write, equivalently,

$$\vec{B}_{rr}(t) = B_{RF}\mathcal{R}_{\vec{n}(t)}(2\omega t)\ \vec{n}_0(t) \tag{2.50a}$$

with

$$\hat{n}(t) = \mathcal{R}_x(\gamma B_{RF} t)\ \hat{z} \quad \text{and} \quad \hat{n}_0(t) = \mathcal{R}_{\hat{n}(t)}(2\varphi)\ \hat{x}. \tag{2.50b}$$

As we have discussed in § **2.2.5**, such quickly rotating fields ($\omega \gg 2\gamma B_{RF}$) may be replaced by

$$\vec{B}_{rr}(t) \Rightarrow \frac{\gamma B_{RF}^2}{4\omega}\hat{n}(t) = \frac{\gamma B_{RF}^2}{4\omega}\mathcal{R}_x(\gamma B_{RF} t)\hat{z}.$$

So, we obtain a replacement field which also rotates quickly since $\gamma B_{RF} \gg (\gamma B_{RF})^2/4\omega$. Therefore we may apply the second replacement

$$\vec{B}_{rr}(t) \to B_{rr}\hat{x}$$

with the effective field in the doubly rotating frame

$$B_{rr} = \frac{1}{32}\left(\frac{B_{RF}}{B_0}\right)^2 B_{RF}.$$

Thus we find the solution for $\vec{S}_{rr}(t)$ and high frequencies:

$$\vec{S}_{rr}(t) = \mathcal{R}_x^{-1}(\gamma B_{rr} t)\ \vec{S}_{rr}(0).$$

Back in the laboratory system, the spin is given by

$$\vec{S}(t) = \mathcal{R}_z^{-1}(\omega t + \varphi)\ \mathcal{R}_x^{-1}(\gamma(B_{RF} + B_{rr})t)\ \mathcal{R}_z(\varphi)\ \vec{S}(0).$$

Since $B_{rr} \ll B_{RF}$ we neglect B_{rr}. Then this result is the same as for a circularly polarized field Eq.(2.44). In summary:

The solution of the Larmor equation for a spin flipper with linear RF field:

$$\vec{B}(t) \;=\; (2B_{RF}\cos(\omega t+\varphi), 0,\; B_0) \tag{2.51a}$$

$$\text{with} \qquad \omega=\gamma B_0; \qquad t_{RF}=\pi/\gamma B_{RF} \tag{2.51b}$$

reads

$$\vec{S}(t_{RF}) \;=\; \mathcal{R}_z^{-1}(\gamma B_0 t_{RF}+2\varphi)\,\mathcal{R}_x^{-1}(\pi)\;\vec{S}(0) \tag{2.51c}$$

which has to be compared with Eqs.(2.44). Note that only half of the amplitude $2B_{RF}$ is effective in the spinflipper. We emphasize that this result is valid only when $B_0 \gg B_{RF}$. The result for the circularly polarized field is exact and valid for all B_0 and B_{RF}.

We conclude that a **linearly polarized** RF-field is equivalent to an RF-field which is **circularly polarized**, apart from a factor 2 in effective amplitude.

2.3 Space dependent fields

In this section we consider magnetic fields $\vec{B}(\vec{r},t) \equiv \vec{B}(\vec{r})$ which depend on $\vec{r}$ but **not** on time t. Then, the solution of the Schrödinger equation (2.4) can be written as

$$\psi(\vec{r},t) = e^{-i\omega t}\psi(\vec{r}),$$

where $E=\hbar\omega$ is the total energy of the neutron. As a result, the 2-dim. spinor $\psi(\vec{r})$ satisfies the **time-independent** Schrödinger equation

$$\left(-\frac{\hbar^2}{2m}\Delta - \frac{1}{2}\,\hbar\gamma\vec{\sigma}\cdot\vec{B}(\vec{r})\right)\psi(\vec{r}) = E\;\psi(\vec{r}). \tag{2.52}$$

In § **2.2.3** we already obtained the solution of the Larmor equation in a homogeneous field, universally present, but now we are interested in solutions which describe an incoming neutron beam with given energy E in vacuum (i.e. $\vec{B}(\vec{r})=0$) entering a region where $\vec{B}(\vec{r}) \neq 0$.

In the following we let the neutron move in the x-direction. For this physical situation the solutions $\psi(\vec{r})$ have been extensively studied in the theory of neutron reflectometry and we mention here the main results, as far as relevant in our investigation.

2.3.1 Semi-infinite space

Most basic is a neutron beam with spinor $|\chi^+_\alpha\rangle$ (hence macroscopic spin $\vec{S}_0 = \hat{\alpha}$, where $\hat{\alpha} = \hat{x}, \hat{y}, \hat{z}$), which enters the semi-infinite volume V for $x \geq 0$ where $\vec{B}(x) = B\hat{\beta}$ is constant. This is schematically drawn in Fig. 2.12.

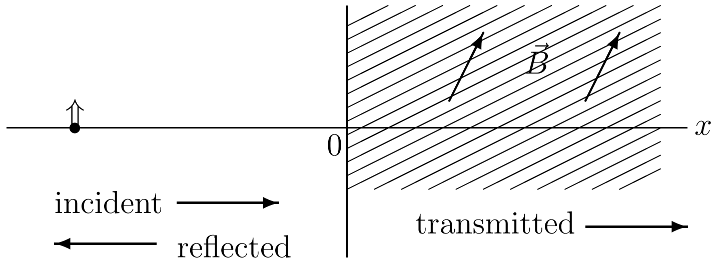

Figure 2.12: Polarized neutron beam in the x-direction entering a region with constant field $\vec{B}$.

The Schrödinger equation separates into two equations:

$$\left(-\frac{\hbar^2}{2m}\Delta\right)\psi(\vec{r}) = E\,\psi(\vec{r}) \qquad (x \leq 0) \tag{2.53a}$$

$$\left(-\frac{\hbar^2}{2m}\Delta - \frac{1}{2}\,\hbar\gamma B\sigma_\beta\right)\psi(\vec{r}) = E\,\psi(\vec{r}) \qquad (x > 0) \tag{2.53b}$$

with the requirements that $\psi(\vec{r})$, $\frac{\partial}{\partial x}\psi(\vec{r}), ..\frac{\partial}{\partial z}\psi(\vec{r})$ are continuous at $x = 0$. The solution for $x \leq 0$ reads:

$$\psi(x) \;=\; e^{ik_0x}|\chi^+_\alpha\rangle \;-\; R_+e^{-ik_0x}|\chi^+_\beta\rangle \;-\; R_-e^{-ik_0x}|\chi^-_\beta\rangle \qquad (x \leq 0)$$

with

$$E = \hbar\omega = \frac{\hbar^2k_0^2}{2m} = \frac{1}{2}\,mv_0^2.$$

The first term represents the incoming beam (going to the right) with energy E, velocity v_0 and spin $\vec{S}_0 = \hat{\alpha}$. The second and third terms are reflected beams (going to the left) with also energy E and spins $\hat{\beta}$ and $-\hat{\beta}$, respectively. R_+ and R_- are the corresponding reflection coefficients.
For $x \geq 0$ we use the fact that $|\chi^+_\beta\rangle$ and $|\chi^-_\beta\rangle$ are the eigenstates for the operator σ_β with eigenvalues $+1$ and -1 respectively, so

$$\psi(x) \;=\; T_+e^{ik_+x}|\chi^+_\beta\rangle \;+\; T_-e^{ik_-x}|\chi^-_\beta\rangle. \qquad (x \geq 0)$$

The first term represents a beam to the right with spin $\hat{\beta}$ and kinetic energy

$$E_+ \;=\; \frac{\hbar^2k_+^2}{2m} \;=\; E + \frac{1}{2}\,\hbar\gamma B \;=\; \frac{\hbar^2k_0^2}{2m} + \frac{1}{2}\,\hbar\gamma B.$$

The second term is a beam also going to the right but with spin $-\hat{\beta}$ and kinetic energy

$$E_- \;=\; \frac{\hbar^2 k_-^2}{2m} \;=\; E - \frac{1}{2}\,\hbar\gamma B \;=\; \frac{\hbar^2 k_0^2}{2m} - \frac{1}{2}\,\hbar\gamma B.$$

The wavevectors k_+ and k_- are related to k_0 by

$$k_+ = \sqrt{k_0^2 + \frac{m\gamma B}{\hbar}} \quad \text{and} \quad k_- = \sqrt{k_0^2 - \frac{m\gamma B}{\hbar}}. \tag{2.54}$$

T_+ and T_- are the corresponding transmission coefficients. One obtains the coefficients $R_\pm$ and $T_\pm$ from the continuity of $\psi(x)$ and its derivative at $x=0$. This gives, respectively:

$$|\chi_\alpha^+\rangle \;=\; (T_+ + R_+)|\chi_\beta^+\rangle \;+\; (T_+ + R_-)|\chi_\beta^-\rangle$$

$$|\chi_\alpha^+\rangle \;=\; (\frac{k_+}{k_0}T_+ - R_+)|\chi_\beta^+\rangle \;+\; (\frac{k_-}{k_0}T_+ - R_-)|\chi_\beta^-\rangle$$

and one finds the solutions, using the orthogonality relations Eq.(2.10):

$$T_\pm = \frac{2k_0}{k_\pm + k_0}\,\langle\chi_\beta^\pm|\chi_\alpha^+\rangle \qquad R_\pm = \frac{k_\pm - k_0}{k_\pm + k_0}\,\langle\chi_\beta^\pm|\chi_\alpha^+\rangle. \tag{2.55}$$

Thus we have derived exact expressions for this physical "scattering" process on a magnetic field boundary. Now we discuss some special cases.

2.3.2 Spin and field parallel or anti-parallel

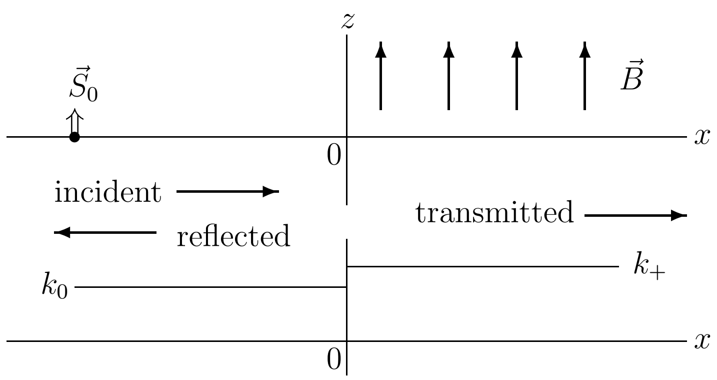

Figure 2.13: Polarized neutron beam in the x-direction; incoming spin and field parallel to z. k_0 and k_+ are the corresponding wavenumbers.

First, we apply the field **parallel** to z. Our assumptions regarding incoming spin and field mean: $|\chi_\alpha^+\rangle = |\chi_z^+\rangle$ and $\vec{B}(\vec{r}) = B\hat{z}$ with $B > 0$. It is illustrated in Fig. 2.13. The solution reads

$$\psi(x) = \;\; e^{ik_0x}|\chi_z^+\rangle \;-\; R_+e^{-ik_0x}|\chi_z^+\rangle \qquad (x \le 0) \tag{2.56a}$$

$$\psi(x) = \;\; T_+e^{ik_+x}|\chi_z^+\rangle \qquad (x > 0) \tag{2.56b}$$

$$T_+ = \frac{2k_0}{k_+ + k_0} \qquad R_+ = \frac{k_+ - k_0}{k_+ + k_0} \tag{2.56c}$$

This solution means: the spins in the incoming, reflected and transmitted beams are the same (no flip) and only k_+ occurs in the transmitted beam.
When the field is **anti-parallel** to z, we take again $|\chi_\alpha^+\rangle = |\chi_z^+\rangle$, but $\vec{B}(\vec{r}) = -B\hat{z}$ with $B > 0$. The solution is

$$\psi(x) = \; e^{ik_0x}|\chi_z^+\rangle \; - \; R_- e^{-ik_0x}|\chi_z^+\rangle \qquad (x \leq 0) \tag{2.57a}$$

$$\psi(x) = \; T_- e^{ik_-x}|\chi_z^+\rangle \qquad (x > 0) \tag{2.57b}$$

$$T_- = \frac{2k_0}{k_- + k_0} \qquad R_- = \frac{k_- - k_0}{k_- + k_0} \tag{2.57c}$$

Again, the spins in the incoming, reflected and transmitted beams are the same (no flip), but now only k_- occurs in the transmitted beam.
As a conclusion, for a polarized beam of neutrons (all spins in the same direction), magnetic fields in $\pm$ the spin-direction have **no** effect on the spins. One uses such fields as "guide fields" for polarized neutron beams. The fields are chosen smaller than the corresponding neutron kinetic energy to avoid unwanted reflection (for thermal neutrons this is satisfied in practice, since the kinetic energy $\simeq$25 meV is much larger than the magnetic term in Eq.(2.3) which even for a field of 1T is as low as 6.030×10^{-5} meV); they are taken larger than the disturbances from the outside world, like the earth magnetic field. They are necessary to keep spins aligned over large distances.

2.3.3 Spin orthogonal to field

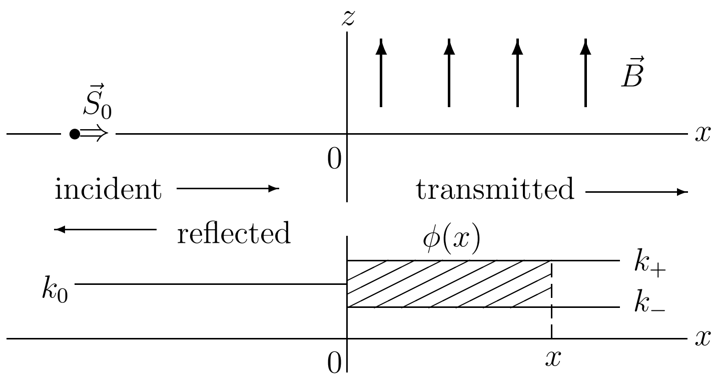

Figure 2.14: Polarized neutron beam in the x-direction; incident spin parallel to x and field parallel to z; k_0 and $k_\pm$ are the corresponding wavenumbers. The shaded area $\phi(x)$ is the rotation angle of the spin.

We take $|\chi_\alpha^+\rangle = |\chi_x^+\rangle$ and again $\vec{B}(\vec{r}) = B\hat{z}$ with $B > 0$. So the initial spin $\vec{S}_0 = \hat{x}$ is in the direction of the beam and perpendicular to the field. This is illustrated in Fig. 2.14. The solution is

$$\begin{aligned}\psi(x) &= e^{ik_0x}|\chi_x^+\rangle \;-\; R_+e^{-ik_0x}|\chi_z^+\rangle \;-\; R_-e^{-ik_0x}|\chi_z^-\rangle \qquad (x \leq 0)\\ &= T_+e^{ik_+x}|\chi_z^+\rangle \;+\; T_-e^{ik_-x}|\chi_z^-\rangle \qquad (x > 0)\end{aligned}$$

$$T_\pm = \frac{1}{\sqrt{2}}\,\frac{2k_0}{k_\pm + k_0} \qquad\qquad R_\pm = \frac{1}{\sqrt{2}}\,\frac{k_\pm - k_0}{k_\pm + k_0}.$$

In this case the spins in the incoming, reflected and transmitted beams are different, which makes it possible to manipulate them.
For the transmitted beam ($x \geq 0$) the expectation value of the spin, as defined by Eq.(2.6), is given by

$$\vec{S}(x) = \begin{pmatrix} 2T_+T_-\cos(k_+ - k_-)x \\ -2T_+T_-\sin(k_+ - k_-)x \\ T_+^2 - T_-^2 \end{pmatrix}.$$

So $\vec{S}(x)$ has a constant z-component, while the x and y components rotate as a function of x around the $\hat{B} = \hat{z}$-direction. Thus we can write $\vec{S}(x)$ as

$$\vec{S}(x) = (T_+^2 - T_-^2)\hat{z} \;+\; 2T_+T_-\mathcal{R}_z^{-1}(\phi(x))\hat{x}$$

where the rotation angle $\phi(x)$ equals $(k_+ - k_-)x$. One observes that this angle is equal to the shaded area shown in Fig. 2.14, as we will use later.
Now we consider neutron beams with a kinetic energy much larger than the magnetic interaction, i.e.

$$\hbar k_0^2 \gg m\gamma B,$$

or, equivalently, to small fields B. Then we may expand Eq.(2.54)

$$k_\pm = k_0 \pm \frac{\gamma B}{2v_0} + \mathcal{O}(B^2)$$

with $v_0 \equiv \hbar k_0/m$ the velocity of the incoming neutrons. In this limit one has $T_+ = T_- = 1/\sqrt{2}$ and $R_+ = R_- = 0$, what means that there is no significant reflected beam. Then the solution for $x > 0$ reads, with $\phi(x) = \gamma Bx/v_0$:

$$\psi(x) = \frac{1}{\sqrt{2}}\,e^{ik_0x}\begin{pmatrix} \exp i\phi(x)/2 \\ \exp -i\phi(x)/2 \end{pmatrix},$$

or, equivalently, using the operators introduced below Eqs. (2.14):

$$\psi(x) = e^{ik_0x}\,\mathcal{T}_z^{-1}(\phi(x))\,|\chi_x^+\rangle$$

$$\vec{S}(x) = \mathcal{R}_z^{-1}(\phi(x))\,\hat{x}.$$

2.3.4 Arbitrary directions of spin and field

The incoming neutron beam has spinor $|\chi_0\rangle$, i.e. spin $\vec{S}_0$. The field in the semi-infinite volume $x > 0$ is given by $\vec{B}(x) = B\hat{B}$. The velocity of the neutrons is large compared to the magnetic interaction ("$B \to 0$"), so that no neutrons reflect. Generalizing the previous equations, the solution for $x > 0$ can now be written, with $\phi(x) = \gamma Bx/v_0$:

$$\psi(x) = e^{ik_0x}|\chi(x)\rangle$$

with the spinor part

$$|\chi(x)\rangle = \mathcal{T}_{\hat{B}}^{-1}(\phi(x))\;|\chi(0)\rangle$$
$$\vec{S}(x) = \mathcal{R}_{\hat{B}}^{-1}(\phi(x))\;\vec{S}(0).$$

where $|\chi(0)\rangle = |\chi_0\rangle$ and $\vec{S}(0) = \vec{S}_0$ are the spinor and spin of the incoming beam. One observes a complete analogy with the solutions given by Eqs.(2.20) for neutrons at rest in a constant field. In fact, there is an equality when one substitutes $x = v_0t$. This is the basis of the semi-classical approximation discussed in § **2.3.6**.

2.3.5 Field over finite distance

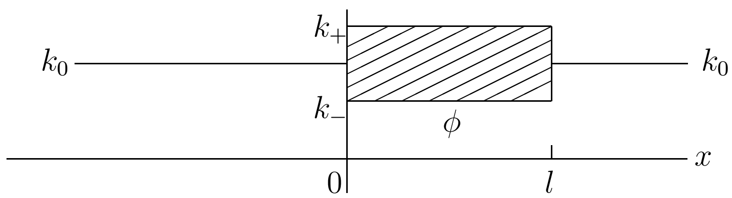

Figure 2.15: Field over finite length l. The shaded area is the total rotation angle of the spin.

A similar exact calculation can be made for a constant magnetic field over a finite distance. Now reflected beams appear from the entrance ($x=0$) and from the exit ($x=l$). We mention the fundamental property of the time-independent Schrödinger equation: **The neutrons which eventually come through the region ($0 < x < l$) with field, have the same energy as the incoming neutrons.**

The exact calculation is straightforward but rather involved due to the many reflection and transmission coefficients. In the limit $\hbar k_0^2 \gg \gamma B$ the results are quite obvious: there are no appreciable reflections at $x = 0$ and $x = l$. The neutron beam just goes through. When the initial spin is parallel to the field, the

spin will not change (as used in guide fields).
When the initial spinor $|\chi_0\rangle = |\chi_x^+\rangle$, spin $\vec{S}_0 = \hat{x}$, is orthogonal to $\vec{B} = B\hat{z}$ one finds for the transmitted beam, $x \geq l$:

$$\begin{aligned} \psi(x) &= e^{ik_0x}\,|\chi_f\rangle && (2.58a) \\ \vec{S}(x) &= \vec{S}_f && (2.58b) \end{aligned}$$

with outgoing, final, spinor and spin

$$\begin{aligned} |\chi_f\rangle &= \mathcal{T}_z^{-1}(\phi)\,|\chi_0\rangle && (2.58c) \\ \vec{S}_f &= \mathcal{R}_z^{-1}(\phi)\,\vec{S}_0, && (2.58d) \end{aligned}$$

where $\phi{=}\gamma Bl/v_0$ is the total rotation angle around the z-axis (cf. Fig. 2.15).
Such finite layers with fixed fields and length are used as monochromatic polarization rotators or spin flippers: one can rotate a spin $\vec{S}_0$ over any desired angle ϕ, but only for a single velocity v_0.

2.3.6 Semi-classical approximation

We consider a neutron beam in vacuum with velocity v_0 and spin $\vec{S}_0$ entering a finite layer of thickness l with a **spatially** varying field $\vec{B}(\vec{r}) = \vec{B}(x)$. If the kinetic energy of the neutrons is large (cf. § **2.3.3**), i.e. $\hbar k_0^2/m \gg \gamma B$, with $k_0 = mv_0/\hbar$ the wavenumber, we may neglect all reflections and write the 2D-spinor for all x

$$\psi(\vec{r}) = e^{ik_0x}\,|\chi(x)\rangle,$$

where

$$\begin{aligned} |\chi(x)\rangle &= |\chi_0\rangle \qquad (x \leq 0) && (2.59) \\ |\chi(x)\rangle &= |\chi_f\rangle. \qquad (x \geq l) && (2.60) \end{aligned}$$

The corresponding 3D-spin is then given by

$$\vec{S}(x) = \langle\chi(x)|\vec{\sigma}|\chi(x)\rangle$$

where $\vec{S}_0$ corresponds to $|\chi_0\rangle$ for $x \leq 0$ and $\vec{S}_f$ to $|\chi_f\rangle$ for $x \geq l$.
In the "semi-classical approximation" the neutron motion is treated classically but its spinor $|\chi(x)\rangle$ and spin $\vec{S}(x)$ quantum mechanically. That means that each neutron moves through the field $\vec{B}(x)$ with constant velocity v_0 and has a specific location $x = v_0t$. At time t the spinor and spin experience a magnetic field $\vec{B}(x = v_0t)$ and satisfy the time dependent Larmor equations (2.11) and (2.13):

$$\begin{aligned} \frac{d}{dt}|\chi(x = v_0t)\rangle &= \frac{1}{2}\,i\,\vec{\sigma}\cdot\gamma\vec{B}(x = v_0t)\,|\chi(x = v_0t)\rangle && (2.61a) \\ \frac{d}{dt}\vec{S}(x = v_0t) &= i\,\vec{L}\cdot\gamma\vec{B}(x = v_0t)\;\;\vec{S}(x = v_0t). && (2.61b) \end{aligned}$$

which hold for any $\vec{B}(\vec{r})$ as long as the magnetic interaction is smaller than the kinetic energy.
Below, we go one important step further. In § **2.3.8** we will consider magnetic fields $\vec{B}(x,t)$ in a finite layer which essentially depend both on space and time. For such fields we also apply the semi-classical approximation Eqs.(2.61) with the time dependent magnetic field as "seen by the neutron": $\vec{B}(x = v_0 t, t)$. Clearly, our approach is an interpolation: Eqs.(2.61) hold for fields $\vec{B}(x,t) = \vec{B}(t)$ which do not depend on space x and also for fields $\vec{B}(x,t) = \vec{B}(x)$ which do not depend on t.
We assume that the semi-classical approximation is valid for all fields $\vec{B}(x,t)$ and large kinetic energies.

2.3.7 Adiabatic static spin flipper

In Chapters 5 and 7 we consider polarization rotators and spinflippers which are adiabatic and "static", which means that the magnetic fields involved do not depend on time. Here we study a spatially rotating magnetic field $\vec{B}(\vec{r}) = \vec{B}(x)$ using the semi-classical approximation. For $0 \le x \le l$ the field is given by

$$\vec{B}(x) = B\ (0,\ \sin(\pi x/l),\ \cos(\pi x/l))$$

as illustrated in Fig. 2.16.

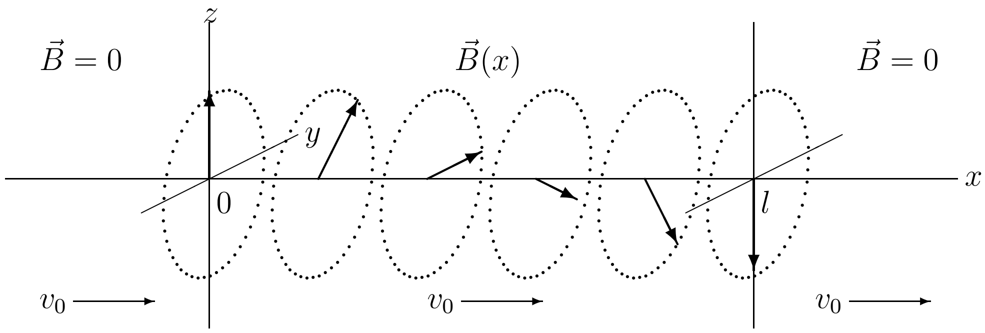

Figure 2.16: Field rotating in space around x

This field rotates uniformly in space from $\vec{B}(0) = B\hat{z}$ to $\vec{B}(l) = -B\hat{z}$ around the x-axis and can be written as

$$\vec{B}(x) = B\mathcal{R}_x^{-1}\left(\frac{\pi x}{l}\right)\hat{z}.$$

For $x = v_0 t$ we have the semi-classical approximation

$$\vec{B}(x = v_0 t) = B\mathcal{R}_{\hat{n}}^{-1}(\omega_g t)\hat{n}_0$$

with $\hat{n} = \hat{x}$; $\hat{n}_0 = \hat{z}$ and the geometric frequency $\omega_g = \pi v_0/l$. The field is of the form of Eq.(2.28) so that the spin is given by (cf. Eq. 2.29):

$$\vec{S}(x = v_0 t) = \mathcal{R}_x^{-1}(\omega_g t)\ \mathcal{R}_{\vec{m}}^{-1}(\Omega t)\ \ \vec{S}(0) \tag{2.62}$$

where

$$\Omega = \sqrt{(\gamma B)^2 + \omega_g^2} \quad \text{and} \quad \hat{m} = \frac{\gamma B}{\Omega}\hat{z} - \frac{\omega_g}{\Omega}\hat{x}.$$

We eliminate $t = x/v_0$ and find for $x \geq 0$:

$$|\chi(x)\rangle = \mathcal{T}_x^{-1}\left(\frac{\pi x}{l}\right)\mathcal{T}_{\hat{m}}^{-1}\left(\frac{\Omega x}{v_0}\right)\ |\chi(0)\rangle.$$

$$\vec{S}(x) = \mathcal{R}_x^{-1}\left(\frac{\pi x}{l}\right)\mathcal{R}_{\hat{m}}^{-1}\left(\frac{\Omega x}{v_0}\right)\ \vec{S}(0)$$

To express this result into elementary x, y, z-rotations we define the adiabaticity parameter as before (cf. Eq. 2.32):

$$k \equiv \frac{\gamma B}{\omega_g}; \qquad \kappa \equiv \sqrt{1 + k^2} = \frac{\Omega}{\omega_g}$$

and the angle α as before (Eq.2.30):

$$\cos\alpha = \frac{\omega_g}{\Omega} = \frac{1}{\kappa}; \quad \sin\alpha = \frac{\gamma B}{\Omega} = \frac{k}{\kappa},$$

so that $\hat{m} = -\mathcal{R}_y(\alpha)\hat{x}$ and we arrive at the result

$$|\chi(x)\rangle = \mathcal{T}_x^{-1}\left(\frac{\pi x}{l}\right)\mathcal{T}_y(\alpha)\mathcal{T}_x\left(\frac{\pi x \kappa}{l}\right)\mathcal{T}_y^{-1}(\alpha)\ |\chi(0)\rangle$$

$$\vec{S}(x) = \mathcal{R}_x^{-1}\left(\frac{\pi x}{l}\right)\mathcal{R}_y(\alpha)\mathcal{R}_x\left(\frac{\pi x \kappa}{l}\right)\mathcal{R}_y^{-1}(\alpha)\ \vec{S}(0).$$

We write the spin of the outgoing beam ($x{=}l$) as $\vec{S}(x{=}l) = \vec{S}_f$ so that

$$\vec{S}_f = P(k)\ \vec{S}_0$$

where $P(k)$ is the so-called ($3{\times}3$) polarization matrix which only depends on k and is given by

$$P(k) = \mathcal{R}_x^{-1}(\pi)\mathcal{R}_y(\alpha)\mathcal{R}_x(\pi\kappa)\mathcal{R}_y^{-1}(\alpha), \tag{2.63}$$

or explicitly

$$P(k) = \begin{pmatrix} 1 - \frac{2k^2}{1+k^2}\sin^2\frac{\pi}{2}\kappa & \frac{k}{\kappa}\sin\pi\kappa & -\frac{2k}{1+k^2}\sin^2\frac{\pi}{2}\kappa \\ \frac{k}{\kappa}\sin\pi\kappa & -\cos\pi\kappa & \frac{1}{\kappa}\sin\pi\kappa \\ \frac{2k}{1+k^2}\sin^2\frac{\pi}{2}\kappa & -\frac{1}{\kappa}\sin\pi\kappa & -1 + \frac{2}{1+k^2}\sin^2\frac{\pi}{2}\kappa \end{pmatrix}. \tag{2.64}$$

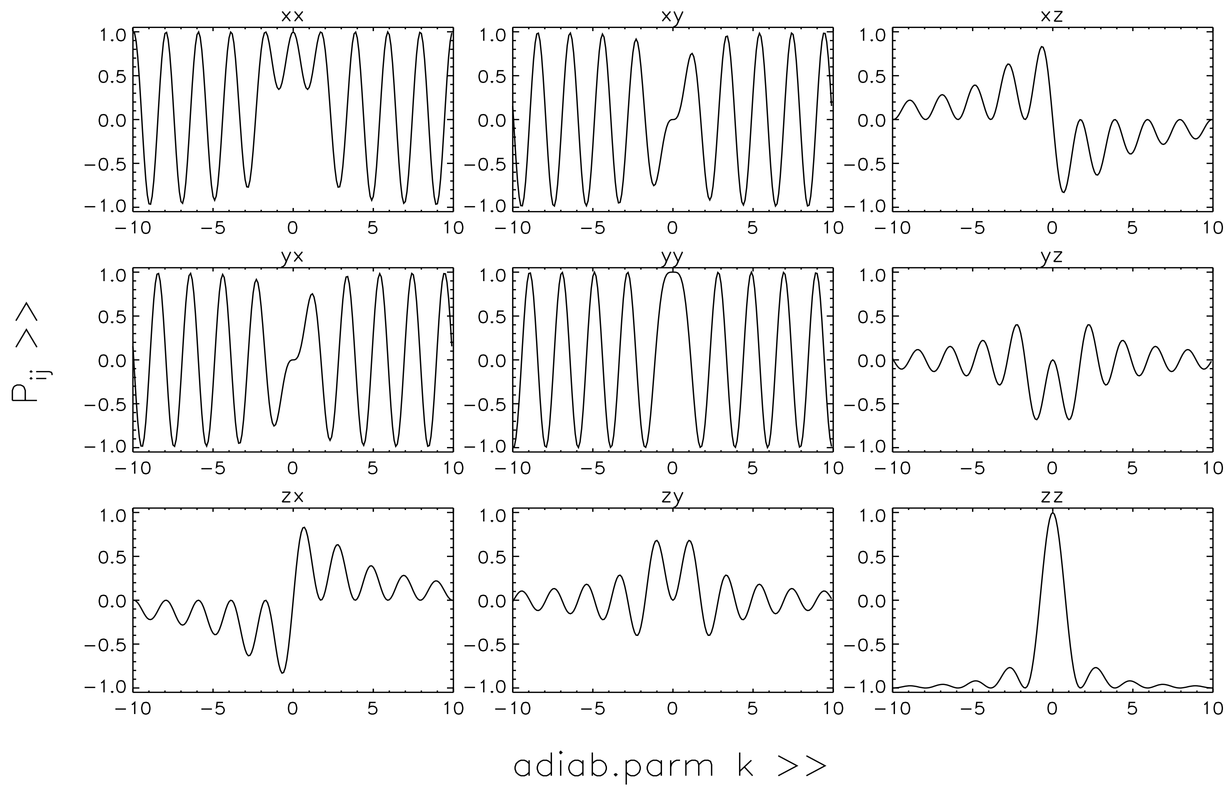

Figure 2.17: The elements of the polarization matrix $P(k)$ of Eq. (2.64) as a function of the adiabaticity parameter k.

The elements of this matrix are shown as a function of k in Fig. 2.17.
There is an adiabatic region of slow neutrons:

$$0 < \omega_g \ll \gamma B \Rightarrow k \gg 1; \qquad \alpha = \pi/2; \qquad \kappa = k$$

for which $P(k) = \mathcal{R}_x^{-1}(\pi)\mathcal{R}_z^{-1}(\pi k)$. One observes that initial spins are flipped from $-\hat{z}$ to $\hat{z}$ and vice versa. A derivation of the zz-element of $P(k)$ in Eq.(2.64) was published by Robiscoe [11]. In the next chapter we study this static flipper in more detail.

2.3.8 Adiabatic RF Spin Flipper

Here we study a device called "adiabatic RF spin flipper" as built for the first time in Gatchina, published in 1974 [12]. A first theoretical description appeared in 1975 [13]. It flips spins adiabatically just like the the static (time-independent) flipper of the previous paragraph. The essential difference is that the present flipper produces a field $\vec{B}(\vec{r}, t)$ which depends on space $\vec{r}$ **and** time t. We explain the advantage of this extra time dependence later.

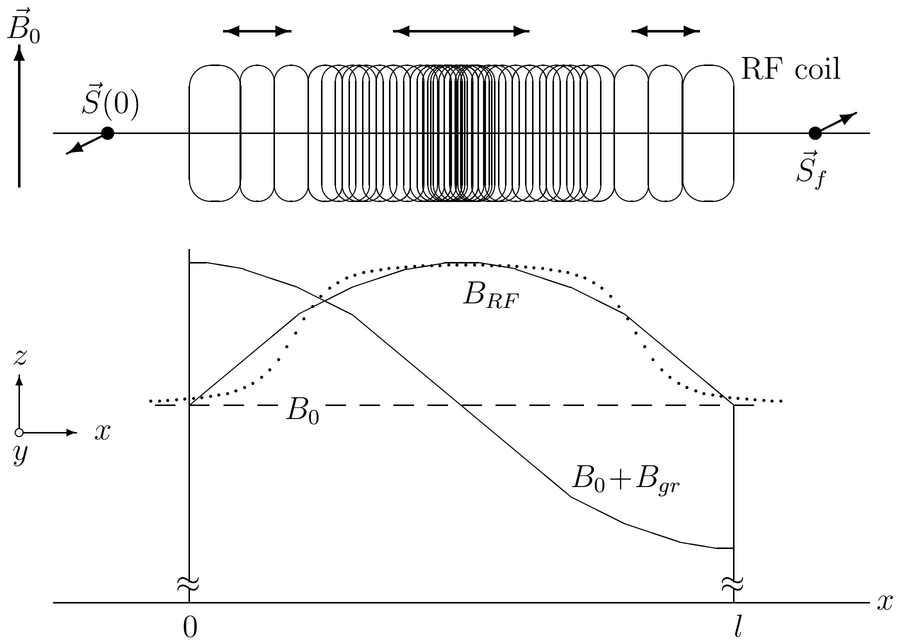

Figure 2.18: Adiabatic RF Spin Flipper. A polarized beam running in the x-direction has initial spin $\vec{S}_0$ and final spin $\vec{S}_f$. An RF coil - with highest winding density halfway - produces an RF field in the x-direction with amplitude $B_{RF}(x)$ shown in the bottom part (full line: idealized; dotted line: in practice). There is also a static space dependent field $B_0 + B_{gr}$ in the z-direction.

In Fig. 2.18 we sketch the essentials.
The resulting magnetic field $\vec{B}(x,t)$ for $0 \leq x \leq l$ is given by

$$\vec{B}(x,t) = (B_0 + B_{gr} \cos\left(\frac{\pi x}{l}\right))\ \hat{z} + 2B_{RF} \sin\left(\frac{\pi x}{l}\right) \cos(\omega t + \varphi)\ \hat{x}. \qquad (2.65)$$

The first term is a static field in the z-direction consisting of a strong homogeneous field B_0 with superimposed a weak "gradient field" $B_{gr}\cos(\pi x/l)$. The second term is an RF field in the x-direction, generated by a coil carrying currents with frequency ω. In practice this is a homogeneously wound coil of finite length with length/diameter ratio $\simeq 2$. The strength of its field along the axis qualitatively looks like the dotted line in Fig. 2.18.
We use this flipper in resonance condition $\omega = \gamma B_0$. Moreover we set $B_{RF} = B_{gr}$ and $B_0 \gg B_{RF}$.
We let a neutron enter the device at time $t = 0$ with velocity v_0 along the x-axis. This neutron experiences a time dependent field $\vec{B}(t) \equiv \vec{B}(x = v_0 t, t)$ which can be written as (with $B_{gr} = B_{RF}$):

$$\vec{B}(t) = B_0\hat{z} + B_{RF}\mathcal{R}_z^{-1}(\omega t + \varphi)\mathcal{R}_y(\omega_g t)\hat{z} + B_{RF}\mathcal{R}_z(\omega t + \varphi)\sin(\omega_g t)\hat{x}$$

with $\omega_g = \pi v_0/l$ the geometric rotation frequency. The corresponding Larmor

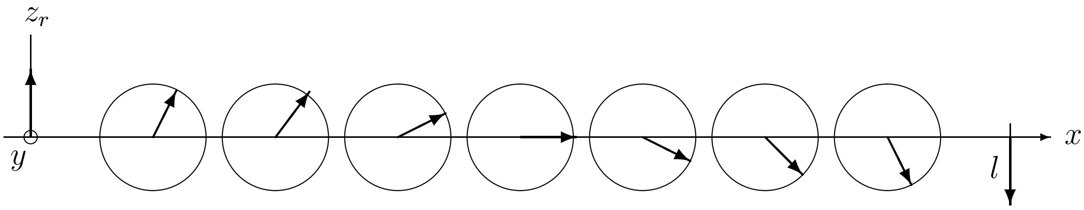

Figure 2.19: Magnetic field in the singly rotating coordinate system.

equation reads (cf. Eq.2.13):

$$\frac{d}{dt}\vec{S}(t) = i\ \vec{L}\cdot\gamma\vec{B}(t)\ \ \vec{S}(t). \tag{2.66}$$

We define the spin in the frame rotating at frequency ω around $\hat{z}$ as

$$\vec{S}_r(t) \equiv \mathcal{R}_z(\omega t + \varphi)\ \vec{S}(t)$$

For the corresponding Larmor equation one finds, using $\omega = \gamma B_0$:

$$\frac{d}{dt}\vec{S}_r(t) = i\ \vec{L}\cdot\gamma\vec{B}_r(t)\ \ \vec{S}_r(t) \tag{2.67a}$$

with

$$\vec{B}_r(t) = B_{RF}\mathcal{R}_y(\omega_g t)\hat{z} + B_{RF}\mathcal{R}_z(2\omega t + 2\varphi)\sin(\omega_g t)\ \hat{x}. \tag{2.67b}$$

The first term is sketched in Fig. 2.19. In the doubly rotating frame the spin is

$$\vec{S}_{rr}(t) \equiv \mathcal{R}_y^{-1}(\omega_g t)\vec{S}_r(t)$$

and the corresponding Larmor equation reads

$$\frac{d}{dt}\vec{S}_{rr}(t) = i\ \vec{L}\cdot\gamma\vec{B}_{rr}(t)\ \ \vec{S}_{rr}(t) \tag{2.68a}$$

with

$$\vec{B}_{rr}(t) = \frac{1}{\gamma}\Omega\vec{m} + B_{RF}\mathcal{R}_y^{-1}(\omega_g t)\mathcal{R}_z(2\omega t + 2\varphi)\sin(\omega_g t)\ \hat{x}. \tag{2.68b}$$

The first term is a constant field with

$$\Omega = \sqrt{\gamma B_{RF}^2 + \omega_g^2}; \qquad \vec{m} = \frac{\gamma B_{RF}}{\Omega}\hat{z} + \frac{\omega_g}{\Omega}\hat{y}. \tag{2.68c}$$

Its magnitude is of order B_{RF} (or larger, depending on ω_g). The second term is a field with maximum amplitude B_{RF} rotating around the origin at high frequency $2\omega = 2\gamma B_0$. We have seen in § **2.2.5** that the effect of such a field can be replaced by a constant field which is at most of magnitude $(B_{RF}/B_0)B_{RF}$, see (2.34a). Since $B_{RF}/B_0 \ll 1$ we may neglect the second term in Eq.(2.68b) and obtain the solution:

$$\vec{S}_{rr}(t) = \mathcal{R}_{\vec{m}}^{-1}(\Omega t)\vec{S}_{rr}(0).$$

We go back to the laboratory system and find

$$\vec{S}(t) = \mathcal{R}_z^{-1}(\omega t + \varphi)\mathcal{R}_y(\omega_g t)\mathcal{R}_{\vec{m}}^{-1}(\Omega t)\mathcal{R}_z(\varphi)\ \vec{S}(0).$$

We define the angle β by

$$\hat{m} = \mathcal{R}_x^{-1}(\beta)\ \hat{z}; \quad \sin\beta = \omega_g/\Omega$$

and have the final result in resonance condition

$$\vec{S}(t) = \mathcal{R}_z^{-1}(\omega t + \varphi)\mathcal{R}_y(\omega_g t)\mathcal{R}_x^{-1}(\beta)\mathcal{R}_z^{-1}(\Omega t)\mathcal{R}_x(\beta)\mathcal{R}_z(\varphi)\ \vec{S}(0). \tag{2.69}$$

We are interested in the spin which comes out of the flipper at time $t = l/v_0$ so that $\omega_g t = \pi$. We obtain for the final spin $\vec{S}_f \equiv \vec{S}(t = l/v_0)$:

$$\vec{S}_f = \mathcal{R}_z^{-1}\Big(\frac{\omega}{\omega_g}\pi + \varphi\Big)\ \mathcal{R}_y(\pi)\mathcal{R}_x^{-1}(\beta)\ \mathcal{R}_z^{-1}\Big(\frac{\Omega}{\omega_g}\pi\Big)\ \mathcal{R}_x(\beta)\mathcal{R}_z(\varphi)\ \ \vec{S}(0). \tag{2.70a}$$

$$\omega_g = \pi v_0/l; \quad \Omega = \sqrt{\gamma^2 B_{RF}^2 + \omega_g^2}; \quad \sin\beta = \omega_g/\Omega. \tag{2.70b}$$

We now show how our device works as an adiabatic spin flipper.
For fixed RF amplitude B_{RF} there is a range of neutron velocities v_0 for which $0 \le \omega_g \ll \gamma B_{RF}$, hence $\beta \downarrow 0$; $\Omega \downarrow \gamma B_{RF}$. For this "adiabatic" region one has

$$\vec{S}_f = \mathcal{R}_z^{-1}\Big(\frac{\omega}{\omega_g}\pi + \varphi\Big)\ \mathcal{R}_y(\pi)\mathcal{R}_z^{-1}\Big(\frac{\gamma B_{RF}\ \pi}{\omega_g}\Big)\ \mathcal{R}_z(\varphi)\ \ \vec{S}(0).$$

Applying the relations (2.43) twice gives

$$\vec{S}_f = \mathcal{R}_z^{-1}\Big(\frac{\omega}{\omega_g}\pi + \varphi\Big)\ \mathcal{R}_z\Big(\frac{\gamma B_{RF}\ \pi}{\omega_g}\Big)\ \mathcal{R}_z^{-1}(\varphi)\mathcal{R}_y(\pi)\ \vec{S}(0)$$

or, summarizing:

The solution of the Larmor equation for an adiabatic RF flipper with

$$\vec{B}(x,t) = \Big(2B_{RF}\sin\frac{\pi x}{l}\cos(\omega t + \varphi),\ 0,\ B_0 + B_{gr}\cos\frac{\pi x}{l}\Big) \quad (0 \le x \le l)$$

with $\qquad B_{RF} = B_{gr}; \quad \omega = \gamma B_0; \quad \omega_g = \pi v_0/\ell \ll \gamma B_{RF} \ll \gamma B_0$
yields the final spin ($x \ge l$)

$$\vec{S}_f = \mathcal{R}_z^{-1}(\Phi + 2\varphi)\ \mathcal{R}_y(\pi)\ \ \vec{S}(0), \tag{2.71}$$

$$\Phi = \gamma(B_0 - B_{RF})\pi/\omega_g$$

for a neutron which enters at $t = 0$ with velocity v_0.

For any phase φ one sees that if $\vec{S}(0) = +\hat{z} \Rightarrow \vec{S}_f = -\hat{z}$ and if $\vec{S}(0) = -\hat{z} \Rightarrow \vec{S}_f = +\hat{z}$, so our device acts as a spin flipper for all slow neutrons for which $\omega_g \ll \gamma B_{RF}$.
To see what happens for arbitrary initial spin $\vec{S}(0)$, we consider a classical incoming beam of neutrons, all with the same spin $\vec{S}(0)$ and velocity v_0 as sketched in Fig. 2.20. Let neutron 1 enter the flipper at $t = 0$. Its final spin is then according to Eq.(2.71): $\vec{S}_{f,1} = \mathcal{R}_z^{-1}(\Phi + 2\varphi)\mathcal{R}_y(\pi)\ \vec{S}(0)$. The second neutron arrives a time $\Delta t = \Delta x/v_0$ later at the entrance of the flipper. It sees a phase $\varphi_2 = \omega\Delta t + \varphi$, so its final spin is $\vec{S}_{f,2} = \mathcal{R}_z^{-1}(\Phi + 2\varphi_2)\mathcal{R}_y(\pi)\ \vec{S}(0)$. Thus we conclude that at any time t two neutrons in the outgoing beam separated by a distance Δx have **different** spins, related by

$$\vec{S}_{f,1} = \mathcal{R}_z\left(\frac{2\omega}{v_0}\Delta x\right)\ \vec{S}_{f,2}. \tag{2.72}$$

Classically, the outgoing beam consists of a train of (different) neutrons moving to the right with velocity v_0, with progressing spins as we observe farther to the right.
It is of interest to give a quantum mechanical description of such a particular beam. For $x \geq l$ we define the 2D spinor

$$|\psi(x,t)\rangle = a_+\ e^{i\phi_+ + ik_+x - i\omega_v(k_+)t}|\chi_z^+\rangle + a_-\ e^{i\phi_- + ik_-x - i\omega_v(k_-)t}|\chi_z^-\rangle$$

where $\omega_v(k)$ is the vacuum dispersion relation:

$$\omega_v(k) \equiv \hbar k^2/2m.$$

One recognizes that $|\psi(x,t)\rangle$ is an exact solution of the time-dependent Schrödinger Equation (2.4) in vacuum for all real values of a_+, a_-, ϕ_+, ϕ_-, k_+ and k_-.
According to Eq.(2.6) the macroscopic spin $\vec{S}(x,t)$ corresponding to $|\psi(x,t)\rangle$ is

$$\vec{S}(x,t) = \mathcal{R}_z^{-1}(\ (k_+ - k_-)(x - v_0 t)\ )\begin{pmatrix} 2a_+a_-\cos(\phi_+ - \phi_-) \\ -2a_+a_-\sin(\phi_+ - \phi_-) \\ a_+^2 - a_-^2 \end{pmatrix}$$

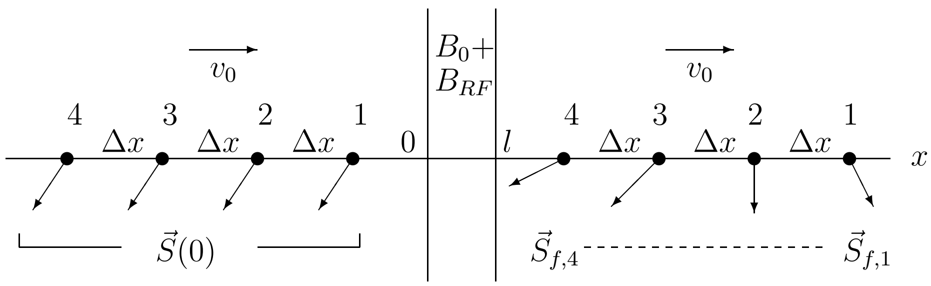

Figure 2.20: Visualization of zero field precession.

where v_0 is the averaged velocity

$$v_0 \equiv \frac{\hbar(k_+ + k_-)}{2m}$$

and we have the relation for all $x \geq l$, $\Delta x \geq 0$:

$$\vec{S}(x,t) = \mathcal{R}_z((k_+ - k_-)\Delta x)\ \vec{S}(x + \Delta x, t).$$

This relation is the same as Eq.(2.72) when we take $k_+ - k_- = 2\omega/v_0$. We conclude that the 2D-spinor $|\psi(x,t)\rangle$ indeed describes quantum mechanically the outgoing beam for our adiabatic RF spin flippers. As noted in § **2.3.5** such spinors in vacuum are impossible to get from static spin flippers.

2.3.9 Zero field precession in space

Here we discuss "zero field precession" in space for a polarized incoming neutron beam with fixed spin $\vec{S}(0)$ moving along the x-axis with velocity v_0. We let the beam go through an adiabatic RF flipper from $0 \leq x \leq l$ and through a second identical flipper from $L \leq x \leq L + l$. The two flippers are identical and **synchronized**, i.e. their RF fields are given by Eq.(2.65). We follow the neutron

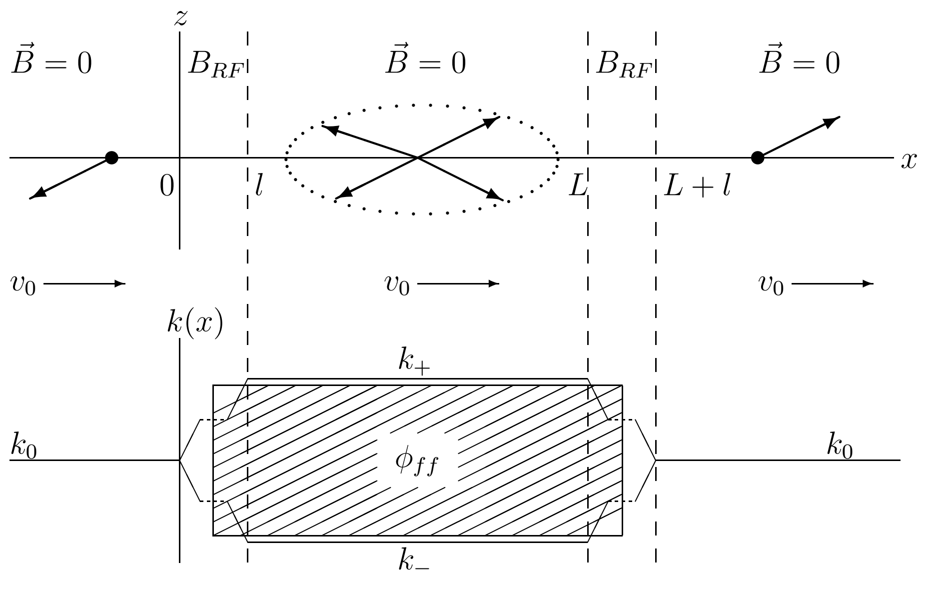

Figure 2.21: Zero field precession between two adiabatic RF flippers

that arrives at time t_0 at $x = 0$. It sees a phase of the RF-field: $\varphi_0 = \omega t_0 + \varphi$. According to Eq.(2.71) its spin after the first flipper is

$$\vec{S}(t = t_0 + l/v_0) = \mathcal{R}_z^{-1}(\Phi + 2\varphi_0)\mathcal{R}_y(\pi)\ \vec{S}(0).$$

As discussed above, $\vec{S}(t)$ depends on the arrival time t_0 and can have any direction in the x, y-plane as sketched in Fig. 2.21. This neutron arrives at the second flipper at $t^* = t_0 + L/v_0$ and sees a phase $\varphi^* = \omega t^* + \varphi_0 = \omega L/v_0 + \varphi_0$. The final spin for $x \geq L + l$ is then

$$\vec{S}_{ff} = \mathcal{R}_z^{-1}(\Phi + 2\varphi^*)\mathcal{R}_y(\pi)\mathcal{R}_z^{-1}(\Phi + 2\varphi_0)\mathcal{R}_y(\pi)\ \vec{S}(0).$$

Applying the relations (2.43) twice gives, with $\omega = \gamma B_0$

$$\vec{S}_{ff} = \mathcal{R}_z^{-1}(2\gamma B_0 L/v_0)\ \vec{S}(0). \tag{2.73}$$

So, all spins in the transmitted beam are **the same**, i.e the spin $\vec{S}_{ff}$ does not depend on the arrival time t_0. In fact one sees that $\vec{S}_{ff}$ is obtained "as if" a magnetic field $2B_0\hat{z}$ was present all the way from $x = 0$ to $x = L$, hence "zero field precession" as sketched schematically in the bottom of Fig. 2.21. We write $\vec{S}_{ff} = \mathcal{R}_z^{-1}(\phi_{ff})\ \vec{S}(0)$ with $\phi_{ff} = (k_+ - k_-)L$ equal to the shaded area. By combining this with Eq.(2.73) we find

$$k_\pm = k_0 \pm \gamma B_0/v_0.$$

We conclude that two RF flippers separated by a distance L have the same effect as a homogeneous field of twice the strength of the field in the flippers over that distance L. In Spin Echo Spectrometers one needs such strong homogeneous fields over distances L as large as possible (up to several meters). Such long fields require correction devices to homogenize their line integrals over an acceptably large beam cross section [14],[15]. One may replace a homogeneous field by two RF flippers located as far apart as needed and separated by zero field, as was proposed by Golub and Gähler [16] and as we have shown here.

Chapter 3

Basic techniques to handle neutron spins

In this Chapter we discuss the basic experimental techniques to handle polarized neutron beams which are used in the experiments described in Chapters 4-9. All experiments are performed on three set-ups for polarized neutrons installed in beam lines of the 2 MW nuclear research reactor HOR ("Hoger Onderwijs Reactor") at IRI. These instruments are known as "PANDA" ("Poly Axis Neutron Depolarization Analysis"), "SP" ("Spiegel Polarimeter") and "SESANS".

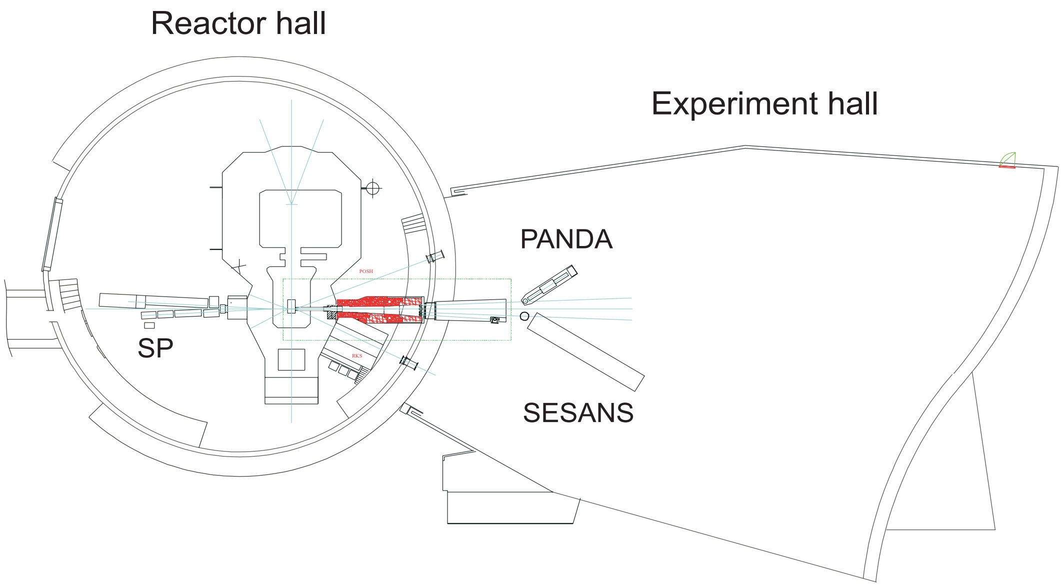

Figure 3.1: Reactor Hall and Experiment Hall at IRI showing the positions of the instruments SP, PANDA and SESANS

Fig. 3.1 gives an overview how these instruments are situated in the Reactor Hall and the Experiment Hall at IRI. We discuss these instruments below. First we consider the essential parts.

3.1 White neutron beams

As the neutron beams emerge from the beam ports of the reactor, they have a so called "thermal" neutron velocity ($\equiv$ wavelength) distribution, with an excess of "hot" neutrons (so called "white" beam). To give an idea, the thermal neutron spectrum $J(\lambda)$, as predicted by statistical theory for a source temperature of 300 K - in terms of wavelength $\lambda = h/(mv)$ - is given in Fig. 3.2. In practice the

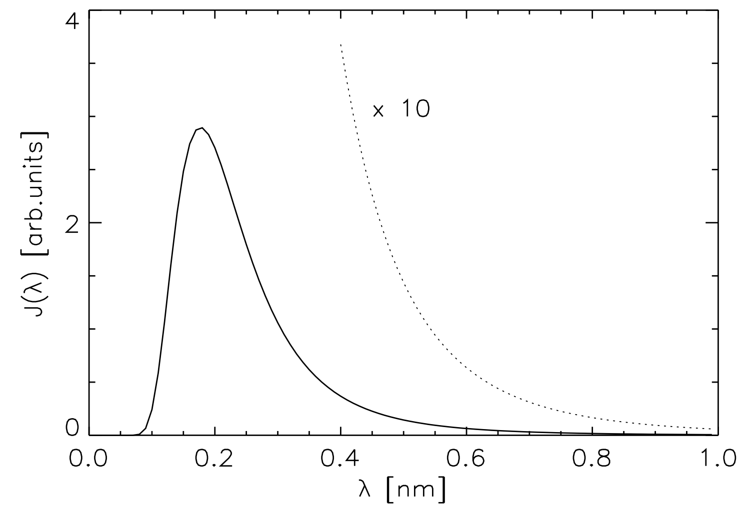

Figure 3.2: Theoretical neutron spectrum $J(\lambda)$ in the beam lines of the HOR.

spectrum starts at $\lambda = 0.05$ nm, reaches a maximum at $\lambda \approx 0.17$ nm and decays rapidly above $\lambda = 0.4$ nm.
The neutrons in this white beam $J(\lambda)$ have a spin which is arbitrarily directed in any direction, i.e. their average spin is zero ("unpolarized").

3.2 Monochromators

We use monochromators to select from the white beam $J(\lambda)$ a monochromatic beam, i.e. a beam with limited velocity v (wavelength λ) range with a spread Δv ($\Delta\lambda$). In practice we mainly employ a pyrolytic graphite (PG) crystal and apply Bragg's law

$$\lambda = 2d \sin\theta$$

to reflect a monochromatic neutron beam. Here d=0.69 nm is the lattice constant of PG and 2θ is the angle between the incoming and the reflected beam. By choosing θ (and $\Delta\theta$) we obtain the desired wavelength λ (and $\Delta\lambda$). The PG crystal has no effect on the spin, hence the resulting reflected monochromatic beam is still unpolarized.

3.3 Neutron Spin Polarizers

The most essential part in neutron spin technology is the "polarizer" which transforms an unpolarized beam (spin in all directions) into a "polarized" beam (spin in one direction). Our polarizers are based on total reflection from "magnetic mirrors".

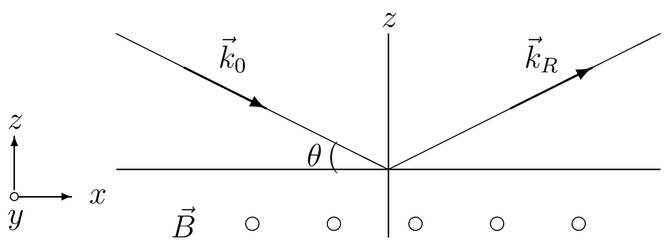

Figure 3.3: Reflection of a neutron beam on a magnetized surface. The amount of reflection $R_\pm$ depends on the initial spin state ($\pm$).

The principal mechanism of reflection is sketched in Fig. 3.3. For $z \leq 0$ there is a homogeneous magnetic field $\vec{B} = B\hat{y}$. The incoming neutron beam has velocity v and angle of incidence θ so that, with $k = mv/\hbar$

$$\vec{k}_0 = k\,(\cos\theta,\ 0,\ -\sin\theta).$$

We write the 2D spinor for $z \geq 0$ as

$$\psi_\pm(\vec{r}) \equiv e^{i\vec{k}_0\cdot\vec{r}}\,|\chi_y^\pm\rangle - R_\pm e^{i\vec{k}_R\cdot\vec{r}}\,|\chi_y^\pm\rangle.$$

The first term is the incident beam, the second term the reflected beam with

$$\vec{k}_R = k\,(\cos\theta,\ 0,\ \sin\theta)$$

and the spin is either parallel or anti-parallel to y. Using the methods of § **2.3.1** one finds for the reflection coefficients

$$R_\pm = \frac{\sqrt{1\pm\xi}-1}{\sqrt{1\pm\xi}+1},$$

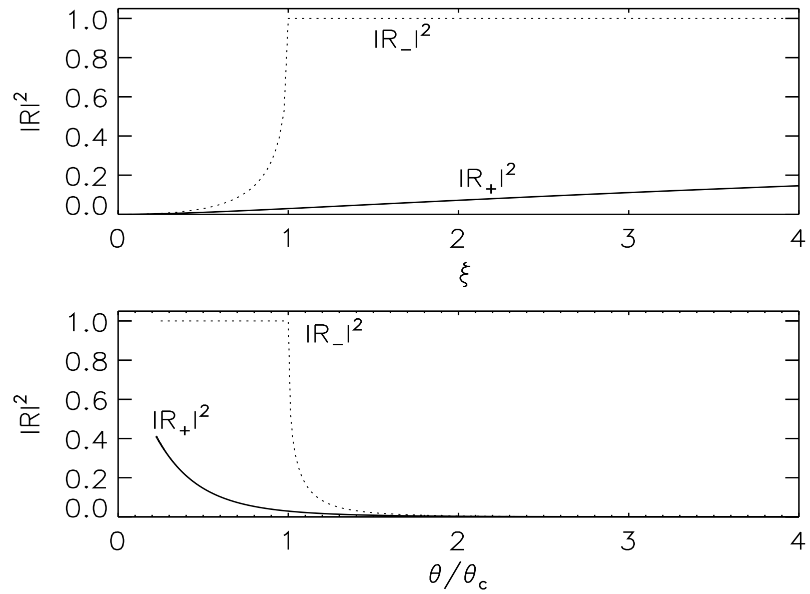

Figure 3.4: Reflection coefficients $|R_+|^2$ and $|R_-|^2$ as a function of ξ and θ/θ_c.

with the dimensionless ratio $\xi = m\gamma B/(\hbar k^2 \sin^2\theta)$.
One sees in Fig. 3.4 that $|R_-|^2 = 1$ for $\xi \geq 1$. This corresponds to total reflection for neutrons with spin $-\hat{y}$ and angles $\theta \leq \theta_c$ where the critical angle θ_c is

$$\theta_c = \arcsin\sqrt{\frac{m\gamma B}{\hbar k^2}}.$$

Since, in practice $\gamma B \ll \hbar k^2/m$, the critical angle θ_c is very small (order of one degree). One also sees from Fig. 3.4 that for $1 < \xi < 4$ we have $|R_+|^2 \ll |R_-|^2 = 1$. This corresponds to reflection angles $\frac{1}{2}\theta_c \leq \theta \leq \theta_c$. Therefore, when the incoming unpolarized beam (50% up, 50% down) touches the surface at such angles, the reflected beam is nearly perfectly polarized and we have a "polarizer".
In the last 10 years the critical angle θ_c could be increased by using a "multilayer" of alternately non-magnetic and magnetic material, selected such that neutrons of one magnetic state don't notice the multilayer at all [17]. Therefore, only neutrons of the opposite magnetic state will reflect.
In PANDA and SP one uses stacks of glass substrates (length $\simeq$ 1m) carrying such multilayers, with channels (width $\simeq$ 1mm) in between. Moreover this complete stack is slightly curved to prevent neutrons from passing through the stack without touching a multilayer. This is shown in Fig. 4.5 in Chapter 4. We point out that polarizers of this design work well for the full thermal spectrum $J(\lambda)$ (Fig. 3.2), contrary to several other types of polarizers in common use. The second half of Chapter 4 deals with measurements of the quality - polarizing and transmitting efficiency - of such polarizers.

3.4 Neutron Spin Rotators

To manipulate polarized neutron beams further, we apply "spin rotators" which transform spins according to

$$\vec{S}_{out} = \mathcal{R}_\alpha(\phi)\ \vec{S}_{in}.$$

This means that the incoming spin $\vec{S}_{in}$ is rotated over an angle ϕ around the axis $\alpha = (x, y, z)$ and we obtain a neutron beam with spin $\vec{S}_{out}$ in any direction we want. Such spin rotators were independently introduced around 1970 by Rekveldt [18] and Mezei [19]. We use standard (monochromatic) spin rotators which consist of a finite layer of constant magnetic field as explained in § **2.3.5** and with $\phi = \pi/2$ in most cases. When ϕ is large ($\gg 1$) a spin rotator is usually called a "precession device". We also employ more advanced adiabatic devices which we discuss further below (section **3.10** and Chapters 5 and 6).

3.5 Neutron Detector

Neutrons are collected by the reaction ${}^3_2\mathrm{He} + {}^1_0\mathrm{n} \rightarrow {}^3_1\mathrm{H}^- + {}^1_1\mathrm{p} + \gamma$ in a Helium-3 gas detector installed at the end of the instrument. The negative ${}^3_1\mathrm{H}^-$ particles and the protons create ionisation tracks in the gas; electrons are collected at the cathode, thus making a "pulse". This pulse is amplified and feeded into a computer controlled "counting register".

The counting register for the detector bank (device MD in Fig. 3.3) has the option of also registering the arrival time of the detected neutrons in each detector. This is used in the "time-of-flight" method, to be discussed below.

3.6 Neutron Spin Analyzers

A "Neutron Spin Analyzer" can be conceived as a device to actually measure the spin of a given neutron beam. Such a device consists of a polarizer as described above (section **3.3**) combined with a detector. The action of this combination is as follows.

Consider a neutron beam running in the x-direction with arbitrary fixed spin $\vec{S} = (S_x, S_y, S_z)$. The 2D-spinor corresponding to such a beam can be written in the most general way as

$$\psi(\vec{r}) = e^{ikx}\ (a_+ e^{i\phi_+}|\chi^+_\alpha\rangle + a_- e^{i\phi_-}|\chi^-_\alpha\rangle) \tag{3.1}$$

where $\alpha = x, y, z$ may be in any chosen direction and $a_\pm$ and $\phi_\pm$ are real parameters. This spinor is arbitrarily normalized and the corresponding macroscopic spin component $\vec{S}_\alpha$ is therefore

$$S_\alpha = \frac{\langle\ \psi(\vec{r})|\ \sigma_\alpha\ |\psi(\vec{r})\ \rangle}{\langle\ \psi(\vec{r})\ |\ \psi(\vec{r})\ \rangle} = \frac{a_+^2 - a_-^2}{a_+^2 + a_-^2}. \tag{3.2}$$

We let the beam go through a perfect analyzer $(\alpha, +)$ which only transmits the first term in Eq.(3.1). The intensity measured in the detector is then $I_\alpha^+ \equiv a_+^2$. We let the same beam go through an analyzer $(\alpha, -)$ which only transmits the second term in Eq.(3.1) yielding the intensity $I_\alpha^- = a_-^2$. From these two measurements we thus obtain the spin component

$$S_\alpha = \frac{I_\alpha^+ - I_\alpha^-}{I_\alpha^+ + I_\alpha^-},$$

which is the basic relation in polarized neutron technology to measure spins. From six such measurements $(\alpha = x, y, z)$ one determines the full spin $\vec{S} = (S_x, S_y, S_z)$ of any neutron beam.
We notice that analyzers are technically the same as polarizers and in general are huge with a magnetic field in their surrounding. Therefore they cannot be rotated so easily in any direction $(\alpha, \pm)$ without disturbing the polarization. To resolve this experimental problem we let the "static" analyzer preceed by a spin rotator (section **3.4**) which has the same effect as rotating the analyzer toward a desired direction $(\alpha, \pm)$.

3.7 Instruments PANDA and SP

The instruments PANDA and SP are schematically drawn in Fig. 3.5. They both consist of a polarizer (P), an analyzer (A), two spin rotators (R1,R2) an PG crystal (PG) and one or more detectors (D, MD). PANDA works at one wavelength (λ = 0.201(0.05) nm) selected by PG at the beginning. For SP a PG crystal is placed at the end and one can study a number of wavelengths simultaneously (usually in the range 0.19$\leq$ λ $\leq$ 0.24 nm). The heart of both instruments is the sample chamber (S) where the incoming spin $\vec{S}_{in}$ and final spin $\vec{S}_{out}$ are related by

$$\vec{S}_{out} = \ P\ \vec{S}_{in}, \tag{3.3}$$

where P is the so-called 3×3 "polarization matrix" which characterizes the magnetic properties of the sample. The initial spin $\vec{S}_{in}$ can be taken along any direction using the spin rotator R1 (see Fig.3.5). All components of the final spin $\vec{S}_{out}$ can be measured using spin rotator R2 and from the measured intensities $I^{\pm}_{\alpha,\beta}$, $(\alpha, \beta = x, y, z)$ one obtains the elements $P_{\alpha\beta}$ of the polarization matrix:

$$P_{\alpha\beta} = \frac{I^+_{\alpha,\beta} - I^-_{\alpha,\beta}}{I^+_{\alpha,\beta} + I^-_{\alpha,\beta}}. \tag{3.4}$$

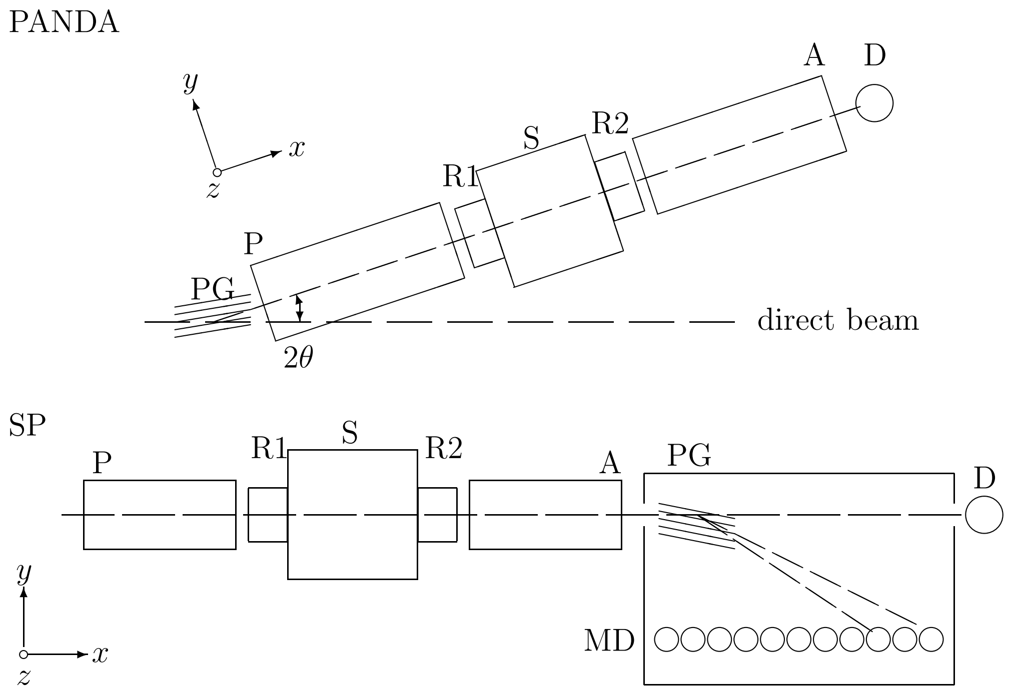

Figure 3.5: Schematic representation of the instruments "PANDA" and "SP". PG: pyrolytic graphite monochromator, P: polarizer, A: analyzer, R1,R2: polarization rotators, S: sample chamber, D: detector, MD: multi-detector (comprising 32 detectors).

The first combination of sample chamber with spin rotators was built in 1969 [18] and has been improved ever since [20], as also discussed in Chapter 5 of this thesis.

3.8 Time-of-flight analysis of neutron spectra

Some measurements discussed in the following Chapters were performed in the direct beam emerging from the beam port. To sort the measuring results by wavelength, the very old, common technique of "time-of-flight" (TOF) was used. In this technique a chopper is installed in the beginning of the neutron beam, which "chops" the continuous beam into bunches of neutrons which simultaneously start to run the distance L to the detector. The time needed to arrive at the detector and to produce a pulse is proportional to the wavelength. The pulses are stored in a sequence of time channels, so in successive channels pulses by neutrons of ever increasing wavelength are recorded. The wavelength is found from the time t of the channel in which the neutron pulse was stored, by

$$\lambda = h/(mL)\, t.$$

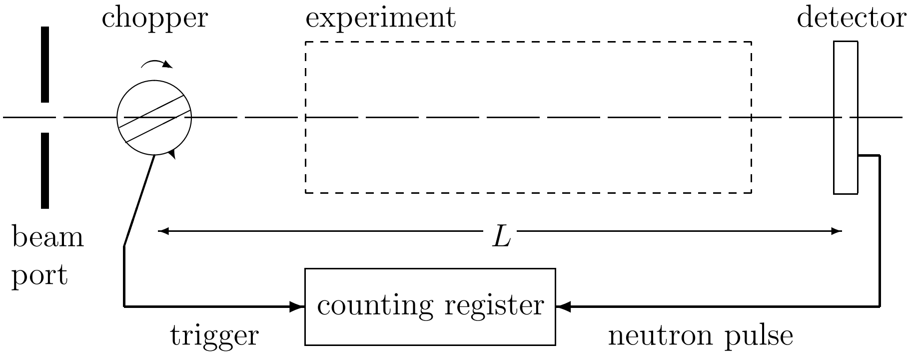

Figure 3.6: Schematic representation of time-of-flight technique.

Thus one obtains directly the intensity $J(\lambda)$ of the neutron beam as a function of wavelength.
We notice that the TOF method is insensitive to the spin of the neutrons.

3.9 Fourier Analysis of neutron spectra

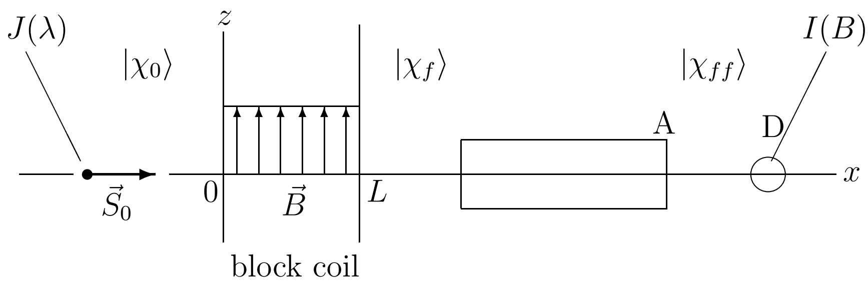

Figure 3.7: Setup for Fourier analysis to determine the spectrum $J(\lambda)$ of a neutron beam from the intensity $I(B)$ in the detector.

An important alternative for the TOF method is to measure a neutron spectrum $J(\lambda)$ using Fourier analysis. The setup for Fourier analysis is schematically shown in Fig. 3.7. The essential device is a spin rotator denoted as "block coil", shown in Fig. 3.8. It produces an homogeneous magnetic field $\vec{B} = B\hat{z}$ from $0 \leq x \leq L$ in the neutron beam, which is running in the x-direction. The incoming neutron beam has a velocity v (or wavelength λ) distribution $J(\lambda)$ which we want to measure. It is crucial that the incoming beam is fully polarized. All neutrons have the same spin $\vec{S}_0$ which we take in the x-direction (orthogonal to $\vec{B}$). Therefore the initial spinor can be written

$$|\chi_0\rangle = |\chi_x^+\rangle = \frac{1}{\sqrt{2}} \begin{pmatrix} 1 \\ 1 \end{pmatrix}.$$

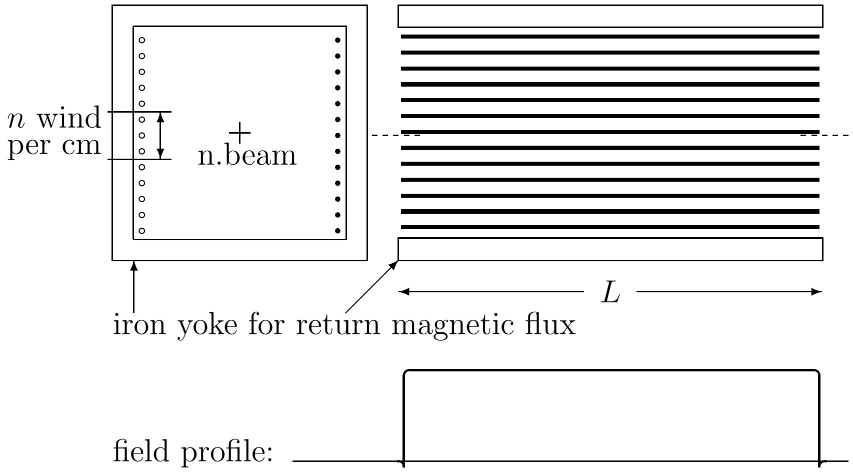

Figure 3.8: Block coil: cross section, side view and field profile.

The spinor after the block coil is then given by (cf. Eq.2.58d):

$$\begin{aligned} |\chi_f\rangle &= \mathcal{T}_{\hat{z}}^{-1}(\phi)\,|\chi_0\rangle \\ &= \cos\frac{\phi}{2}\,|\chi_x^+\rangle + i\,\sin\frac{\phi}{2}\,|\chi_x^-\rangle, \end{aligned}$$

where

$$\phi = \gamma BL/v = \frac{\gamma Lm}{h} B\lambda \equiv c' B\lambda$$

with $c' = \gamma Lm/h$ a constant specific for the block coil. After the analyzer $(x, -)$ the spinor is

$$|\chi_{ff}\rangle \;=\; i\,\sin\frac{\phi}{2}\,|\chi_x^-\rangle$$

and the detector measures an intensity for neutrons with wavelength λ in field B as

$$I_-(\lambda, B) = \sin^2\frac{\phi}{2} = \frac{1}{2}(1 - \cos\, c'\lambda B).$$

The incoming beam consists of a distribution of wavelengths $J(\lambda)$, so the total intensity measured by the detector is

$$I_-(B) = \frac{1}{2}\int_0^\infty d\lambda\; J(\lambda)(1 - \cos c' B\lambda).$$

By varying the magnetic field in the block coil one obtains the spectrum $I_-(B)$ which is in fact the Fourier transform of $J(\lambda)$. To obtain $J(\lambda)$ we first determine experimentally the "shim" intensity by

$$I_s = I_-(B{=}\infty) = \int_0^\infty d\lambda\; \frac{J(\lambda)}{2}$$

so that

$$2(I_s - I_-(B)\ ) = \int_0^\infty d\lambda\ J(\lambda) \cos c' B\lambda.$$

We obtain $J(\lambda)$ from the inverse Fourier transformation

$$J(\lambda) = \frac{4c'}{\pi} \int_0^\infty dB\ \ \cos c' B\lambda (I_s - I_-(B)).$$

We point out in Chapter 4 that this method of calculating $J(\lambda)$ can be pushed to a high wavelength resolution, if the range in the field B is sufficiently extended. We use this method in Chapter 4 to determine $J(\lambda)$.
In Chapter 7 we go one step further and also measure the intensity $I_+(B)$ of the reversed analyzer $(x, +)$ which yields similarly

$$I_+(B) = \frac{1}{2} \int_0^\infty d\lambda\ J(\lambda)(1 + \cos c' B\lambda).$$

We express the results in terms of the polarization

$$P(B) = \frac{I_+(B) - I_-(B)}{I_+(B) + I_-(B)}$$

which is the average final spin component in the $+x$-direction (with initial spin $+\hat{x}$). Thus we have

$$P(B) = \frac{\int_0^\infty d\lambda\ J(\lambda) \cos cBL\lambda}{\int_0^\infty d\lambda\ J(\lambda)},$$

where we have written $c' = cL$ with $c = \gamma m/h = 4.63 \times 10^{14}\ \mathrm{T^{-1}m^{-2}}$ a constant of the neutron (not of the instrument).
The most basic form of $P(B)$ is obtained for a neutron beam with a normalized Gaussian wavelength distribution

$$J(\lambda) = \frac{1}{\sqrt{\pi}\Delta\lambda}\ e^{-\left(\frac{\lambda-\lambda_0}{\Delta\lambda}\right)^2} \tag{3.5}$$

with λ_0 the average wavelength and $\Delta\lambda$ the Gaussian width. When $\Delta\lambda \ll \lambda_0$ one finds in a straightforward way

$$P(B) = \cos(cBL\lambda_0) e^{-\frac{1}{4}(cBL\Delta\lambda)^2}.$$

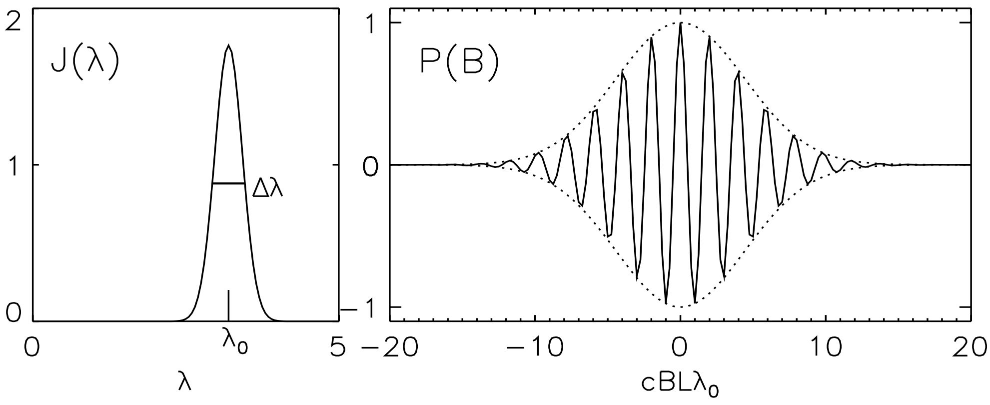

Figure 3.9: Most basic forms of $J(\lambda)$ and $P(B)$ ($\Delta\lambda/\lambda = 0.08$). The dotted curve is the Gaussian envelope of the signal.

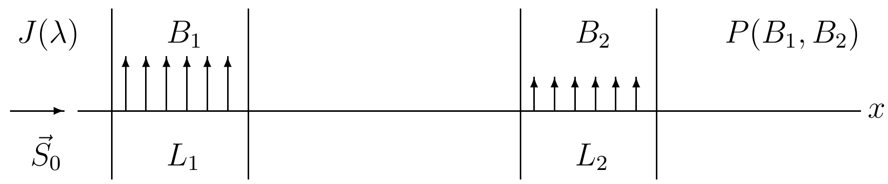

Figure 3.10: Succession of two coils with fields B_1 and B_2 in the z-direction yielding the final polarization $P(B_1, B_2)$.

We sketch $J(\lambda)$ and $P(B)$ in Fig. 3.9. From the oscillations in $P(B)$ one reads off λ_0 and from the Gaussian envelope (damping) one sees $\Delta\lambda$ directly.

Next we consider a succession of two coils with lengths L_1 and L_2 and fields $B_1\hat{z}$, $B_2\hat{z}$, respectively, as drawn in Fig. 3.10. The polarization of the final beam is then given by

$$P(B_1, B_2) = \cos(c(B_1L_1 + B_2L_2)\lambda_0)e^{-\frac{1}{4}(c(B_1L_1+B_2L_2)\Delta\lambda)^2}. \tag{3.6}$$

For given B_1, L_1 and L_2, the behaviour of $P(B_1, B_2)$ is illustrated in Fig. 3.11. $P(B_1, B_2)$ at fixed B_1 as a function of B_2 in Fig. 3.11 has the same shape as $P(B)$ in Fig. 3.9, but the center of the Gaussian envelope is now located at a shifted value $B_2 = B_2^* = -(L_1/L_2)B_1$. This is the basis of the "Spin Echo" or "compensation" method. From a measurement of B_2 in the second coil one derives the magnetic field B_1 in the first coil, using that

$$B_1L_1 + B_2^*L_2 = 0.$$

Actual spectra are displayed in Fig. 7.3 of Chapter 7.

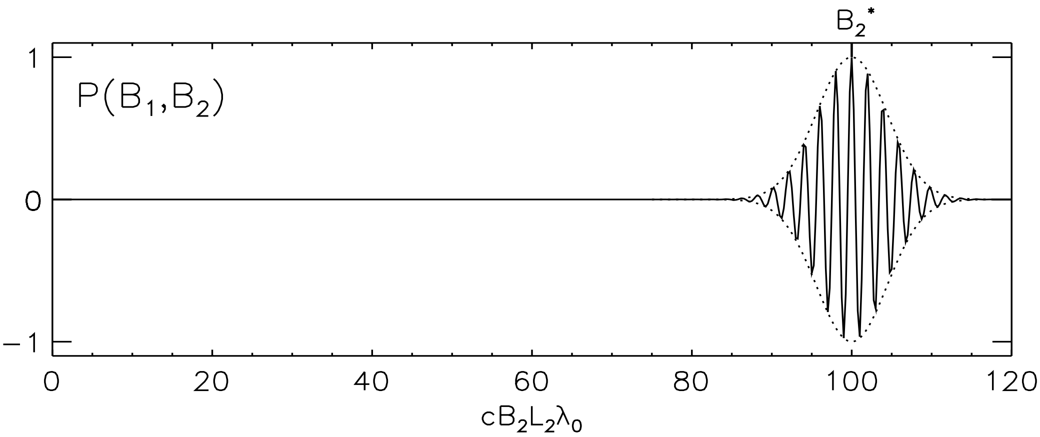

Figure 3.11: Typical behaviour of $P(B_1, B_2)$ as a function of B_2 for fixed B_1 (here $\Delta\lambda/\lambda$ =0.08, $cB_1L_1\lambda_0$=−100 and $L_1 = L_2$). The center of the signal B_2^* is determined by the compensation condition $B_1L_1 + B_2^*L_2$=0.

3.10 Adiabatic static Spin Flippers

Here we discuss spin rotators (flippers) which are adiabatic (spins rotate for a whole spectrum $J(\lambda)$ of neutrons) and static (only time independent magnetic fields $B(x)$). First we consider the flipper theoretically discussed in § **2.3.7**. Experimentally we use the DC coils twisted over π sketched in Fig. 3.12. They

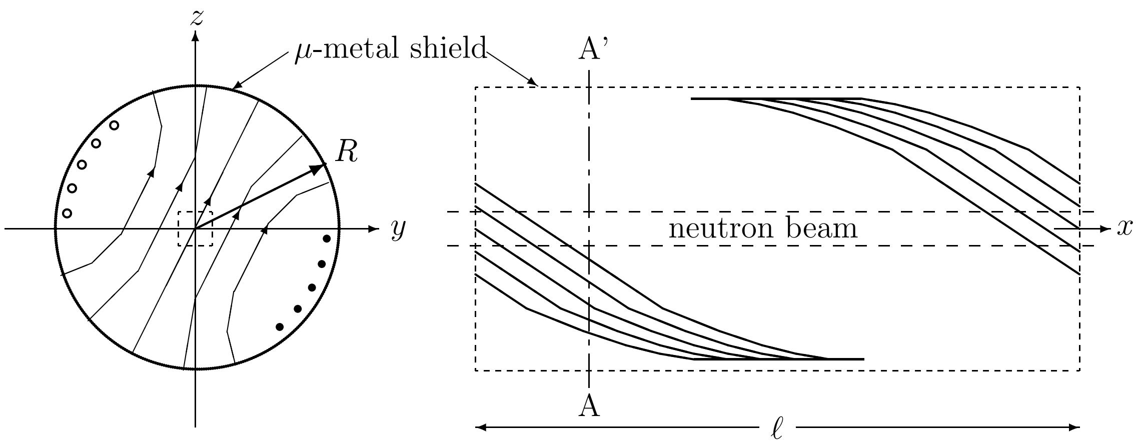

Figure 3.12: Twisted coil used for the measurements in Figs. 3.7 and 3.8: cross section (left) with field line pattern, corresponding to the line AA' in the side view (right).

are cylinders of length ℓ (30 cm and 15 cm) and radius R = 2 cm, surrounded with material with very high magnetic permeability ("μ-metal"). We take the cylinder axis as the x-axis. The current windings are such that, combined with the μ-metal, their field is described by

$$\vec{B}(x) = B(0,\ \sin(\pi x/\ell),\ \cos(\pi x/\ell))$$

as in § **2.3.7** and Fig. 2.16. The amplitude B is related to the current I in the windings by $B = \mu_0 NI/(2R)$, where N =10 is the number of windings, hence the Larmor frequency is $\omega_L = \gamma B \mu_0 NI/(2R)$.
Such coils were placed in the sample chamber S of PANDA (Fig. 3.5) with a neutron beam of wavelength λ=0.201 nm, corresponding to a velocity v=1970 m/s. Then the geometric frequency is $\omega_g = \pi/(\ell/v) = \pi h/(m\ell\lambda)$.
As discussed in § **2.3.7** the final neutron spin $\vec{S}_f$ is related to the initial spin $\vec{S}_0$ by $\vec{S}_f = P(k)\vec{S}_0$, where $P(k)$ is the 3×3 polarization matrix explicitly given by Eq.(2.64). In the present case the adiabaticity parameter k is given by

$$k \equiv \frac{\omega_L}{\omega_g} = \frac{\gamma \ell B}{\pi v} = \frac{\gamma m \ell \lambda}{\pi h} B. \tag{3.7}$$

In our experiment we vary B (not λ) which is equivalent to varying λ (not B). We cover a range $-10 \leq k \leq 10$ and show the results for ℓ=30 cm in Fig. 3.13. One sees a good overall agreement between theory and experiment. Thus we can study this adiabatic static flipper in detail.
Most relevant is the matrix element $P_{zz}(k)$ which is the z-component of the final spin $\vec{S}_f \cdot \hat{z}$ when the initial spin $\vec{S}_0 = \hat{z}$, i.e. in the $+z$-direction. We observe: for $k = 0$ we have $P_{zz} = 1$, the final spin is $+\hat{z}$ (no flip) and for $k = \pm 10$ we have $P_{zz} = -1$, so the final spin is $-\hat{z}$ (full flip).
It is illustrative to define the "flipping efficiency" $\epsilon(k)$ by

$$\epsilon(k) = \frac{1 - P_{zz}(k)}{2}. \tag{3.8}$$

Then $\epsilon(k)$ will always be between 0 and 1 and $\epsilon(k) = 0$ means that the spin has not flipped and $\epsilon(k) = 1$ means that it has flipped perfectly. In fact $\epsilon(k)$ can be interpreted as the probability to find a final spin $-\hat{z}$ when the initial spin is $+\hat{z}$. We show $\epsilon(k)$ in Fig. 3.17a. One observes that $\epsilon(k) \simeq 1$ for all $k \geq 3$. It is easy to choose B such that, e.g. the full spectrum $J(\lambda)$ of Fig. 3.2 is flipped at once.
For initial spin $\vec{S}_0$ not in the z-direction we characterize the action of the spin flipper as follows. We take $\vec{S}_0 = \hat{y}$ and write the final spin as

$$\begin{aligned} \vec{S}_f &= (P_{xy}(k),\ P_{yy}(k),\ P_{zy}(k)\ ) \\ &= P_{zy}(k)\hat{z} + \sqrt{P_{xy}^2(k) + P_{yy}^2(k)}\ (\sin\phi(k),\ \cos\phi(k),\ 0), \end{aligned}$$

where we have defined the "precession phase"

$$\phi(k) = \tan^{-1}\frac{P_{xy}(k)}{P_{yy}(k)}, \tag{3.9}$$

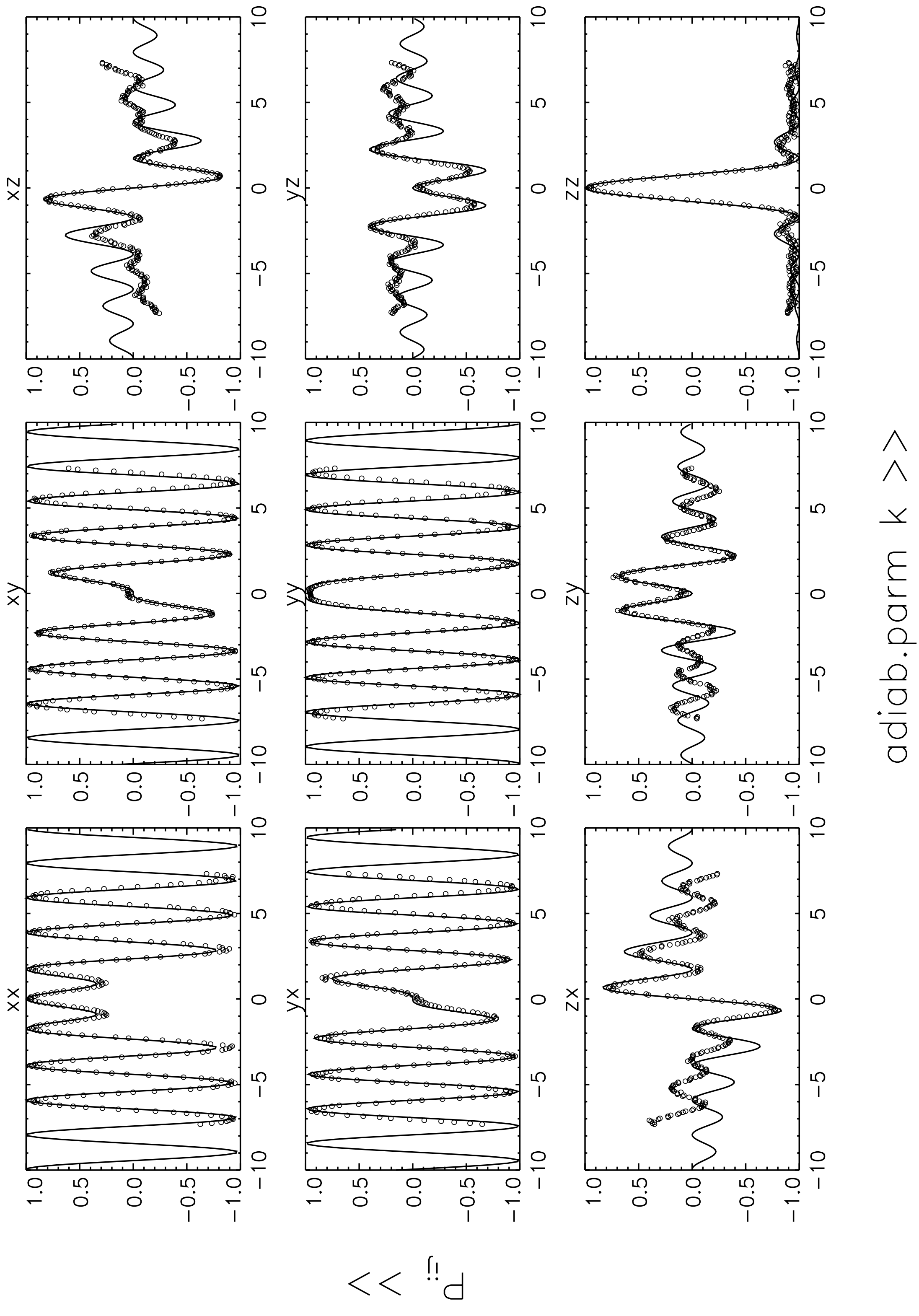

Figure 3.13: Matrix elements $P_{ij}(k)$ of the adiabatic static spin flipper as functions of k in theory (full lines, Eq.(2.64), Fig. 2.17) and experiment (circles)

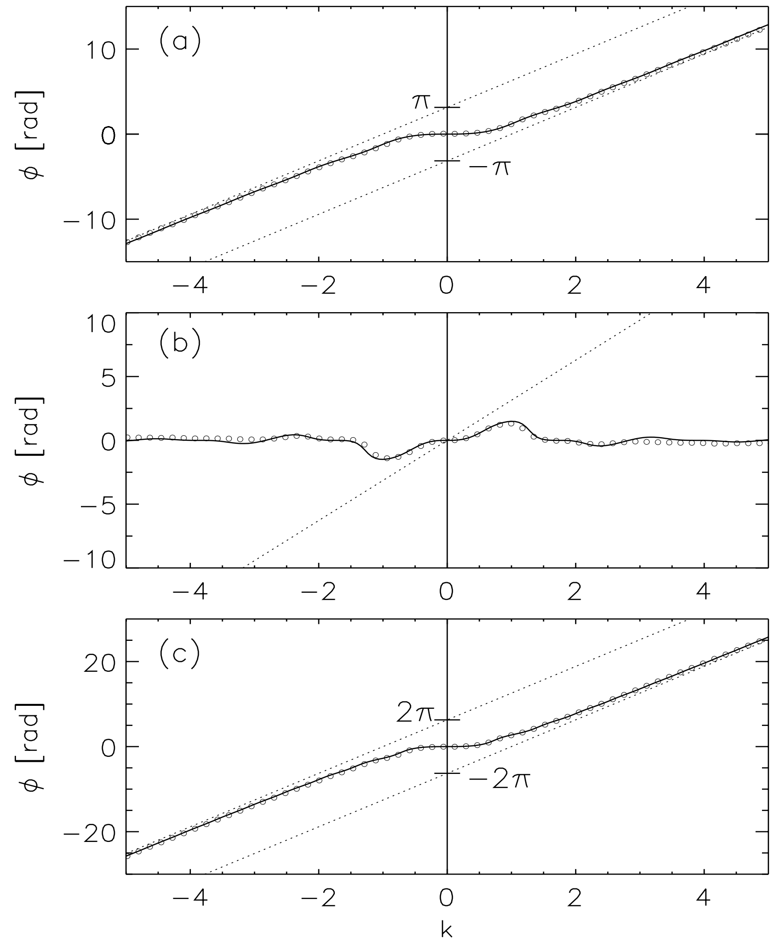

Figure 3.14: Precession phases ϕ of three twisted coils in theory (line), and experiment ($\circ$); k calculated by means of Eq.(3.7). – (a) coil twisted by π over 30 cm; (b) twisted by π over 15 cm and twisted back over 15 cm; (c) twisted by 2π over 30 cm. The geometrical term appears as the intersections of the dotted lines with the vertical axis.

which is the rotation angle around the z-axis needed to transform the initial spin $\vec{S}_0 = \hat{y}$ into the final spin $\vec{S}_f$. We show $\phi(k)$ in Fig. 3.14a as a function of k, where theory and experiment agree almost perfectly. One observes that $\phi(k)$ is a very smooth function of k, which is remarkable since both $P_{xy}(k)$ and $P_{yy}(k)$ are quickly oscillating (cf. Fig. 3.13). For this reason the precession phase is a useful parameter to characterize adiabatic spin flippers for initial spins orthogonal to the initial field.

For $k \to \infty$ one observes in Fig. 3.14a that $\phi(k) \to \pi k - \pi = \gamma B\ell/v - \pi$. Here $\gamma B\ell/v$ is the precession angle in a constant field $\vec{B} = B\hat{z}$. The additional term $-\pi$ is called the "geometric phase" discussed by Berry [21].

Measurements similar to those plotted in Fig. 3.14a were done in a set of two coils

of length 15 cm, where the fields rotate over $+\pi$ and $-\pi$ (b) and over 2π (c). The corresponding precession phases are shown in Fig. 3.14b and c. In Fig. 3.14b one observes that the geometric phase is absent; in the configuration of Fig. 3.14c it is 2π. These experiments are similar to an experiment by Bitter e.a. [22].
In Chapters 5 and 7 we consider "V-coils" which are a practical version of the twisted DC coils discussed here.

3.11 Adiabatic RF Spin Flipper

Next we study the "adiabatic RF Spin Flipper" as introduced theoretically in Chapter 2 § **2.3.8**. The magnetic field $\vec{B}(x,t)$ is given by Eq.(2.65):

$$\vec{B}(x,t) = (B_0 + B_{gr}\cos\left(\frac{\pi x}{\ell}\right))\,\hat{z} + 2B_{RF}\sin\left(\frac{\pi x}{\ell}\right)\cos(\omega t+\varphi)\,\hat{x} \tag{3.10}$$

and sketched in Fig. 2.18. The actual RF flipper is sketched in Fig. 6.5 in Chapter 6. Its RF coil has a length ℓ=10 cm. We consider monochromatic neutrons in our beam with v=1970 m/s (λ=0.2 nm). Hence we have the geometric frequency $\omega_g = \pi v/\ell$=62 kHz, corresponding to a field $B^* \equiv \omega_g/\gamma$=3.4 G. The adiabaticity parameter k is then $k = \gamma B_{RF}/\omega_g = B_{RF}/B^*$.
The RF frequency is determined by the electric circuit containing the RF coil and is therefore fixed at ω=6.78 MHz, corresponding to a field $B_0^0 = \omega/\gamma = 370$ G. The initial spin is $\vec{S}_0 = \hat{z}$ and we measure the z-component of the final spin $\vec{S}_f\cdot\hat{z} \equiv P_{zz}$. We express our experimental results in terms of the flipping efficiency

$$\epsilon(B_0,\ B_{gr},\ B_{RF}) = \frac{1-P_{zz}}{2},$$

which is a function of B_0, B_{gr} and B_{RF}. We remark that the theories derived in Chapter 2 only partially cover this 3D parameter space B_0, B_{gr}, B_{RF}. We summarize the subspaces where theoretical predictions are available.
First, when $B_{RF} = 0$ one has in Eq.(2.65) a static field in one direction ($\hat{z}$). As discussed in § **2.2.6** no flip can occur and one obtains $\epsilon(B_0, B_{gr}, 0) = 0$. When $B_{gr} = 0$ we use Eq.(2.39) with $t = \ell/v$ to describe the approach of B_0 to the resonance condition $B_0 = B_0^0$ (or $\gamma B_0 = \omega$):

$$\epsilon(B_0,\ 0,\ B_{RF}) = \frac{1}{2}\,\frac{B_{RF}^2}{B_{RF}^2 + (B_0 - B_0^0)^2}. \tag{3.11}$$

We note that the $\sin^2$-factor in Eq.(2.39) is very sensitive to its argument when $B_0 \neq B_0^0$ ($\gamma B_0 \neq \omega$). Therefore in practice we observe its average 1/2.
When exactly $B_0 = B_0^0$ and $B_{gr} = 0$, we have a resonance flipper and we may use

Eq.(2.39) with $t = \ell/v$, so

$$\epsilon(B_0^0, 0, B_{RF}) = \sin^2 \frac{\pi}{2}\frac{B_{RF}}{B^*}. \tag{3.12}$$

When $B_0 = B_0^0$ and $B_{RF} = B_{gr}$ we have the result given by Eq.(2.39) which reads ($k = B_{RF}/B^*$):

$$\epsilon(B_0^0,\ B_{RF},\ B_{RF}) = 1 - \frac{1}{1+k^2}\ \sin^2\left(\frac{\pi}{2}\sqrt{1+k^2}\right). \tag{3.13}$$

Thus we collected all theoretical expressions to compare with.
Experimentally we measured $\epsilon(B_0,\ B_{gr},\ B_{RF})$ for fixed $B_{RF} = 24$ G as a function of B_0 and B_{gr} and the result is given in Fig. 3.14 as a contour map.

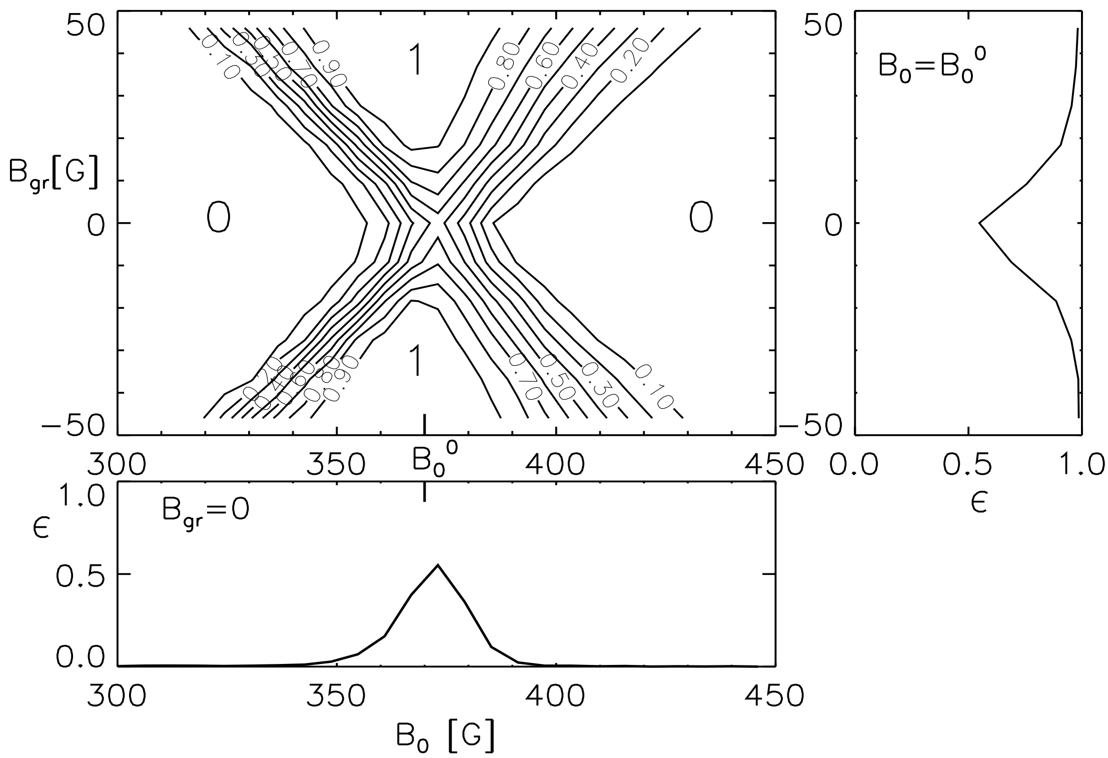

Figure 3.15: Contour map of the flipping efficiency $\epsilon(B_0,\ B_{gr},\ B_{RF})$ of an adiabatic RF flipper at B_{RF}=24 G. Resonance occurs at $B_0 = B_0^0$=370 G. Ideal flipping regions ϵ=1 appear for $B_0 = B_0^0$ and $|B_{gr}| > B_{RF}$.

Along the line $B_{gr} = 0$, $\epsilon(B_0, 0, B_{RF})$ behaves as given by Eq.(3.11), i.e. it is a Lorentzian in B_0 located at the resonance condition $B_0 = B_0^0 = 370$ G with a half width $B_{RF} = 24$ G (lower panel in Fig. 3.15). When $|B_{gr}|$ increases one sees the appearance of two identical flipping regions with $\epsilon = 1$. They are located near the resonance condition $B_0 = B_0^0$ and $|B_{gr}| \geq 25$ G. This is consistent with the

theoretical prediction Eq.(3.13). When $B_{gr} = B_{RF} = 24$ G one has $k = 7.4$ and $\epsilon = 1$, just as in experiment.
In Fig. 3.16 we show our results for $\epsilon(B_0^0, B_{gr}, B_{RF})$ as a function of B_{gr} and B_{RF} for the resonance condition $B_0 = B_0^0 = 370$ G. One sees that $\epsilon(B_0^0,\ B_{gr},\ 0) = 0$, in agreement with theory.

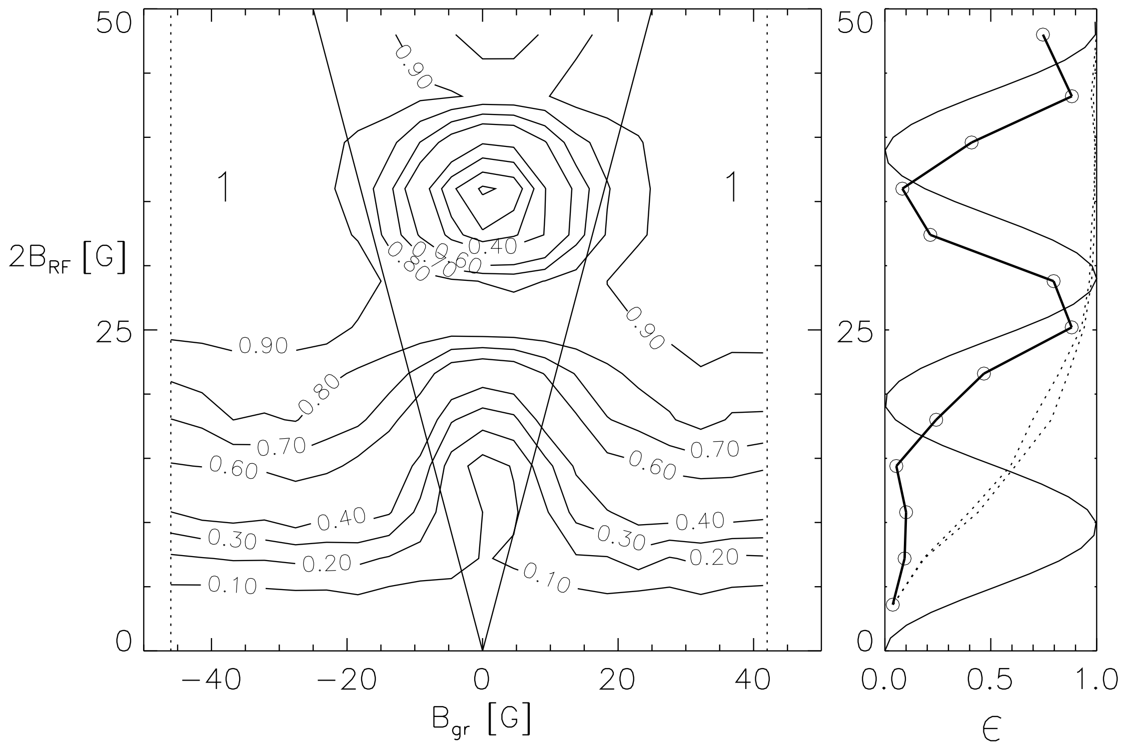

Figure 3.16: Contour map of the flipping efficiency $\epsilon(B_0, B_{gr}, B_{RF})$ of an adiabatic RF flipper for $B_0 = B_0^0 = 370$ G. Right panel: sections through this map at $B_{gr} = -46$ and $+42$ G (dotted) and at B_{gr}=0 (fat line with circles). Thin line: theoretical prediction for ϵ according to Eq.(3.12), for $B_{gr} = 0$. Ideal flipping regions with $\epsilon = 1$ appear in the main panel for high B_{RF} to the right of the line $B_{RF} = B_{gr}$ and to the left of the line $B_{RF} = -B_{gr}$.

For B_{gr}=0 the efficiency $\epsilon(B_0^0,\ 0,\ B_{RF})$ is given by Eq.(3.12) which oscillates as a function of B_{RF} with a period $2B^*$=6.8 G. This is shown as the smooth thin line in the right panel of Fig. 3.16. The experimental $\epsilon(B_0^0,\ 0,\ B_{RF})$ in Fig. 3.16 (right panel) shows the correct periodicity, but the first maximum at $B_{RF} = B^*$ is far too low. Most likely, small disturbance fields in our device (of order 3 G) destroy the first spin flip by the RF field. However, the next maxima at $B_{RF} = 3B^*$ and $5B^*$ are well reproduced. We conclude that the first spin flip is almost killed by disturbances but that the second and third spin flip appear correctly.
One observes regions of perfect flipping ϵ=1 in the left and right upper corners

- which is our interest for realizing a spin echo setup discussed in the next section. We study the approach to these regions taking $B_{gr} = B_{RF}$ (straight lines in Fig. 3.16) and plot $\epsilon(B_0^0\ , B_{RF}\ , B_{RF})$ in Fig. 3.17b as a function of $k \equiv B_{RF}/B^*$. Clearly the agreement with theory, Eq.(3.13) is very poor for $k < 5$ for reasons as explained above. However, for $k \geq 5$, the efficiency ϵ indeed reaches its adiabatic limit $\epsilon = 1$ as predicted by theory.

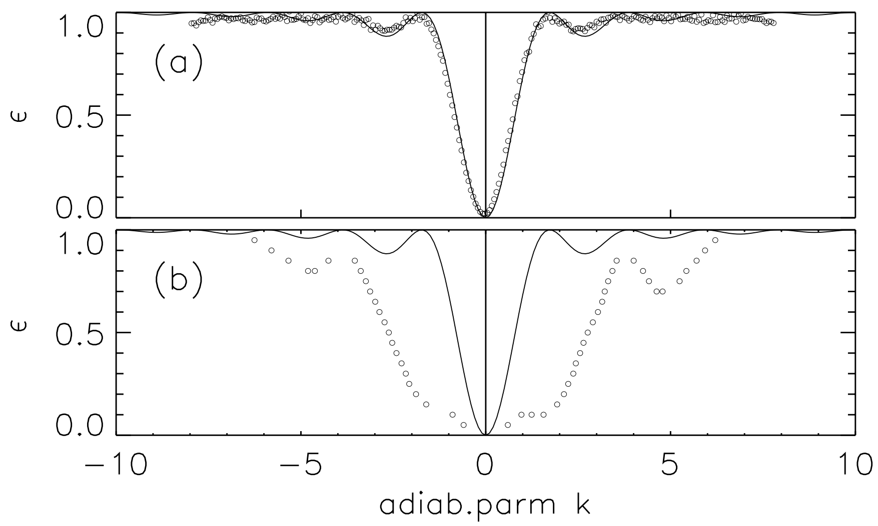

Figure 3.17: Flipping efficiency $\epsilon(k)$: (a) for a DC-coil twisted over π and (b) for an adiabatic RF flipper, along the "diagonals" in the map of Fig. 3.16. The full lines represent ϵ as derived theoretically in Eq.(2.39) and Eq.(3.13).

We conclude that the RF flipper acts according to theory but only when the RF field amplitude B_{RF} is larger than the disturbance fields present in the experimental setup. To be sure in practical applications one should take $k \geq 5$ at least. Such difficulties do not arise in the static spin flipper, as is clear from Fig. 3.17a.

3.12 SESANS

Chapter 8 deals with the application of adiabatic RF spin flippers in the technique of "Spin Echo Small Angle Neutron Scattering" (SESANS). The final instrument is indicated in the plan of Fig. 3.1 in this Chapter. The outcome of the investigations in Chapters 6, 7 and 8 contributed to its design. The measurements shown in Chapter 8 were performed on SP, built as a prototype instrument for SESANS containing adiabatic RF flippers. To see the purpose of these flippers we first explain the SESANS technique itself.

In Fig. 3.18 we show the basic principle which is based on ideas put forward

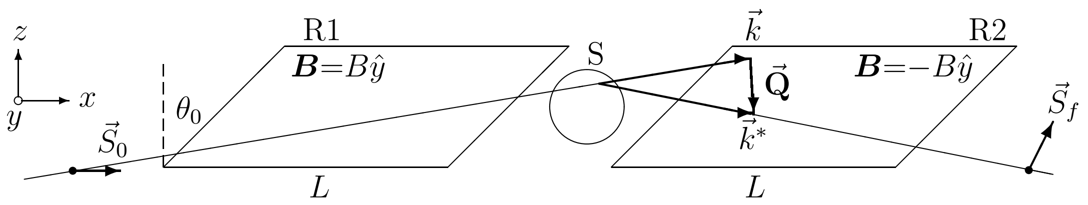

Figure 3.18: Basic geometry of SESANS. R1 and R2 are identical precession devices with magnetic fields in the $+y$ and $-y$ direction. The sample S scatters a neutron with wavevector $\vec{k}$ to $\vec{k}^*$. The initial spin $\vec{S}_0 = \hat{x}$ and one measures the spin $\vec{S}_f$ of the outgoing beam.

already by Pynn in 1978 [23]. The incoming polarized neutron beam along the x-axis has a wavelength λ, spin $\vec{S}_0 = \hat{x}$ and spinor $|\chi_0\rangle = |\chi_x^+\rangle$. The divergence of the incoming beam is finite but small. We follow a neutron with wavevector $\vec{k}$, which, in polar coordinates is given by

$$\vec{k} = k(\cos\vartheta_1,\ \sin\vartheta_1 \sin\varphi_1,\ \sin\vartheta_1 \cos\varphi_1)$$

and wavenumber $k = 2\pi/\lambda$. The angle ϑ_1 with the x-axis is small (order of $1°$) and $0 \leq \varphi_1 \leq 2\pi$, with equal probability. This neutron passes through a precession device R1 with a constant field in the y-direction: $\vec{B} = B\hat{y}$, which has the shape of a parallelogram with length L and device angle θ_0 (cf. Fig. 3.18). The path length l_1 of the neutron trajectory through the field $\vec{B}$ in R1 follows from geometry and is given exactly by

$$l_1 = \frac{L}{\cos\vartheta_1 - \tan\theta_0 \sin\vartheta_1 \cos\varphi_1} \tag{3.14}$$

and the spin rotates around the y-axis over an angle

$$\phi_1 = (\gamma m/h)\ B\lambda l_1 \equiv cB\lambda l_1.$$

The constant $c \equiv \gamma m/h = 4.63 \times 10^{14}\mathrm{T}^{-1}\mathrm{m}^{-2}$. The neutron hits the sample (S) where Small Angle Neutron Scattering (SANS) happens. The sample has no effect on the neutron spin and is described by $\Sigma(\vec{k}|\vec{k}^*)$ which is the probability that the neutron is scattered from $\vec{k}$ to $\vec{k}^*$. The scattering is elastic, i.e. $|\vec{k}^*| = |\vec{k}| = k$, so that we can write, in polar coordinates:

$$\vec{k}^* = k(\cos\vartheta_2,\ \sin\vartheta_2 \sin\varphi_2,\ \sin\vartheta_2 \cos\varphi_2).$$

We further follow the neutron with wavevector $\vec{k}^*$. It passes through the second precession device R2 which is the same as R1 except that the magnetic field is reversed: $\vec{B} = -B\hat{y}$. The path length l_2 through R2 is exactly

$$l_2 = \frac{L}{\cos\vartheta_2 - \tan\theta_0 \sin\vartheta_2 \cos\varphi_2} \tag{3.15}$$

and the spin rotates in R2 around the y-axis over the angle $\phi_2 = -cB\lambda l_2$. Hence this neutron appears at the end with a final spinor

$$|\chi_f\rangle = \cos\frac{\phi}{2}|\chi_x^+\rangle + i\,\sin\frac{\phi}{2}|\chi_x^-\rangle,$$

where

$$\phi = \phi_1 + \phi_2 = cB\lambda(l_1 - l_2)$$

is the total rotation angle around the y-axis. As before (section **3.9**) we use an analyzer $(x,-)$ and a detector to measure the rotation ϕ. Thus, for neutrons which scatter from $\vec{k}$ to $\vec{k}^*$ one finds the intensity in the detector

$$I_-(\vec{k}|\vec{k}^*) = \sin^2\frac{\phi}{2} = \frac{1}{2}\,[(1-\cos(cB\lambda(l_2-l_1)\,)]. \tag{3.16}$$

Here one sees the essentials of the spin echo (SE) technique: **when there is no scattering** ($\vec{k}=\vec{k}^*$, $l_1=l_2$ and $\phi=0$), **we will have** $I_-(\vec{k}|\vec{k}^*) = 0$**.** Thus, our spin echo device probes the probability function $\Sigma(\vec{k}|\vec{k}^*)$ of the sample.
Next we use that the sample scatters isotropically:

$$\Sigma(\vec{k}|\vec{k}^*) = \Sigma(\vec{Q}) = \Sigma(Q_x, Q_y, Q_z) = \Sigma(Q)$$

where $Q = |\vec{Q}|$ and $\vec{Q}$ is the wavevector transfer $\vec{Q} = \vec{k}^* - \vec{k}$ (cf. Fig. 3.18). Small angle scattering means that $\Sigma(\vec{Q})$ has a typical cut-off-wavenumber $Q_c \ll k$ for which $\Sigma(\vec{Q}) = 0$ when $Q > Q_c$. Therefore, when $\Sigma(\vec{Q}) \neq 0$ one has $Q < Q_c \ll k$, or $|\vec{k}^* - \vec{k}| \ll k$, so the angle ϑ_2 in Eq. (3.15) is also small (a few degrees). Expansion of $\vec{Q}(\vartheta_1, \vartheta_2, \varphi_1, \varphi_2)$ in ϑ_1 and ϑ_2 yields, up to linear order included, and for all φ_1, φ_2:

$$\vec{Q} = (0,\; k(\vartheta_2\sin\varphi_2 - \vartheta_1\sin\varphi_1),\; k(\vartheta_2\cos\varphi_2 - \vartheta_1\cos\varphi_1)\,).$$

For $l_2 - l_1$ one finds up to linear order in ϑ_1 and ϑ_2

$$l_2 - l_1 = L\tan\theta_0\;(\vartheta_2\cos\varphi_2 - \vartheta_1\cos\varphi_1) = (L\tan\theta_0/k)\;Q_z.$$

Introducing the SESANS (spin echo) correlation length

$$Z \equiv \frac{cB\lambda L\tan\theta_0}{k} = \frac{c\lambda^2 BL\tan\theta_0}{2\pi}, \tag{3.17}$$

the argument of the cosine in Eq. (3.16) can be written $cB\lambda(l_2 - l_1) = ZQ_z$. Integration of Eq. (3.16) over all final states $\vec{k}^*$ yields the fundamental result for the SESANS intensity

$$I_-(Z) = \frac{1}{2}\int_{-\infty}^{+\infty} dQ_y \int_{-\infty}^{+\infty} dQ_z\;\Sigma(Q_x = 0, Q_y, Q_z)\;(1-\cos ZQ_z), \tag{3.18}$$

Experimentally we obtain $I_-(Z)$ as a function of Z by varying B or L or both. In principle one covers the huge range $0 \leq Z \leq 10^4$ nm, using realistic values of λ, B, L and θ_0.
Theoretically, the intensity $I_-(Z)$ is the Fourier transform of the function $\Sigma^{'}(Q_z) \equiv \int_{-\infty}^{+\infty} dQ_y\ \Sigma(0, Q_y, Q_z)$, i.e.

$$I_-(Z) = \frac{1}{2} \int\limits_{-\infty}^{+\infty} dQ_z\ \Sigma^{'}(Q_z)(1 - \cos ZQ_z).$$

Like $\Sigma(\vec{Q})$, the function $\Sigma^{'}(Q_z)$ vanishes for $Q_z > Q_c$. Hence, according to Fourier's rule, the variations in $I_-(Z)$ are on the scale $Z \sim 2\pi/Q_c$. Since $\Sigma(\vec{Q})$ is the Fourier transform of the inhomogeneities in the sample, one also has $Q_c \sim 2\pi/L_c$, with L_c their typical size. Hence $I_-(Z)$ varies on a scale $Z \sim L_c$; it is "as if" $I_-(Z)$ probes the sample "in real space".

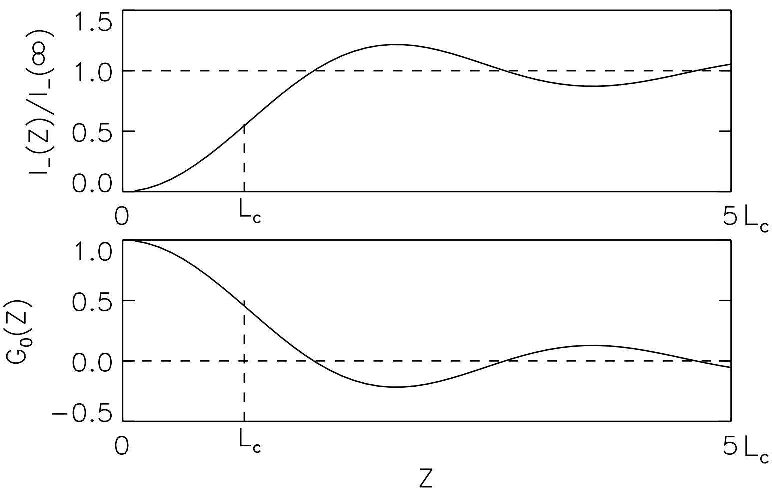

Figure 3.19: General shape of the functions $I_-(Z)$ and $G_0(Z)$ showing the size L_c of the inhomogeneities of the sample.

Fig. 3.19 (top) shows the basic shape of $I_-(Z)$. This function starts as $\propto Z^2$ and approaches on a scale L_c its final limit

$$I_-(\infty) = \frac{1}{2} \int\limits_{-\infty}^{+\infty} dQ_z\ \Sigma^{'}(Q_z) = \frac{1}{2} \int\limits_{-\infty}^{+\infty} dQ_y \int\limits_{-\infty}^{+\infty} dQ_z\ \Sigma(0, Q_y, Q_z).$$

To characterize the intrinsic properties of the sample (independent of experiment) one defines the normalized SESANS correlation function

$$G_0(Z) = \frac{I_-(\infty) - I_-(Z)}{I_-(\infty)} = \frac{\int_{-\infty}^{+\infty} dQ_z\ \Sigma^{'}(Q_z) \cos ZQ_z}{\int_{-\infty}^{+\infty} dQ_z\ \Sigma^{'}(Q_z)}.$$

Clearly, $G_0(Z)$ is the Fourier transform of $\Sigma^{'}(Q_z)$ with $G_0(0)=1$ and $G_0(\infty)=0$ as sketched in Fig. 3.19. The actual approach of $G_0(Z)$ to its final limit $G_0(\infty) = 0$ on the scale $Z \sim L_c$ reveals the detailed properties of the sample, which is what one wants to measure in SESANS.
In SESANS, equivalent descriptions occur (cf. Chapter 8). When the analyzer in the outgoing beam is reversed to $(x, +)$, one gets the intensity

$$I_+(Z) = T + \frac{1}{2}\int\limits_{-\infty}^{+\infty} dQ_z\ \Sigma^{'}(Q_z)(1 + \cos ZQ_z).$$

Here $0 < T < 1$ is the fraction of neutrons which do **not** scatter (hence final spin $+\hat{x}$) and the second term is the contribution of the scattered neutrons. The transmission coefficient T can be obtained from a separate measurement. Then, using that $I_+(Z) + I_-(Z) = 1$, one finds

$$\int\limits_{-\infty}^{+\infty} dQ_z\ \Sigma^{'}(Q_z) = 1 - T$$

and one can write

$$I_+(Z) = \frac{1}{2}(1+T) + \frac{1}{2}(1-T)G_0(Z) \qquad (3.19a)$$

$$I_-(Z) = \frac{1}{2}(1-T) - \frac{1}{2}(1-T)G_0(Z) \qquad (3.19b)$$

Usually, in SESANS, one expresses the experimental result in terms of the polarization $P(Z)$ which is the averaged spin component in the $+\hat{x}$ direction of the outgoing beam. Using Eqs.(3.19) we have

$$P(Z) = \frac{I_+(Z) - I_-(Z)}{I_+(Z) + I_-(Z)} = T + (1-T)G_0(Z) \qquad (3.20)$$

so that $P(0) = 1$ and $P(\infty) = T$.

Correction for multiple scattering in SESANS

So far we disregarded the possibility that the neutrons could scatter twice in the sample. As usual in neutron scattering experiments such multiple scattering events can only be neglected when almost all neutrons go unscattered through the sample, i.e. when T is almost 1, typically $0.9 \leq T \leq 1$. Therefore our results given above are restricted to this region of large T-values. A great advantage of the SESANS technique is that all contributions of multiple scattering can be included exactly in the theory [24]. This was also confirmed experimentally [25]. To show this, we need that the transmission through any sample can be written:

$$T = \exp(-\sigma^{'}\ell) \tag{3.21}$$

with ℓ the thickness and $\sigma^{'} = n\sigma$ the inverse attenuation length. Here n is the number density of scattering centers and σ the total cross section of one center (or "inhomogeneity"). Then the total polarization, including all multiply scattered neutrons can be written as

$$P(Z) = \sum_{j=0}^{\infty} p_j P_j(Z), \tag{3.22}$$

where

$$p_j = \frac{1}{j!}\, e^{-\sigma^{'}\ell}\, (\sigma^{'}\ell)^j \tag{3.23}$$

is the probability that the neutron has scattered precisely j times and $P_j(Z)$ is the corresponding contribution to the polarization.
We note that $p_0 = T$ is the transmission coefficient and $P_0(Z) = 1$ (unscattered neutrons remain fully polarized). Using the symmetry properties of $\Sigma(\vec{Q})$ we can write the contribution of the single-scattered neutrons as

$$P_1(Z) = G_0(Z) = \int d\vec{Q}\, \overline{\Sigma}(\vec{Q}) e^{i\vec{Q}\cdot\vec{Z}}$$

where $\vec{Q} = (0, Q_y, Q_z)$, $\vec{Z} = (0, 0, Z)$, $d\vec{Q} = dQ_y dQ_z$ and

$$\overline{\Sigma}(\vec{Q}) = \frac{\Sigma(\vec{Q})}{\int d\vec{Q}\Sigma(\vec{Q})}$$

is the normalized transition probability from $\vec{k}$ to $\vec{k}^*$ with $\vec{Q} = \vec{k}^* - \vec{k}$.
For doubly scattered neutrons one has then

$$P_2(Z) = \int d\vec{Q}_1 \int d\vec{Q}_2\, \overline{\Sigma}(\vec{Q}_1)\overline{\Sigma}(\vec{Q}_2)\; e^{i(\vec{Q}_1+\vec{Q}_2)\cdot\vec{Z}}$$

so that $P_2(Z) = G_0(Z)^2$. In general one finds in a similar way $P_j(Z) = G_0(Z)^j$ and we arrive at the central relation in SESANS, valid for all transmissions T:

$$P(Z) = e^{\ln T(1-G_0(Z))} = e^{\sigma^{'}\ell\,(G_0(Z)-1)}. \tag{3.24}$$

In Chapter 8 we use this relation in the form $-\ln P(Z)/(\sigma^{'}\ell) = 1 - G_0(Z)$ and apply it to the results for limestone and graphite (Fig. 8.3). One sees the approach of $1 - G_0(Z)$ to 1 on a scale Z ~80 nm which is then an estimate for the size of the inhomogeneities in these samples.

In our investigations to build a SESANS instrument it appeared almost impossible to incorporate static precession devices R1 and R2 of the shape of a parallelogram shown in Fig. 3.18. The reason is that precession regions realized with magnetic poles of any shape (including parallelograms) inevitably have a minimum of the field in the central plane $y = 0$. Outside this plane the field increases toward the poles quadratically with the distance from the central plane [26].
As a consequence, the actual precession angles ϕ_1 and ϕ_2 in the devices R1 and R2 increasingly deviate from Eqs.(3.14) and (3.15), as we go out of the center of the beam. This leads to a considerable contribution in the intensity $I_-(Z)$ due to unscattered neutrons. It was shown by Rekveldt [27] that reversing the spin of the neutrons at some place in the precession device will largely reduce this effect and double the factor $\tan\theta_0$ in Eq.(3.17). This will increase the range in SESANS correlation length Z by a factor of 2.
Following these predictions and the idea of zero field precession § **2.3.9** we show in Chapter 8 that these devices R1 and R2 can be replaced successfully by sets of adiabatic RF flippers.

3.13 Zero field precession

Here we illustrate experimentally the phenomenon of zero field precession. The

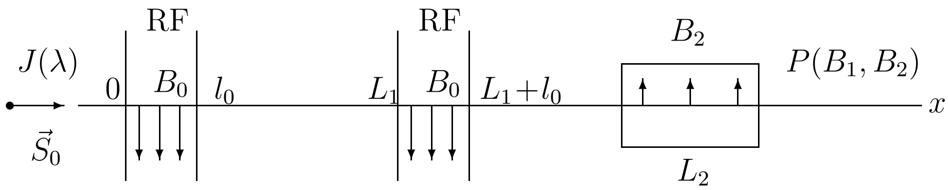

Figure 3.20: A neutron beam with spectrum $J(\lambda)$ and $\vec{S}(0) = \hat{x}$ passes through 2 RF flippers and a block coil (B_2, L_2) yielding the final polarization $P(B_1, B_2)$.

setup is illustrated schematically in Fig. 3.20. The neutron beam in the $\hat{x}$-direction is fully polarized and has a Gaussian wavelength distribution $J(\lambda)$ as given by Eq.(3.5). The average wavelength is λ_0=0.22 nm (v_0=1800 m/s) and the width $\Delta\lambda$ is small but finite. The beam goes through two identical resonance RF flippers, which produce a magnetic field (cf. Eq.2.51a)

$$\vec{B}(t) = (2B_{RF}\cos\omega t + \varphi,\ 0,\ B_0)$$

over the path lengths $0 \leq x \leq l_0$ and $L_1 \leq x \leq L_1+l_0$. Here l_0 is the effective length of one flipper and L_1 is their center-to-center distance.

We apply a RF frequency ω=1.83 MHz and a corresponding strong field $B_0 = -100$ G to fulfill the resonance condition $\omega = \gamma B_0$. We choose B_{RF} such that $\gamma B_{RF} t_{RF} = \pi$, 3π, 5π,... where $t_{RF} = l_0/v_0$ is the time spent in one flipper. The final spin after the two flippers is then given by Eq.(3.6):

$$\vec{S}_f = \mathcal{R}_z^{-1}(2\gamma B_0 L_1/v_0)\, \vec{S}(0).$$

Therefore, in theory, the neutron experiences a field $B_1 \equiv 2B_0 = -200$ G over a length L_1. The beam passes through a block coil with field $\vec{B}_2 = B_2\hat{z}$ and length L_2=32.5 cm and at the end we measure the polarization $P(B_1, B_2)$ as introduced in section **3.9** and given by Eq.(3.6).

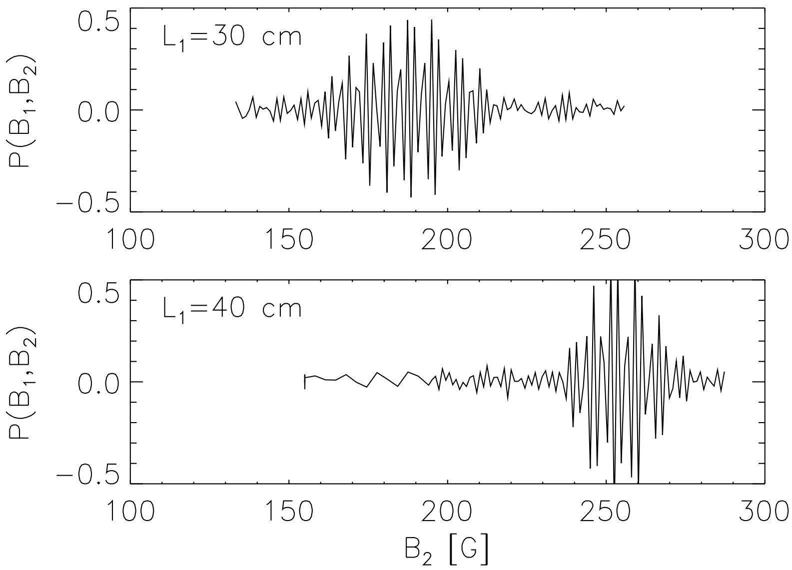

Figure 3.21: Polarization $P(B_1, B_2)$ measured for the setup of Fig. 3.20 when L_1=30 cm and L_1=40 cm. The center $B_2 = B_2^*$ of the signal is determined by $B_1L_1 + B_2L_2 = 0$ with $B_1 = 2B_0 = -200$ G and L_2=32.5 cm.

We show $P(B_1, B_2)$ as a function of B_2 in Fig. 3.21 (top), where L_1=30 cm. One sees that the center of the signal is indeed located near $B_2 = B_2^* = -L_1B_1/L_2 =$ 185 G. We also measured $P(B_1, B_2)$ for L_1=40 cm and the result is given in Fig. 3.21 (bottom). The center of the signal is now shifted to $B_2 = B_2^* = -L_1B_1/L_2 = 250$ G. This confirms experimentally the phenomenon of zero field precession: the neutron experiences an effective field $B_1 = 2B_0$ over a length L_1 which is the distance between the two RF flippers unrelated to their intrinsic length l_0.

Chapter 4

Neutron Larmor Precession Transmission Experiments

W.H. Kraan, J.B. van Tricht and M.Th. Rekveldt

Interfacultair Reactor Instituut, Delft University of Technology, Mekelweg 15, 2629 JB Delft, The Netherlands

Appeared in Nucl.Instr.& Methods A **276** (1989) 521-28

A polarized thermal neutron beam passes through a precession coil. The intensity after an analyzer is measured as a function of the magnetic induction in the coil. Fourier transformation of the recorded intensity yields the spectrum of the neutron beam emerging from the analyzer. This method is used in a quantitative way in two examples. First, we measure the transmission of α-SiO_2 to determine its scattering cross section as a function of wavelength. In the second example, the transmission of a polarizing mirror system consisting of coated curved silicon wafers is determined. Because the neutron beam emerging from the analyzer is polarized, we are able to determine the polarizing power of the mirror system as a function of wavelength by comparing the transmitted polarized and depolarized spectra.

4.1 Introduction

In a recent paper Rekveldt and Kraan [28] discussed some applications of neutron Larmor precession as a tool for energy analysis of an initially polarized white neutron beam. They established the qualitative use of the method and indicated that quantitative experiments should be undertaken. In the present paper we report on the quantitative application of the method in transmission experiments on two examples chosen from widely different fields. A preliminary account was

given in Ref. [29]. In the first experiment we compare the thermal neutron total scattering cross section of vitreous silica derived from Larmor precession with accurate data by Sinclair and Wright [30]. Knowledge of the total scattering cross section is of great importance for precise diffraction work on liquids and amorphous materials [31]. Especially the corrections for multiple scattering would benefit from accurately known total scattering cross sections.
Secondly, we determine the transmission $T(\lambda)$ and the polarizing power $P(\lambda)$ of a curved polarizing mirror system as a function of wavelength. The quantities $P(\lambda)$ and $T(\lambda)$ in general may be considered to characterize any mirror system and will be relevant in discussions about the feasibility of the various applications of Larmor precession reviewed in Ref. [28]. Moreover, data of $P(\lambda)$ - obtained so far by the time-of-flight method - are scarce in literature [32][33][34].

In Section **4.2** of this paper we introduce the Larmor precession method and its mathematical formulation, followed by a brief error analysis. Section **4.3** contains a description and an analysis of transmission experiments in vitreous silica. Finally, in Section **4.4** the results of the experiments on a polarizing mirror system are presented and discussed. Some conclusions are given in Section **4.5**.

4.2 Larmor precession method

4.2.1 Outline of the method

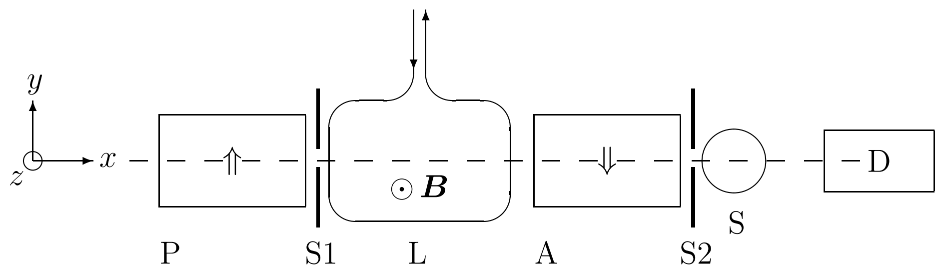

Figure 4.1: Schematic top view of the setup. P, A: polarizing mirror systems; L: Larmor precession coil with B//z; S: sample to be transmitted; D: detector; S1, S2: vertical slits to define the incident beam for the test of a third polarizing mirror system (Fig. 4.5).

The experimental setup shown in Fig. 4.1 is the same as described in Ref. [28]. However, in the present setup only the neutron intensity $I(B)$ in the direct beam is measured as a function of the magnetic induction $\boldsymbol{B}$ $(//z)$ inside the Larmor precession coil L. The polarization of the beam, which is perpendicular to $\boldsymbol{B}$, precesses (in the xy plane) around $\boldsymbol{B}$ during passage through the coil. The polarizing and analyzing systems P and A are aligned antiparallel. Hence the intensity measured after the analyzer A is

$$I(B) = \int_0^\infty \frac{J(\lambda)}{2} \left[1 - P(\lambda) \cos(c\lambda B)\right] d\lambda. \tag{4.1}$$

Defining the "shim" intensity

$$I_S = \int_0^\infty \frac{J(\lambda)}{2} d\lambda, \tag{4.2}$$

and $\tilde{J}(\lambda) = \frac{1}{2} J(\lambda) P(\lambda)$, Eq. (4.1) may be rewritten

$$I(B) - I_S = \int_0^\infty \tilde{J}(\lambda) \cos(c\lambda B) d\lambda. \tag{4.3}$$

i.e. the measured intensity $I(B)$ minus the shim intensity is the Fourier cosine transform of the quantity $\tilde{J}(\lambda)$: half the product of the neutron wavelength spectrum $J(\lambda)$ and the wavelength dependent polarization $P(\lambda)$. By performing the inverse Fourier transformation we obtain $\tilde{J}(\lambda)$ itself:

$$\tilde{J}(\lambda) = -\frac{2}{\pi} \int_{-\infty}^{\infty} \left[I(B) - I_S\right] \cos(c\lambda B) d(cB), \tag{4.4}$$

where the quantity $c = -(4\pi g \mu_N m_N / h^2) l$. Here g is the neutron gyromagnetic constant, μ_N the nuclear magneton, m_N the neutron mass, h Planck's constant and l the length of the coil.

4.2.2 Practical realization

In practice, the Fourier transformation of Eq. (4.4) is performed numerically after the intensity $I(B)$ has been measured in a finite number $2(N+1)$ of equidistant points B_k over a range $-B_M < B_k < +B_M$. In this case Eq. (4.4) takes the form of a summation:

$$\tilde{J}(\lambda) = -\frac{2}{\pi} c(B_M/N) \sum_{k=-N}^{N} \left[I(B_k) - I_S\right] \cos(c\lambda B_k), \tag{4.5}$$

where the field step $\Delta(cB) = c(B_M/N)$ and has the dimension $[\text{length}]^{-1}$. Because the summation is taken over a finite interval, the outcome is a convolution of $\tilde{J}(\lambda)$ with the function $F(\lambda) = (\sin cB_M\lambda)/\lambda$. This entails that $\tilde{J}(\lambda)$ is effectively weighed by $F(\lambda)$ over an interval $\Delta\lambda$, to be considered as the resolution of the method:

$$\Delta\lambda = \pi/(cB_M). \tag{4.6}$$

This convolution introduces oscillations into the obtained $\tilde{J}(\lambda)$. Their amplitude will merge within the standard deviation $S_{\tilde{J}}$ due to statistics, if B_M is chosen such that $I(B) - I_S$ becomes of the order of $S_{\tilde{J}}$.
The coil used in this study (see Fig.3.5 in Chapter 3) is 130 mm long, hence the constant c equals $5.99(5) \times 10^4$ nm^{-1} T^{-1} [5.99 nm^{-1} G^{-1}]. We may produce a maximum induction $B_M = 60 \times 10^{-4}$ T (60 G), so $\Delta\lambda$ obtainable with this simple coil according to Eq. (4.6) equals 0.009 nm. In the present experiments a B_M of only 25×10^{-4} T was chosen, hence $\Delta\lambda$ equals 0.02 nm. The maximum wavelength λ_M to be analyzed is:

$$\lambda_M = \frac{\pi}{\Delta(cB)}. \tag{4.7}$$

Hence, for $\lambda_M = 1.0$ nm, the field step $\Delta(cB)$ should be smaller than 3.14 nm^{-1}, i.e. for the length and maximum field specification of our coil, N should be greater than 112.

4.2.3 Propagation of counting errors

The obtained intensities $I(B_k)$ are stochastics with a Poisson probability distribution. The majority of these intensities differs little from I_S, so we suppose the variance in each of them equal to I_S. (A more rigorous treatment to account for the variances is given by Verkerk [35]). The variance in I_S is a factor $1/(2N+1)$ smaller than in the $I(B_k)$, so we neglect it. The variance s_k^2 in the quantities $I(B_k) - I_S$ is then, approximately [36]:

$$s_k^2 = I_S\left(1 + \frac{1}{2N+1}\right) \approx I_S. \tag{4.8}$$

The variance $S_{\tilde{J}}^2$ of $\tilde{J}(\lambda)$ in Eq. (4.5), calculated according to the law of error propagation, is:

$$S_{\tilde{J}}^2 = \left(\frac{2}{\pi}\right)^2 \sum_{k=-N}^{N} s_k^2 \cos^2(c\lambda B_k)\Delta^2(cB).$$

Substitution of Eq. (4.8) and writing $\Delta(cB) = cB_M/N$ gives:

$$S_{\tilde{J}}^2 = \left(\frac{2}{\pi}\right)^2 \left(\frac{cB_M}{N}\right)^2 I_S \sum_{k=-N}^{N} \cos^2(c\lambda B_k).$$

The summand in this equation is written $(1/2)[1+\cos(2c\lambda B_k)]$. After reduction to the interval $[0,2\pi]$, the arguments of the cosine term are distributed uniformly over this interval, giving zero upon summation. Hence:

$$S_{\tilde{J}}^2 = \left(\frac{2}{\pi}\right)^2 \left(\frac{cB_M}{N}\right)^2 \frac{I_S}{2}(2N+1) \approx \frac{I_S}{N}\left(\frac{2cB_M}{\pi}\right)^2, \tag{4.9}$$

so the standard deviation $S_{\tilde{J}}$ in the obtained $J(\lambda)$ is independent of λ.
For a given total measuring time the product NI_s is fixed. Then Eq. (4.9) entails that $S_{\tilde{J}}^2 \propto 1/N^2$, i.e. the standard deviation $S_{\tilde{J}} \propto 1/N$. So $S_{\tilde{J}}$ has the same dependence on N as $\tilde{J}(\lambda)$ itself. As a consequence the *relative* standard deviation in $\tilde{J}(\lambda)$ is independent of N.
The variance in the total cross section σ_T found in a transmission experiment of a sample with atomic density n and length d may be calculated using the above result in the law of error propagation:

$$S_{\sigma_T}^2 = \frac{1}{nd}\left(S_{\tilde{J}_t}^2/\tilde{J}_t^2 + S_{\tilde{J}_e}^2/\tilde{J}_e^2\right), \tag{4.10}$$

where $S_{\tilde{J}_t}^2/\tilde{J}_t^2$ and $S_{\tilde{J}_e}^2/\tilde{J}_e^2$ are the standard deviations calculated according to Eq. (4.9) and where the suffixes t and e represent the transmitted and the "empty" beam respectively.

4.3 Transmission of vitreous silica

4.3.1 Introduction

Two measurements are required in a transmission experiment, one with open beam, $J_0(\lambda)$, and one with the sample in the beam, $J_t(\lambda)$:

$$J_t(\lambda) = J_0(\lambda)\exp[-n\sigma_T(\lambda)d]; \tag{4.11}$$

n is the number of SiO_2 units per cm^3, d is the length of the sample in the beam and σ_T is the total scattering cross section per SiO_2 unit given by:

$$\sigma_T(\lambda) = \sigma_S(\lambda) + \sigma_A(\lambda), \tag{4.12}$$

where $\sigma_S(\lambda)$ is the scattering cross section and $\sigma_A(\lambda)$ the absorption cross section. In order to minimize the statistical error in the outcome of a transmission experiment performed within a fixed time interval, the sample thickness, monitor efficiency and the fractions of time devoted to measuring $J_t(\lambda)$, $J_0(\lambda)$ and background should be strictly chosen. The optimal transmission experiment has been studied by Burge [37] for the case of constant flux in the beam, and by Fredrikze [38] for the case of a monitored beam. The optimal situation for the latter case is given in Table 4.1 together with the actual situation.

4.3.2 Experiments

The sample is a cylindrical rod, 16 mm in diameter and 100 mm long with overall transmission 0.128. The vitreous silica sample, "Spectrosil B" was purchased from Thermal Syndicate Ltd. The instrument was not designed for transmission experiments, hence the situation was by no means optimal as can be seen from Table 4.1. Instead, equal relative errors in $\tilde{J}_t(\lambda)$ and $\tilde{J}_0(\lambda)$ were aimed at.

Table 4.1: Experimental real and optimal settings

Transmission		Lin attenuation coeff		Monitor efficiency	
real	optimal	real	optimal	real	optimal
0.128	0.04536	2.05	3.09	0.025	0.2768

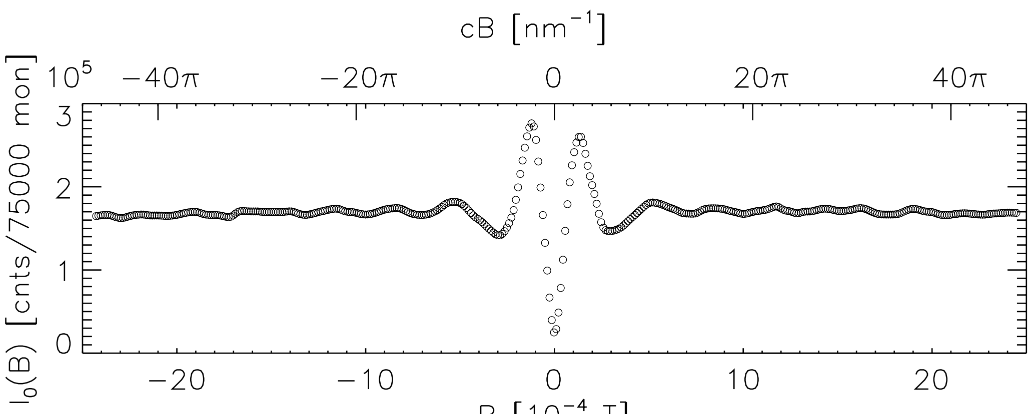

Figure 4.2: Measured intensity in the open beam for the SiO_2 transmission experiment as a function of the magnetic induction in the Larmor coil and as a function of the variable cB introduced in Eq. (4.4). The standard deviation due to statistics does not exceed the size of the symbols.

The polarized neutron beam was collimated to a diameter of 13 mm at both ends of the silica rod by means of Cd diaphragms. Measurements were made without and with the sample at position "S" (Fig. 4.1), yielding $I_0(B)$ and $I_t(B)$, respectively. The background intensity was measured with the beam closed; it did not exceed 2.5% of the lowest intensity: $I_t(B=0)$. A dead time correction was applied as well, it amounts to 2.5% at most. Measurements against preset monitor were taken in repeated series of 501 data points and checked for mutual consistency. The combined measuring times with and without the sample and those for background are 1.5 min per data point. In Fig. 4.2 $I_0(B)$ is shown. The Fourier transformed intensities $\tilde{J}_0(\lambda)$ and $\tilde{J}_t(\lambda)$ are shown in Fig. 4.3a.

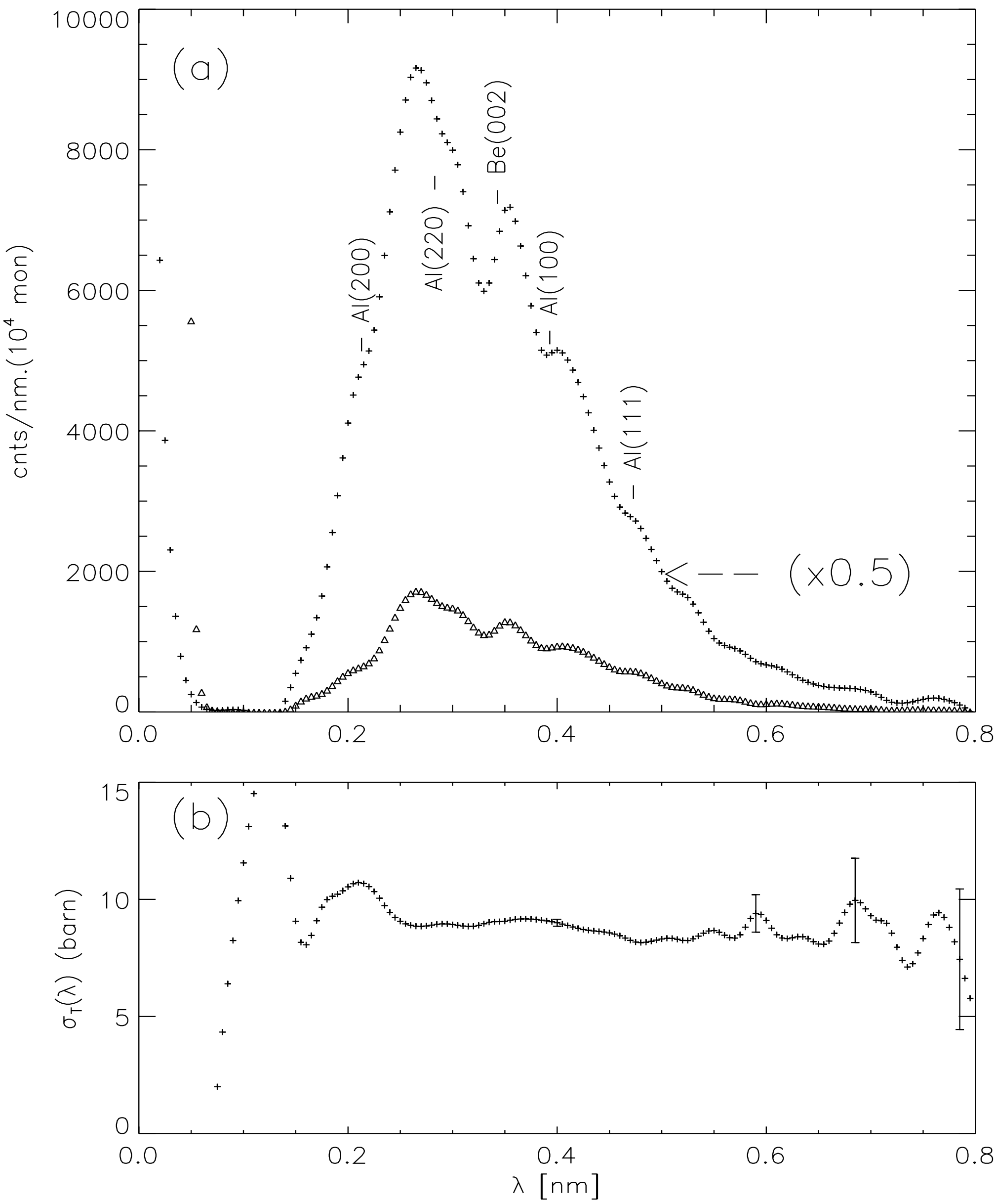

Figure 4.3: (a) Spectra obtained after Fourier transformation in the SiO_2 transmission experiment. Error bars are $2S_{\sigma_T}$ due to statistics. (b) $\sigma_T(\lambda)$ obtained from the spectra in (a) and Eqs. (4.11) and (4.12). The error bars correspond to $2S_{\sigma_T}$ due to statistics.

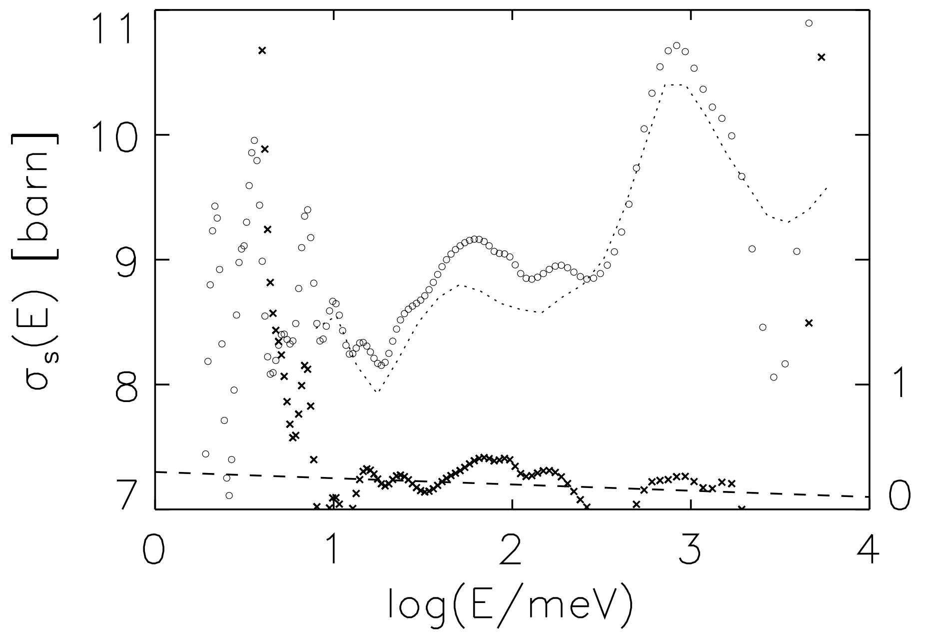

Figure 4.4: $\sigma_S(E)$ for SiO_2 derived from our data (circles) and data in Ref. [30] (dots). The dashed line is the H_2O correction, subtracted in Ref. [30] in order to obtain the data as displayed (scale to the right). The crosses are the difference between our data and Ref. [30].

The P and A devices (Fig. 4.1) have a negligible transmission for $\lambda < 0.2$ nm, hence this part of the reactor spectrum is not available. Several dips in the spectra are due to materials in the beam channel: Al, Be and Si; the attributed causes are indicated. Beyond $\lambda = 0.35$ nm the intensity falls due to the reactor spectral distribution. The error bars correspond to the standard deviation calculated according to Eq. (4.9). The scattering cross section as a function of wavelength is shown in Fig. 4.3b derived from $T(\lambda)$ using Eqs. (4.11) and (4.12). The error bars correspond to $2S_{\sigma_T}$ calculated according to Eq. (4.10):

$$\sigma_S(\lambda) = -\frac{1}{nd}\log T(\lambda) - \sigma_A(\lambda), \quad \text{with} \tag{4.13}$$

$$\sigma_A^{\mathrm{SiO_2}} = 0.8929\lambda \times 10^{-23}\mathrm{cm}^2(\lambda \text{ in nm }); \quad n = 22.2 \times 10^{22}\mathrm{cm}^{-3}. \tag{4.14}$$

The scattering cross section σ_S shows a smooth behaviour over that part of the spectral distribution where the intensity is at least 0.2 of the peak intensity: outside this range the standard deviation in the signals $\tilde{J}_0(\lambda)$ and $\tilde{J}_t(\lambda)$ becomes of the same order as these signals themselves, hence large fluctuations develop.

4.3.3 Discussion

The average scattering cross section σ_S takes a value close to the weighted value for the free atom cross sections per unit SiO_2, rather than the bound atom cross section. This confirms the outcomes for σ_S for α-SiO_2 obtained by Sinclair and Wright [30] in a linac setup. In Fig. 4.4 we compare σ_S obtained with the Larmor method with the outcomes of their experiment, adapting scales to energy instead of wavelength, according to $\sigma(E)dE = \sigma(\lambda)d\lambda$. The Larmor experimental values are well above those of Sinclair and Wright. It is fortunate that the samples in both experiments are the same in quality, "Spectrosil B". We determined the difference between their and our dataset (crosses in Fig. 4.4: scale to the right): this gives a value almost equal to the calculated [30] contribution of "water content" that was subtracted by Sinclair and Wright. This contribution should also be read from the right hand scale in Fig. 4.4 and amounts to about 0.25 b at $E=$ 10 meV. However, at closer inspection the H_2 contribution thus determined for the present experiment is slightly larger. From the present data we conclude that the Larmor precession determination of the scattering cross section can be accomplished accurately within a few tenths of a percent in an admittedly restricted energy range compared to the linac method within 12 h of beam time at a 2 MW swimming pool reactor. For diffraction experiments an extension towards larger energies would be attractive, the manufacture of polarizing mirror systems extending the energy range to above 100 meV is feasible, the extension towards smaller neutron energies calls for more neutrons rather than for better polarizing mirror arrangements.

4.4 Transmission and polarization of a polarizing mirror system

4.4.1 Introduction

In this section the technique of Sec. **4.2** is applied to determine the transmission and polarizing power of a mirror system of the same design as system A in Fig. 4.1. This is important for a number of reasons:

- As shown in Sec. **4.2**, the product $\tilde{J}(\lambda)$ of the spectral density $J(\lambda)$ and the polarization $P(\lambda)$ is measured rather than $J(\lambda)$ itself. It is necessary to know $P(\lambda)$ in order to obtain $J(\lambda)$.

- Data on $P(\lambda)$ and the transmission $T(\lambda)$ of the mirror systems developed at IRI and described earlier [40] can be compared with predictions based on the formulae given in the same article and previously, e.g. Ref. [41]. Such data will be helpful in discussions about the feasibility of the applications of Larmor precession spectroscopy mentioned in Ref. [28].

- Although various curved single or multichannel mirror systems have been described in the literature [32][33][34], few results of transmission experiments have been published.

The system to be tested (Fig. 4.5) is of the type described in Ref. [40]. It is a stack of silicon wafers with a spacing between successive wafers equal to their thickness. The stack is bent over an angle 2β=16 mrad. Both the wafers and the spacings in between act as neutron channels. The polarizing mirrors are realized as FeCo layers sputtered on both sides of the wafers. Each type of channel is faced by FeCo mirrors of a composition such that θ_c^- is equal to zero. Absorbing layers containing Gd are provided between the mirrors. To avoid reflection, the Gd is alloyed with Ti in a degree that the net scattering length is zero. The dimensions of the system are indicated in Fig. 4.5.

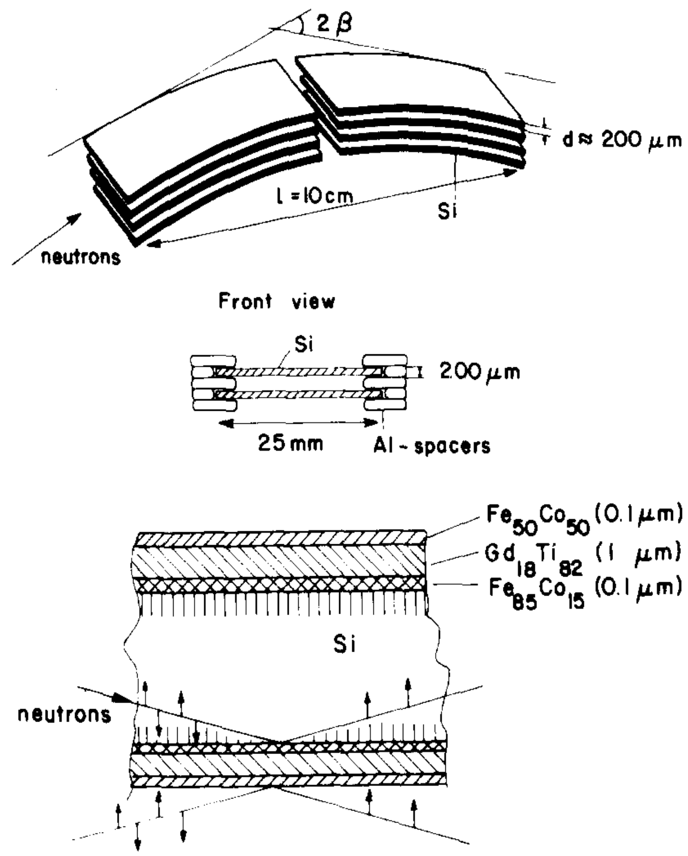

Figure 4.5: The mirror system tested.

4.4.2 Definition of transmission

In Ref. [40] the transmission problem is considered in two dimensions. An intensity $J_0(\lambda)\delta$ merges isotropically (i.e. into 2π) into the entrance of a single channel (width δ) between two curved mirrors. Denoting the outcoming intensity $J_t(\lambda)$, the transmission of the channel is defined:

$$T(\theta_c) = J_t/(2J_0\theta_c\delta). \tag{4.15}$$

The denominator represents the number of neutrons entering the channel from an angular interval θ_c on either side of the tangent to the mirror plane at the entrance. Since θ_c is proportional to λ, the divergence of the incoming beam in Eq. (4.15) depends on λ. (In the present definition $T(\theta_c)$ is a factor of 2 smaller than in Ref. [40].) Using the result given in Eqs. (4) and (5) of Ref. [40], we have

$$\begin{aligned} T(\theta_c(\lambda)) &= \tfrac{2}{3}\, x^2(\lambda) && (x(\lambda) < 1) \\ T(\theta_c(\lambda)) &= \tfrac{2}{3}\, \tfrac{x^3(\lambda)-(x^2(\lambda)-1)^{3/2}}{x} && (x(\lambda) > 1), \end{aligned} \tag{4.16}$$

where

$$x(\lambda) = \theta_c/\beta = b\lambda/\beta.$$

The quantity b depends on the atomic densities (N_m, N_c) and the scattering lengths $(b_m,\ b_c)$ of the material of the mirrors (m) and the filling material inside the channel (c), respectively:

$$b = \sqrt{(\langle N_c b_c\rangle - \langle N_m b_m\rangle)/\pi}.$$

In the system to be tested b equals 18.5 and 18.7 mrad/nm for a mirror along a silicon filled channel and an empty channel, respectively, where it is assumed that the neutron spin is parallel to the magnetisation of the mirror. Hence, the characteristic wavelength giving $x(\lambda)=1$ equals 0.43 nm.

4.4.3 Measurements

An incoming beam of well defined divergence was realized by means of two vertical slits S1 and S2 of width 1.1 and 5.1 mm respectively (Fig. 4.1) giving a profile with FWHM Δ equal to 6.4 mrad, sketched in the insert of Fig. 4.6a. Because S1 and S2 are vertical, whereas the mirrors in the systems P and A are horizontal, the beam profile behind S2 is independent of λ.
The intensity $I_0(B)$ of the beam thus prepared was measured. Its Fourier transform ,$\tilde{J}_0(\lambda)$ is given in Fig. 4.6a as small + signs. The system to be tested was

placed in this beam with its mirrors vertical, i.e. parallel to the slits S1 and S2. In this way the assumptions of Eqs.(4.15) apply to the horizontal plane.
Since, in addition to the transmission, the polarizing power of the system was to be measured, it was surrounded by a configuration of permanent magnets. The superposition of its stray field with the stray field of the analyzer A was the guide field for the adiabatic rotation over $\pi/2$ needed to obtain the polarization in the plane of the mirrors of the system being tested. The latter could be rotated about a vertical axis by means of a computer controlled stepping device. The axis of rotation coincided with the center of the entrance window. The transmitted intensity (at $B=0$) and with a shim between P and A) was measured as a function of stepping angle to determine the setting of maximum overall intensity.
In this setting Larmor spectra $I_t^+(B)$ and $I_t^-(B)$ were taken without and with a depolarizing shim between A and the system being tested. Their Fourier transforms, denoted $\tilde{J}_t^+(\lambda)$ and $\tilde{J}_t^-(\lambda)$, are given in Fig. 4.6a. The error bars correspond to $2S_{\tilde{J}}$ according to Eq. (4.9).

4.4.4 Results and interpretation

Transmission

We define the transmission function $T_{exp}(\lambda)$ found experimentally:

$$T_{exp}(\lambda) = 2\tilde{J}_t^s(\lambda)/\tilde{J}_0(\lambda). \tag{4.17}$$

In Fig. 4.6b the experimental result $T_{exp}(\lambda)$ is plotted (open circles) together with the theoretical $T^*(\lambda)$ for β equal to 6.0 and 8.0 mrad (dashed and dash-dotted lines). Before we can compare $T_{exp}(\lambda)$ and $T^*(\lambda)$, we must consider three corrections to $T^*(\lambda)$.
In the first place, we should make a correction for the absorption in the Si filled channels. The silicon wafers are cut from a monocrystal oriented such that none of the (100) planes can satisfy the condition for Bragg reflection, hence losses due to coherent scattering need not be taken into account for $\lambda > 0.4$ nm. The full line in Fig. 4.6b represents $T^*(\lambda)$ for $\beta = 6$ mrad and corrected for absorption in one out of two channels.
In the second place, $T_{exp}(\lambda)$ is determined for the depolarized beam, which means a reduction of the intensity by a factor of 2. This is, however, already accounted for in the definition (4.17).
In the third place, we should realize that $T_{exp}(\lambda)$ was obtained with an incoming beam of fixed divergence Δ whereas in $T^*(\lambda)$ the incoming beam is supposed to have a λ-dependent divergence $2\theta_c$. For $\lambda = \lambda_0$ given by

$$2\theta_c(\lambda_0) = \Delta, \tag{4.18}$$

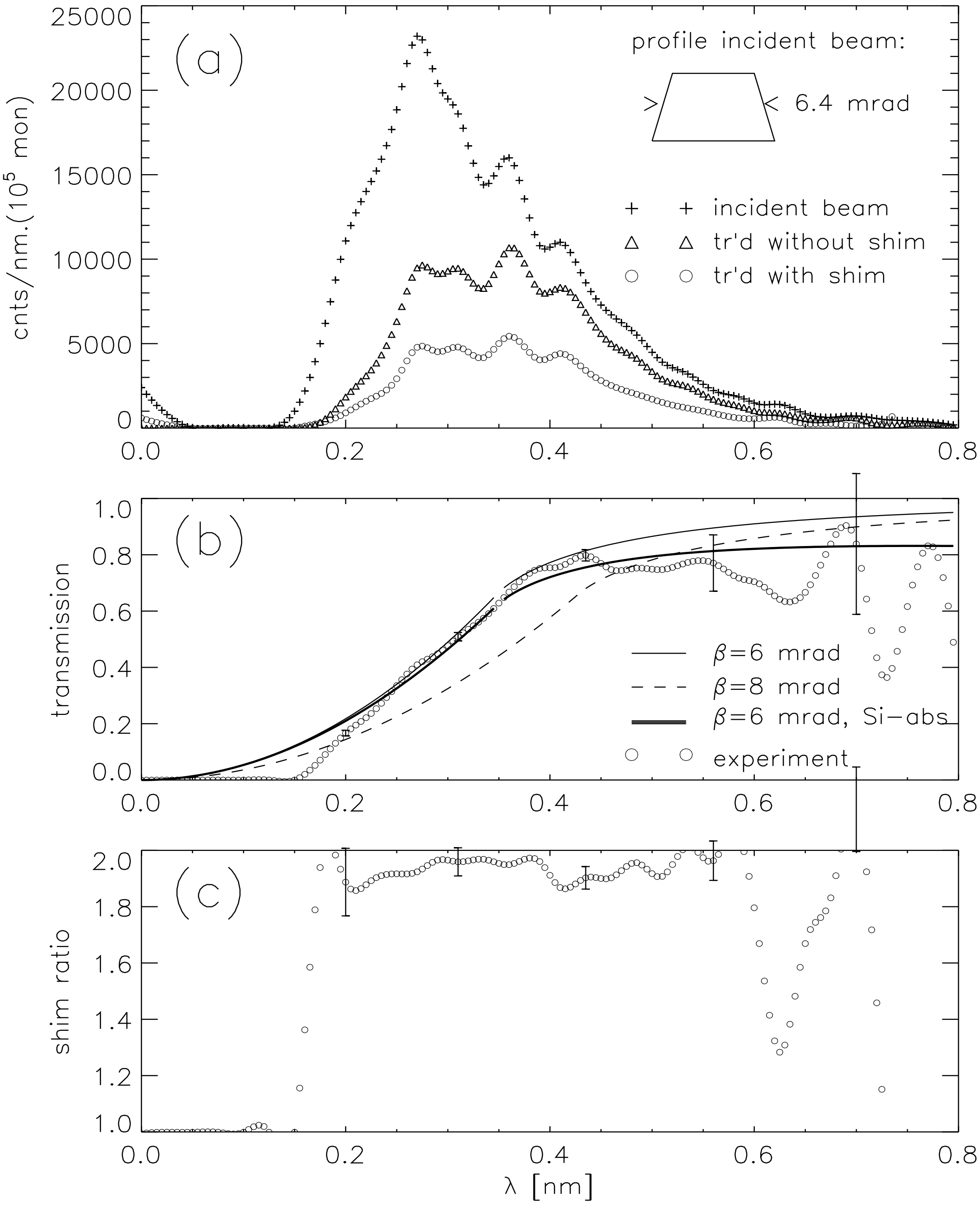

Figure 4.6: (a): Spectra obtained after Fourier transformation in testing the mirror system of Fig. 4.5: incident beam on the mirror system, transmitted beam and transmitted depolarized beam through the system. (b): Comparison of transmission $T_{\mathrm{exp}}(\lambda)$ found experimentally and $T^{*}(\lambda)$ calculated with Eq. (4.16) for curvatures $\beta = 6$ and 8 mrad. The thick line is for $\beta = 6$ mrad with Si absorption in one out of two channels. (c): Shim ratio $s(\lambda)$ (Eq.4.19) for the system combined with a "polarizer" consisting of the complete setup of Fig. 4.1 in front of S2. The error bars correspond to the standard deviation due to statistics.

(whence $\lambda_0 = 0.17$ nm), the divergence of the actual beam corresponds to $2\theta_c$. For $\lambda < \lambda_0$ the quantity $T^*(\lambda)$ should have to be reduced by λ/λ_0 in order to compensate for the fact that the system was illuminated with a more divergent beam than it could accept. However, because this correction applies to the λ-region in which no neutrons are present, it is not relevant.
Making the first correction, it appears that $T_{\text{exp}}(\lambda)$ is in good accordance with $T^*(\lambda)$ for $\beta = 6$ mrad from the onset at $\lambda = 0.17$ nm up to 0.35 nm. This value for β is 25% less than its design value 8 mrad, For λ increasing from 0.4 to 0.6 nm, $T_{\text{exp}}(\lambda)$ falls increasingly short of $T^*(\lambda)$. Because of the low value of $J_0(\lambda)$ for $\lambda > 0.6$ nm in comparison with its standard deviation (Eq. (4.10)), the data beyond 0.6 nm are not relevant. For $\lambda > \lambda_0$ the divergence of the incident beam is smaller than the acceptance of the mirror system. We assume that $T_{\text{exp}}(\lambda)$ in this case represents its transmission properties over the whole $2\theta_c$ range.

Polarization

The polarizing power of a combination consisting of two polarizing systems 1 and 2 is characterized by its shim ratio s:

$$s = J^+/J_s = 1 + P_1 P_2, \tag{4.19}$$

where J^+ and J_s are the intensities measured behind system 2 without and with a shim between the systems, respectively and where P_1 and P_2 are their polarizing powers. In the present case P_1 is the polarizing power of the complete setup of Fig. 4.1 in front of S2 and P_2 the polarizing power of the system being tested.
In Fig. 4.6c the quantity $s(\lambda) = \tilde{J}_t^+(\lambda)/\tilde{J}_t^s(\lambda)$ is plotted as a function of λ. Within the standard deviation of 0.1, s appears to have a constant value of 1.9 over the wavelength range $0.2 < \lambda < 0.6$ nm. Since P_1 is known from earlier experiments to be 0.95, we conclude that P_2 is 0.95 (± 0.1).

4.4.5 Discussion

Reflectivity

After the corrections for Si absorption and beam divergence, the function $T^*(\lambda)$ appears to give a good account of the experimental result $T_{exp}(\lambda)$ for β equal to 6 mrad. This indicates that the reflectivity of the mirrors is very good, i.e. above 0.9 over the whole λ-range.

Curvature

Because the curvature β appears less than its design value, a fraction $g = \delta^*/l$ of the incoming neutrons can get through the system without being reflected (δ^*

is the "free" opening between successive mirrors). Since the effective curvature β= 6 mrad, an upper limit for δ^* is 0.05 mm, hence g equals 0.08. This implies that for all wavelengths the transmission $T_{exp}(\lambda)$ contains 4% reversed spins. On the other hand, the polarizing power $P(\lambda)$ has a constant value of 0.9($\pm$0.1) over the whole λ range. This is due to the "free" opening. (In a subsequent optical measurement of the curvature a mean effective curvature β equal to 6 mrad was indeed found.)

Polarization

If a θ_c^- existed, it would lead, according to Eq. (4.16), to a contribution of reversed spins proportional to λ^2. This would result in a drop in $P(\lambda)$ with increasing λ. It is observed, however, that $P(\lambda)$ is constant over the whole λ-range. This indicates that no reflection of reversed spins occurs. We therefore conclude that the mirror material meets the FeCo composition needed for θ_c^- being zero and that the mirror material is magnetically saturated.

4.4.6 Summary

From the transmission experiments on a polarizing mirror system we can state:

- Sputtered FeCo layers with polished silicon as a substrate have a reflectivity of better than 90% over the wavelength interval studied.
- From the wavelength dependence of the polarization it is concluded that the composition of the mirrors in our system is equal to the composition required for100% polarization.
- The curvature of our system appears to be 25% less than critical.
- A period of four years elapsed between production and the present test of the system. Its good specifications have lasted for this period, so it has a satisfactory long term stability.

4.5 Conclusion

In this article the technique to produce neutron spectra by means of Larmor precession followed by Fourier transformation was demonstrated in two examples of a transmission experiment. We conclude that the spectra obtained are accurate enough to make a meaningful division in order to get a transmission function over the wavelength range $0.2 < \lambda < 0.6$ nm. The fact that the beam emerging from the analyzer of the Larmor setup is polarized enables us to equally measure the polarizing properties of (e.g.) a polarizing mirror system as a function of wavelength. The present results have encouraged us to engage in optimizing the method and to exploit the applications suggested in our earlier article.

Acknowledgement

The authors are grateful to V.O. de Haan for many fruitful discussions.

Chapter 5

Adiabatic rotators for 3-D neutron polarization analysis

W.H. Kraan, M.Th. Rekveldt and P.T. Por

Interfacultair Reactor Instituut, Delft University of Technology, 2629 JB Delft, The Netherlands

Appeared in Nucl. Instr.& Methods A **300** (1991) 35-42

A set of two polarization rotators designed according to the principle of adiabatic rotation of the polarization vector of a polychromatic thermal neutron beam is described. The adjustment of the polarization vector along the axes of the laboratory coordinate system is examined by 3-dimensional polarization analysis over the λ range of 0.15-0.55 nm. The spectra needed for this analysis are obtained by means of the method of Larmor precession followed by Fourier transformation.

5.1 Introduction

The technique of 3-dimensional analysis of the polarization vector of a thermal neutron beam is nowadays widely used in magnetic neutron diffraction and neutron depolarization. At IRI, this technique has been applied since 1970 to monochromatic beams. For a polychromatic beam the possibility of depolarization experiments with 3-dimensional analysis was opened using the method of wavelength analysis by Larmor precession to a field which is varied stepwise, followed by Fourier transformation. This calls for polarization rotators which, contrary to the present ones, realize an orthogonal adjustment of the polarization vector for the whole thermal neutron spectrum.

For this purpose a set of two polarization rotators was developed based upon the principle of "adiabatic rotation" like the ones already installed in Leningrad [42] and Vienna [43]. However, the second is used for adjustment of a monochromatic beam. This article deals with the realization of such rotators and their testing by means of the Larmor modulation method described in an earlier article [44].

5.2 Principle of operation

The operation of the rotators is based upon the equation of motion for the polarization vector $\boldsymbol{P}$ in a magnetic field $\boldsymbol{B}$:

$$d\boldsymbol{P}/dt = \gamma[\boldsymbol{P} \times \boldsymbol{B}] \tag{5.1}$$

(γ is the gyromagnetic ratio). In a homogeneous field its solution is a rotation of the vector $\boldsymbol{P}$ around the vector $\boldsymbol{B}$ with the angle between $\boldsymbol{P}$ and $\boldsymbol{B}$ remaining constant. This is the well known Larmor precession which occurs at an angular frequency $\omega_L = \gamma|\boldsymbol{B}| = 2g_n\mu_n|\boldsymbol{B}|/\hbar$ (where g_n is the splitting factor and μ_n is the magnetic moment of the neutron and $\hbar$ is Planck's constant divided by 2π). If the field is inhomogeneous, one should consider the rate of change ω_G of the direction of $\boldsymbol{B}$ as seen in a coordinate system moving with the neutron. If

$$\omega_G << \omega_L \tag{5.2}$$

and the initial angle between $\boldsymbol{P}$ and $\boldsymbol{B}$ is zero, the vector $\boldsymbol{P}$ will precess around the local $\boldsymbol{B}$ and the angle between $\boldsymbol{P}$ and $\boldsymbol{B}$ will remain less than ω_G/ω_L. The vector $\boldsymbol{P}$ is said to follow $\boldsymbol{B}$ adiabatically. Considering this, an adiabatic rotation of the vector $\boldsymbol{P}$ from its initial direction (y) into a desired direction x, y, z can be accomplished by providing a magnetic field along the beam path which gradually turns from y to x, (y) or z. If the strength of the field is chosen such that condition (5.2) is fulfilled for the minimum wavelength in the neutron spectrum, it will be fulfilled over the entire spectrum.

5.3 Realization

Fig. 5.1 (top) gives a schematic view of the first rotator (D_1) placed behind the polarizer. Its length is 15 cm; it has a square cross section in the yz plane of 16×16 cm. The stray (y) field of the polarizer (open arrow at left; dotted line in Fig. 5.1 (bottom)) is combined with the fields of coils 1, 2 or 3 for the required rotations of the polarization vector. For rotation from y to x or z, coils 1 and 3 are energized, respectively; coil 2 is energized for adjustment of the vector $\boldsymbol{P}$ parallel to y. (For clarity in Fig. 5.1 only coils 2 are shown; coils 3 are similar

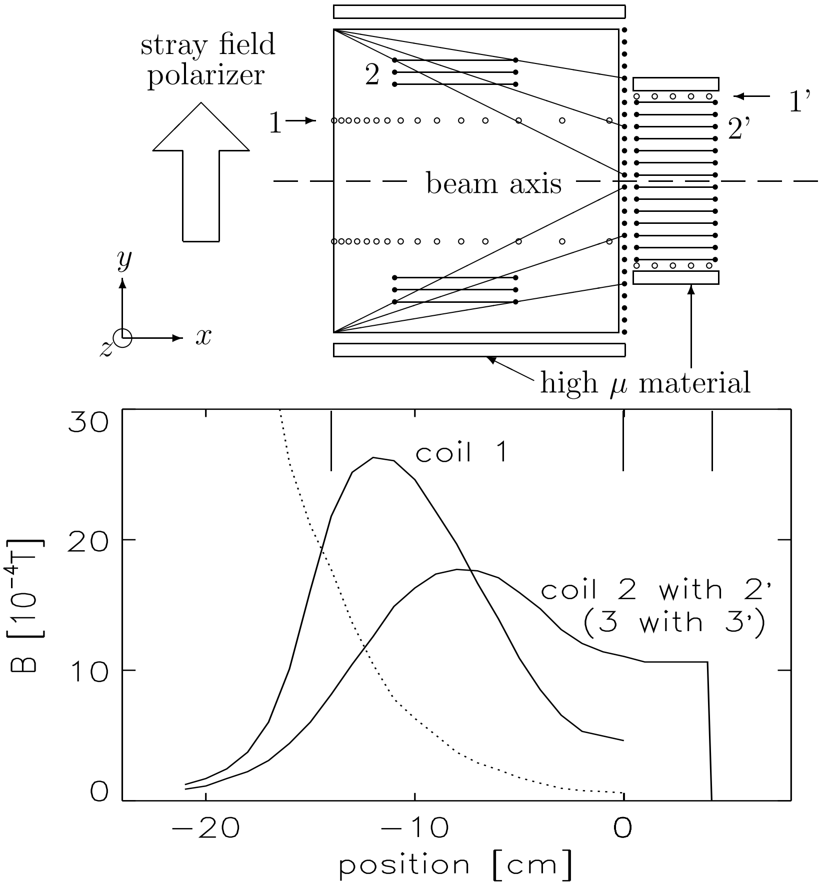

Figure 5.1: (Top) Top view of the first rotator (D_1) including the coils 1 with l' and 2 with 2' for adjustment of the polarization vector parallel to the x- and y-axis respectively. For simplicity the coils 3 with 3' for adjustment parallel to the z-axis (analogous to 2 combined with 2', but rotated by $\pi/2$ around x) are omitted. Bottom: Magnetic induction of the coils for a current of 0.5 A. The dotted line is the stray field of the polarizer.

to coils 2 but rotated by $\pi/2$ around the x axis.) The window of the sample chamber (see next section) contains a set of three orthogonal coils denoted l', 2' and 3'. They are energized together with 1, 2 and 3, respectively.

Fig.5.1 (bottom) displays the fields generated by coils 1 and 2 (or 3) for a current of 0.5 A. Coils 2 and 3 are shaped in such a way that their fields abruptly drop to zero beyond D_1 as seen along the neutron path. Hence, the vector $\boldsymbol{P}$ is no longer affected after the neutron beam leaves D_1. For coil 1 (rotation with respect to x) this is impossible because of Maxwell's equations; it only can be shaped in such a way that the decay of its field along the neutron path is slow enough not to give a too strong inhomogeneity over the beam cross section to cause appreciable depolarization. The shape and the operation of rotator D_2 in front of the analyzer is mirror symmetrical.

5.4 Theory of test procedure

Fig. 5.2 represents the setup for testing the performance of the rotators D_1 and D_2. They are sandwiched around the sample chamber S between polarizer P and analyzer Q. This assembly, referred to as "depolarization module" (DM), is tested by means of the "Larmor module" (LM) consisting of the analyzer Q, a precession coil (L) and a second analyzer R. S contains a pair of coils to generate a magnetic field over about a 10 mm path length parallel to the y- or z-axis. The procedure described below is performed without field in S, with a y-field and with a z-field in S.

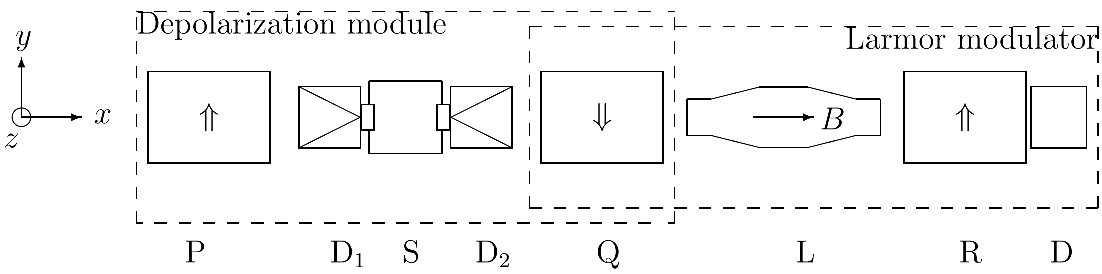

Figure 5.2: Schematic top view of the test setup for the adiabatic rotators D_1 and D_2.

For each mode $i(=x,y,z)$ of D_1 and each mode $j(=x,y,z)$ of D_2 the intensity $I_{ij}(B)$ is recorded as a function of the field B in the precession coil. Moreover, the intensities $I_{-xx}(B)$ and $I_{-zz}(B)$ are recorded. It was pointed out earlier [44] that from the *intensities* $I_{ij}(B)$ the *spectra* $J_{ij}(\lambda)$ are obtained by the Fourier transformation:

$$J_{ij}(\lambda) = -\frac{2}{\pi}\int\limits_{-\infty}^{\infty}[I_{ij}(B) - I_s]\cos(c_L\lambda B)d(c_L B). \tag{5.3}$$

Here I_s is the intensity measured when a depolarizing shim is placed between Q and R (I_s does not depend on B). c_L is a constant characterizing the precession coil; it can be determined from $I(B)$ for a monochromatic beam of known wavelength. The spectra $J_{-xx}(\lambda)$ and $J_{-zz}(\lambda)$ are obtained from $I_{-xx}(B)$ and $I_{-zz}(B)$ according to the same procedure.

From these spectra the uncorrected depolarization matrix elements D^*_{ij} for D_1 operating together with D_2 in the ij mode are defined according to:

$$D^*_{ij}(\lambda) = 1 - \frac{J_{ij}(\lambda)}{J_s(\lambda)}, \tag{5.4}$$

where $J_s(\lambda)$ is the spectrum obtained with a depolarizing shim in S. ($J_s(\lambda)$ should not be confused with I_s in Eq. (5.3).) The depolarization matrix elements corrected for the total depolarization in the setup are calculated by:

$$D_{ij}(\lambda) = \frac{J_s(\lambda) - J_{ij}(\lambda)}{J_s(\lambda) - J_{\min}(\lambda)}. \tag{5.5}$$

In practise one takes for $J_s(\lambda)$ the average of $J_{xx}(\lambda)$, $J_{-xx}(\lambda)$, $J_{zz}(\lambda)$ and $J_{-zz}(\lambda)$. The "minimum intensity" $J_{min}(\lambda)$ is taken to be equal to $J_{yy}(\lambda)$, i.e. the mode in which no adiabatic rotation in D_1 and D_2 occurs.

5.5 Results

5.5.1 Without fields to S

The rotators D_1 and D_2 appeared to give the best adjustment of the vector $\boldsymbol{P}$ when the coils 1, 2 and 3 in D_1 and D_2 were operated at a current between 0.4 and 0.5 A. The adjustment proved to depend hardly on the current in coils 2' and 3' (so these were switched in series with 2 and 3), but to depend critically on the current in coil l' (x adjustment). This current must be strong enough to overcome stray fields to the transition region of the sample chamber, but weak enough so that the divergent field outside coil l' does not affect the vector $\boldsymbol{P}$ anymore. A current between 0.15 and 0.20 A (corresponding to a maximum field value of $10{\times}10^{-4}$ T) proved to be optimal. To give a typical result, Fig. 5.3 contains the

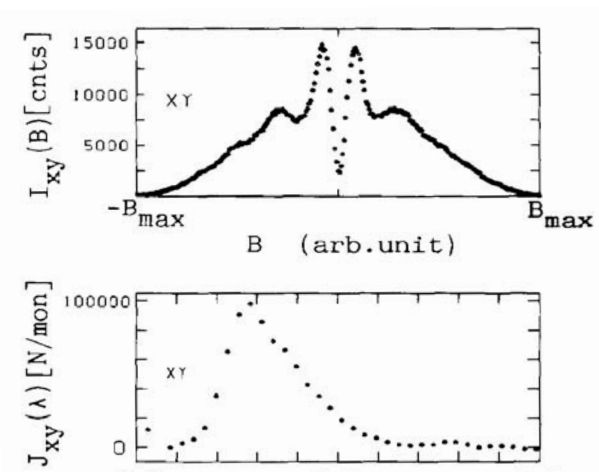

Figure 5.3: (Top) Intensity $I_{xy}(B)$ recorded as a function of the magnetic induction m the Larmor coil L (Fig. 5.2) without field in sample chamber S (Fig.5.2). The decline of the intensity at both ends is due to the "Tukey filter" (see **5.5.1**)). (Bottom) Spectrum $J_{xy}(\lambda)$ obtained from the above measurement after Fourier transformation according to Eq. (5.3).

intensity I_{xy}, recorded as a function of B without field in S and the spectrum $J_{xy}(\lambda)$ obtained according to Eq. (5.3). The fact that the recorded intensities in the plot of $I_{xy}(B)$ tend to zero at both ends is due to the measuring time devoted to each B-point. This time (preset monitor value) was adjusted according to a "Tukey filter" [45], i.e. equal to

$$\cos^2\left(\frac{B}{B_{\max}}\frac{\pi}{2}\right) \text{times the time at } B = 0,$$

in order to reduce the truncation effect in the Fourier transformation according to Eq. (5.3). From the plot of $J_{xy}(\lambda)$ it appears that the available spectrum begins at λ=0.15 nm and drops rapidly beyond λ=0.4 nm. Therefore the results are considered to be relevant between 0.2 and 0.55 nm, as may be apparent from the error bars in Fig. 5.4.

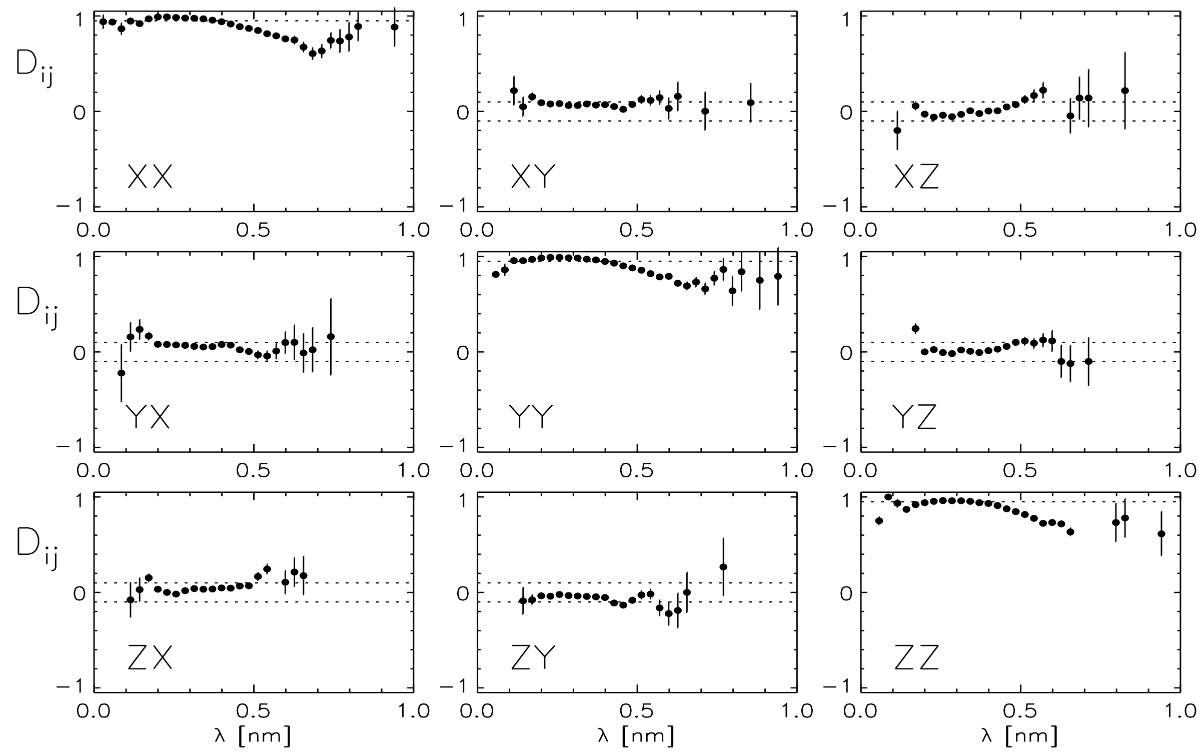

Figure 5.4: "Uncorrected" depolarization matrix elements D_{ij} **without field** in S obtained according to Eq. (5.4) from the spectra J_{ij}, with the average of the spectra $J_{xx}(\lambda)$, $J_{-xx}(\lambda)$, $J_{zz}(\lambda)$ and $J_{-zz}(\lambda)$ as "shim" intensity.

This figure shows the elements $D^*_{ij}(\lambda)$ for all nine ij modes. It is observed that between 0.15 and 0.4 nm D^*_{xx}, D^*_{yy} and D^*_{zz} are within 0.05 equal to the theoretical value of 1; beyond 0.4 nm these quantities decline rapidly. This observation is discussed in Sec. **5.6.2**. The D^*_{ij} for $i \neq j$ are equal to 0 within 0.1 over the range of 0.2−0.55 nm. The boundaries of these intervals are indicated by the dotted lines in Fig. 5.4.

5.5.2 With an y- or z-field in S

Fig. 5.5 contains the elements D^*_{ij} with a current of 0.7 A in the y-coil (corresponding to a field strength of 8 A/cm over a 10 mm path length) inside the sample chamber S. From the path length of the neutron beam through the coil it follows that D^*_{ij} should be identical with a rotation matrix describing a rotation over $\phi^* = 5.11 \cdot \lambda$ (λ in nm) as given by the dotted lines. It is observed that the measured D^*_{ij} follow the theoretical values reasonably well; the deviations in general do not exceed 0.1. An analogous set of measurements was taken with a z-field inside the sample chamber. The conclusion is likewise.

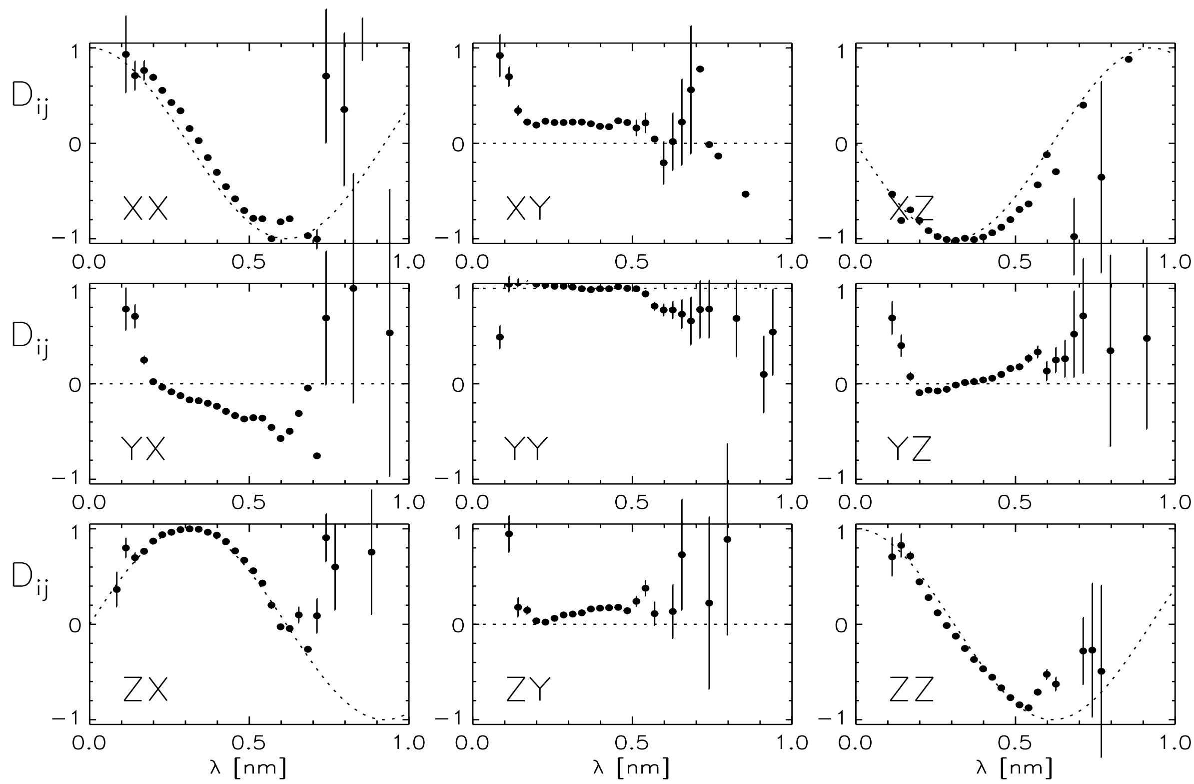

Figure 5.5: Depolarization matrix elements D_{ij} **with a y-field** in S obtained according to Eq. (5.5) from the spectra J_{ij} (Shim intensity: see Fig. 5.4; minimum intensity: see Sec. **5.4**). The dotted lines give the elements for a rotation matrix around y over $\phi^* = 5.11 \cdot \lambda$.

5.6 Discussion

5.6.1 Checking shim intensity

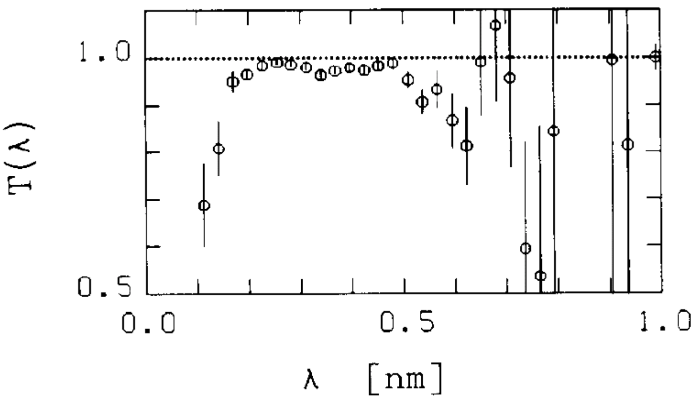

Figure 5.6: Quotient of the "shim" intensity with a shim placed in S and the average of the spectra J_{xx}, J_{-xx}, J_{zz} and J_{-zz}.

Fig. 5.6 contains a plot of the function $T(\lambda)$ found after dividing the spectrum $J_s(\lambda)$ by the average of $J_{xx}(\lambda)$, $J_{-xx}(\lambda)$, $J_{zz}(\lambda)$ and $J_{-zz}(\lambda)$. It is seen that this average is a good representation of the shim intensity $J_s(\lambda)$ as obtained by actually placing a depolarizing shim plate in the sample chamber S. In fact $T(\lambda)$ is the transmission of the shim plate and $T(\lambda)$ declines gradually with λ as is to be expected.

5.6.2 Dependence on polarizing powers of polarizer and analyzer

The D^*_{ij} as given in Fig. 5.4 depend upon the polarizing powers $\epsilon_{\rm P}$ and $\epsilon_{\rm Q}$ of P and Q combined with the adjustment of D_1 and D_2. In this subsection quantities α_{ij} are to be introduced and evaluated to characterize the adjustment of D_1 and D_2 alone. All quantities to be mentioned are functions of λ; for readability of the formulas this functional dependence is omitted from here onwards.
In ref. [44] it is stated that the spectra J_{ij} obtained according to Eq. (5.3) are equal to:

$$J_{ij} = \rho \, t_{\rm PQ} t_{\rm R} \, \epsilon_{\rm PQ} \epsilon_{\rm R}, \tag{5.6}$$

where ρ is the spectral density of the beam before P; $\epsilon_{\rm PQ}$ is the effective polarizing power of Q placed in series with P, $\epsilon_{\rm R}$ is the polarizing power of R, and $t_{\rm PQ}$ and $t_{\rm R}$ are the transmissions. To develop an expression for the quantities $\epsilon_{\rm PQ}$ and $t_{\rm PQ}$ to be substituted into this expression, one must recall that the incident intensities I_{in}^{+} and I_{in}^{-} will be changed after transmission through a polarizer of polarizing power ϵ into:

$$I_{\text{out}}^{+} = I_{\text{in}}^{+}(1+\epsilon)/2; \qquad I_{\text{out}}^{-} = I_{\text{in}}^{-}(1-\epsilon)/2. \tag{5.7}$$

Applying these equations to the incident beam into P and into Q, successively, it is found that the polarization of the beam emerging from Q is equal to the polarization of the beam emerging from a "device" with polarizing power:

$$\epsilon_{\text{PQ}} = \frac{\alpha_{ij}\ \epsilon_{\text{P}} - \epsilon_{\text{Q}}}{1 - \alpha_{ij}\ \epsilon_{\text{P}}\epsilon_{\text{Q}}} \tag{5.8}$$

and transmission:

$$t_{\text{PQ}} = t_{\text{P}}t_{\text{Q}}(1 - \alpha_{ij}\ \epsilon_{\text{P}}\epsilon_{\text{Q}})/2. \tag{5.9}$$

ϵ_{P} is multiplied by the factor α_{ij} to account for the fact that the polarization vector is affected by D_1 and D_2 before the neutron beam enters Q. So in fact the quantities α_{ij} characterize the adjustment of D_1 together with D_2. The spectrum J_{ij} is expressed in ϵ_{P}, ϵ_{Q} and ϵ_{R} by substitution of Eqs. (5.8) and (5.9) into Eq. (5.6). The spectrum J_s is found in a similar way and by taking ϵ_{P} equal to 0. Hence the quantities D_{ij}^{*} in Eq. (5.4) become:

$$D_{ij}^{*} = \alpha_{ij}\frac{\epsilon_{\text{P}}}{\epsilon_{\text{Q}}}, \tag{5.10}$$

so the factor α_{ij} may be written as a function of ϵ_{P}, ϵ_{Q} and the measured D_{ij}^{*} by:

$$\alpha_{ij} = D_{ij}^{*}\frac{\epsilon_{\text{Q}}}{\epsilon_{\text{P}}}. \tag{5.11}$$

In order to know α_{ij} the polarizing powers ϵ_{P} and ϵ_{Q} should be known. The setup of Fig. 5.2 allows no measurement of ϵ_{P} and ϵ_{Q} decoupled from the rotators D_1 and D_2. Therefore, these quantities had to be determined in a separate experiment in which an extra polarizer PP was inserted between P and D_1 and a monochromator was installed directly behind Q. For five settings of the monochromator the polarizing powers ϵ_{P}, ϵ_{PP} and ϵ_{Q} were determined according to the "3-polarizer-2-shim" procedure [65].

The "3-polarizer-2-shim" procedure is applied to a setup consisting of three polarizers in series with polarizing powers ϵ_1, ϵ_2 and ϵ_3. For simplicity their directions are assumed to be parallel; reversal of a polarizer is simply done by changing the sign of the corresponding ϵ. In a detector behind the third polarizer the following intensities are measured:

I_{s1s2}	with shims between 1 and 2 and 2 and 3;
I_{s1}	with a shim between 1 and 2;
I_{s2}	with a shim between 2 and 3;
I_0	without any shim.

On the other hand, these intensities can be calculated using Eq. (5.7). It appears that the equation for I_{s1s2} may be divided out, so the following equations in the *reduced* intensities i_{s1}, i_{s2} and i_0 remain:

$$\begin{aligned} i_{s1} &= 1 + \epsilon_2\epsilon_3, \\ i_{s2} &= 1 + \epsilon_1\epsilon_3, \\ i_0 &= 1 + \epsilon_1\epsilon_2 + \epsilon_1\epsilon_3 + \epsilon_2\epsilon_3. \end{aligned} \tag{5.12}$$

The solution is:

$$\epsilon_1 = \sqrt{a_2 a_3/a_1}, \qquad \epsilon_2 = \sqrt{a_1 a_3/a_2}, \qquad \epsilon_3 = \sqrt{a_1 a_2/a_3}. \tag{5.13}$$

where

$$a_1 = i_{s1} - 1, \qquad a_2 = i_{s2} - 1, \qquad a_3 = i_0 - 1 - a_1 - a_2.$$

Defining $\epsilon_3 > 0$, the signs of ϵ_1 and ϵ_2 are determined by Eq. (5.13). It should be noted that the obtained ϵ_1 and ϵ_3 include all (depolarization) effects on the polarization vector before transmission through the next polarizer.
The results for ϵ_P and ϵ_Q obtained according to the above procedure (Eqs. (5.13)) are given in Table 5.1, together with the D^*_{ii} (from Fig. 5.4) and α_{ii} (using Eq. (5.11)). Because the second polarizer PP is directly behind P and magnetically parallel with it, the quantity ϵ_P will include no depolarization effect.

Table 5.1: Polarizing powers ϵ_P and ϵ_Q of P and Q, and α_{ii} obtained from D^*_{ii} using Eq. (5.11).

λ nm	ϵ_P	ϵ_Q	D^*_{xx} Fig. 5.4	α_{xx}	D^*_{yy} Fig. 5.4	α_{yy}	D^*_{zz} Fig. 5.4	α_{zz}
0.270	0.99(3)	0.95(3)	0.984(2)	0.95	0.994	0.96	0.968	0.93
0.300	0.91(3)	0.97(3)	0.980(2)	1.04	0.992	1.06	0.966	1.03
0.343	0.99(3)	0.95(3)	0.970(3)	0.93	0.977	0.93	0.958	0.93
0.429	0.79(4)	0.91(3)	0.910(4)	1.05	0.921	1.06	0.901	1.04
0.495	0.72(5)	0.81(5)	0.858(9)	0.97	0.872	0.99	0.832	0.94

The inaccuracy of ϵ_P and ϵ_Q leads to an inaccuracy in α_{ii} exceeding 0.05 above 0.4 nm, so the mutual differences between the α_{ii} become irrelevant. It is nevertheless concluded that the α_{ii}, contrary to the D^*_{ii} as shown in Fig. 5.4, remain close to l over the whole spectral range. Apparently, the decline of the D^*_{ii} beyond 0.4 nm is due to the quotient ϵ_P/ϵ_Q and not due to the rotators D_1 and D_2. The values of D^*_{ii} for $i \neq j$ are corrected by the same factor after applying Eq. (5.11). Since they are close to zero, their levels as shown in Fig. 5.4 will hardly change.

5.6.3 Orthogonality

The misadjustment caused by rotators D_1 and D_2 relative to the laboratory system is described by Rekveldt et al. [47] by matrix elements denoted P_{ij} and Q_{ij}, respectively $(i, j = x, y, z)$. The elements for $i \neq j$ are assumed to have an absolute value smaller than 0.1. Hence the elements P_{ii} and Q_{ii} will be equal to 1 in first order. Expressed in P_{ij} and Q_{ij}, the experimental result **without field** in S may be written (neglecting terms of order higher than 1):

$$D_{ij}^{(0)} = \begin{pmatrix} 1 & P_{xy} + Q_{xy} & P_{xz} + Q_{xz} \\ P_{yx} + Q_{yx} & 1 & P_{yz} + Q_{yz} \\ P_{zx} + Q_{zx} & P_{zy} + Q_{zy} & 1 \end{pmatrix} . \tag{5.14}$$

Writing $c = \cos c_s \lambda B^{(y)}$ and $s = \sin c_s \lambda B^{(y)}$, the experimental result **with a field** $B^{(y)}$ in the y direction in S may be written (again neglecting higher order terms):

$$D_{ij}^{(y)} = \begin{pmatrix} c + s(Q_{xz} - P_{zx}) & cP_{xy} - sP_{zy} + Q_{xy} & c(P_{xz} + Q_{xz}) - s \\ cP_{yx} + Q_{yz} + P_{yx} & 1 & cQ_{yz} + sQ_{yx} + P_{yz} \\ c(P_{zx} + Q_{zx}) + s & cP_{zy} + sP_{xy} + Q_{zy} & c + s(P_{xz} - Q_{zx}) \end{pmatrix} . \tag{5.15}$$

An analogous expression is found for $D_{ij}^{(z)}$ with a z-field in S.
After identifying the elements of $D_{ij}^{(y)}$ and $D_{ij}^{(z)}$ with their corresponding experimental results (as shown for $D_{ij}^{(y)}$ in Fig. 5.5), the matrices P_{ij} and Q_i can be determined as a function of λ. Once these quantities are known, a procedure can be developed to correct any measured depolarization matrix to the depolarization matrix as it should read in the laboratory system.
For many applications of the depolarization technique, only the rotation angle ϕ around a known axis and the absolute value of $\boldsymbol{B}$ are to be determined. In most cases one can choose the y- or z-axis for this axis, e.g. by the direction of the magnetizing field. For the y-axis and an ideal adjustment of $\boldsymbol{B}$ by the rotators, ϕ and $|\boldsymbol{B}|$ are given by

$$\phi^{(y)} = \arctan \frac{D_{zx} - D_{xz}}{D_{xx} + D_{zz}} \; ; \tag{5.16}$$

and

$$|\boldsymbol{B}| = D_{yy} \sqrt{D_{xx} D_{zz} - D_{xz} D_{zx}} \tag{5.17}$$

(for a field along the z-axis, the indices should be changed accordingly). For these equations the correction procedure outlined above can be performed easily. Correction of $\phi^{(y)}$ is done by substitution of the expressions for D_{zx}, D_{xz} , D_{xx} and D_{zz}, of Eq. (5.15) into Eq. (5.16). This gives:

$$D_{zx} - D_{xz} = 2s + c[(P_{zx} + Q_{zx}) - (P_{xz} + Q_{xz})]$$

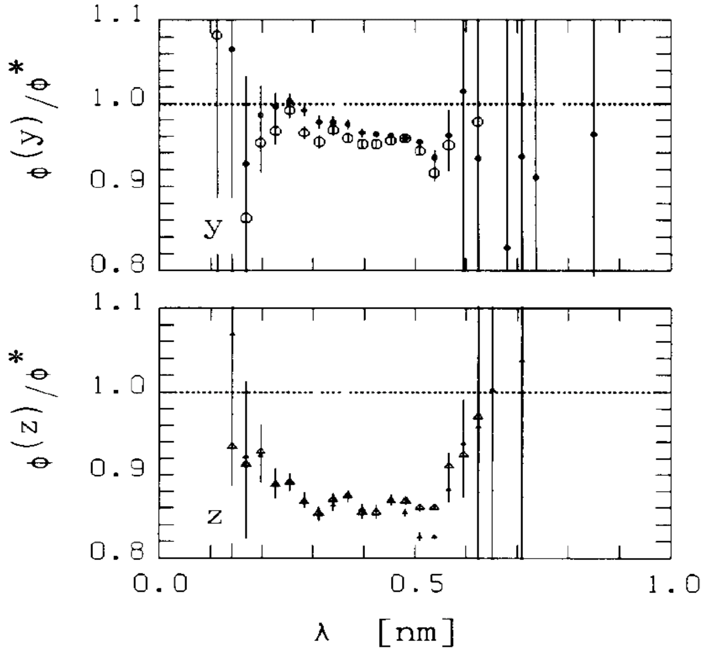

Figure 5.7: Evaluation of the precession angle of the polarization vector in a field coil in S. Small symbols: before correction for the misadjustment of D_1 and D_2 (Eq. (5.16)); big symbols: after this correction (Eq. (5.18)). The angles are normalized to $\phi^* = 5.11 \cdot \lambda$ i.e. the angle according to length and field strength of the coil. (Top) y-field; (Bottom) z-field.

and

$$D_{xx} + D_{zz} = 2c + s[(P_{xz} + Q_{xz}) - (P_{zx} + Q_{zx})].$$

According to Eq. (5.14), the correction terms $P_{xz} + P_{zx}$ and $P_{xz} + Q_{xz}$, can be taken from the elements $D_{zx}^{(0)}$ and $D_{xz}^{(0)}$ in the measurement without field. Hence one uses instead of Eq. (5.16):

$$\phi_c^{(y)} = \arctan\left(\frac{D_{zx}^{(y)} - D_{xz}^{(y)} - c(D_{zx}^{(y)} - D_{xz}^{(y)})}{D_{xx}^{(y)} + D_{zz}^{(y)} - s(D_{xz}^{(y)} - D_{zx}^{(y)})}\right), \tag{5.18}$$

with for c and s the "0th order" result according to Eq. (5.16). (For a field along the z-axis, the indices should be changed accordingly).
Eq. (5.17) will not change upon correction, since the matrices P_{ij} and Q_{ij} are unitary (to first order). Fig. 5.7 gives the result for $\phi^{(y)}/\phi^*$ and $\phi^{(z)}/\phi^*$ as functions of λ before (small symbols) and after (big symbols) correction. Before correction, ϕ for both fields tends to fall increasingly short of its theoretical value ϕ^* given by the dotted horizontal lines. After correction both $\phi^{(y)}$ and $\phi^{(z)}$ remain lower than ϕ^*, however without a unique tendency to decrease or increase relative to

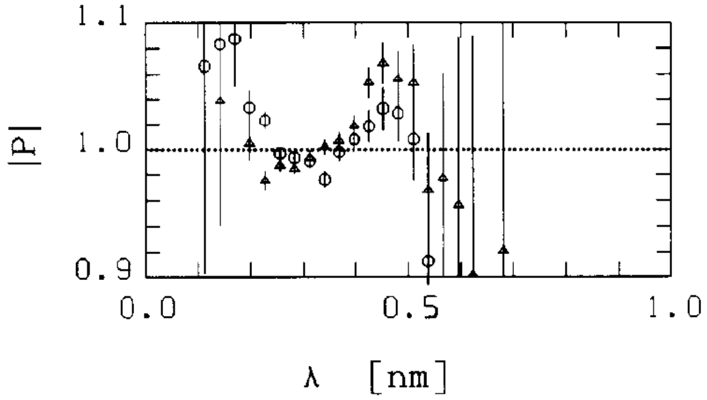

Figure 5.8: The length |P| of the polarization vector after precession in a field coil in S according to Eq. (5.17). ◯: y-field; △: z-field.

ϕ^*. The fact that ϕ is lower than ϕ^* is due to the "back flux" of the (finite) y and z-coils used. Although both coils are of identical design, the magnetic short circuiting by their common yoke acts differently for y and z flux. In Fig. 5.8 the quantity $|\boldsymbol{B}|$ for both fields is plotted as a function of λ. It is seen that $|\boldsymbol{B}|$ is determined with a precision of a few percent over the λ range 0.15-0.55 nm.
The fact that within this range the ϕ's after correction tend to be better on a horizontal line than before correction, suggests that the correction procedure in principle acts properly; however, the errors in the obtained ϕ and $|\boldsymbol{B}|$ after correction seem to be systematical rather than due to statistics. This suggests that the origin of these errors is in the Fourier transformation to get the spectra. These errors may arise because of a misadjustment of the polarization vector in the "Larmor module" combined with an improper processing of the data (filtering, normalisation, contribution of sinus transformation, etc.).

5.7 Summary and conclusions

From the results shown in this paper, it can be concluded that the present neutron spectra obtained by means of Larmor precession and subsequent Fourier transformation have a quality such that polarization analysis based upon these spectra gives reliable results over the wavelength range of 0.15-0.55 nm. Outside this range errors due to mis-setting of the polarization vector at the beginning and the end of the precession coil and due to the procedure around the Fourier transformation (filtering, contribution of sinus-transformation, normalization) exceed the statistical errors in the present data.
Using the spectra thus obtained, the "uncorrected" depolarization matrix ele-

ments $D^*_{ij}, (i, j = x, y, z)$ have been calculated. The D^*_{ij} for $i = j$ decline from 0.99 at λ= 0.15 to 0.6 at λ= 0.55 nm. These quantities include the polarizing powers of the polarizer and analyzer in the test setup. By adding an extra polarizer directly behind the first polarizer, it is possible to calculate these polarizing powers themselves and hence to evaluate the net adjustment of the rotators as a function of λ. The results indicate that less than 5% depolarization occurs up to λ= 0.5 nm. Hence, the poor value for $D^*_{ij}, (i = j)$ is due to the polarizers used in the test setup rather than due to the rotators. Due to the misadjustment of the polarization vector by the rotators, the D^*_{ij} for $i \neq j$ rise up to 0.1 from zero. For some (i, j) the deviations from zero are λ-dependent.

The elements of the depolarization matrix D_{ij} have been determined with a y- and a z-field in the sample chamber. These elements appear to be equal within 0.15 to the theoretical values for a pure rotation around y and z over the λ range mentioned. From the D_{ij}, the rotation angle of the polarization vector due to the precession to the fields and its absolute value have been determined. Before correction for the misadjustment of the rotators, this angle appears to be slightly less than proportional to λ. After correction this angle tends to be more proportional to λ. The absolute value of the polarization vector appears to be equal to 1 within 3%.

Chapter 6

Test of adiabatic spin flippers for application at pulsed neutron sources

W.H. Kraan[1], S.V. Grigoriev[2], M.Th. Rekveldt[1], H. Fredrikze[1], C.F. de Vroege[1], J. Plomp[1]

[1] Interfacultair Reactor Instituut, TUDelft, 2629 JB Delft, The Netherlands
[2] Petersburg Nuclear Physics Institute, 188350 Gatchina, Russia

Appeared in Nucl.Instr.& Methods A **510** (2003) 334-345

Experimental results on the flipping efficiency are shown for a set of 2 V-coils as spin flipper and for a high-frequency flipper with adiabatic transition. The influence of the adiabaticity parameter is discussed. The merits of these adiabatic flippers are compared with the use of "monochromatic" flippers, when operated in a beam from a pulsed neutron source. It is concluded that for "long pulse" sources adiabatic flippers will be superior.

6.1 Introduction

Spin flippers are essential components in setups using polarized neutrons. To take full advantage of a pulsed neutron source flippers must have a good efficiency over the full thermal spectrum. Flippers based on various principles (e.g. resonance [48], Larmor precession in some magnetic field configuration [49],[50]) operate over a limited wavelength-band. By proper design parameters this band can be extended, sometimes at the expense of including wavelengths with non-full flipping efficiency. In principle, such flippers are monochromatic.

Alternative types of flipper work over the full thermal spectrum. An example is the high-frequency flipper with static gradient field [51] using the principle of adiabatic rotation of the polarization vector of the neutron beam from the initial to the opposite direction. Another example has a static field, changing sign gradually over a finite beam path length [52].
By flipping we do not understand a geometrical inversion of the orientation of the neutron polarization, but an inversion relative to the local magnetic field, or mirroring about the plane perpendicular to the field. Hence a device in which the field together with the polarization rotate as a screw over π over some beam path length, is not a flipper.
In the flipping process the beam might be depolarized, in other words, the efficiency of flipping might be less than 1. The polarization of a beam with initial polarization P_0 after a flipper of efficiency ϵ is converted to $P_1 = (1 - 2\epsilon)P_0$, hence:

$$\epsilon = (-P_1/P_0 + 1)/2. \tag{6.1}$$

After 2 flippers P_2 is again parallel to P_0, so $\epsilon_1\epsilon_2 = (P_2/P_0 + 1)/2$.
The behaviour of the polarization vector $\mathbf{P}$ in a flipper is determined by the precession equation: $d\mathbf{P}/dt = (\mu_n/\hbar)[\mathbf{P} \times \mathbf{B}]$, where $\mathbf{B}$ is the magnetic induction and μ_n the neutron's magnetic moment. Its solution is the well known rolling of the vector $\mathbf{P}$ over a cone with axis $\mathbf{B}$. If $\mathbf{B}$ depends on position along the beam axis - i.e. on time as seen in the frame moving with the neutron - the solution is characterized by the adiabaticity parameter k, which is equal to the local Larmor precession frequency $\omega_L = \mu_n|B|/\hbar$, divided by the rotation frequency $\omega_{geo} = v|d\alpha/dx|$ of the field as in the frame moving with the neutron (where the neutron moves at velocity $v = h/(m\lambda)$ in the x direction, and α is the angle between the z-axis and the resultant field at any position along the beam):

$$k = \frac{2\pi\mu_n m|B|}{h^2|d\alpha/dx|}\lambda. \tag{6.2}$$

Two limiting cases are evident immediately: (i) $\omega_L \gg \omega_{geo}$, i.e. $k \to \infty$. The axis of the precession cone "follows" the vector $\mathbf{B}$, hence no flip occurs ("adiabatically following"); (ii) $\omega_L \ll \omega_{geo}$, i.e. $k \to 0$. The axis of the precession cone does not follow $\mathbf{B}$ at all, so spin flip occurs.
For k between 0 and ∞, the solution of the precession equation for a field transition in the shape of a uniform screw over half a turn can be found in literature (e.g. Robiscoe [53]). ϵ is given by:

$$\epsilon = 1 - \frac{\sin^2((\pi/2)\sqrt{1+k^2})}{k^2+1}. \tag{6.3}$$

In this article we discuss 2 types of adiabatic flippers. The first is a set of 2 V-coils (see Fig. 6.1), as developed in Delft 10 years ago [54]. In fact, this flipper was a byproduct of polarization rotators for 3-D polarization analysis applicable for the full "white" neutron spectrum. In these rotators a $\pi/2$ turn of the polarization vector is produced. V-coils can also be used in a spin-echo setup to orient the polarization perpendicular to the precession field ($\pi/2$-flipper). A very similar type of flipper was built by Takeda c.s. [55].

The second type is the longitudinal high frequency (RF) coil inside a static gradient field mentioned above (Fig. 6.5), proposed and developed already in 1973 in Gatchina [56] and treated theoretically by Taran [57]. At present such flippers are applied at many places (e.g. see [58]). For application at high fields we extended this type to frequencies up to 2 MHz [59], [60], [61]. As a matter of fact, to test this RF flipper, we used V-coils as π- and as $\pi/2$ flipper.

For both types we present data for ϵ as a function of wavelength, combined with an analysis of the parameter k as derived from field measurements along the beam. Contrary to Weinfurter e.a. [62] who give an analytical ansatz to improve ϵ by properly shaping the fields inside the flipper, we add some field around the position along the beam where k is minimum. We will demonstrate the improvement in efficiency. We point out that ϵ for a V-coil flipper is in principle smaller than 1, in both modes flip and non flip; the RF flipper, however, has $\epsilon = 1$ in the mode flip.

In the last section we compare the efficiency of these adiabatic flippers with the efficiency of a "monochromatic" flipper, installed in a beam from a pulsed source. This flipper is tuned in time such that it remains optimized ($\epsilon \simeq 1$) for all successive time channels [63], [64]. With the advent of "long pulse" sources, the pulse duration can be so long that a neutron spectrum of finite width is present in the flipper at any time. We will see that this spectrum, moreover, gets wider as the flipper is positioned closer to the source. Therefore, optimal tuning of the flipper will become problematic. Eventually, an adiabatic flipper will have better overall efficiency.

6.2 V-coils as flipper

This flipper is a set of 2 V-shaped coils (dimensions 15×15×15 cm^3) inside a magnetic shielding to provide a path without magnetic resistance for the return flux. Fig. 6.1a gives a top and a side view. At $x = r$ (dashed line) are 2 screens of parallel wires, traversed by the neutrons. Each coil produces a horizontal field terminated at the screen position.
In the mode "flip" (f) the fields in the V-coils are $//-y$ and $+y$, successively.

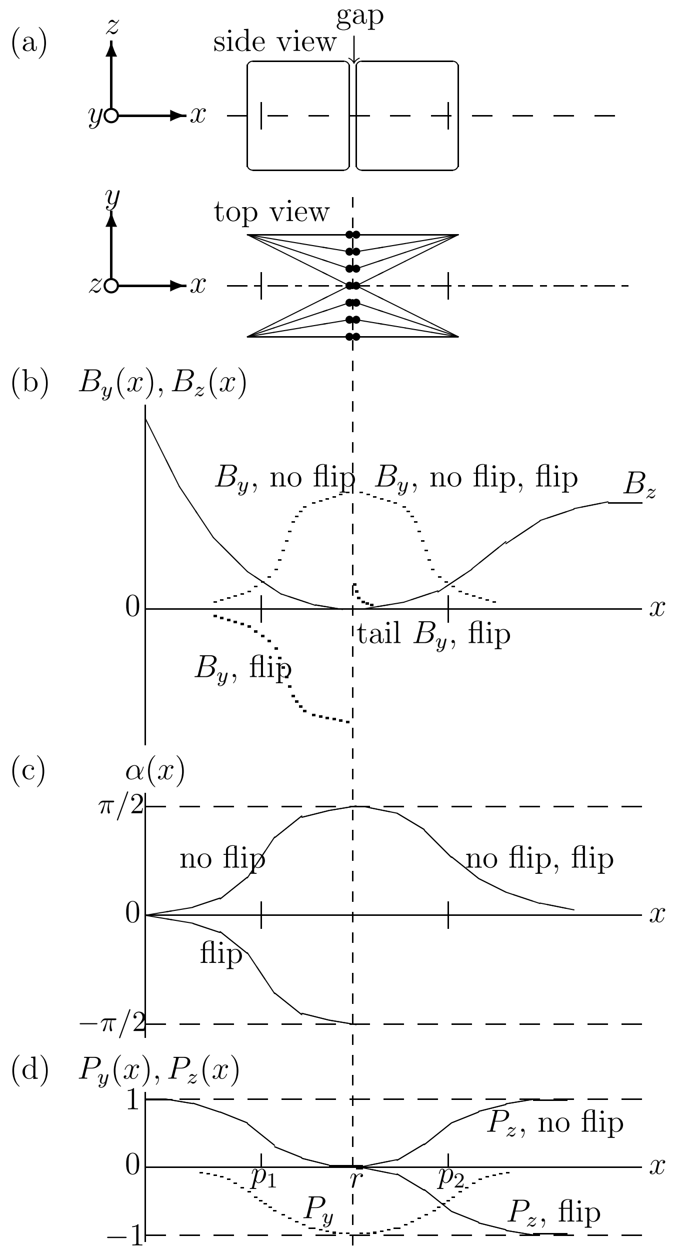

Figure 6.1: **(a):** Side and top view of a flipper made of 2 V-coils, positioned between a polarizer magnetized along z and a guide field // z **(b):** Schematic plots of the y and z components of the resulting field in the V-coils; **(c):** its angle α toward the z-axis; **(d):** the polarization components P_y (dotted line) and P_z (full line) along the beam line (x-axis).

Between the polarizer and the first V-coil the polarization follows the local field adiabatically from z (direction stray field polarizer) to $-y$ (field direction deep inside first V-coil). At $x=r$ the polarization does not follow the field reversal (field second V-coil $//+y$), so beyond $x=r$ it is anti-parallel to the local field. In this relative orientation it follows the local resultant field adiabatically over the length between the second V-coil (field $//y$) and the guide field ($//z$), hence the polarization ends in the "flipped" state.
In the mode "no flip" (n) the field in the first V-coil is switched parallel to the second (y) and no spin flip occurs at $x=r$.
The components of the field are plotted in Fig. 6.1b; they suggest that the absolute value of the resulting field is minimum at $x=p_1$ and p_2 where $B_y=B_z$. The angle $\alpha(x)$ between the local resulting field and the z-axis is given in Fig. 6.1c, showing that $d\alpha(x)/dx$ will be maximum in these points. Hence, the parameter k will be minimum at these positions. These minima effectively determine the quality of the flipper.

6.2.1 Test method of this flipper

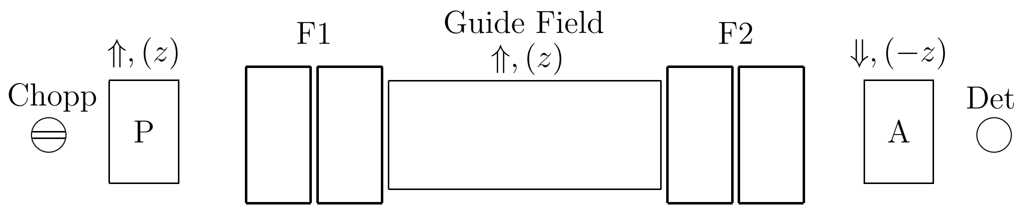

Trans.region:	T1	r_1	T2	T3	r_2	T4
no flip (n):	$z \rightarrow y$		$y \rightarrow z$	$z \rightarrow -y$		$-y \rightarrow -z$
flip (f):	$z \rightarrow -y$		$y \rightarrow z$	$z \rightarrow -y$		$y \rightarrow -z$

Figure 6.2: Side view of test setup.

For testing, a time-of-flight (TOF) setup with 2 identical V-coil flippers was built (Fig. 6.2), between a polarizer and an analyzer which are antiparallel to each other. The field transitions T1...T4 in front of and behind the flippers F1 and F2 are characterized for both modes (flip (f), no flip (n)) of both flippers. TOF spectra I_{nn}, I_{nf}, I_{fn} and I_{ff} were taken in all modes. In the modes nn and ff (0,2 flips) the neutron spin just beyond r_2 has the same orientation as just in front of r_1. From this orientation it rotates adiabatically in region T4 to the orientation of the analyzer, hence the spectra I_{nn} and I_{ff} are "light" (high intensity). The other spectra involve 1 flip, so the spin beyond r_2 is opposite to the previous case; these spectra are "dark".

The problem of analyzing such a set of spectra has been treated by several authors, e.g. Wildes e.a. [66]. We follow the analysis by Fredrikze e.a. [67] who give equations for the intensities $I^0_{pp}, I^0_{aa}, I^0_{pa}$ and I^0_{ap} measured in a neutron reflectometer with polarization facility, for the case without sample. In [67] the indices p and a refer to a fixed orientation in space, both at the polarizer and analyzer side of the sample position. In our case the first index p/a (referring in [67] to the polarizer side; here to F1) becomes n/f, respectively. Because our analyzer is anti-parallel to the polarizer, the second index p/a (analyzer side; F2) becomes f/n, respectively.

Each flipper will depolarize the beam. The full depolarization in mode nn is accounted for by a factor Q. As pointed out in the Introduction, V-coil flippers will give depolarization in both modes. Following [67] we assume that the depolarization D_n per flipper in mode n might differ from the depolarization D_f in mode f, by introducing the factors $\rho = D_n/D_f$ for flipper F1 and $\alpha = D_n/D_f$ for flipper F2. So, the full depolarization factors for the modes nn, nf, fn and ff become Q, αQ, ρQ and $\alpha\rho Q$, respectively. Then, the equations for for I_{nn}, I_{nf}, I_{fn} and I_{ff} (corresponding to I^0_{pa}, I^0_{pp}, I^0_{aa} and I^0_{ap} in ref [67]) become:

$$
\begin{aligned}
I_{nn} &= (I_0/2)(1 + \mathcal{P}_p\mathcal{P}_a\, Q), && (6.4)\\
I_{nf} &= (I_0/2)(1 - \mathcal{P}_p\mathcal{P}_a\, \alpha Q) && (6.5)\\
I_{fn} &= (I_0/2)(1 - \mathcal{P}_p\mathcal{P}_a\, \rho Q) && (6.6)\\
I_{ff} &= (I_0/2)(1 + \mathcal{P}_p\mathcal{P}_a\, \alpha\rho Q), && (6.7)
\end{aligned}
$$

where $\mathcal{P}_p\mathcal{P}_a$ is the product of the intrinsic polarizing efficiencies $\mathcal{P}_p$ and $\mathcal{P}_a$ of the polarizer and analyzer. These equations contain I_0, α, ρ and the product $\mathcal{P}_p\mathcal{P}_a$ as unknowns which can be solved. The solution reads:

$$
\begin{aligned}
I_0 \text{ (net spectrum)} &= 2\,\frac{I_{ff}I_{nn} - I_{nf}I_{fn}}{I_{nn} + I_{ff} - I_{fn} - I_{nf}}, && (6.8)\\
\mathcal{P}_p\mathcal{P}_a\, Q \text{ (depolarization)} &= \frac{(I_{nn} - I_{fn})(I_{nn} - I_{nf})}{I_{nn}I_{ff} - I_{nf}I_{nf}}, && (6.9)\\
\rho \text{ (asymmetry F1)} &= \frac{I_{ff} - I_{fn}}{I_{nn} - I_{nf}}, && (6.10)\\
\alpha \text{ (asymmetry F2)} &= \frac{I_{ff} - I_{nf}}{I_{nn} - I_{fn}}. && (6.11)
\end{aligned}
$$

6.2.2 Results: polarization empty beam

To separate the depolarization Q due to the flippers from the product $\mathcal{P}_p\mathcal{P}_a$ calculated according to Eq. (6.9), we need to find the product of the polarizing efficiencies $\mathcal{P}_p$ and $\mathcal{P}_a$. To find this product, we removed both flippers, so the setup consisted only of the polarizer and the anti-parallel analyzer. Their stray fields were extended until halfway between. We measured the TOF spectra "I_{min}" (with halfway a field step device containing antiparallel V-coils) and "I_{plus}" (with halfway a device in which the magnetic induction (5 mT) rotates uniformly over 180° over 0.3 m; the parameter k for 0.1 nm of this device equals 180, so the polarization follows adiabatically). The polarization:

$$P_0 = (I_{plus} - I_{min})/(I_{plus} + I_{min}) \tag{6.12}$$

is plotted in Fig. 6.3 as a function of TOF channel (i.e. λ) as a bold line.

Another way to find $\mathcal{P}_p\mathcal{P}_a$ is to multiply the data of the net polarizing efficiencies of polarizer and analyzer as determined by means of the 3P2F method [65] in earlier TOF experiments with the explicit purpose to determine $\mathcal{P}_p$ and $\mathcal{P}_a$ of the same polarizers [68]. The product $\mathcal{P}_p\mathcal{P}_a$ found in this way is plotted in Fig. 6.3a as a dotted line. (The irregularity around λ=0.8 nm is from noise pulses of the chopper. The discrepancy below λ=0.2 nm is due to a lack of intensity in the setup for the 3P2F method: it contains 3 instead of 2 polarizers having transmissions approaching 0 at low wavelength).

In the 3P2F method (published in [65] as "3P2S" method) 3 polarizers P, X and R are aligned in a beam, their magnetic directions being chosen at convenience. P, X and R could be all of different construction. Flippers (in [65] shims) installed in the gaps P-X and X-R are each operated in both modes, giving 4 intensities with the polarizing efficiencies $\mathcal{P}_p$, $\mathcal{P}_x$, $\mathcal{P}_r$ and the "intrinsic" intensity as unknowns. The solution for $\mathcal{P}_p$ and $\mathcal{P}_r$ includes the full depolarization (including flippers) in the gaps P-X and X-R, respectively. The result $\mathcal{P}_x$ - efficiency polarizer being tested - includes no depolarization.

Fig. 6.3a shows that P_0 is indeed equal to the product $\mathcal{P}_p\mathcal{P}_a$ of the intrinsic polarizing powers of the polarizers to within 1%. This means that the product $\mathcal{P}_p\mathcal{P}_a$ can be reliably divided out of the result for Eq. (6.9), hence the value found for Q can be attributed to the flippers.

6.2.3 Efficiency flippers in mode n

The result for $\mathcal{P}_p\mathcal{P}_a\,Q$ (Eq. (6.9)) with the flippers in their initial shape, is given as the dotted line in Fig. 6.3b (beam cross section 10×30 mm^2). Division by $\mathcal{P}_p\mathcal{P}_a$ (Fig. 6.3a, full line) gives Q, the depolarization due to 2 identical flippers in mode nn. Identifying $Q \equiv P_2/P_0$ (Eq. (6.1)) gives the average efficiency $<\epsilon>$ per flipper for mode n. It is plotted as the dotted line in Fig. 6.3c. We see that $<\epsilon>$ rises in an oscillating way, approaching 1 at $\lambda \simeq 0.4$ nm.

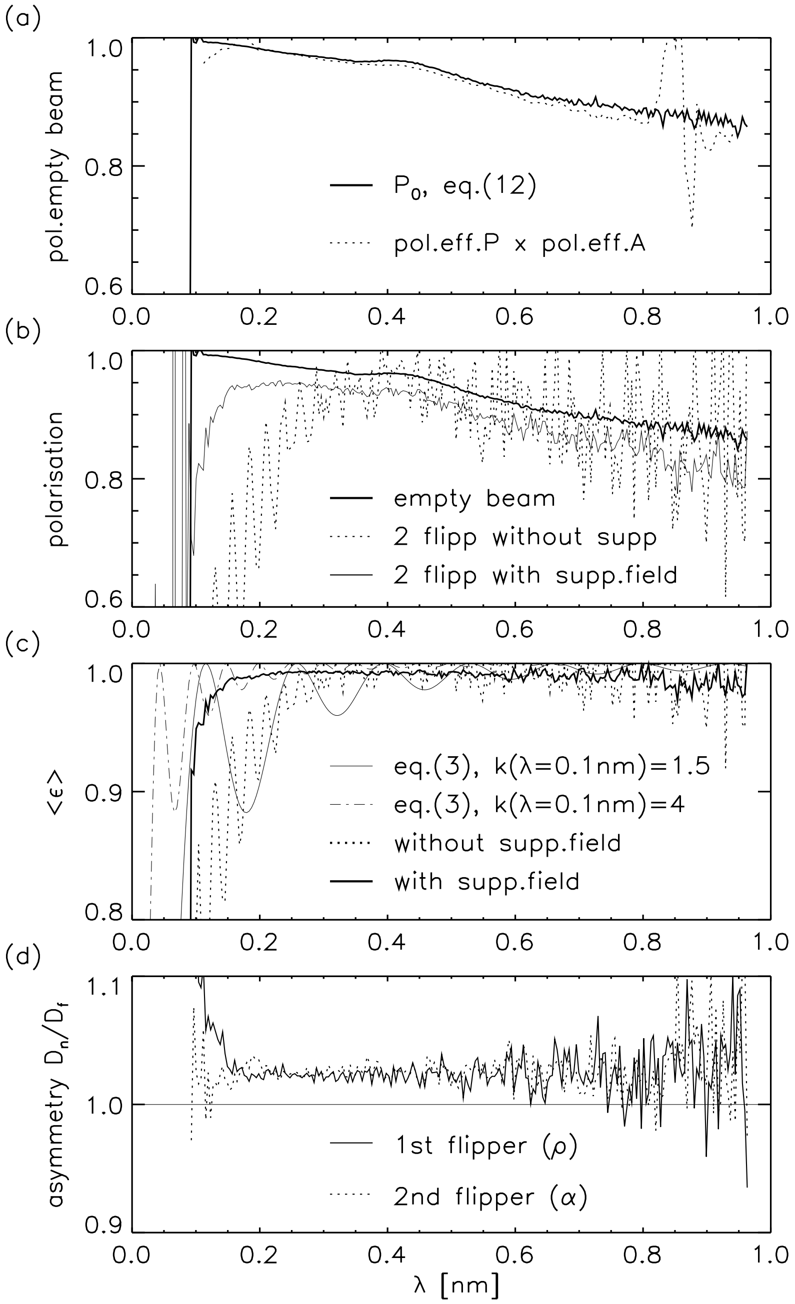

Figure 6.3: V-coil flipper: **(a):** polarization empty beam without flippers and as imposed by the efficiency $\mathcal{P}_p$ and $\mathcal{P}_a$ of the polarizers; **(b):** effective polarization with both flippers in mode n; **(c):** average efficiency $< \epsilon >$ per flipper, found using Eq. (6.1) after dividing the effective polarization (b) by the empty beam polarization (a). Also shown: $< \epsilon >$ according to Eq. (6.3), with adiabaticity paramater $k(\lambda$=0.1 nm) chosen to be 1.5 and 4; **(d):** asymmetry between n and f (Eqs. (6.6), (6.10(, (6.11)), with support field.

6.2.4 Adiabaticity parameter

These oscillations can be qualitatively understood from the behaviour of ϵ predicted by Eq. (6.3). In Fig. 6.3c ϵ is plotted for k chosen to be 1.5 and 4 for $\lambda = 0.1$nm. By comparing the decrease and periodicity in ϵ as measured with this prediction, it can be only said that $k(\lambda = 0.1\text{nm})$ ranges between 1 and 10. The failure to give a quantitative description of $< \epsilon >$ as a function of λ is due to the fact that the fields in the regions T1...T4 do not rotate uniformly, as assumed in Eq. (6.3).

Fig. 6.4 shows how this was analyzed. Fig. 6.4a gives the field profiles of flipper F1, measured in its initial configuration. Fig. 6.4b contains the angle α and its derivative needed to calculate ω_{geo} using Eq. (6.2); Fig. 6.4d gives the result, together with ω_L found from $|B|$, plotted in Fig. 6.4a. The bold lines without symbols in Fig. 6.4d give the adiabaticity parameter k. Near the points $x = r_1$ and r_2 characterized in Fig. 6.1 k drops nearly to 1.

The left minimum was raised by adding some z-field ("support field") by means of permanent magnets. The resulting field profiles for F1 are shown in Fig. 6.4c. The parameter k after this modification is given in Fig. 6.4d by the bold line with symbols. (F2 was improved in analogous way). $\mathcal{P}_p\mathcal{P}_a Q$ and $<\epsilon>$ measured after this modification are plotted as full lines in Figs.6.3b and c (beam cross section 30×30 mm^2). For λ as low as 0.15 nm $<\epsilon>$ appears to approach 1.

For an account of this result using Eq. (6.3), we should take $k(\lambda = 0.1\text{nm})$ at least 10. The period in the oscillations becomes so small that it damps out in view of the wavelength resolution of our TOF setup.

If space around the beam permits, other ways to improve k would be: to position the flipper properly in the stray fields of the adjacent devices, or to increase the dimensions of the flipper perpendicular to the beam. This will make the positioning of the flipper less critical.

6.2.5 Asymmetry between n and f

Fig. 6.3c gives the asymmetries ρ and α for flippers F1 and F2 after the modification. The asymmetry might have two origins.

First, the z-fields from the polarizer and the guide field around F1 in principle extend beyond its mid point $x = r$. As a consequence, the polarization vector just before $x = r$ has some z-component which is transferred into the second V-coil together with the y-component. This means that in mode f the flip at $x = r$ is not exact. For the mode n it has no consequences.

Secondly, the field of the V-coils does not end exactly at $x = r$, but has some negative tail beyond this point (Fig. 6.1b: "tail B_y, flip"). In mode f the tails

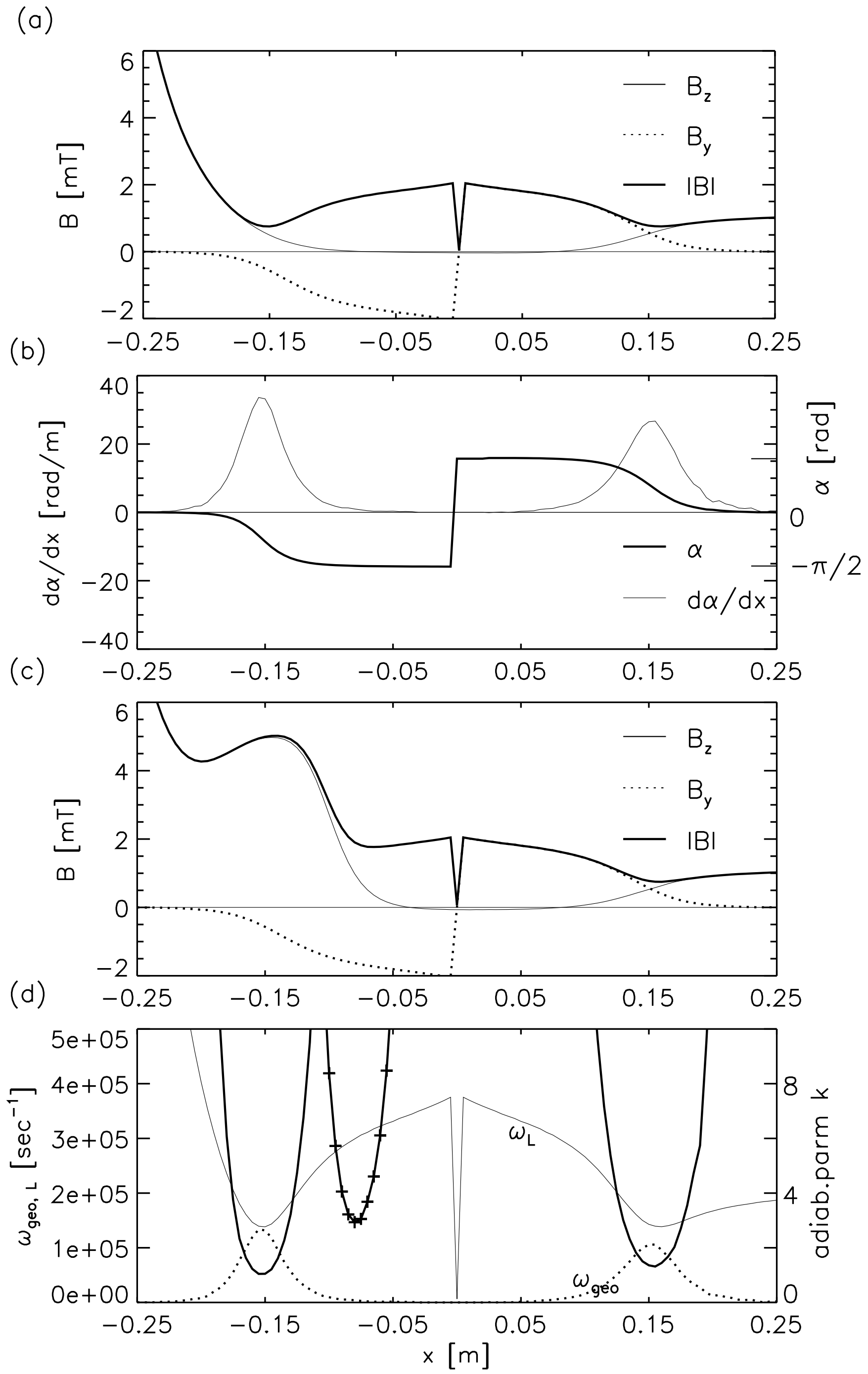

Figure 6.4: V-coil flipper: **(a):** Measured field profiles without support field; **(b):** angle $\alpha(x)$ between resulting field and z-axis (scale to the right) and $d\alpha/dx$; **(c):** Field profiles after improvement with support field. **(d):** Larmor frequency ω_L (from $|B|$) and "geometrical" frequency ω_{geo} (from $d\alpha/dx$, for λ =0.1 nm) as initially, without support field. Bold lines (without/with symbols): adiabaticity parameter k for the configurations (without/with) support field (scale to the right).

produced by the 2 adjacent V-coils largely cancel each other, but in the mode n they add, so in the gap (1mm) between the coils (see Fig. 6.1a) a y-field of the order 2mT exists. The polarization which already has some z-component by the previous effect, precesses in this gap over an angle amounting in the worst estimation to $\simeq 0.3$ rad for $\lambda = 0.5$nm. This precession, happening only in mode f, might explain why ρ and α are both greater than 1. (The data for the initial state of the flippers without support field are too poor to see the asymmetry).

6.3 Adiabatic RF flipper with gradient field

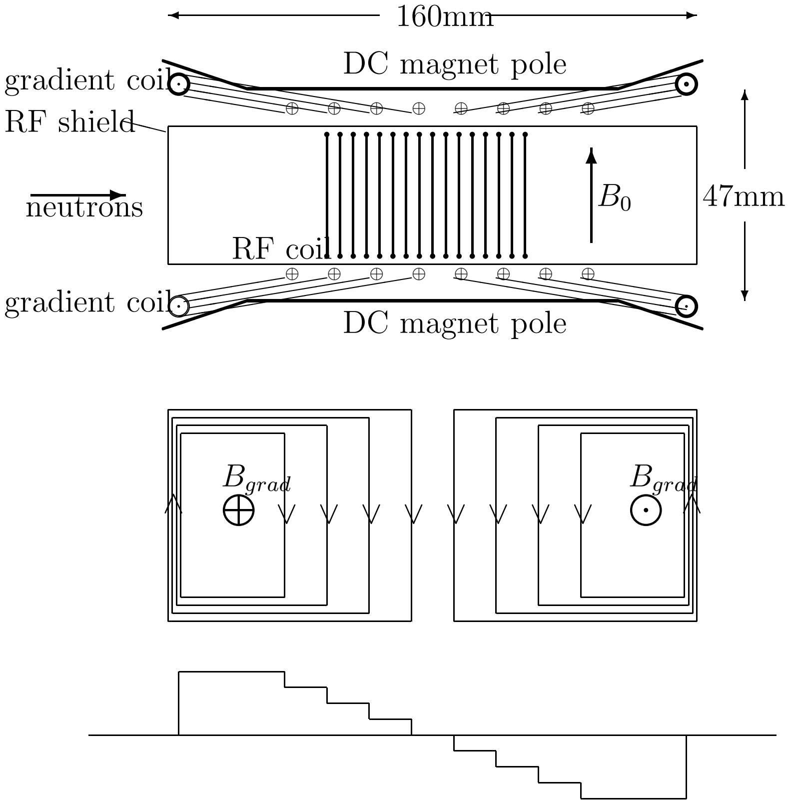

Figure 6.5: Side view of an adiabatic RF flipper and top view of the coils generating the gradient field, which is shown schematically in the bottom profile.

The second type of flipper is a "RF flipper with adiabatic transition", shown in Fig. 6.5. It consists of a longitudinal high- frequency (RF) coil (length 60 mm; diameter 30mm; 19 windings) in a static transversal field, composed of a "homogeneous" contribution B_0 and a static gradient field. 2 capacitors could be switched parallel to the RF coil, giving resonance at 1.08 and 2.25 MHz. The frequency must be chosen such that at some point inside the coil, it corresponds

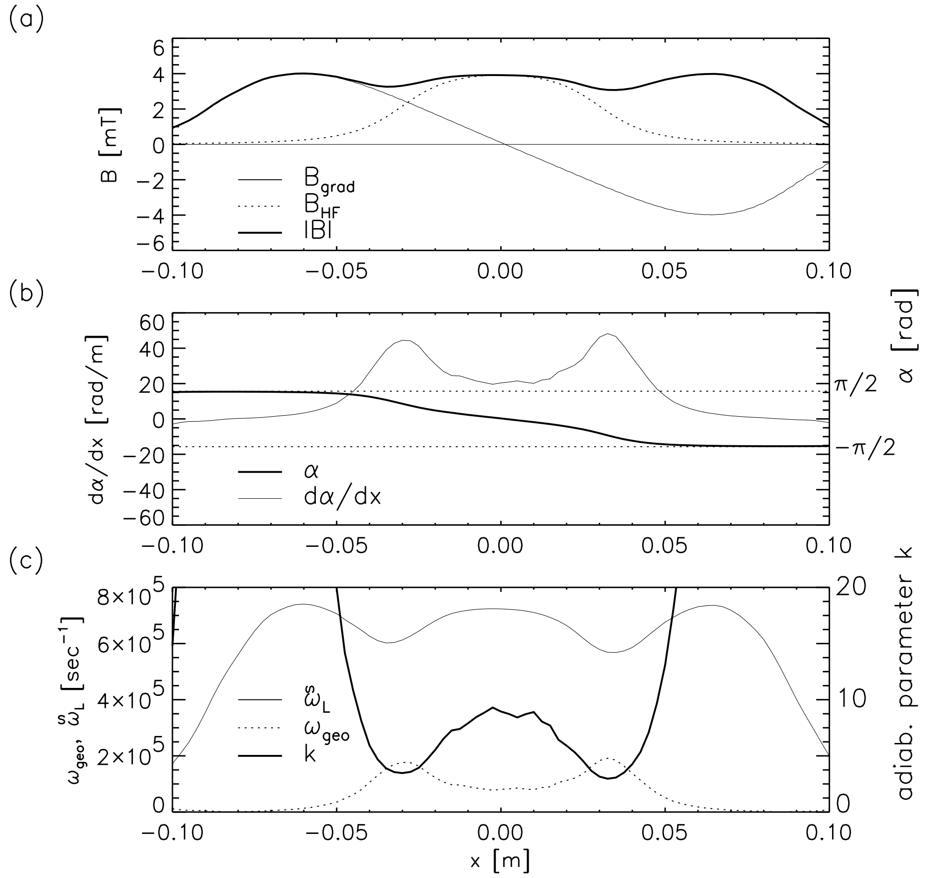

Figure 6.6: Adiabatic RF flipper: **(a):** Profiles of the DC-gradient field (measured with the DC-current adjusted for 4 mT amplitude), of the RF field (calculated analytically for a current such that max=4 mT) and of the absolute value of the resulting field; **(b):** angle α and $d\alpha/dx$ of resulting field toward xy-plane; **(c):** $\tilde{\omega}_L$ (from $|B|$) and ω_{geom} (from $d\alpha/dx$) and adiabaticity parameter (scale to the right).

to the Larmor frequency $\omega_0 = \mu_n B_0/\hbar$ of the resulting static field. Therefore the static field B_0 was set to 36 and 77 mT, respectively. It is generated by an electromagnet; the gradient field is produced by the extra windings against the poles shown in Fig. 6.5.

Fig. 6.6a shows the measured field profile, for a current such that the maximum field (denoted gradient amplitude A_{grad}) equals 4 mT. The field profile of the RF coil was calculated analytically (dotted line in Fig. 6.6a) for a current such that its maximum A_{RF} also equals 4 mT. In practice A_{RF} was measured and set by means of a pick-up coil placed at the position of the maximum. The behaviour of the neutron spin in the combined magnetic fields is explained in several papers mentioned above, e.g. [51] and [58]. It can be understood in a coordinate system $(\tilde{x}, \tilde{y}, z)$ rotating around the direction of the static field at the frequency ω_0 imposed on the RF coil. In this system the field B_0 is "transformed away", hence only the gradient field remains as a static field parallel to z. If we imagine a RF field component along y, shifted by $\pi/2$ with respect to the existing RF field, we have a RF field rotating at ω_0 around z. In the system $(\tilde{x}, \tilde{y}, z)$ it has a fixed orientation in the $\tilde{x}\tilde{y}$-plane. The phase angle of this field (denoted $\tilde{B}_x$) can be chosen such that it is parallel to $\tilde{x}$. The plots in Fig. 6.6a can be considered to represent the remaining gradient field and the field $\tilde{B}_x$. The absolute value of this field determines a Larmor frequency $\tilde{\omega}_L = \mu_n \sqrt{\tilde{B}_x^2 + B_{grad}^2}$, plotted in Fig. 6.6c as a full thin line. The neutrons, moving through this field configuration, experience a field rotating in the $\tilde{x}z$-plane from $+z$ to $-z$. Its angle $\alpha = \arctan(B_{grad}/B_{RF})$ toward the $\tilde{x}\tilde{y}$-plane and $d\alpha/dx$ are plotted in Fig. 6.6b. The derivative $d\alpha/dx$ translates itself through the neutron velocity into the "geometrical" frequency ω_{geo} of the resulting field, plotted for λ=0.1 nm as the dotted line in Fig. 6.6c. Dividing $\tilde{\omega}_L$ by ω_{geo} gives the adiabaticity parameter k according to Eq. (6.2), plotted for $\lambda = 0.1$ nm in Fig. 6.6c (bold line). Ref [59] contains a quantitative solution of the precession in this field configuration for idealized field profiles $B_{grad} = A_{grad} \sin(\tilde{x}/l)2\pi$ and $B_{RF} = A_{RF} \cos(\tilde{x}/l)2\pi$ (l: length RF coil; origin of the system $(\tilde{x}, \tilde{y}, z)$ is at its center).

6.3.1 Measuring $\epsilon(A_{RF}, A_{grad})$ at λ=0.22 nm

To measure the efficiency $\epsilon(A_{RF}, A_{grad})$ of one flipper, 4 such flippers were installed between the polarizer and analyzer of the instrument "SP" for 3D polarization analysis (different from the test setup for the V-coil flipper). This instrument lacks the TOF facility, but has a pyrolytic graphite crystal (see Fig. 6.7a) to make monochromatic analysis possible. In front of the analyzer a V-coil flipper was installed. To calculate the polarization of the beam, detector intensities in both modes of this flipper were measured. First, the polarization P_0 was measured with all the flippers switched off. After one RF flipper (F4, Fig. 6.7a) was switched on, the polarization P_1 was measured with various settings of A_{RF} and A_{grad}. The efficiency of this flipper, calculated according to Eq. (6.1) for the signals of the monochromatic detector for λ =0.22 nm, is shown in Fig. 6.7b. It is unnecessary to calibrate the efficiency of the V-coil flipper because it cancels in numerator and denominator. The need to separate the empty beam polarization, as in testing the V-coil flipper, does not arise here, because it is identical with P_0 measured in the mode non-flip (n) where depolarization is absent.

Fig. 6.7b illustrates the transition from a "resonance flipper" to an adiabatic RF flipper, as the gradient amplitude A_{grad} increases from 0. In the resonance

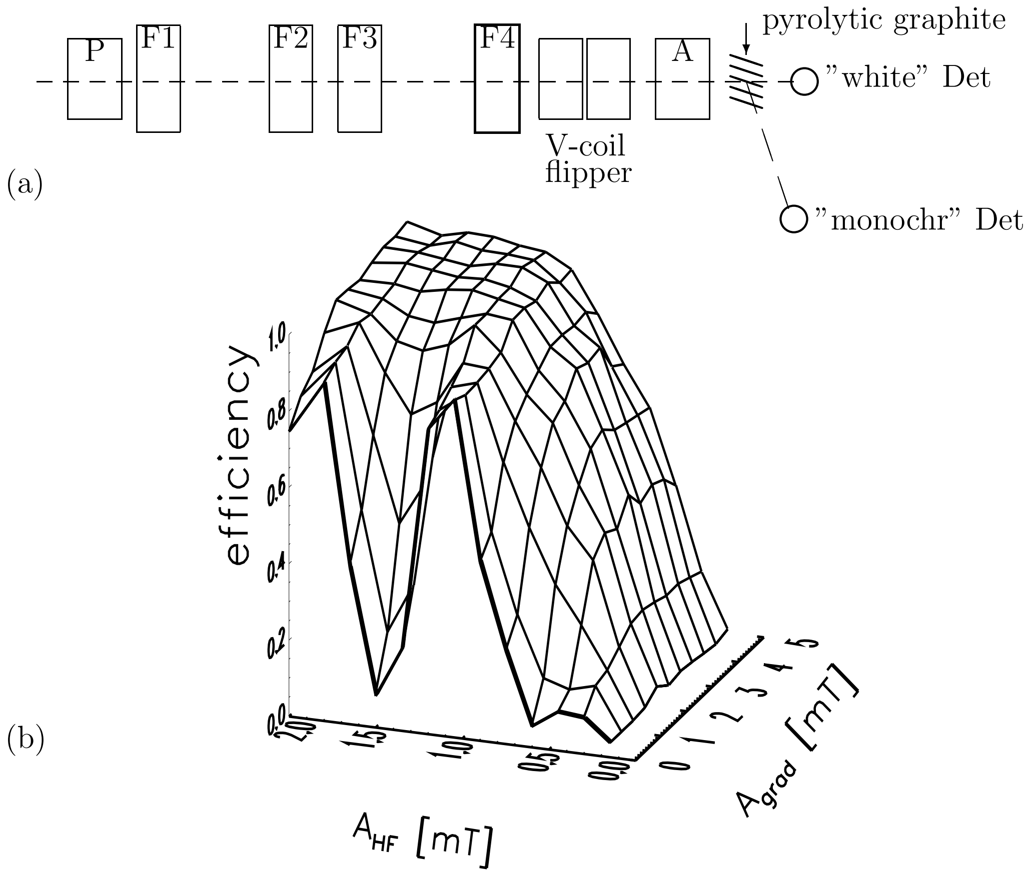

Figure 6.7: Adiabatic RF flipper: **(a):** setup for measuring the flipping efficiency $<\epsilon>$ in F4, for a monochromatic beam, λ=0.22 nm. **(b):** $<\epsilon>$ measured for RF=1.08 MHz, B_0=37 mT as a function of the amplitudes A_{RF} and A_{grad} of the RF and gradient field.

mode ($A_{grad}=0$) the period in the efficiency corresponds to an amplitude A_{RF} such that $\frac{\gamma_N}{h}\int B_{RF}(\tilde{x})\,d\tilde{x} \simeq \frac{\gamma_N}{h}A_{RF}l/2 = \pi$. This periodicity is confirmed. The irregularity in period for $A_{grad} \to 0$ is due to the inhomogeneity of the field B_0 and to a threshold in the output of the RF generator used to trigger the circuit containing the RF coil.

6.3.2 Measuring $\epsilon(\lambda)$

To measure the efficiency as a function of λ, we used a Fourier method [69]. To do this, the setup of Fig. 7a was modified to the configuration of Fig. 6.8a. The $\pi/2$ flippers (V-coils) cause the polarization vector to precess around the static fields B_0 inside and around the flippers. By switching the static fields of F1 and F2 antiparallel to those of F3 and F4, the setup operates in the spin echo mode. The induction B inside the coil between flipper F2 and F3 is varied in order to offset

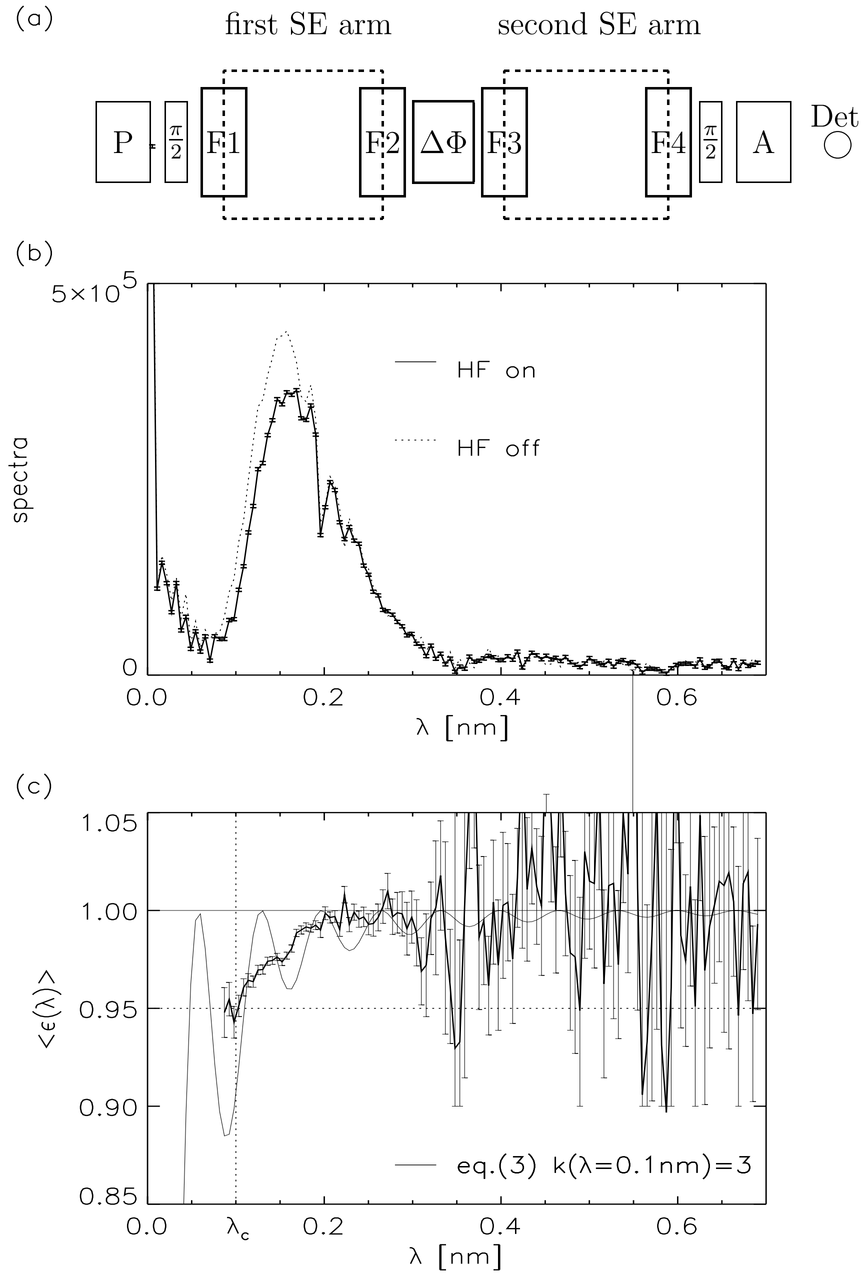

Figure 6.8: Adiabatic RF flipper: **(a):** Spin echo setup for simultaneous test of 4 flippers. **(b):** Spectra obtained using Eq. (6.13) for RF=1.08 MHz. The dip at 0.2 nm is due to the Al (200) Bragg cutoff of the windings of the coil $\Delta\Phi$. **(c):** average efficiency per flipper $<\epsilon>$. Dotted straight lines: illustrating λ_c for minimum efficiency equal to 0.95.

the setup around the echo condition. As a consequence, for any wavelength the intensity $I(B)$ in the detector behind the analyzer **A** will oscillate as a function of B. All wavelengths in the neutron spectrum together give (after subtracting the average intensity I_s):

$$I(B) - I_s \equiv I(c^*B) - I_s = \int_0^\infty F(\lambda)\cos(c^*\lambda B)d\lambda,$$

which is the cosine Fourier transform of the quantity $F(\lambda)$, being the product of the spectral density and the effective polarization as a function of λ. (The value of the constant c^* connecting the variables λ and B is determined by the construction of the coil "$\Delta\Phi$". It can be calculated from the period in B measured for a monochromatic beam). Upon performing the inverse transformation we get $F(\lambda)$ itself:

$$F(\lambda) = \int_{-B_{max}}^{+B_{max}} [I(B) - I_s\cos(c^*\lambda B)]d(c^*B). \tag{6.13}$$

Measurements taken with flippers off or on (A_{grad}=5 mT; A_{RF}=2 mT) yield F_n and F_f, given in Fig. 6.8b as a function of wavelength. Applying Eq. (6.1), we have for any λ:

$$\frac{F_f}{F_n} = \frac{P_f}{P_n} = -\frac{P_n(1-2\epsilon)}{P_n},$$

where ϵ is the result of 4 independent flippers, supposed to be equal. Therefore we substitute $\epsilon = <\epsilon>^4$, where $<\epsilon>$ is the efficiency of a single flipper. So:

$$<\epsilon> = \sqrt[4]{\frac{F_f/F_n + 1}{2}}$$

(The spectral density of the beam and the efficiency of the $\pi/2$ flippers cancel in this calculation). The result as a function of λ for 1.08 MHz is given in Fig. 6.8c, for a beam of cross section 5×5 mm^2. We notice, in analogy with Fig. 6.3, that $<\epsilon>$ starting from 0.1 nm increases quickly to 1, because the adiabaticity parameter k increases with wavelength. To illustrate this, $<\epsilon>$ as expected according to Eq. (6.3) with the assumption $k(\lambda$=0.1nm)=3 is also plotted.

We point out that in spite of the inaccuracy of the data in Figs. 3 and 9, the efficiencies of both the V-coil flipper and the RF adiabatic flipper must approach 1 as λ increases, according to Eq. (6.3), since k is proportional to λ. Hence, it is meaningful to characterize a flipper by its critical wavelength λ_c, defined as the wavelength beyond which its efficiency exceeds a chosen value $<\epsilon_c>$. For example for $<\epsilon_c>$=0.95, Fig. 6.8c shows that λ_c equals 0.1 nm.

6.4 Monochromatic flippers at a pulsed source

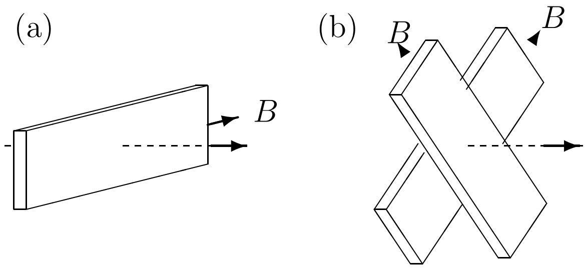

Figure 6.9: 2 options for monochromatic flippers.

We discuss 2 models of monochromatic flippers: a flat π-rotating coil (Fig. 6.9a) and a configuration of 2 π-rotating flat coils with field at 45° and −45° to the vertical (Fig. 6.9b). They are embedded in a small homogeneous vertical guide field (negligible compared with the fields inside the flipper), hence, after passage through the flipper the relative orientation between polarization and local field is reversed. If the fields in the coils are set such that exact flip occurs at wavelength λ_0, it is easily seen that their efficiencies as a function of wavelength are:

$$\epsilon_{(a)}(\lambda_0, \lambda) = \frac{1}{2}\left[-\cos(\tfrac{\lambda}{\lambda_0}\pi) + 1\right] \qquad \text{(Fig. 6.9a)} \tag{6.14}$$

$$\epsilon_{(b)}(\lambda_0, \lambda) = \frac{1}{2}\left[-\cos(\tfrac{\lambda}{\lambda_0}\pi) + \tfrac{1}{2}\sin^2(\tfrac{\lambda}{\lambda_0}\pi) + 1\right] \qquad \text{(Fig. 6.9b)} \tag{6.15}$$

These functions are shown in Fig. 6.10 for 2 different settings of λ_0.

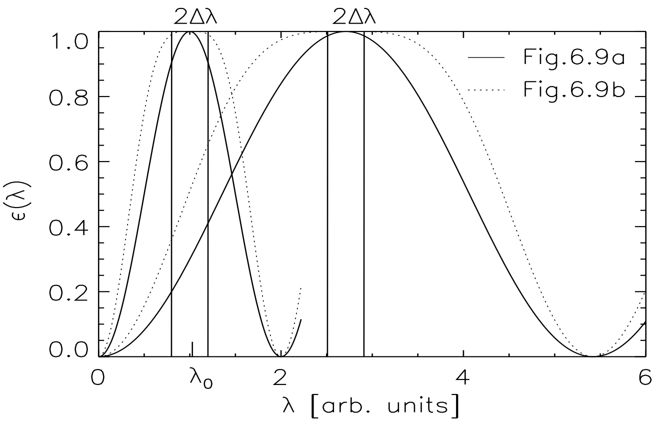

Figure 6.10: Efficiency for the monochromatic flippers of Fig. 6.9. When used in a pulsed beam, the flipper can be tuned such that the argument of the cosine in Eqs. (6.14) and (6.15) remains π, hence $\epsilon \simeq 1$, as neutrons of increasing wavelength pass through (i.e. the interval $2\Delta\lambda$ moves to the right). The flip efficiency $\epsilon(\lambda)$ is shown for 2 different time channels ($\equiv \lambda_0$ values).

When such a flipper is installed in a neutron beam from a pulsed source, the wavelength λ_0 for optimal flip can be adapted (by properly decreasing the current in the coil) such that ϵ remains 1 for the neutrons collected in any time channel. Flippers operating according to this principle are installed at ILL [63] and being developed in Japan by Maruyama c.s. [64]. [63].

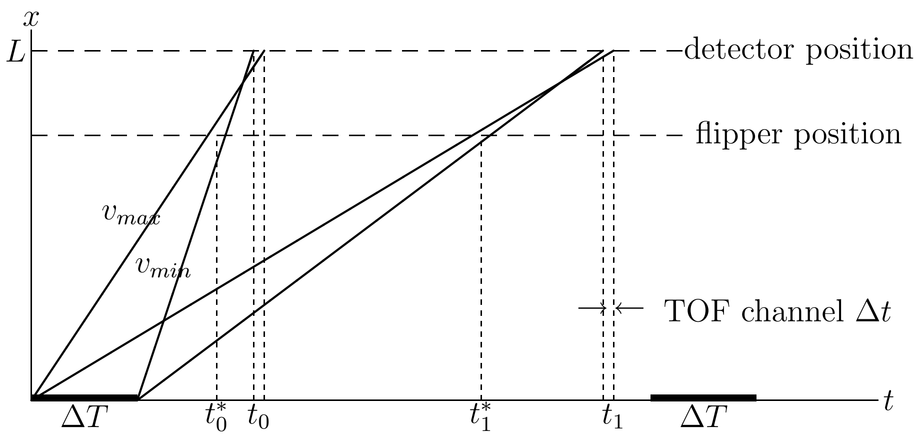

Figure 6.11: World diagram of a pulsed neutron beam with a flipper and a detector operated in TOF mode. The beam is assumed to be "on" during the time intervals ΔT and "off" in the remaining time. The thick lines are the minimum and maximum neutron velocity at the flipper position in the time channels at t_0 and t_1. (No devices are assumed to affect the time profile of the beam intensity).

However, in any time channel the duration ΔT of the beam pulse gives non-monochromatic neutrons inside the flipper between v_{min} and v_{max}, indicated in the "world diagram" in Fig. 6.11 for the time channels at t_0 and t_1. It is seen from this diagram that this velocity interval remains constant in time. In terms of wavelength, its width $2\Delta\lambda$ is:

$$2\Delta\lambda = \frac{\Delta T}{L}\frac{h}{m}, \tag{6.16}$$

where L is the distance from the source to the detector, h is Planck's constant and m the neutron mass. The efficiency of the flipper over this interval will be:

$$<\epsilon> (\lambda_0, \Delta\lambda) = \frac{1}{2\Delta\lambda} \int_{\lambda_0-\Delta\lambda}^{\lambda_0+\Delta\lambda} \epsilon(\lambda_0, \lambda) d\lambda.$$

Fig. 6.10 illustrates this integration for 2 different values of λ_0. Upon substituting Eqs. (6.14) and (6.15), one gets (dropping the index $_0$ from λ):

$$< \epsilon_{(a)} > (\lambda, \Delta\lambda) = \tfrac{1}{2}\left[1 + \tfrac{\sin(A_1(\lambda))}{A_1(\lambda)}\right] \qquad \text{(Fig. 6.9a)}$$

$$< \epsilon_{(b)} > (\lambda, \Delta\lambda) = \tfrac{1}{2}\left[1 + \tfrac{\sin(A_1(\lambda))}{A_1(\lambda)} + \tfrac{1}{4} - \tfrac{1}{4}\tfrac{\sin(A_2(\lambda))}{A_2(\lambda)}\right] \qquad \text{(Fig. 6.9b)}$$

with

$$A_1(\lambda) = \frac{\Delta\lambda}{\lambda}\pi, \qquad A_2(\lambda) = \frac{2\Delta\lambda}{\lambda}\pi,$$

and $2\Delta\lambda$ given by Eq. (6.16).

As an example we take a flipper installed at the projected source ESS at a distance L =10m from the "short pulse" target station (SPTS, pulse length, incl. decay time 140 μs) and from the "long pulse" target station (LPTS, pulse length 2 ms) [70]. The integration interval $2\Delta\lambda$ for both pulse lengths is found using Eq. (6.16). The results for $< \epsilon > (\lambda)$ are plotted in Fig. 6.12.

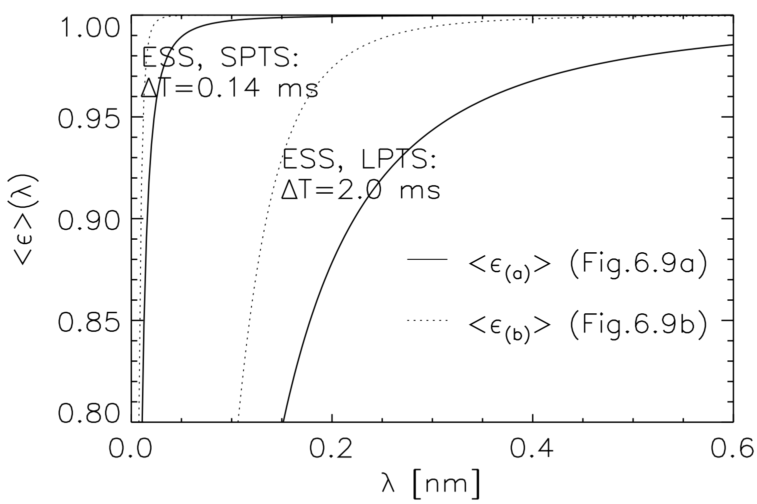

Figure 6.12: Efficiencies for the "monochromatic" flippers of Fig. 6.9, when placed at L = 10m from the "Short Pulse" Target Station (SPTS) and the "Long Pulse" TS (LPTS) at the ESS spallation source. The wavelength interval $2\Delta\lambda$ is determined by Eq. (6.16).

6.5 Summary and Conclusion

Results for two types of adiabatic spin flippers are presented: V-coils (operating with DC current) and the RF adiabatic flipper with DC gradient field (operating at 1 and 2 MHz).

Results of the flipping efficiency as a function of λ for the V-coil type are presented

for the first time. Due to their geometry, the neutron beam must cross 2 screens of parallel current-carrying wires, at the expense of 1% of intensity. In the mode *non-flip* these screens might produce a net field in the gap between these screens. In the mode *flip* it is absent. Therefore the flip efficiency for this type of flipper is in principle asymmetric. A small asymmetry (1%) was indeed found. It can be reduced by a better magnetic short-circuiting, specially at the position of this gap.
The RF adiabatic flipper has the amplitudes of the RF field and the gradient field as variables. By increasing the gradient field amplitude from zero to some maximum we demonstrate the transition from a "resonance flipper" to an RF adiabatic flipper: the efficiency, initially varying periodically between 0 and 1, rises to 1, for any RF amplitude. The initial period depends on wavelength.

From the definition of the adiabaticity parameter it follows that the efficiency for any flipper goes asymptotically to 1 with increasing wavelength. This is confirmed in our results for both flippers as a function of wavelength. For a chosen efficiency value (e.g. 0.95) a critical wavelength (λ_c) can be found, which is the lower wavelength limit for that efficiency. For a flipper installed in a magnetic surrounding, λ_c is determined by the minimum of the "adiabaticity parameter" along the beam line in and around the flipper. From the field profiles in the V-coil flipper we found initially that this parameter (reduced to λ=0.1nm) drops locally below 2. Indeed, upon raising this minimum by adding some local support field, λ_c decreased from 0.4 to 0.15 nm. In principle, a similar improvement could also be achieved by maximizing the dimensions of the flipper (if possible). Also, positioning the flipper will become less critical.

In a beam from a pulsed source (with or without choppers to further modify the pulse duration) one can use a monochromatic flipper, with good efficiency over a limited wavelength band. We give 2 examples of such flippers: flat coil and double flat coil. By proper adjustment of the current, such a flipper can be tuned to have an optimal efficiency synchronized with the neutrons of various wavelengths as they pass through the flipper. The value of this optimum depends on the wavelength range received in the detector. This range is determined by the pulse duration and the distance from the source (chopper) to the detector. For a "long duration source" and detector at small distance this means that the wavelength band in the detector will be so long that an insufficient efficiency of the flipper results. Therefore, at such sources adiabatic flippers are preferable.

Chapter 7

Zero-field precession induced by adiabatic RF Spin Flippers

W.H. Kraan[1], S.V. Grigoriev[2], R. Kreuger[1], F.M. Mulder[1] and M.Th. Rekveldt[1]

[1] Interfacultair Reactor Instituut, TUDelft, 2629 JB Delft, The Netherlands
[2] Petersburg Nuclear Physics Institute, 188300 Gatchina, Russia

Appeared in Physica B **297** (2001) 23-37

A neutron "precession device" consisting of 2 adiabatic gradient field RF spin flippers was built. The "Zero Field Precession" (ZFP) is demonstrated over the path length between them in a Spin Echo experiment in which a DC coil is used for compensation. Signals as a function of this DC field are shown for a single wavelength and for a "white" neutron spectrum. This development extends the use of ZFP to white neutron beams. The requirements on the DC field shape in these flippers to obtain uniform precession over a finite beam cross section, are less severe than in a precession device with only DC magnets.

7.1 Introduction

Several applications based on Larmor precession of polarized neutrons are currently being considered at IRI [71], [72], [73]. For some applications an inclination angle is required between the beam and the front and end face of the "precession devices". For high resolution diffraction a "white" neutron beam is sometimes desired.

In principle such a precession device could be a DC coil shaped as a parallelogram, positioned such that the neutrons pass through the windings. However, for the precession angles required to obtain sufficient resolution (10^3 - 10^4 rad) such coils become too thick to have good neutron transmission, so we arrive at a design of electromagnets with poles shaped as parallelograms placed over a length $\simeq 1$ m along the neutron beam.

To avoid the necessity of such poles we adopted the technique of zero-field precession (ZFP) [74] over the path length between 2 RF spin flippers. Each flipper is a DC magnet generating a transverse field ($\parallel z$) with an RF coil generating a longitudinal field ($\parallel x$). The effective precession rate over the path length between the flippers is 2 times the rate corresponding to the DC field in the RF flippers.

Contrary to devices for ZFP built in Berlin [75], our flippers are "adiabatic RF gradient flippers" (see Chapter 6, Sec.**6.3**), [76], [77]. We show in the present paper that with such flippers, ZFP over the whole wavelength spectrum can be induced and not for a small wavelength region alone.

7.2 Precession angle in a ZF device

An adiabatic gradient RF spin flipper consists of a DC field (along z) shaped such that over some length along the neutron beam, a field profile having a gradient around a mean value B_{DC}, ranging from $+B_{grad}$ to $-B_{grad}$ is realised. In this field, a coil which generates a longitudinal (along x) RF field over some distance along the beam is placed. The action of this configuration on the neutron spin is understood in a coordinate system moving with the neutron and rotating around the DC field at a frequency equal to the RF frequency (this frequency will correspond to the Larmor frequency at some point inside the flipper):

$$\omega_{RF} = \mu_N B_{DC}/\hbar \tag{7.1}$$

For an explanation, how the neutron spin flip takes place in such a device, we refer to Ref.[77]. At some distance downstream of this flipper, we install a second similar flipper. Over the path length between the flippers, a change of the phase of the wave functions for spin-up and -down takes place [74] which results in a precession phenomenon referred to as ZFP. (Some stray field is present between the flippers, but nevertheless we refer to this precession as "ZFP".) The configuration consisting of two adiabatic RF flippers is called a "precession device". The total precession ϕ_{RF} after this device is made up of a contribution ϕ_{DC} due to the DC fields and a contribution of ZFP. ϕ_{RF} can be represented in a "(k, x)"-diagram (i.e., the behaviour of the wave vector of spin-up neutrons along the x-axis, [78]) by the shaded area in Fig. 7.1. Here, the field gradients on both sides of the DC magnets and the gradient fields themselves are represented as straight lines. We can find points x_0 and x_1 such that the total precession is equal to the rectangular area of length L (see Fig. 7.1).

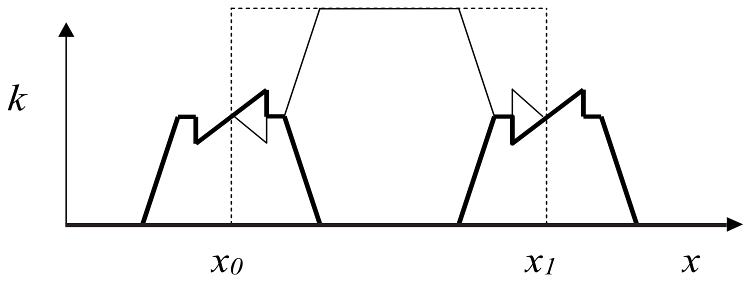

Figure 7.1: (k, x)-diagram of a precession device made up of 2 RF flippers. The points x_0 and x_1 are at the "centers of gravity" of the DC fields of the flippers. The shaded area represents the total precession $\phi = \phi_{DC} + \phi_{RF}$. It is equal to the rectangle between x_0 and x_1, independent of the actual shape of the gradients.

7.3 Experimental setup

The DC magnet poles of each RF spin flipper had an area 10×10 cm; they were 4.7 cm apart. The RF coils were operated at $\omega_{RF}/2\pi = 0.291$ MHz, i.e. a DC field $B_{DC} = 9.9$ mT (Eq. (7.1)). They had a rectangular cross section 2×2 cm and length $l_{RF} = 6$ cm. The amplitude B_{RF} of the RF field could be made as high that $B_{RF} > 1$ mT. Sets of coils were installed near the poles to produce a (non linear) DC field gradient from $B_{grad} = -1.5$ to $+1.5$ mT over a path length 0.1 m. We could also operate the flipper as a "resonant flipper" (in which flipping occurs only over a limited λ-range) by switching off the gradient coils. With this arrangement of DC magnet and RF coil there are no current carrying leads in the neutron beam.

After preliminary experiments to test a single RF flipper, we installed 2 flippers at center-to-center distance L. This configuration is considered as the first "arm" of a spin echo setup. The second "arm" is a block shaped coil (see Fig. 3.5 in Chapter 3) producing a homogeneous field B_{LAR} over a length $L_{LAR} = 32.5$ cm. The total precession ϕ_{RF} is measured by determining the value B_{LAR} at which SE is observed. The complete SE setup is drawn schematically in Fig. 7.2. $\pi/2$-rotators with only DC coils were installed in front of the first RF flipper and behind the block coil to put the polarization vector perpendicular (y) to the DC field direction(z) of the flippers, and to analyze the y component after transmission through the SE balance. So the precession occurs in the (xy)-plane in both "arms". A DC spin flipper was set between the second $\pi/2$-rotator and the "analyzer" in order to measure in 2 anti-parallel modes to calculate the degree

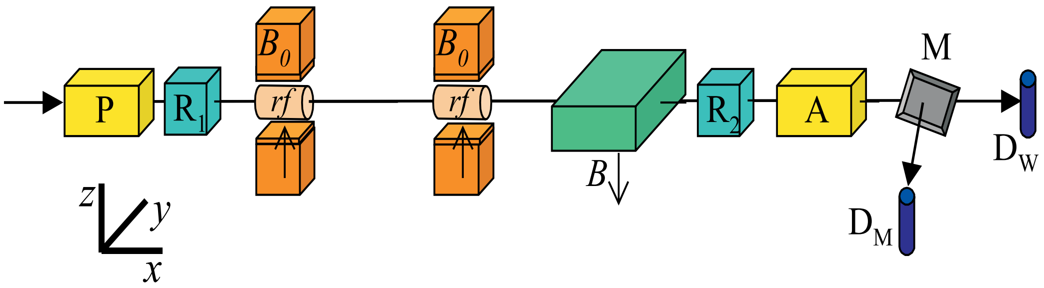

Figure 7.2: Lay-out of the spin-echo setup with the adiabatic gradient RF flippers and a "block" coil for precession compensation.

of polarization P of the SE signal. (In fact the second $\pi/2$-rotator was the first half of this DC flipper).

Behind the analyzer, a set of pyrolytic graphite crystals was installed for simultaneous monochromatisation at a number of wavelengths between 0.19 and 0.26 nm. In addition, the neutron spectrum after transmission through these crystals was detected at the end of the setup.

7.4 Results

Fig. 7.3 gives the polarization at $\lambda = 0.22$ nm with the RF coils off (top) and on (but gradient coils off, so the flippers operate as "resonant flippers, i.e. at one wavelength only), for L (see Fig. 7.2) equal to 30 (center) and 40 cm (bottom). It is seen that the field B_{LAR} needed to compensate ϕ_{RF} indeed increases by moving the RF flippers further apart. This means that for $\lambda \simeq 0.22$ nm the angle ϕ_{RF} increases. The shift of the SE pattern with reference to the point $B_{LAR} = 0$ is exactly proportional to L. This confirms that ϕ_{RF} can be represented by the rectangular area in Fig. 7.1. The irregularity of the patterns is due to the step width of the field B_{LAR} in the block coil that interferes with the polarization oscillations. In later measurements this step was made smaller. The next measurements were done with gradient coils switched on (so the flippers operate as "adiabatic flippers"), at various amplitudes of the RF fields and at constant distance $L = 40$ cm. Fig. 7.4a gives the polarization P of the SE signal with RF coils switched off at $\lambda = 0.220$ nm (dotted line) and for the "white" spectrum (full line) as a function of B_{LAR}; Fig. 7.4b gives P at maximum power of the RF coils. From these and observations at various RF power (not shown), we conclude that the RF flippers induce ZFP, which is in agreement with the description of these flippers in [77].

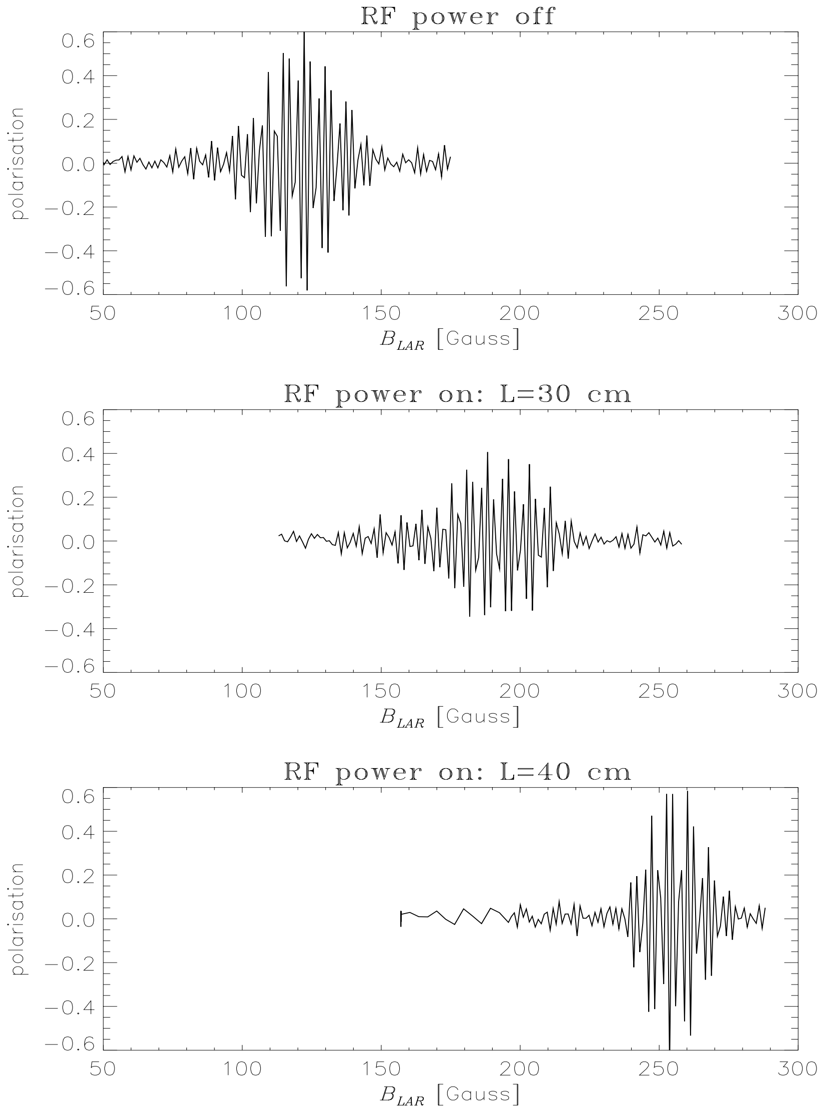

Figure 7.3: Precession after 2 RF resonance flippers, brought to echo (SE) by a DC block coil (depicted in Fig. 3.5): polarization around SE for $\lambda = 0.22$ nm with RF coils off, and with RF coils on with length L between the RF flippers 30 cm and 40 cm.

7.5 Spectra of DC and RF precession

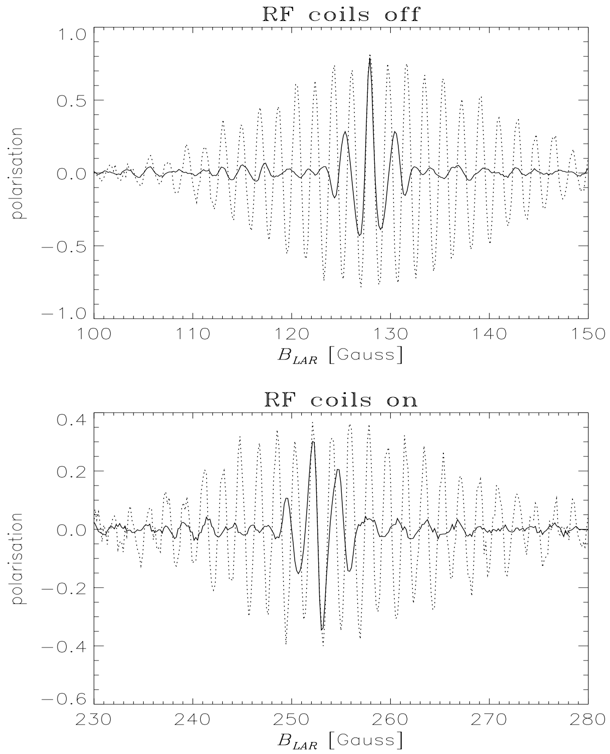

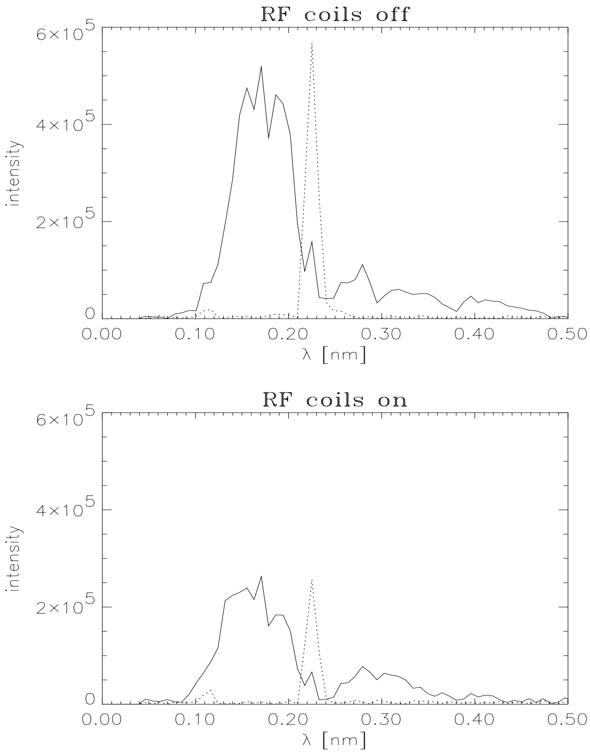

Figure 7.4: Polarization around SE for a monochromatic beam (dotted) and "white" spectrum (full line) with RF coils in adiabatic flippers off and on.

Figure 7.5: Fourier transforms of the signals of Fig. 7.4

The scans around the SE point made with the block coil are equivalent to "Larmor precession Spectroscopy" as published 10 years ago (Chapter 4), [79]. It was pointed out that the obtained signal $I(B_{LAR})$ is the cosine Fourier transform of the quantity $P(\lambda)J(\lambda)$:

$$I(B) - I_s = -\int P(\lambda)J(\lambda)\cos(c\lambda B_{LAR}L_{LAR})d\lambda$$

The only difference is that the argument of the cosine in the present scans around SE is shifted by an amount corresponding to ϕ_{DC} or ϕ_{RF}. The product $P(\lambda)J(\lambda)$ can be recovered by the inverse Fourier transformation. Fig. 7.5 gives the transforms of the signals given in Fig. 7.4 in the same order.
The "white" spectra of with RF coils off and on are roughly equal, differing by a factor $\simeq 2$. This is mainly due to the poor flipping probability of the RF flippers, which apparently amounts to $\sqrt{2}$ per flipper. The dips in the spectra are due

to the filtering by the monochromators positioned in front of the "white beam" detector.

This proves that the RF flipper brings the whole spectrum into the mode of ZFP (for the time being with probability less than 1).

7.6 Discussion

For future application of a ZFP device the overall precession ϕ_{RF} must be constant over a large beam cross section. In a beam of extended cross section, neutron trajectories exist in which both the gradients of the DC fields of the flippers and the gradient fields depart from the shapes in Fig. 7.1, which can be assumed to represent the situation along the axis of the flippers. Variation of B_{DC} in the RF flippers by 5% (i.e. within the range of the gradient field) had some effect on their flipping probability; however, the field B_{LAR} in the block coil needed to find SE corresponding to ϕ_{RF} hardly changed. Apparently, the phase "picked up" by the neutrons during travel through an adiabatic RF flipper is insensitive to the actual DC field profile, provided the point where the RF frequency matches the local field value is within the path length where the RF field is sufficiently strong. This means that for beams of large cross section a homogeneous precession can be generated, using a "precession device" consisting of two adiabatic RF flippers. It suggests moreover that a precession device with inclined faces can be realised by simply tilting the DC fields.

This work is part of the program of "Stichting voor Fundamenteel Onderzoek der Materie (FOM)", which is financially supported by the "Nederlandse Organisatie voor Wetenschappelijk Onderzoek (NWO)". This work is also supported as part of the INTAS project (Grant INTAS-97-11329).

Chapter 8

Spin Echo SANS based on adiabatic HF flippers in dipole magnets with skew poles

W.H. Kraan[1], S.V. Grigoriev[2], M.Th. Rekveldt[1], W.G. Bouwman[1], O. Uca[1]

[1] Interfacultair Reactor Instituut, TUDelft, 2629 JB Delft, The Netherlands
[2] Petersburg Nuclear Physics Institute, 188350 Gatchina, Russia

Appeared in Appl.Phys A 74[Suppl.],(2002) S79-S81

We built a spin-echo set-up for SANS consisting of precession devices each made up of 2 adiabatic RF flippers. For angle labelling of the neutron beam, the poles of the dipole magnets for these flippers are shaped as parallelograms. SANS in a sample placed in the beam shows up as depolarization, i.e. decrease of the amplitude of the spin-echo signal. Spin-echo SANS measurements in 2 samples are given, showing the difference in particle size distribution. Since adiabatic RF flippers work for the full white spectrum, the method works also on pulsed sources.

PACS: 03.75.Be; 61.12.Ex

8.1 Introduction

Spin-echo SANS (SESANS) as a theoretical possibility was discussed 5 years ago in several papers [80], [83]. The basis of this technique is "angle labelling" of the incident beam by attributing an unique precession angle to each direction. This is achieved by transmitting the incident beam through a precession device

with inclined front- and end faces. The same is done in the scattered beam, in a precession device with anti-parallel field. This means that the setup is operated in spin-echo mode. The technique of angle labelling eliminates the need of a highly collimated narrow incident beam.
We are trying several options to realise such precession devices (see e.g. [82]). One option is based on "zero field precession" [81] over the path length between two RF resonance spin flippers. Recently, using a related type of flippers: "adiabatic RF flippers", we demonstrated this mode of precession to work simultaneously for the white neutron spectrum (previous Chapter), [84].
In the present paper it is shown that a precession device with inclined faces (as required for SESANS) using this type of flippers is simply realised by shaping the poles of the flipper's DC magnets as parallelograms ("skew" poles).

8.2 Angle labelling

The precession angle for the polarization of a parallel neutron beam transmitted through a region with homogeneous magnetic field shaped as a parallelogram, is (see Fig. 8.1a):

$$\varphi = c\lambda BL[1 + \tan\theta_0\theta + O(\theta^2, \theta^4, ..)]$$
$$\simeq c\lambda BL + [c\lambda BL\tan\theta_0]\theta \equiv c\lambda BL + \Gamma\theta.$$

The constant c equals $2\pi\mu_n m_n/h^2$ [$= 4.63 \times 10^{14}$ $\mathrm{T}^{-1}\mathrm{m}^{-2}$; μ_n and m_n are the neutron magnetic moment and mass, respectively]. The linear term in θ is the angle labelling: a sub beam of given θ has a unique precession angle.

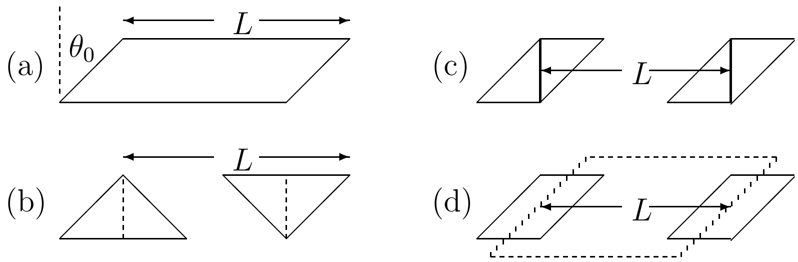

Figure 8.1: Options for angle labelling using triangular precession regions

Angle labelling is also realized if the region containing field is reduced to the triangles drawn in Fig. 8.1b. Thin spin flippers placed at the position of the dotted lines in Fig. 8.1b will extinguish the labelling effect; it will be restored upon mirroring the right halves of the triangular regions (Fig. 8.1c).
Another option to get angle labelling is using resonance flippers. Figure 1d shows

the field shape needed to create a parallelogram shaped region (dotted) with "zero field precession" generated by such flippers.
A complete spin-echo setup for SESANS takes the configuration of Fig. 8.2 in which the spin flippers are "adiabatic RF flippers". In this configuration the term producing angle labelling has for coefficient:

$$\Gamma = 2c\lambda BL\tan\theta_0. \tag{8.1}$$

8.3 Spin-echo setup for SESANS

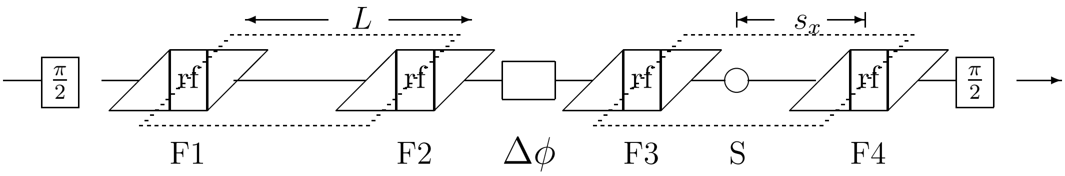

Figure 8.2: SESANS setup with "zero field" precession between adiabatic RF flippers F1 and F2 and between F3 and F4. The symbols "rf" represent the longitudinal RF coils. Because their frequency equals a fixed 1.08 MHz, the length s_x is the variable to scan the sample's (S) correlation function $g(z)$ with z given by Eq. (8.2). (The polarizer, analyzer and detection system are omitted).

Each flipper consists of a longitudinal RF coil (dimensions 30×30×60 mm^3; frequency 1.08 MHz; max. RF field in center 20 Gauss) placed between the parallelogram shaped poles ($\theta_0 = 45°$; pole distance 47 mm; $B = 360$ Gauss) of an electromagnet. The DC gradient (maximum gradient 40 Gauss over 100 mm) required for flipping, is produced by a special set of windings on the poles of the electromagnet (see Fig. 6.5 in Chapter 6). The gradients of all flippers are parallel. The distance L in Fig. 8.2 was 600 mm. To obtain spin-echo, the DC fields of flippers 1 and 2 are anti-parallel to the fields in flippers 3 and 4. Around the point where the field goes through 0, instead of a π-flipper, a small coil ("$\Delta\phi$" in Fig. 8.2) is placed, producing a homogeneous field over a length of 120 mm. By varying its field, the setup can be operated up to several rotations away from the echo point. The degree of polarization in the spin-echo situation is the amplitude of the detector signal measured as the field in this coil is varied.

8.4 SESANS in Limestone and Graphite

Our samples are packages of limestone (with a sharp surface structure) and carbon grains (with a "fractal" surface structure). This was concluded from their

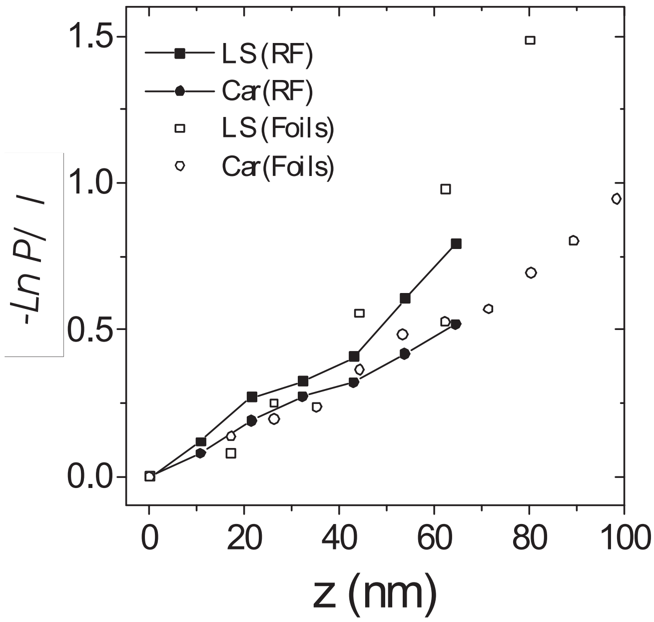

Figure 8.3: Depolarization [plotted as $-\log(P)/\sigma l$), thick symbols connected by lines; l sample thickness] measured in limestone (LS) and graphite (Car) as a function of z obtained from the length s_x (Fig. 8.2) by Eq. (8.2). For comparison also the results for the same samples in the "foil option" [82] to realize a SESANS setup are given [open symbols]. The different slopes for LS and Car reflect the different surface structures in both samples.

behaviour in ordinary SANS measurements as a fuction of wavevector transfer q: in the high q range scattering decreased approximately according to q^{-4} and $q^{-2.6}$ in limestone and carbon [84].

Placing a sample at any point in the spin-echo setup (either inside one arm or between the precession arms) gives depolarization of the beam, due to path length differences for the trajectory of the scattered neutrons in the first and second precession arm. It was shown in [80] that the depolarization of the spin-echo signal (as a function of the field in coil "$\Delta\phi$") is closely related with the sample's pair correlation function $G(z)$, where the "probed correlation length" z is given by

$$z = \frac{cB\lambda^2 \tan\theta_0}{2\pi} s_x. \tag{8.2}$$

Here s_x is the distance from the sample to the center of the last flipper. In case the sample is placed between the arms of the spin-echo setup, s_x is replaced by the length L of one arm, (see Fig. 8.2). Since the RF coils in our flippers had to be operated at fixed frequency (hence B is constant), the parameter s_x instead

of B remained as a variable to scan z. Fig. 8.3 gives the result as a function of z in 6.35 mm of limestone and in 5 mm of Carbon (thick symbols connected by lines). In these observations the full white neutron spectrum was used, with $\sqrt{<\lambda^2>} = 0.2$ nm. To make the result independent of the sample thickness, we plotted the quantity $-(\log P)/(\sigma l)$ which can be shown [85] to be equal to $1-TG(z)$, where l is the thickness and σ the total cross section of the sample. [P is the polarization of the depolarized beam in the spin-echo situation, normalized to the polarization of the empty beam in Spin Echo].
For comparison we also show results obtained earlier for the same samples in the "foil option" [82] to realize a SESANS setup. In this case observations had been simultaneously taken at several wavelengths between 0.19 and 0.23 nm. The results show nicely the difference of the slope of $G(z)$ for different surface structures in limestone and in carbon.

8.5 Discussion

When the RF flippers are omitted, an angle labelling characterized by Eq. (8.1) is also obtained, provided the magnet poles are shaped as in Fig. 8.1c. With the present pole shape (configuration of Fig. 8.2) measurements of the spin-echo signal were taken for various beam cross sections, both with the RF coils in the flippers switched on and off. [Due to the pole shape no angle labelling is obtained without flipping]. As shown in Fig. 8.4, the amplitude of the spin-echo signal with RF off is smaller than with RF on, especially for great beam width or beam height. The low amplitude of the signal with RF off is due to the fact that the neutron beam passes through the rising and falling gradients of the DC magnets of all 4 flippers. These gradients give rise to an inhomogeneity of the line integral over the beam height and hence to a de-focusing of the precession phase in both arms of the setup. As a consequence the amplitude of the spin-echo signal decreases. This effect is compensated by the flipping action inside each magnet when RF is switched on [86]. This is a reason for using spin flippers in devices with inclined faces to start and stop the precession in spin-echo setups.

8.6 Conclusion

This work shows that adiabatic RF flippers can be used for angle labelling of a polarized neutron beam, needed for Small Angle Neutron scattering in spin-echo mode. Great stability of the precession phase in spin-echo is achieved by the fact that this phase is determined basically by the frequency of an RF generator.
The full white spectrum is in the "zero field" precession mode. This can be used

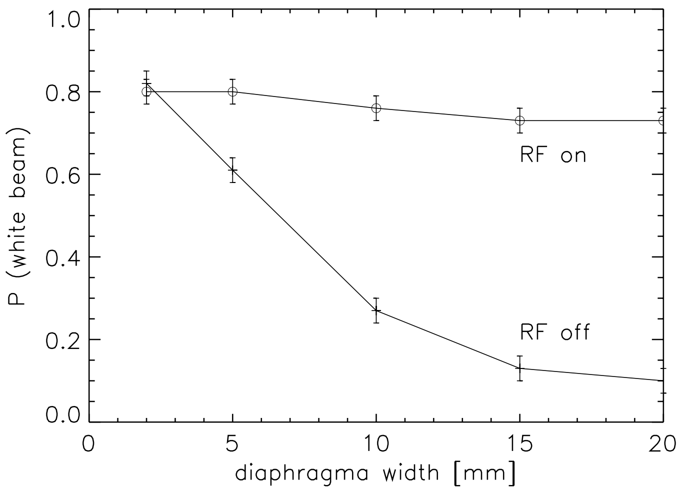

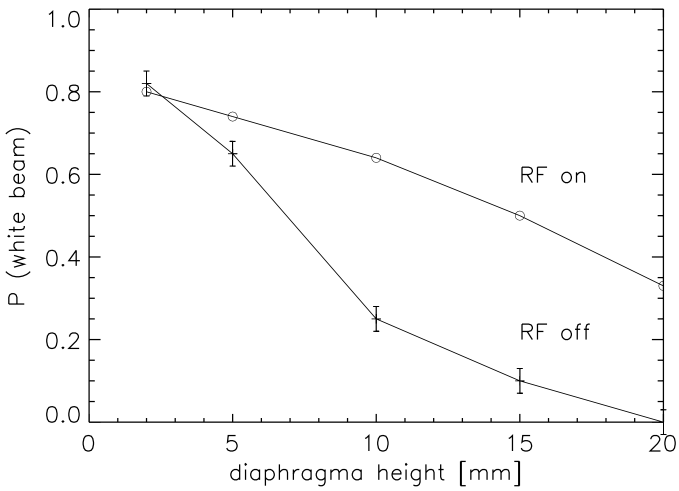

Figure 8.4: Amplitude of the spin-echo signal in the configuration of Fig. 8.2 for various beam cross sections with RF coils switched on and off.

for simultaneous analysis of the spin-echo signal at several wavelengths (or time channels in case of a pulsed source) in order to obtain detailed coverage of the sample's correlation function.
Different samples are shown to have different behaviour of their correlation function.

Acknowledgements This work is part of the research programme of the 'Stichting voor Fundamenteel Onderzoek der Materie (FOM)' which is financially supported by the 'Nederlandse Organisatie voor Wetenschappelijk Onderzoek (NWO)'.

Chapter 9

Observation of 4π-periodicity of the spinor using neutron resonance interferometry

W.H. Kraan[1], S.V. Grigoriev[2], M.Th. Rekveldt[1]

[1] Interfacultair Reactor Instituut, TUDelft, 2629 JB Delft, The Netherlands
[2] Petersburg Nuclear Physics Institute, 188350 Gatchina, Russia

Appeared in Europhysics Letters, **66** (2004) 164-170

A polarized neutron beam is passed through a gradient resonance flipper. By the amplitude of their RF field, such flippers can be set at flip probability ρ=0, 1, or $\frac{1}{2}$. At $\frac{1}{2}$, the neutron wave splits into a flipped and a non-flipped part with different precession. We measure the polarization after a spin-echo (SE) setup with each precession arm made up of 2 such flippers. Offset from SE is made by varying the static fields in one flipper while the other flippers stay unchanged. This shows up as a periodic behaviour of the polarization. With incoming polarization parallel to the static field in the flippers - set at $\rho = \frac{1}{2}$ - this period is twice the period measured for both $\rho = 0$ and 1 and with polarization perpendicular to the static field. In the latter experiments both components of the spinor are affected, whereas in the former experiment we create spin states in which only one spinor component in one state is affected. Hence, this experiment demonstrates explicitly the 4π-periodicity of the spinor.

keywords: Larmor precession, spin flipper, spinor
PACS 07.55.-w, 29.25.Dz, 29.27.Hj, 29.27.Eg

9.1 Introduction

Larmor Precession of the polarization of a neutron beam in a magnetic field can be described by means of specific changes in the spinor, i.e. a normalized vector in 2-dim space with complex components:

$$|\psi\rangle = \begin{pmatrix} a\ \exp(i\phi_1) \\ b\ \exp(i\phi_2) \end{pmatrix} = a\ \exp(i\phi_1) \begin{pmatrix} 1 \\ 0 \end{pmatrix} + b\ \exp(i\phi_2) \begin{pmatrix} 0 \\ 1 \end{pmatrix}, \tag{9.1}$$

where the phases ϕ_1 and ϕ_2 characterize the spinor in its initial form. (Their value is irrelevant, since our interest concerns the change in these phases). From this spinor the components S_i $(i = x, y, z)$ of the average spin (=polarization) are calculated according to $S_i = \langle\psi|\sigma_i|\psi\rangle$, where σ_i is the component i of the Pauli matrix vector $\vec{\sigma}$. The most general unitary operator to apply to the spinor in order to describe Larmor precession over an angle α around a field in the direction of the unit vector $\vec{n}$, takes the form: $\hat{R} = \exp(-i\vec{\sigma}.\vec{n}\ (\alpha/2))$. By expanding the exponential this operator, it can be shown to be equal to

$$\hat{R} = \cos(\alpha/2)\hat{I} - i\vec{\sigma}.\vec{n}\sin(\alpha/2), \tag{9.2}$$

where $\hat{I}$ is the (2×2) identity matrix. If we choose the coordinate system such that the field is parallel to z, the dot product $\vec{\sigma}.\vec{n}$ reduces to $\sigma_z = \left(\begin{smallmatrix} 1 & 0 \\ 0 & -1 \end{smallmatrix}\right)$, so applying this operator to the spinor means, that we **add** $\alpha/2$ to the phase of the component along $\binom{1}{0}$ and simultaneously **subtract** $\alpha/2$ from the phase of the component along $\binom{0}{1}$. When we calculate the components of the average spin $\vec{S}$, we find that this vector has rotated by α around the z-axis. Taking $\alpha/2 = 2\pi$, this means that a full period of 2π for the components of the spinor gives a rotation of the "observable" polarization vector $\vec{S}$ over 4π. Hence, recovery of the initial spinor is obtained only after 4π rotation of the polarization. This is called the 4π periodicity of the spinor.

The common way to add/subtract a certain phase in the components of the spinor is to subject the neutron beam over some path length to a magnetic field B. The neutron wave with initial wavenumber k_0, once in the field, splits into plane waves corresponding to the spin-up $\binom{1}{0}$ (or $|\uparrow\rangle$) and spin-down $\binom{0}{1}$ (or $|\downarrow\rangle$) states with wavenumbers $k^+ = k_0 + \frac{2\mu_n B}{\hbar v}$ and $k^- = k_0 - \frac{2\mu_n B}{\hbar v}$ (μ_n =magnetic moment, v=velocity of the neutrons). Their phases increase at different rates. At the end of the field k^+ and k^- return to k_0, so from this point on the phases grow again at equal rates. The thin lines in Fig. 9.1a illustrate this for a succession of 2 DC magnets (x is the travelling direction of the waves). The phase acquired by the terms for $\binom{1}{0}$ and $\binom{0}{1}$ in the spinor equals $\int(k^+(x) - k_0(x))dx$ and $\int(k_0(x) - k^-(x))dx$, respectively. The polarization precessed over an angle equal to the sum

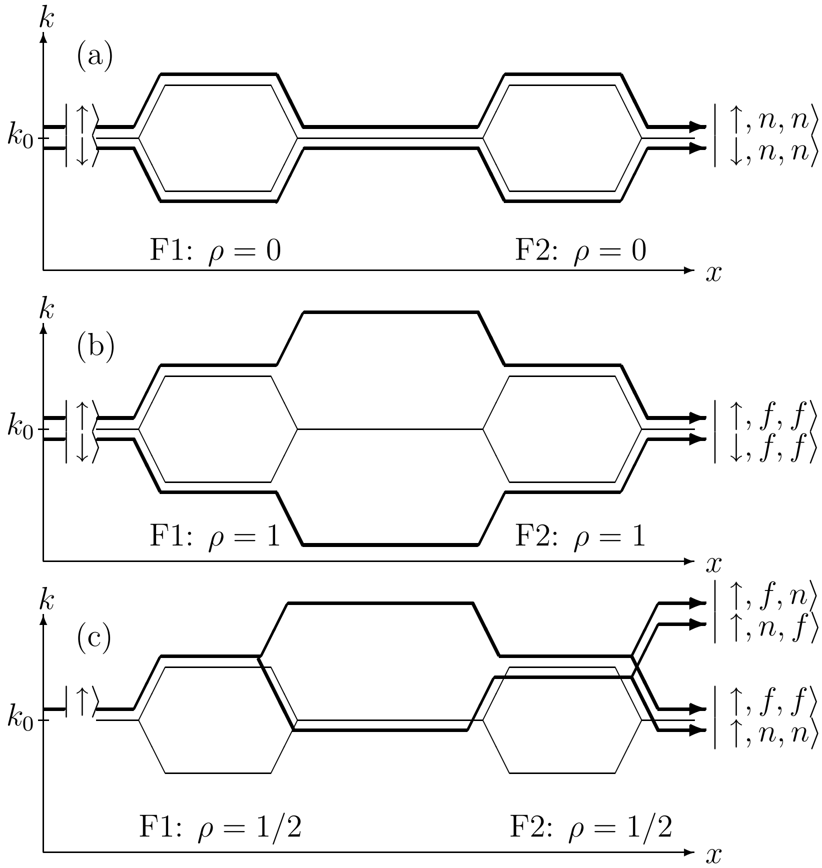

Figure 9.1: (k, x) diagram for the first arm of a spin-echo setup consisting of 2 neutron resonance spin flippers. The thin lines schematically show the splitting of the wavevector $k(x)$ for the initial states $|\uparrow\rangle$ and $|\downarrow\rangle$ in the fields of the flippers F1 and F2 in case no flip happens. The thick lines mark "pathways" in (k, x)-space, discussed in the text. (The actual flippers contain gradient fields giving a slight modification of these lines which is irrelevant here).

of these integrals. It is the area between the thin lines for k^+ and k^-, marked by thick lines. The $|..\rangle$ symbols indicate that no flip (n) happened in the magnetic fields labelled F1 and F2. This mode of precession is called "DC mode".

When a spin flipping device sits in the first field and spin flip happens, the wavenumbers k^+ and k^- jump to $k^{++} = k^+ + \frac{2\mu_n B}{\hbar v}$ and $k^{--} = k^- - \frac{2\mu_n B}{\hbar v}$ upon leaving the field. This means that the phase difference between the waves increases as a function of x twice as fast as in DC mode. This is called "zero field precession" by Gähler et al. [87][88][89]. We refer to it as "RF mode". To halt this precession, one needs spin flip by a flipping device in the second magnetic field, which returns k^{++} and k^{--} to k_0. In (k, x)-space this mode of precession is represented by the thick lines in Fig. 9.1b. The $|..\rangle$ symbols indicate that flip (f)

happened. We produced this mode of precession for the full white spectrum, by passing the polarization in adiabatic way through 2 gradient NR flippers [90],[91]. The above descriptions of DC and RF precession lead to the idea of a **pathway** of a neutron wave in (k, x)-space.

One could imagine to increase the phase of only one component of the spinor by α and leave the other component unchanged. This would produce a precession of the polarization vector $\vec{S}$ about the field direction (z) over α, in other words, the observed period of the polarization would be **equal** to the period of the spinor. This was done by several authors in neutron interferometers. They modified the precession phase along one of 2 spatially separated paths by a magnetic field along that path [92] [93] [94] [95] and thus demonstrated the 4π periodicity of the spinor in response to the magnetic field.

The aim of this paper is to demonstrate this in (k, x)-space. For an interference experiment in (k, x)-space we consider the diagrams in Fig. 9.1 as the first arm of a neutron spin echo (SE) interferometer. A second SE arm (which is left unchanged) compensates the phases of the waves in the first arm, which do change when we vary parameters acting on the phase of waves travelling along different paths in (k, x)-space.

In the experiments of Fig. 9.1a and b, the polarization of the beam at entrance was perpendicular to the field direction, which means that we feed the initial states $\mid\uparrow\rangle$ and $\mid\downarrow\rangle$ equally. Now, let us operate the flippers at probability $\frac{1}{2}$ (called "DC/RF mode") and feed the interference experiment with only state $\mid\uparrow\rangle$ (by aligning the incoming polarization not perpendicular, but parallel to the field). The initial single state $\mid\uparrow\rangle$ will double after each flipper. This means that we "realize" the pathways marked as thick lines in Fig. 9.1c. This is the technique of "separated coils" introduced by Ramsey [96]. Of the 4 pathways after flipper 2, only the phase difference between the pairs $[\mid\uparrow, f, f\rangle$ - $\mid\uparrow, n, n\rangle]$ and $[\mid\downarrow, f, n\rangle$ - $\mid\downarrow, n, f\rangle]$ can be observed. (We observed these interferences in earlier experiments [90][97]). The phase difference between the other combinations oscillates in time and will average out in the static experiments discussed below. So, neutrons, as far in the states involved in these interferences add as background in the observed intensities. Below, we explain that gradient NR flippers provide parameters which "work" on only one state of the pairs mentioned above.

9.2 NR flipper with adiabatic passage

The flippers in this experiment consist of a **static** field along the neutron path $x = [0, l]$ (l = length of the flipper), written as: $B(x) = B_0 + A_{gr} \cos(\pi x/l)$, where the cosine term is a **gradient** field added to the homogeneous field B_0).

Such a gradient field is absent in a mere resonant flipper [98]. Superposed on this is a longitudinal field **oscillating** at frequency ν_{rf} such that the resonant point ($2\pi\nu_{rf} = \frac{\mu_n B_0}{\hbar} \equiv \gamma B_0$) is near the center of the flipper. The field B_{rf} must vary along the range $x = [0, l]$ from 0 at $x = 0$ to a maximum halfway and back to 0 at $x = l$: $B_{rf}(x) = A_{rf} \sin(\pi x/l) \exp(i\, 2\pi\nu_{rf} t)$.

When the resonance condition is fulfilled, the neutrons, as seen in the frame $(\tilde{x}, \tilde{y}, z)$ rotating at the frequency $\omega_0 = 2\pi\nu_{rf}$ about the z-axis, are affected by the sum of two fields: the static gradient field pointing along the z axis - reduced by the value B_0 -, and the oscillating field B_{rf} which in this system also appears static. For a neutron flying with velocity v, the effective field B_{eff} rotates in the $\tilde{x}z$ plane with frequency $\Omega = \pi/\tau$, where $\tau = l/v$ is the time which the neutron needs to pass this interval. During this time the spin rotates about B_{eff} at a frequency $\omega_L = \gamma A$, where A is the magnitude of the effective field. If A is large enough, i.e. the adiabatic condition $\omega_L \gg \Omega$ is satisfied (or the adiabaticity parameter $k \equiv \gamma A l/(\pi v) \gg 1$), the neutron spin follows the effective field. Back in the laboratory system, this means that spin is reversed.
The **spin flip probability** ρ for such a configuration is [90] [98]:

$$\rho = 1 - \sin^2\phi/(k^2 + 1), \tag{9.3}$$

where ϕ is the phase of the spin in the magnetic field of the rotating frame. ρ may be readily changed between 1 and 0 by changing the amplitude A_{rf} of the oscillating field from some maximum to 0, i.e. by changing the adiabaticity parameter k from $\gg 1$ to 0.
For the **precession phase** we must distinguish between f and n. The **non flipped** part of the spinor neither gains nor looses energy. This means that it did not interact with B_{rf}. Its phase is:

$$\Delta\phi_n = \frac{\gamma}{v}\int_0^l B_0(x)dx = \frac{\gamma}{v}\int_0^l B_0 + A\cos(\pi x/l)dx = \frac{\gamma}{v}B_0 l. \tag{9.4}$$

The phase for the **flipped** part of the neutron wave in our magnetic field configuration is $\Delta\phi_f = \omega_0\tau + (\pm)\phi = \omega_0\tau + (\pm)(\pi\sqrt{k^2+1})$, as was shown in [2] for the case $A_{gr} \approx A_{rf} \approx A$ and the adiabatic condition fulfilled ($k \gg 1$). The term $\omega_0\tau$ is the contribution of the rotating frame, as in a conventional flipper [1,3-5]. The second term is the precession phase itself in the rotating frame. Its sign depends on the sign of the gradient field with respect to the spin. We can rewrite the phase $\Delta\phi_f$ as:

$$\Delta\phi_f \approx \omega_0\tau + \frac{\gamma}{v}\int_0^l |B_{eff}(x)|dx = \omega_0\tau + \frac{\gamma}{v}\int_0^l \sqrt{B_{x,eff}^2(x) + B_{z,eff}^2(x)}dx, \tag{9.5}$$

where $B_{x,eff}(x) = A\sin(\pi x/l)$ and $B_{z,eff}(x) = B_0 - \omega_0/\gamma + A\cos(\pi x/l)$. In principle the field B_0 is chosen such that the terms B_0 and ω_0/γ cancel, but in practical reality as long as $|B_0 - \omega_0/\gamma| < A/2$, the flipper will work, so Eq.(9.5) remains valid and a second order effect on $\Delta\phi_f$ due to a variation of B_0 will be present. We neglect it for the purpose of this work.
Combining these equations for the case of incomplete flip, we conclude:

(1) the constant permanent field B_0 determines the phase of the non-flipped part of the wave and has a second order effect on the phase of the flipped part;

(2) the amplitudes A_{gr} and A_{rf} as set by the experimentalist, determine the phase of the flipped part of the neutron wave, but not of the non-flipped part.

9.3 Layout of the NRSE experiment

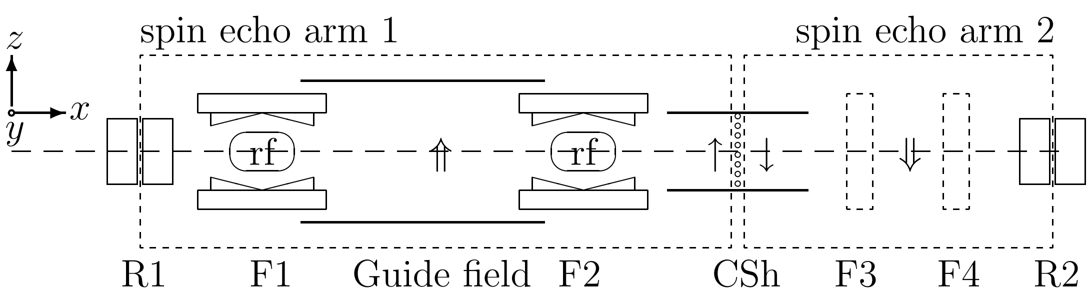

Figure 9.2: Schematic side view of the spin-echo (SE) interferometer installed between a polarizer and analyzer (not shown). The ovals "rf" in the flippers F1 and F2 in the first SE arm represent the longitudinal RF coils, the triangles represent the gradient coils. The second arm is schematized.

The setup is shown schematically in Fig. 9.2. A polychromatic polarized neutron beam enters rotator R1 where the polarization can be rotated towards the y axis ($\perp$ field direction in SE arms) or kept parallel to the initial direction z (= field direction in SE arms). Behind the SE setup sits a mirrored rotator R2. The combined rotators allow to apply and analyze the polarization perpendicular (denoted P_{yy}) or parallel to the field direction (denoted P_{zz}). In addition, rotator R2 allowed for measuring in 2 anti-parallel modes, which in any setting enabled us to calculate the beam polarization. Spin-echo arm 1 is a set of two gradient NR spin flippers F1 and F2 at center-to-center distance 0.9 m. Details of their construction are given elsewhere [99]. To "smooth" the field gradients between the flippers and for guide fields, iron plates are mounted below and above the beam axis. Spin-echo arm 2 is identical with 1, but with opposite static field. The current sheet CSh produces a stepwise field transition between the SE arms.

In each flipper we could independently vary the parameters: magnetic field B_0 (0-1000 G), amplitude A_{gr} of the gradient field (0-40 G), and amplitude A_{rf} of the RF field (0-20 G). Data were collected in a detector bank placed in the reflected beam of a monochromator crystal behind the analyzer. The wavelength in various detectors ranged from $\lambda = 0.19...0.23$ nm with a spread $\simeq$0.02 nm.

9.4 Setting flipping probability

To find how to set the flipping probability ρ, we first measured ρ in mode P_{zz}

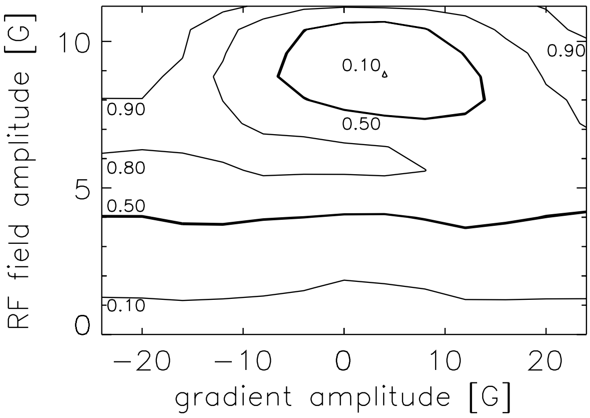

Figure 9.3: Flipper F1: Map of the flipping probability ρ at B_0=414 G, λ=0.193 nm, showing the locus of points where $\rho = \frac{1}{2}$ (thick lines).

for each flipper as a function of A_{gr} and A_{rf}, in the way published in [99]. As an example, Fig. 9.3 shows results for F1. One sees that $\rho \simeq 1$ (exceeds 0.85) for $A_{rf} \approx 12$ G (upper edge of the map) and that $\rho \simeq 0.5$ for $A_{rf} = 4$ G, both irrespective of the value of the gradient amplitude.

9.5 Interference experiments

Prior to each experiment the parameters of all flippers were set and the SE interferometer was balanced by means of a "phase coil" in SE-arm 1. In the experiments we varied the parameters of flipper F1, the other flippers being unchanged.

First, following the scheme of Fig. 9.1a, with all flippers off (ρ=0, DC mode), we change the gradient amplitude in flipper F1. Eq.(9.4) predicts that this will affect the phases of neither $|\uparrow, n, n\rangle$ nor $|\downarrow, n, n\rangle$, so the polarization (when the rotators are set for measuring P_{yy}) will not vary. This is shown in Fig. 9.4a for 2 detectors.

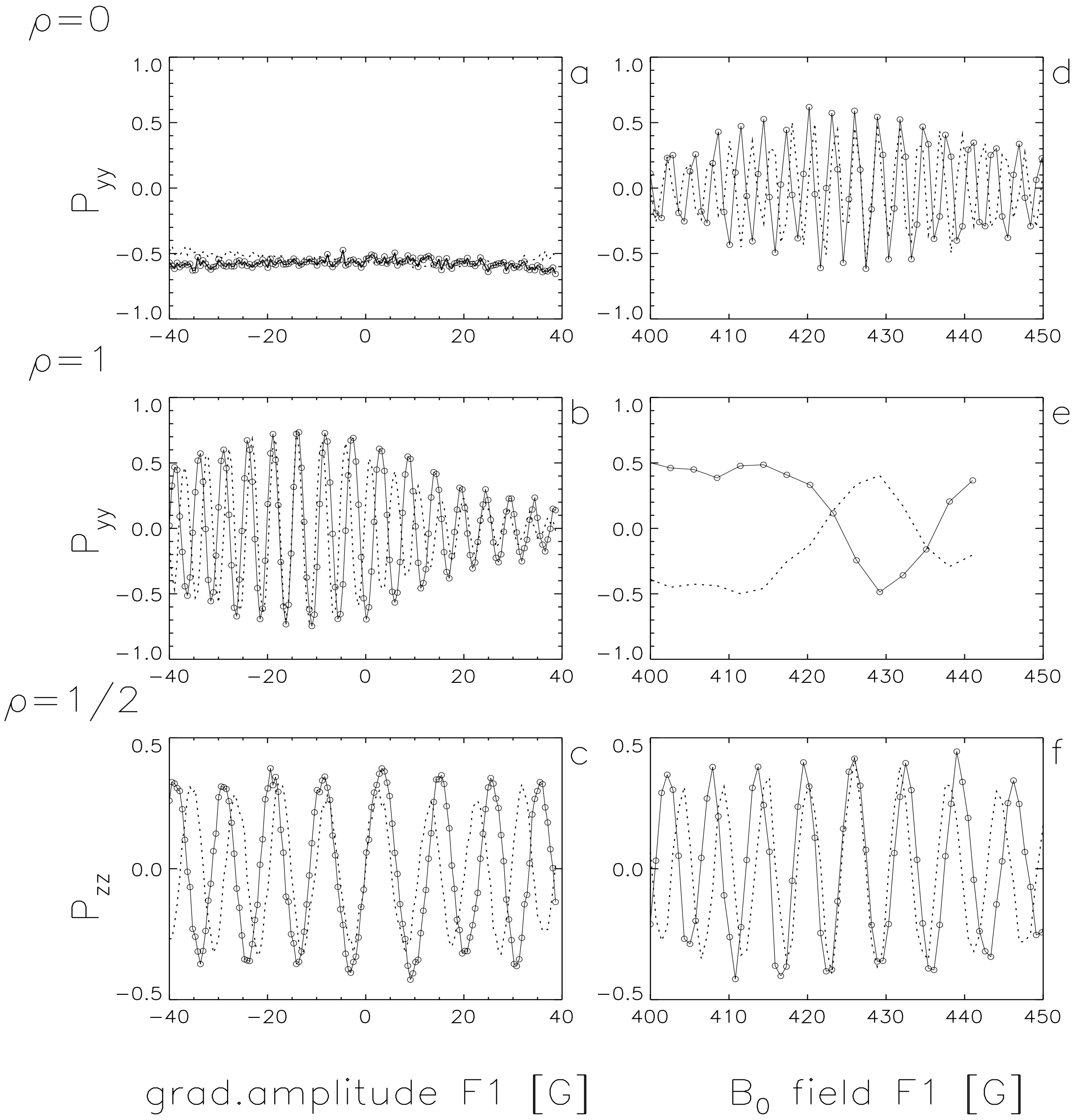

Figure 9.4: Polarizations measured in interference experiments for the pathways through (k,x) space of Fig. 9.1, while varying the parameters gradient A_{gr} (left) and constant field B_0 (right) of flipper F1. Full lines: detector observing λ=0.193 nm; dotted lines: idem λ=0.217 nm.

Next, all flippers are set to flip probability $\rho = 1$, (RF precession mode), Fig. 9.1b. According to Eq.(9.5) the phases of both the states $|\uparrow, f, f\rangle$ and $|\downarrow, f, f\rangle$ will change, hence the polarization varies periodically as a function of the gradient amplitude of F1, as shown in Fig. 9.4b.

Now we do the same, with rotators R1 and R2 set for measuring P_{zz}, with the flippers at $\rho = \frac{1}{2}$ (DC/RF mode, Fig. 9.1c). Varying the gradient amplitude of flipper F1 will affect $|\uparrow, f, f\rangle$, but not $|\uparrow, n, n\rangle$. Therefore, the phase difference between these 2 states changes at half the rate of the previous experiment, so the polarization will vary with the **double** period. This is confirmed by the result in Fig. 9.4c.

A similar set of experiments can be done by varying the permanent field B_0 of flipper F1. In the mode of DC precession (Fig. 9.1a) the phases of $|\uparrow, n, n\rangle$ and $|\uparrow, n, n\rangle$ change and we see a periodic variation of the polarization P_{yy}. (Fig. 9.4d). No phase variation is seen (in first order) in RF precession mode (Fig. 9.1b), what is shown in Fig. 9.4e. Again, for the polarization P_{zz}, the observed period in B_0 doubles, when the flippers are operated at $\rho = \frac{1}{2}$ (DC/RF mode), because $|\uparrow, n, f\rangle$ is affected but not $|\uparrow, f, n\rangle$. This is shown by Fig. 9.4f.

In both sets of experiments the **absolute** period of the signals can be accounted for (to a precision of 20 %) on basis of Eq.(9.5) and the known profiles of the static B_0-field and of the gradient field [99]. In the interpretation this imprecision plays no role, since we observed 2 distinct periods in both sets of experiments with a **ratio** equal to 2 within 2%.

9.6 Interpretation and Conclusion

The spinor, represented as the vector $\begin{pmatrix} \alpha \exp(i\phi_1) \\ \beta \exp(i\phi_2) \end{pmatrix}$, may be affected by three different tools, which are driving parameters of the gradient NR spin flipper: B_{rf}, and A_{gr}, and B_0. We selected the parameter B_{rf} to set the spin flip probability ρ equal to 0, 1, or $\frac{1}{2}$, in order to observe the spinor behavior in the modes DC (Fig. 9.1a), RF (Fig. 9.1b), or DC/RF (Fig. 9.1c), respectively.

The parameter A_{gr}, in DC mode, lets the spinor unchanged; in RF mode it is changed into

$$\begin{pmatrix} \alpha \exp(i\phi_1 + i\chi(A_{gr})) \\ \beta \exp(i\phi_2 - i\chi(A_{gr})) \end{pmatrix}$$

and in DC/RF mode into

$$\begin{pmatrix} \alpha \exp(i\phi_1 + i\chi(A_{gr})) \\ \beta \exp(i\phi_2) \end{pmatrix}.$$

Here $\chi(A_{gr})$ is the phase shift in the flipped part of the neutron wave. In terms of the observables one gets: $P \sim \cos(\phi_1 - \phi_2)$ for DC mode (Fig. 9.4a); $P \sim \cos[(\phi_1 - \phi_2) + 2\chi(A_{gr})]$ for RF mode (Fig. 9.4b); and $P \sim \cos[(\phi_1 - \phi_2) + \chi(A_{gr})]$ for DC/RF mode (Fig. 9.4c).

The same consideration applies when the parameter B_0 varies. In observables one gets: $P \sim \cos[(\phi_1 - \phi_2) + 2\chi(B_0)]$ for DC mode (Fig. 9.4d); $P \sim \cos(\phi_1 - \phi_2)$ for RF mode (Fig. 9.4e); and $P \sim \cos[(\phi_1 - \phi_2) + \chi(B_0)]$ for DC/RF mode (Fig. 9.4f) with $\chi(B_0)$ as a phase shift produced by the permanent field B_0 in the unflipped part of the neutron wave.

This consideration demonstrates that in DC/RF mode the observable P shows the "true" periodicity of the spinor while in the RF and DC modes the periodicity of observable is twice less than that of the spinor. Furthermore, it has been shown in many experiments that the observable P changes periodically under a magnetic field with 2π-periodicity. Therefore we can conclude that in DC/RF mode one observes the 4π-periodicity of the spinor.

This work was partly supported by the INTAS foundation (grant INTAS-03-51-6426). One of the authors (S.V.G.) thanks project **SS-1671.2003.2** and the Russian State Programme "Neutron Research of the Condensed State".

Bibliography

[1] J. Chadwick, Proc.Roy.Soc. London 136 (1932) 692

[2] J.G. Hoffman, M.S. Livingstone and H.A. Bethe, Phys.Rev. 51 (1937) 214

[3] K. Brückner, W. Hartsough, E. Howard and W.M. Powell, Phys.Rev. 75 (1949) 555

[4] T.E. Sherwood, T.E. Stephenson, C.P. Stanford and S. Bernstein, Phys.Rev. 96, 1546

[5] C.G. Shull, E.O. Wollan and J. Koehler, Phys.Rev.81 (1951) 626, ibid 84 (1951) 912

[6] O. Schärpf, AIP-Conference-Proceedings. 89 (1982) 182

[7] Yu.V. Taran and F.L. Shapiro, JETP 44 (1963) 2185

[8] K.P. Coulter e.a. Nucl.Instr.Meth. A 288(1990) 463

[9] F. Mezei, Z.Physik 255 (1972) 146-160

Chapter 2

[10] David J. Griffiths, *Introduction to Quantum Mechanics*, Upper Saddle River: Prentice-Hall, 1995

[11] R.T. Robiscoe, Am. J. of Physics 39 (1971) 146

[12] A.I. Egorov, V.M. Lobashev, V.A. Nazarenko, G.D. Porsev and A.P. Serebrov, Sov.J. Nucl. Phys. 19 (1974) 300

[13] Yu.V. Taran, Dubna Report JINR P3-8577, Dubna, 1975

[14] C.M.E. Zeyen, P.C. Rem, R.A. Hartmann and L.J.M. Van de Klundert, IEEE-Transactions-on-Magnetics. March 1988; 24 pt. 1 (1988) 1540

[15] M. Monkenbusch, Nucl.Instr.Meth. A287 (1990) 465; ibid. A437 (1999) 455

[16] R. Gähler and R. Golub and T. Keller, Physica-B. 180-181 (1992) 899

Chapter 3

[17] O. Schärpf, AIP-Conference-Proceedings. 89 (1982) 182

[18] M.Th. Rekveldt, Z.Physik 259 (1973) 391

[19] O. Schärpf in *Neutron Spin Echo* Ed. F. Mezei, Berlin: Springer, 1980

[20] M.Th. Rekveldt and F.J. van Schaik, Nucl.Instr.Methods 166 (1979) 277

[21] M.V. Berry, Proc. Roy. Soc. London A392 (1984) 451

[22] T. Bitter, D. Dubbers, Phys.Rev.Lett. 59 (1987) 251

[23] R. Pynn, J. Phys.E: Sci Instr. 11 (1978) 1133

[24] M.Th. Rekveldt e.a. in *"Neutron Spin Echo Spectroscopy"*, Eds F. Mezei, C. Pappas and T. Gutberlet, Springer, 2003

[25] T.V. Krouglov, W.G. Bouwman, J. Plomp, M.Th. Rekveldt, G.J. Vroege, A.V. Petukhov and D.M.E. Thies-Weesie, J. Appl. Cryst. 36 (2003) 1417

[26] O. Uca, W.H. Kraan, W.G. Bouwman and M.Th. Rekveldt, Physica B 297 (2001) 28

[27] M.Th. Rekveldt, W.G. Bouwman, W.H. Kraan, S.V. Grigoriev, J. Plomp, O. Uca, Appl.Phys A74 [supp] (2002) S94

Chapter 4

[28] M.Th. Rekveldt and W.H. Kraan, Nucl.Instr.Meth. B28 (1987) 117

[29] W.H. Kraan, J.B. van Tricht and M.Th. Rekveldt, Physica-B. 156-157 (1989) 657

[30] R.N. Sinclair and A.C. Wright, J. Non-Cryst. Sol. 57 (1983) 447

[31] A.C. Wright, J. Non-Cryst. Sol. 76 (1985) 187

[32] G.M. Drabkin, A.I. Okorokov, A.F. Schebetov, N.V. Bororikova, A.G. Gukasov, V.A. Kudrishov and V.V. Runov, Nucl.Instr.Meth. 133 (1976) 453

[33] J.B. Hayter, J. Penfold and W.G. Williams, J. Phys. Ell (1978) 454

[34] Y. Endoh, J. Mizuki, Y. Sasaki and H. Ono, Proc. ICANS-IV (KEK, 1980) 609

[35] P. Verkerk, Comp. Phys. Comm. 25 (1982) 325

[36] B.R Martin, *Statistics for Physicists* (Academic Press, London, 1971)

[37] E.J. Burge, Nucl.Instr.Meth. 144 (1977) 547

[38] H. Fredrikze, unpublished results. The optimum choice of beam time distribution between empty beam and beam with a sample can be derived from the following. If α is the transmission of the monitor and $x = N\sigma d$, then the fraction f of the allotted beam time to be devoted to the empty beam measurement is

$$f = \{1 + [(1-\alpha)e^x + \alpha]^{1/2}\}^{-1}.$$

This gives the minimum relative error in the determination of x.

[39] S.F. Mughabghab and D.l. Garber, USAEC Rept. BNL 325, 3rd ed. (1973)

[40] M.Th. Rekveldt and W.H. Kraan, Physica 120B (1983) 81

[41] B. Farnoux, B. Hennion and J. Fagot. Proc. IAEA Symp. on Neutron Inelastic Scattering (Vienna, 1968) 353

Chapter 5

[42] A.I. Okorokov, V.V. Runov and A.G. Gukasov, Nucl.Instr.Meth. 157 (1978) 487

[43] G. Janeschitz, Dissertation Tech. Univ. Vienna (1983)

[44] W.H. Kraan, J.B. van Tricht and M.Th. Rekveldt, Nucl.Instr.Meth. A 276 (1989) 521

[45] A. Virjo, Nucl.Instr.Meth. 73 (1969) 189

[46] P.T. Por, W.H. Kraan and M.Th. Rekveldt, Nucl.Instr.Meth. A 339 (1994) 550

[47] M.Th. Rekveldt and F.J van Schaik, Nucl.Instr.Meth. 166 (1979) 277

Chapter 6

[48] L.W. Alvarez, F. Bloch, Phys.Rev 57 (1940) 111

[49] M.Th. Rekveldt, J. Phys, Colloq. C1 32, C1-579 (1971); Z. Physik 259 (1973) 391

[50] F. Mezei, Z. Physik 255 (1972) 146

[51] A.N. Bazhenov, e.a., Nucl.Instr.Meth. A 332(1993) 534

[52] G.M. Drabkin, JETP 43 (1962) 1107

[53] R.T. Robiscoe, Am. J. of Physics 39 (1971) 146

[54] W.H. Kraan, M.Th. Rekveldt and P.T. Por, Nucl.Instr.Meth. A 300 (1991) 35

[55] T. Takeda, H. Seto and Y. Kawabata, Appl.Phys.A 74 [Supp](2002), S177

[56] A.I. Egorov, V.M. Lobashev, V.A. Nazarenko, G.D. Porsev and A.P. Serebrov, Sov.J. Nucl. Phys. 19 (1974) 300

[57] Yu.V. Taran, Dubna Report JINR P3-8577, Dubna, 1975

[58] T. Keller e.a., Nucl.Instr.Meth. A 451 (2000) 474

[59] S.V. Grigoriev, R. Kreuger, W.H. Kraan, F.M. Mulder and M.Th. Rekveldt, Phys.Rev. A 64 (2001) 013614/1-14

[60] W.H. Kraan, S.V. Grigoriev, R. Kreuger, F.M. Mulder and M.Th. Rekveldt, Physica B 297 (2001) 23

[61] W.H. Kraan, S.V. Grigoriev, and M.Th. Rekveldt, Appl.Phys. A 74 [Supp](2002), S79

[62] H. Weinfurter and G. Badurek, Nucl.Instr.Meth. A 275 (1989) 233

[63] B. Farago, Neutron News 12-4 (2001) 34

[64] R. Maruyama, T. Ebisawa, S. Tasaki, M. Hino, M. Takeda, T. Kawai, Y. Kawabata and K. Sakai, Physica B 335 (2003) 238

[65] P.T. Por, W.H. Kraan and M.Th. Rekveldt, Nucl.Intsr.Meth. A 339(1994) 550

[66] A.R. Wildes, Rev. Sc. Instr. 70, 11 (1999) 4241

[67] H. Fredrikze and R.W.E van de Kruijs, Physica B 297 (2001)143

[68] A.F. Schebetov, S.V. Metelev, B.G. Peskov, N.K. Pleshanov, V.M. Pusenkov, V.G. Syromyatnikov, V.A. Ul'yanov, W.H. Kraan, C.F. de Vroege and M.Th. Rekveldt, Physica B 335 (2003) 223

[69] W.H. Kraan, J.B. van Tricht and M.Th. Rekveldt, Nucl.Instr.Meth.A 276(1989) 521

[70] ESS Council, ESS Project Vol I, 2002

Chapter 7

[71] M.Th.Rekveldt, Mat.Science Forum (ed. Trans. Techn. Publ) 321-324 (1999) 258

[72] W.G. Bouwman M. van Oossanen, O. Uca, W.H. Kraan and M.Th. Rekveldt, J.Appl.Cryst. 33 (2000) 767

[73] F.M. Mulder, R.Kreuger, S.V. Grigoriev, W.H. Kraan, M.Th. Rekveldt, A.A. van Well, Physica B 276-278 (2000)132

[74] R. Golub, R. Gaehler, T. Keller Am.J.Phys 62 (1994)779

[75] T. Keller, R.Golub, F.Mezei, R.Gaehler, Physica B 241 (1998)101

[76] A.N. Bazhenov, V.M. Lobashev, A.N. Pirozhkov and V.N. Slusar, Nucl.Instr.Meth. A 332 (1993) 534

[77] S.V. Grigoriev, A.I. Okorokov, V.V.Runov, Nucl.Instr.Meth. A 384 (1997) 451

[78] M.Th.Rekveldt, W.H.Kraan, J.Neutron Res 8 (1999) 53

[79] W.H.Kraan, J.B.van Tricht, M.Th.Rekveldt, Physica B 156-157 (1989) 657

Chapter 8

[80] M.Th. Rekveldt, J. Nucl.Instr.Meth. B 114 (1996) 366

[81] R. Golub and R. Gähler and T. Keller, Am. J. Phys. 62 (1994) 779

[82] W.G. Bouwman, M. van Oossanen, O. Uca, W.H. Kraan and M.Th. Rekveldt, J. Appl. Cryst 33 (2000) 767

[83] T. Keller, R. Golub, F. Mezei, R. Gähler, H. Kunze, Physica B 241-243 (1998) 101

[84] S.M. King: *Modern Techn. for Polymer Characterisation*, ed. by R.A. Pethrick and J.V. Dawkins (J.Wiley and Sons Ltd, 1999)

[85] M.Th. Rekveldt, W.G. Bouwman, W.H. Kraan, S.V. Grigoriev, O. Uca and R. Kreuger in: *"Neutron Spin Echo Spectroscopy"*, Eds F. Mezei, C. Pappas and T. Gutberlet, Springer, 2003

[86] S.V. Grigoriev, R. Kreuger, W.H. Kraan, F.M. Mulder and M.Th. Rekveldt, Physical Review A 64 (2001) 013614

Chapter 9

[87] R. Golub and R. Gähler, Phys.Lett.A 123 (1987) 43-48

[88] R. Gähler and R. Golub, J. de Phys. (Paris) 49 (1988) 1195-1202

[89] R. Golub, R.Gähler and T.Keller, Am.J.Phys. 62 (1994) 779-788

[90] S.V. Grigoriev, W.H. Kraan, F.M. Mulder, and M.Th. Rekveldt, Phys.Rev.A, 62 (2000) 63601-63609

[91] S.V. Grigoriev, R. Kreuger, W.H. Kraan, F.M. Mulder, and M.Th. Rekveldt, Phys.Rev.A, 64 (2001) 013614

[92] S.A. Werner, R. Colellam, A.W. Overhauser and C.F. Eagen, Phys.Rev.Lett. 35 (1975) 1053

[93] H. Rauch, A. Zeilinger, G.Badurek, A.Wilfing, W. Bauspiess and U. Bonse, Physics Lett. 54A (1975)425

[94] G. Badurek, H. Rauch and J. Summhammer, Physica B 151 (1988) 82-92; Phys.Rev.Lett. 51 (1983) 1015-1018

[95] A. Ioffe and F. Mezei, Physica B 297 (2001) 303-306

[96] N.F. Ramsey, *Molecular Beams* (Clarendon, Oxford) 1956

[97] F.M. Mulder, S.V. Grigoriev, W.H. Kraan and M.Th. Rekveldt, Europhysics Lett. 51 (2000) 13

[98] S.V.Grigoriev, A.I.Okorokov, V.V. Runov, Nucl.Instr.Meth. A 384 (1997) 451

[99] W.H. Kraan, S.V. Grigoriev, M.Th. Rekveldt, H. Fredrikze, C.F. de Vroege and J. Plomp, Nucl.Instr.Meth. A 510 (2003) 334

Conclusion

[100] A.G.M. van Melsen, *"Van Atomos naar Atoom"* Meulenhoff, Amsterdam, 1949

Summary

In this thesis we investigate the devices needed to handle the polarization of thermal neutron beams and illustrate how these devices are used to investigate the properties of matter.

In **Chapter 2** we outline the basic theory for polarized neutron beams running through space and time dependent magnetic fields $\vec{B}(\vec{r},t)$. Starting from the time dependent Schrödinger equation we consider three limiting cases.

1. Fields $\vec{B}(t)$ which depend only on time t
In this case the *kinetic energy* (or velocity $\vec{v}_0$) of each neutron is conserved, implying that each neutron in a beam just goes straight ahead. For the neutron spin (or polarization) we derive the time dependent Larmor equation from the Schrödinger equation. We discuss the exact solutions of the Larmor equation for two basic cases: (i) $\vec{B}(t)$ is (stepwise) constant in time; (ii) $\vec{B}(t)$ rotates uniformly in time with frequency ω and $|\vec{B}(t)|$ is constant. We explain the phenomenon of "zero field precession in time" (as if spins rotate when no field is present) which occurs in between two pulses of a rotating field $\vec{B}(t)$ in resonance condition $\omega = \gamma|\vec{B}(t)|$.

2. Fields $\vec{B}(\vec{r})$ which only depend on space $\vec{r}$.
In this case the *total energy* of each neutron is conserved. The neutron spin is described by the time-independent Schrödinger equation like in the theory of neutron reflection, which we exploit here. We discuss the exact solutions for stepwise constant fields $\vec{B}(\vec{r})$ in space. The essential ingredients are the reflection and transmission coefficients at each boundary where $\vec{B}(\vec{r})$ changes. This is used to understand the phenomenon of total reflection on magnetic layers as in actual neutron polarizers (and analyzers).
Then we consider thermal neutron beams along the x-axis in a stepwise constant field $\vec{B}(x)$. The range of wavelengths λ is typically $0.05 < \lambda < 0.6$ nm corresponding to neutron velocities $8000 < v_0 < 660$ m/s. For such beams we observe that the kinetic energy $\frac{1}{2}mv_0^2$ is much larger than the magnetic interaction energy $|\mu_n B(\vec{r},t)|$. Even for huge fields $B \simeq 10$ T one has only $\mu_n B = 6 \times 10^{-4}$ meV, while for the smallest kinetic energy ($v_0 = 660$ m/s)

one has $\frac{1}{2}mv_0^2 = 1.5$ meV. This implies that no reflections occur at boundaries where $\vec{B}(x)$ changes. The beam just goes straight ahead.
We show that the behaviour of the neutron spin follows from the "semi-classical approximation". This means that the neutron has a classical location $x = v_0 t$ and sees a time dependent field $\vec{B}(x = v_0 t)$. The neutron spin obeys the time-dependent Larmor equation, exactly as in **1** above and we copy the results from there.
We do so in particular for the "adiabatic static spin flipper" which has a (time independent) field $\vec{B}(x)$ rotating around the x-axis. Such devices flip spins "adiabatically" that is: if the neutrons are slow enough (their wavelength λ large enough), the spins follow the field.

3. Fields $\vec{B}(\vec{r}, t)$ such that the kinetic energy of the neutron is much larger than the magnetic energy
In this case there is in general no energy conservation. We use neutron beams running in the x direction through devices with fields $\vec{B}(x, t)$. Most important is the "adiabatic RF flipper" which contains a radio-frequency (RF) field over a finite distance. Applying the semi-classical approximation we calculate the neutron spin at the end of the flipper. It rotates spins adiabatically as efficiently as static flippers above. However, the RF flipper is fundamentally different: there is no energy conservation. This difference makes it possible to create "zero-field precession in space" between two spatially separated RF flippers, very similar to zero field precession in time.

Chapter 3 is a review our basic devices: monochromators, polarizers, analyzers, block coils and adiabatic spin rotators of static and RF type. Also, the principles of the time-of-flight (TOF) and Fourier methods are explained to analyze the spectrum $J(\lambda)$ of neutron beams as a function of λ.
To illustrate how our devices can be used to investigate the properties of matter, we describe the SESANS (Spin Echo Small Angle Neutron Scattering) technique, capable to determine inhomogeneities in a sample on nanometer scale.
Finally we show how "zero-field precession in space" works in practice.

Chapters 4-9 are published papers.

Chapter 4 deals with the technique of Fourier analysis of neutron spectra $J(\lambda)$ as a function of wavelength λ for beams in the x direction. The essential device is the "block coil" which ideally produces a constant magnetic field $\vec{B}$ for $0 \leq x \leq L$ and zero field elsewhere. With this method we study a curved multi-mirror polarizer devised by us in Delft. We find an (at the time) good polarizing power $\mathcal{P}$=0.95. (Later polarizers used in subsequent chapters have $\mathcal{P}$=0.99 in the maximum of the thermal neutron spectrum). Also we demonstrate the use of the Fourier method for measuring the scattering cross section as a function of λ for

vitreous silica. The results are consistent with literature.
In **Chapter 5** we study static adiabatic spin rotators. These novel, so-called V-coils contain time independent fields rotating in space. We measure with the Fourier method of Chapter 4 in how far the spins in a neutron beam follow the field. We find that our V-coils rotate spins over the desired angle $\pi/2$ for the thermal spectrum $0.15 < \lambda < 0.55$ nm. Such coils are now used (c.q. considered) at several places in the world as rotators for 3D polarization analysis.
First, in **Chapter 6** we show that the performance of an adiabatic static flipper (with 2 V-coils) can be improved by applying additional fields in the V-coils. Next, we study newly developed adiabatic RF flippers (containing time-independent fields and an RF field). The time-independent field in this flipper is an order of magnitude stronger than in models elsewhere. We express the results in terms of the flipping efficiency ϵ which is the probability that the neutron spin rotates exactly over 180 degrees, as wanted. Perfect values of the efficiency ($\epsilon = 1$) are obtained for the range of wavelengths 0.2$< \lambda <$0.6 nm.
In **Chapter 7** we use two adiabatic RF flippers separated by a distance L to generate zero-field precession in between (where there is virtually no field). Indeed the neutron spin behaves as if there were a constant field over that distance L. Zero-field precession is very advantageous in comparison with ordinary precession because arbitrarily high precession angles can be realized without magnetic fields over long distances.
The subject of **Chapter 8** is the SESANS technique. Extending the result of Chapter 7 we build a prototype setup with zero-field precession to mimic the necessary constant fields. We thus obtain the first SESANS results in two test systems: limestone and graphite powder.
In **Chapter 9** we consider the following well-known fundamental property of spin-$\frac{1}{2}$ particles (like the neutron). We describe the neutron spin by a 2D spinor ψ which yields a corresponding 3D spin expectation $\vec{S}$.
When we rotate the spin $\vec{S}$ over 2π we get a new spin $\vec{S}'$ which is obviously the same as $\vec{S}$: $\vec{S}' = \vec{S}$. However, the spinor ψ' that corresponds to $\vec{S}'$ is *different* from ψ: $\psi' = -\psi$. This is called the 4π periodicity of the spinor. Using an interference between zero-field precession and ordinary precession, we show explicitly how this 4π periodicity can be actually observed.

The relevance of the work in this thesis is the success of the adiabatic RF flipper. In Chapter 7 we demonstrate "ZFprecession" generated by this type of flippers to work for the "white" spectrum, which to our knowledge is the first such demonstration. This is of eminent importance in view of the present development of instrumentation involving precession of polarized neutrons (at IRI and

elsewhere) for pulsed neutron sources. In competing (monochromatic) technologies for ZFprecession at pulsed sources, instrument parameters must be varied in synchrony with the neutrons of increasing wavelength, as they pass by. This is not needed for our flippers (hence precession devices based on these flippers), eliminating an important amount of control electronics and hence a source of instability.
The interference between zero-field precession and ordinary precession discussed in Chapter 9 implies a coexistence of "non flipped" and "flipped" solutions of the Schrödinger equation. This has an intriguing analogy with the principle of quantum computers in which one creates a coexistence of all paths running from the stating of a problem to its solution along a number of branch points.

Much of the technology developed in the earlier chapters 4-6 was needed for the more "advanced" experiments in the later chapters. In doing these experiments we were inspired by the statement of the Dutch philosopher Van Melsen [100]: "Our hold on nature through knowledge depends on our hold through technology and vice versa".

Samenvatting

In dit proefschrift onderzoeken we toestellen om de polarisatie van een thermische neutronenbundel te manipuleren en hoe we deze toestellen gebruiken om materiaaleigenschappen te bestuderen.

In **Hoofdstuk 2** geven we in het kort de basistheorie voor bundels gepolariseerde neutronen die door magnetische velden $\vec{B}(\vec{r},t)$ lopen die van de plaats in de ruimte en van de tijd afhangen. Uitgaande van de tijdsafhankelijke Schrödinger vergelijking bekijken we drie limietgevallen.

1. Velden $\vec{B}(t)$ die alleen van de tijd t afhangen
   De *kinetische energie* (snelheid $\vec{v}_0$) van het neutron is behouden. Dit betekent dat ieder neutron in de bundel rechtuit loopt. Voor de spin van het neutron (of polarisatie) leiden we uit de Schrödinger vergelijking de tijdsafhankelijke Larmor vergelijking af . We bespreken de exacte oplossingen hiervan voor 2 basisgevallen: (i) $\vec{B}(t)$ (stapsgewijs) constant in tijd; (ii) $\vec{B}(t)$ roteert eenparig met frequentie ω en $|\vec{B}(t)|$ is constant.
   We verklaren het verschijnsel "0-veld-precessie in tijd" (alsof de spins roteren zonder dat er een veld is) hetgeen in de tussentijd gebeurt, als men 2 maal korte tijd een roterend veld $\vec{B}(t)$ inschakelt dat aan de resonantievoorwaarde $\omega = \gamma|\vec{B}(t)|$ voldoet.

2. Velden $\vec{B}(\vec{r})$ die alleen van plaats $\vec{r}$ in de ruimte afhangen.
   In dit geval is de *totale energie* van het neutron behouden. De spin wordt beschreven door de tijdsonafhankelijke Schrödinger vergelijking zoals in de theorie voor neutronenreflectie, waar we hier gebruik van maken. We bespreken de exacte oplossingen voor stapsgewijs constante velden $\vec{B}(\vec{r})$. Essentieel zijn de reflectie- en transmissiecoefficienten op de grenzen waar $\vec{B}(\vec{r})$ verandert. Deze gebruiken we om het verschijnsel totale reflectie aan magnetische lagen te begrijpen die in echte neutronen polarisatoren (en analysatoren) zitten. Het golflengtegebied λ is typisch 0.05 - 0.6 nm, wat overeenkomt met snelheden v_0 van 8000 - 660 m/s.
   Men kan nagaan dat voor zulke bundels de kinetische energie $\frac{1}{2}mv_0^2$ veel kleiner is dan de magnetische interactie energie $|\mu_n B(\vec{r},t)|$. Zelfs voor een

gigantisch veld $B \simeq 10$ T is $\mu_n B$ slechts 6×10^{-4} meV, terwijl de langzaamste neutronen ($v_0 = 660$ m/s) een kinetische energie $\frac{1}{2}mv_0^2 = 1.5$ meV hebben. Dit houdt in dat er geen reflecties plaatsvinden op de bovengenoemde grenzen. De bundel gaat rechtdoor.
We laten zien dat het gedrag van de neutronenspin volgt uit de "semi-classical approximation". Dit houdt in dat het neutron een op klassieke wijze bepaalde plaats $x = v_0 t$ heeft en een tijdsafhankelijk veld $\vec{B}(x = v_0 t)$ voelt. De spin voldoet aan de tijdsafhanklijke Larmor vergelijking net als in geval 1 en we nemen het resultaat daarvan over.
Dit doen we in het bijzonder voor de "adiabatische statische spin flipper" die een (tijdsonafhankelijk) veld $\vec{B}(x)$ heeft dat om de x-as roteert. Zo'n toestel flipt spins op "adiabatische" wijze: als de neutronen langzaam genoeg zijn (golflengte groot genoeg), volgt de spin het veld.

3. Velden $\vec{B}(\vec{r}, t)$ zodanig dat de kinetische energie van het neutron veel groter is dan de magnetische energie
In dit geval is er in het algemeen geen energiebehoud. Wij laten neutronenbundels lopen in de x-richting door toestellen met velden $\vec{B}(x, t)$. Het belangrijkst is de "adiabatische RF flipper" die een radio-frequent (RF) veld bevat over een eindige afstand. Met de "semi-classical approximation" berekenen we de neutronenspin aan het eind van de flipper. Het adiabatisch roteren van de spin blijkt net zo efficient te gebeuren als in bovengenoemde statische flippers. De RF flipper is echter fundamenteel verschillend: er is geen energiebehoud. Dit is de basis van het feit dat men "0-veld-precessie in ruimte" kan opwekken tussen 2 RF flippers op enige afstand van elkaar, analoog met "0-veld-precessie in tijd".

Hoofdstuk 3 beschrijft onze basistoestellen: monochromators, polarisatoren, analysatoren, blokspoelen en adiabatische statische en RF spin rotators. Ook worden de principes van de "time-of-flight" (TOF) en de Fourier methode besproken voor een golflengte-analyse van het spectrum $J(\lambda)$ van een neutronenbundel. Als illustratie hoe men met zulke toestellen materiaaleigenschappen kan onderzoeken, bespreken we de techniek SESANS (Spin Echo Small Angle Neutron Scattering), waarmee men inhomogeneteiten in de orde van nanometers in een preparaat kan meten.
Tenslotte laten we zien hoe "0-veld-precessie in ruimte" in de praktijk werkt.
Hoofdstukken 4-9 zijn gepubliceerde artikelen.
Hoofdstuk 4 gaat over de techniek van Fourier analyse van neutronenspectra $J(\lambda)$ naar golflengte λ voor bundels lopend in de x richting. Het wezenlijke onderdeel is de blokspoel die idealiter een constant magnetisch veld $\vec{B}$ geeft voor $0 \leq x \leq L$ en elders veld 0. Met deze methode onderzoeken we een gekromde

multimirror polarisator die wij in Delft gebouwd hebben. Het polariserend vermogen $\mathcal{P}$ is 0.95, wat voor die tijd goed was. (Polarisatoren gebruikt in latere hoofdstukken hadden $\mathcal{P}$=0.99 in het maximum van het thermische neutronenspectrum). Voorts passen wij de Fourier methode toe om de totale werkzame doorsnede als functie van λ te meten in kwarts. Het resultaat is consistent met de literatuur.

In **Hoofdstuk 5** bespreken we statische adiabatische spin rotators. Deze nieuwe zogenaamde V-spoelen hebben een tijdsonafhankelijk veld dat over de lengte van de spoel een kwart slag in de ruimte maakt. Met de Fourier methode meten wij in hoeverre de spins van de neutronen het veld volgen. Voor het thermische spectrum van 0.15 - 0.55 nm blijken de spins dit inderdaad bevredigend te doen. V-spoelen worden op dit moment op diverse plaatsen in de wereld gebruikt (c.q. overwogen) in opstellingen voor 3D polarisatie analyse.

In het begin van **Hoofdstuk 6** laten we zien dat de werking van een adiabatische statische flipper (bestaande uit 2 V-spoelen) kan worden verbeterd door extra velden in deze spoelen aan te brengen. Hierna bestuderen we nieuw ont-wikkelde adiabatische RF flippers met tijdsonafhankelijke velden en een radio-frequent (RF) veld. Het statische veld in deze flipper is een grootte-orde sterker dan in soortgelijke flippers elders. Wij drukken het resultaat uit als "flip efficiency" ϵ: dit is de kans dat de neutronenspin over precies 180° draait, zoals gewenst. Wij vinden de perfecte waarde $\epsilon = 1$ voor het golflengtegebied 0.2 - 0.6 nm.

Twee adiabatische RF flippers op afstand L van elkaar worden in **Hoofdstuk 7** gebruikt om "0-veld-precessie in ruimte" ertussen op te wekken (waar praktisch geen veld is). Inderdaad blijkt de neutronenspin zich te gedragen alsof er een constant veld aanwezig was over die afstand L. "0-veld-precessie" heeft grote voordelen in vergelijking met gewone precessie, omdat men zeer hoge precessiehoeken kan bereiken zonder sterke velden over lange afstanden.

Hoofdstuk 8 gaat over de SESANS techniek. Voortbouwend op het resultaat van Hoofdstuk 7 realiseren wij een prototype SESANS opstelling met "0-veld-precessie". Hiermee verkrijgen wij de eerste resultaten in 2 testsystemen: kalksteen en grafietpoeder.

In **Hoofdstuk 9** beschouwen we de volgende bekende fundamentele eigenschap van deeltjes met spin $\frac{1}{2}$ (waarvan het neutron er een is). De neutronenspin wordt beschreven met een 2D spinor ψ die een 3D spin-verwachtingswaarde $\vec{S}$ oplevert. Als we de spin $\vec{S}$ over 2π draaien, kijgen we een nieuwe spin $\vec{S}'$ die natuurlijk hetzelfde is: $\vec{S}' = \vec{S}$. De spinor ψ' echter, behorend bij $\vec{S}'$ is *verschillend* van ψ: $\psi' = -\psi$. Dit staat bekend als de 4π periodiciteit van de spinor. Door de interferentie te meten tussen "0-veld-precessie" en gewone precessie, laten we expliciet deze 4π periodiciteit zien.

De relevantie van het werk in dit proefschrift is het succes van de adiabatische RF flipper. In Hoofdstuk 7 tonen we aan dat "0-veld-precessie" opgewekt door zo'n flipper van toepassing is voor het gehele "witte" neutronenspectrum. Voor zover we weten is dit de eerste keer dat dit gedemonstreerd werd. Dit is van eminent belang voor de huidige inspanning (zowel binnen het IRI als elders) voor het ontwikkelen van instrumentatie voor gepulseerde bronnen, waarin precessie een rol speelt. Bij concurrerende (monochromatische) technieken voor 0-veld-precessie bij gepulseerde bronnen moeten instellingen van het instrument gevarieerd worden synchroon met de neutronen van toenemende golflengte, naarmate die het instrument passeren. Voor onze flippers (en daarmee precessietoestellen die daarop gebaseerd zijn), is dit niet nodig, waarmee je een belangrijke hoeveelheid besturings-electronica omzeilt en dus een bron van instabiliteit.
De interferentie tussen 0-veld-precessie en gewone precessie in Hoofdstuk 9 impliceert een coexistentie van "non flipped" and "flipped" oplossingen van de Schrödinger vergelijking. Er is een intrigerende analogie tussen dit en het idee van quantum computers. Hierin probeert men een coexistentie te realiseren van alle paden die vanuit het stellen van een probleem leiden naar de oplossing, langs de vertakkingen bij de beslispunten .

Veel uit de technologie en methoden ontwikkeld in de beginhoofdstukken 4-6 was benodigd bij de meer geavanceerde experimenten in de latere hoofdstukken. Hierbij lieten wij ons inspireren door de uitspraak van de filosoof Van Melsen [100]: "Onze kengreep op de natuur hangt af van de technische greep en onze technische greep van de kengreep."

Publication List

1 **SESANS with a monochromatic beam or with time-of-flight applied on colloidal systems**
Wim G. Bouwman, Wouter Stam, Timofei V. Krouglov, Jeroen Plomp, Serguei V. Grigoriev, Wicher H. Kraan, and M. Theo Rekveldt
Nuclear-Instruments-&-Methods-in-Physics-Research,-Section-A 529 (2004) 16-21

2 **SESANS studies of colloid phase transitions, dairy products and polymer fibres**
Bouwman,-W.-G., Krouglov,-T.-V., Plomp,-J., Grigoriev,-S.-V., Kraan,-W.-H., and Rekveldt,-M.-Th.
Physica B 350, (15 July 2004)Suppl.1, E140-E146

3 **Neutron refraction and transmission studied by SESANS**
Rekveldt,-M.-Th., Bouwman,W.-G., Kraan,-W.-H., and Plomp,-J.
Physica B 350, (15 July 2004)Suppl.1, E791-E794

4 **Magnetic domains in ErCrO4 studied by 3D neutron depolarization**
Jiménez,-E., Kraan,-W.-H., van Dijk,-N.-H., Gubbens,-P.-C.-M., Isasi,-J. and Sáez-Puche,-R.
Physica B 350, (15 July 2004) Suppl.1, E293-E296

5 **Neutron multiwave interference with many resonance coils: a test experiment**
Yu. O. Chetverikov,-Yu.-O., Axelrod,-L.-A, Syromyatnikov,-A.-V., Kraan,W.-H., Rekveldt,-M.-Th. and Grigoriev,-S.V.
Physica B 350, Suppl.1, (15 July 2004) E1039-E1042

6 **Effect of thermomagnetic treatment on the magnetic state of a ferrofluid: a polarised neutron study**
Zabenkin,-V.N., Axelrod,-L.A., Gordeev,-G.P., Kraan,-W.-H., Lazebnik,-I.-M. and Vorobiev,-A.-A.
Physica B 350, (15 July 2004) Suppl.1, E211-E215

7 **Four-wave neutron-resonance spin-echo**
Grigoriev,-S.V., Kraan,-W.H., Rekveldt,-M.-T.
Physical Review A-**69**; (2004): 043615-(1-11)

8 **Observation of 4π-periodicity of the spinor using neutron resonance interferometry**
Kraan,-W.-H., Grigoriev,-S.-V., Rekveldt,-M.-T.
Europhysics Letters **66**; (2004): 164-170

9 **Test of adiabatic spin flippers for application at pulsed neutron sources**
Kraan,-W.-H., Grigoriev,-S.-V., Rekveldt,-M.-T., Fredrikze,-H., de Vroege,-C.-F., Plomp,-J.
Nuclear-Instruments-&-Methods-in-Physics-Research,-Section-A-**510**; (2003): 334-345

10 **Neutron-multiwave-interference experiments with many resonance coils**
Grigoriev,-S.-V.; Chetverikov,-Yu.-O.; Syromyatnikov,-A.-V.; Kraan,-W.-H.; Rekveldt,-M.-T.
Physical-Review-A-Atomic,-Molecular,-and-Optical-Physics. Sept. 2003; 68(3): 33603-1-9

11 **Neutron multiwave interference experiments with many resonance coils**
Grigoriev,-S.-V.; Chetverikov,-Y.-O.; Kraan,-W.-H.; Rekveldt,-M.-T.
Physica-B. July 2003; 335(1-4): 243-6

12 **Improved multichannel neutron polarizers on basis of CoFeV/TiZr supermirrors with TiZrGd underlayer**
Schebetov,-A.-F.; Metelev,-S.-V.; Peskov,-B.-G.; Pleshanov,-N.-K.; Pusenkov,-V.-M.; Syromyatnikov,-V.-G.; Ul'yanov,-V.-A.; Kraan,-W.-H.; de-Vroege,-C.-F.; Rekveldt,-M.-T.
Physica-B. July 2003; 335(1-4): 223-5

13 **Larmor precession applications: magnetised foils as spin flippers in spin-echo SANS with varying wavelength**
Rekveldt,-M.-T.; Bouwman,-W.-G.; Kraan,-W.-H.; Krouglov,-T.-V.; Plomp,-J.
Physica-B. July 2003; 335(1-4): 164-8

14 **SANS study of new magnetic nanocomposites embedded into the mesoporous silica**
Kelberg,-E.-A.; Grigoriev,-S.-V.; Okorokov,-A.-I.; Eckerlebe,-H.; Grigorieva,-N.-A.; Kraan,-W.-H.; Eliseev,-A.-A.; Lukashin,-A.-V.; Vertegel,-A.-A.; Napolskii,-K.-S.
Physica-B. July 2003; 335(1-4): 123-6

15 **Ferromagnetic foils as monochromatic π flippers for application in spin-echo SANS**
Kraan,-W.-H.; Plomp,-J.; Krouglov,-T.-V.; Bouwman,-W.-G.; Rekveldt,-M.-T.
Physica-B. July 2003; 335(1-4): 247-9

16 **Neutron multiwave interference experiments with many resonance coils**
Grigoriev,-S.-V.; Chetverikov,-Y.-O.; Kraan,-W.-H.; Rekveldt,-M.-T.
Physica-B. July 2003; 335(1-4): 243-6

17 **Spin-echo small-angle neutron scattering to study particle aggregates**
Krouglov,-T.; Kraan,-W.-H.; Plomp,-J.; Rekveldt,-M.-T.; Bouwman,-W.-G.
Journal-of-Applied-Crystallography. June 2003; 36 pt. 3: 816-19

18 **Neutron depolarisation in ferrofluids during magnetising/demagnetising cycles**
Zabenkin,-V.-N.; Axelrod,-L.-A.; Gordeev,-G.-P.; Kraan,-W.-H.; Lazebnik,-I.-M.; Orlova,-D.-N.; Vorobiev,-A.-A.
Applied-Physics-A-Materials-Science-Processing. Dec. 2002; A74: S710-12

19 **Overview of new Larmor precession techniques**
Rekveldt,-M.-T.; Bouwman,-W.-G.; Kraan,-W.-H.; Grigoriev,-S.-V.; Uca,-O.; Keller,-T.
Applied-Physics-A-Materials-Science-Processing. Dec. 2002; A74: S323-5

20 **Line-integral corrections in Larmor-precession devices**
Uca,-O.; Bouwman,-W.-G.; Plomp,-J.; Kraan,-W.-H.; Rekveldt,-M.-T.
Applied-Physics-A-Materials-Science-Processing. Dec. 2002; A74: S174-6

21 **First quantitative test of spin-echo small-angle neutron scattering**
Bouwman,-W.-G.; Uca,-O.; Grigoriev,-S.-V.; Kraan,-W.-H.; Plomp,-J.; Rekveldt,-M.-T.
Applied-Physics-A-Materials-Science-Processing. Dec. 2002; A74: S115-17

22 **Magnetised foils as π-flippers in spin-echo spectrometry**
Rekveldt,-M.-T.; Bouwman,-W.-G.; Kraan,-W.-H.; Grigoriev,-S.; Plomp,-J.; Uca,-O.
Applied-Physics-A-Materials-Science-Processing. Dec. 2002; A74: S94-6

23 **Spin-echo SANS based on adiabatic HF flippers in dipole magnets with skew poles**
Kraan,-W.-H.; Grigoriev,-S.-V.; Rekveldt,-M.-Th.; Bouwman,-W.-G.; Uca,-O.
Applied-Physics-A-Materials-Science-Processing. Dec. 2002; A74: S79-81

24 **Precession phase of the neutron spin after adiabatic passage through a resonant spin flipper**
Grigoriev,-S.-V.; Kraan,-W.-H.; Rekveldt,-M.-Th.
Applied-Physics-A-Materials-Science-Processing. Dec. 2002; A74: S76-8

25 **Magnetized foils as pi flippers in neutron spin-echo spectrometry**
Rekveldt,-M.-T.; Bouwman,-W.-G.; Kraan,-W.-H. SO: Journal-of-Applied-Physics. 15 Sept. 2002; 92(6): 3354-62

26 **High-resolution diffraction using Larmor precession of polarized neutrons**
Rekveldt,-M.-T.; Kraan,-W.; Keller,-T.
Journal-of-Applied-Crystallography. Feb. 2002; 35 pt. 1: 28-33

27 **Study of domain structures in FeCo/TiZr multilayers by means of 3D neutron depolarisation**
Kraan,-W.-H.; Rekveldt,-M.-T.; Ul'yanov,-V.-A.; Zabenkin,-V.-N.; Akselrod,-L.-A.; Gordeev,-G.-P.; Pusenkov,-V.-M.; Sellmann,-R.
Journal-of-Magnetism-and-Magnetic-Materials. Nov. 2001; 236(3): 302-11

28 **Magnetic phase transition in disordered Fe-Ni alloys studied by means of small-angle neutron scattering and three-dimensional analysis of the neutron depolarization**
Grigoriev,-S.-V.; Klimko,-S.-A.; Kraan,-W.-H.; Maleyev,-S.-V.; Okorokov,-A.-I.; Rekveldt,-M.-Th.; Runov,-V.-V.
Physical-Review-B-Condensed-Matter-and-Materials-Physics. 1 Sept. 2001; 64(9): 094426/1-10

29 **Neutron wave-interference experiments with adiabatic passage of neutron spin through resonant coils**
Grigoriev,-S.-V.; Kreuger,-R.; Kraan,-W.-H.; Mulder,-F.-M.; Rekveldt,-M.-Th.

Physical-Review-A-Atomic,-Molecular,-and-Optical-Physics. July 2001; 64(1): 013614/1-11

30 **Three-dimensional neutron depolarization study of the ferromagnetic-phase transition in a disordered system**
Grigoriev,-S.-V.; Van-Dijk,-N.-H.; Kraan,-W.-H.; Maleyev,-S.-V.; Rekveldt,-M.-T.; Runov,-V.-V.; Okorokov,-A.-I.
Physica-B. March 2001; 297(1-4): 250-2 Journal-Paper

31 **Line integral corrections in spin-echo small angle neutron scattering instrument**
Uca,-O.; Kraan,-W.-H.; Bouwman,-W.-G.; Rekveldt,-M.-Th.
Physica-B. March 2001; 297(1-4): 28-31

32 **Zero-field precession induced by adiabatic RF spin flippers** Kraan,-W.-H.; Grigoriev,-S.-V.; Kreuger,-R.; Mulder,-F.-M.; Rekveldt,-M.-T.
Physica-B. March 2001; 297(1-4): 23-7

33 **New instrumentation using Larmor precession of polarised neutrons**
Rekveldt,-M.-T.; Keller,-T.; Kraan,-W.-H.
Physica-B. March 2001; 297(1-4): 18-22

34 **Development of spin-echo small-angle neutron scattering**
Bouwman,-W.-G.; van-Oossanen,-M.; Uca,-O.; Kraan,-W.-H.; Rekveld,-M.-T. SO: Journal-of-Applied-Crystallography. June 2000; 33(1) pt. 3: 767-70

35 **Observation of polarized neutron interference in spin space**
Mulder,-F.-M.; Grigoriev,-S.-V.; Kraan,-W.-H.; Rekveldt,-M.-T. SO: Europhysics-Letters. 1 July 2000; 51(1): 13-19

36 **Neutron wave interference in experiments with two resonance spin flippers**
Grigoriev,-S.-V.; Kraan,-W.-H.; Mulder,-F.-M.; Rekveldt,-M.-T.
Physica-B. June 2000; 283(4): 393-6

37 **Magnetic phase transition in a disordered FeNi alloy: percolative scenario**
Grigoriev,-S.-V.; Klimko,-S.-A.; Kraan,-W.-H.; Rekveldt,-M.-T.; Okorokov,-A.-I.; Runov,-V.-V.
Physica-B. March 2000; 276-278: 556-7

38 **Magnetic properties of FeCoV/TiZr multilayers studied by 3D neutron depolarisation and SQUID**
Kraan,-W.-H.; Rekveldt,-M.-T.; Ul'yanov,-V.-A.; Akselrod,-L.-A.; Gordeev,-G.-P.; Pleshanov,-N.-K.; Pusenkov,-V.-M.; Sellmann,-R.
Physica-B. March 2000; 276-278: 640-1

39 **An analysis of magnetic field inhomogeneities in a spin-echo small-angle neutron scattering instrument**
Uca,-O.; Bouwman,-W.-G.; Kraan,-W.-H.; Rekveldt,-M.-T.
Physica-B. March 2000; 276-278: 136-7 Journal-Paper

40 **Test of magnetised foils as a polarisation rotator for a spin echo small-angle neutron scattering instrument**

van-Oossanen,-M.; Kraan,-W.-H.; Bouwman,-W.-G.; Rekveldt,-M.-T.
Physica-B. March 2000; 276-278: 134-5

41 **Spectrometer combining time-of-flight and Larmor modulation**
Mulder,-F.-M.; Kreuger,-R.; Grigoriev,-S.-V.; Kraan,-W.-H.; Rekveldt,-M.-T.; van-Well,-A.-A.
Physica-B. March 2000; 276-278: 132-3

42 **Observation of magnetic nanodomains in TmFeAl**
Mulders,-A.-M.; Kraan,-W.-H.; Gubbens,-P.-C.-M.; Buschow,-K.-H.-J.; Stusser,-N.; Hofmann,-M.
Journal-of-Alloys-and-Compounds. 14 March 2000; 299(1-2): 88-93

43 **Use of the optical theorem in polarized neutron small angle scattering from ferrofluid**
Toperverg,-B.; Vorobyev,-A.; Gordeyev,-G.; Lazebnik,-A.; Rekveldt,-Th.; Kraan,-W.
Physica-B. June 1999; 267-268: 203-6

44 **Neutron depolarization study of the magnetic phase transition in a disordered system**
Grigoriev,-S.-V.; Klimko,-S.-A.; Kraan,-W.-H.; Rekveldt,-M.-T.; Okorokov,-A.-I.; Runov,-V.-V.
Physica-B. June 1999; 267-268: 84-7

45 **Spin echo small angle neutron scattering experiment**
Bouwman,-W.-G.; Kraan,-W.; Rekveldt,-M.-T.
Physica-B. June 1999; 267-268: 79-83

46 **Domain structure in FeCo/TiZr multilayers analysed from 3D neutron depolarisation**
Kraan,-W.-H.; Rekveldt,-M.-T.; Ul'yanov,-V.-A.; Akselrod,-L.-A.; Gordeev,-G.-P.; Pusenkov,-V.-M.
Physica-B. June 1999; 267-268: 75-8

47 **High-resolution neutron diffraction using Larmor precession**
Kraan,-W.-H.; Kaiser,-C.-T.; Rekveldt,-M.-T.
Journal-of-Applied-Crystallography. Oct. 1998; 31 pt. 5: 742-7

48 **On the problem of two magnetic correlation lengths in an invar FeNi alloy above $\mathbf{T}_c$**
Grigoriev,-S.-V.; Klimko,-S.-A.; Kraan,-W.-H.; Rekveldt,-M.-T.; Okorokov,-A.-I.; Runov,-V.-V.
Physica-B. Dec. 1997; 241-243: 582-4

49 **Irreversible effects in the re-entrant spin glass FeNiMn evidenced by neutron depolarization**
Wagner,-V.; Klenke,-J.; Fricke,-M.; Kraan,-W.; Rekveldt,-M.-T.; Hesse,-J.
Journal-of-Magnetism-and-Magnetic-Materials. Jan. 1998; 177-181 pt. 1: 71-2

50 **Neutron diffraction using Larmor precession**
Kraan,-W.-H.; Kaiser,-C.-T.; Rekveldt,-M.-Th.
Physica-B. June 1997; 234-236: 1163-4

51 **The ferromagnetic order in the mixed phase of the re-entrant spin glass FeNiMn**
Klenke,-J.; Fricke,-M.; Hesse,-J.; Kraan,-W.; Kruger,-E.; Rekveldt,-M.-T.; Wagner,-V.
Physica-B. June 1997; 234-236: 590-1

52 **A neutron depolarisation study of the magnetic correlations in a particulate dispersion during milling**
Por,-P.-T.; Kraan,-W.-H.; Mayo,-P.-I.; Rekveldt,-M.-T.; O'Grady,-K.
Journal-of-Magnetism-and-Magnetic-Materials. Sept. 1996; 162(1): 139-44

53 **Determination of the magnetic structure of metal-evaporated tape by small-angle neutron scattering**
Por,-P.-T.; Rekveldt,-M.-T.; Kraan,-W.-H.
Journal-of-Magnetism-and-Magnetic-Materials. March 1996; 155(1-3): 306-8

54 **Small angle neutron scattering in Co-Cr films in perpendicular and non-perpendicular transmission**
Kraan,-W.-H.; Por,-P.-T.; Rekveldt,-M.-T.
Journal-of-Magnetism-and-Magnetic-Materials. March 1996; 155(1-3): 219-21

55 **Magnetic correlations between Co-modified γ-Fe_2 O_3 particles in a solid matrix studied by neutron depolarisation in fields up to 0.5 T**
Por,-P.-T.; Kraan,-W.-H.; Mes,-J.; Rekveldt,-M.-T.
Journal-of-Magnetism-and-Magnetic-Materials. March 1996; 155(1-3): 86-8

56 **Neutron spin-echo technique applied to 3-D neutron polarisation analysis in magnetised media**
Por,-P.-T.; Kraan,-W.-H.; Rekveldt,-M.-T.
Nuclear-Instruments-&-Methods-in-Physics-Research,-Section-A-Accelerators, -Spec- trometers,-Detectors-and-Associated-Equipment. 11 May 1996; 374(1): 79-84

57 **Unique magnetic behaviour of TmFeAl**
Mulders,-A.-M.; Kraan,-W.-H.; Ball,-A.-R.; Brueck,-E.; Buschow,-K.-H.-J.; Gubbens,-P.-C.-M.
Hyperfine-Interactions. Feb. 1996; 97-98(1-4): 109-23

58 **Describing magnetisation and neutron depolarisation of perpendicular Co-Cr film with in-depth varying K_u**
Kraan,-W.-H.; van-der-Graaf,-A.; Fredrikze,-H.; Mikhailova,-V.-E.; Rekveldt,-M.-T.
Journal-of-Magnetism-and-Magnetic-Materials. Feb. 1995; 140-144 pt. 3: 1907-8

59 **Neutron depolarisation in Co-Cr films with magnetic field applied in-plane**
Kraan,-W.-H.; Mikhailova,-V.-E.; Rekveldt,-M.-Th.
Journal-of-Magnetism-and-Magnetic-Materials. Feb. 1995; 140-144 pt. 3: 1905-6

60 **Construction and testing of a multichannel polariser for thermal neutrons**
Schebetov,-A.-F.; Pleshanov,-N.-K.; Pusenkov,-V.-M.; Peskov,-B.-G.; Shmelev,-G.-E.; Kraan,-W.-H.; Por,-P.-T.; Rekveldt,-M.-Th.; Mikhailova,-V.-E.
Nuclear-Instruments-&-Methods-in-Physics-Research,-Section-B- Beam-Interactions-with-Materials-and-Atoms. Dec. 1994; B94(4): 575-80

61 **Separating the polarising power from depolarisation in a set-up with 3 neutron polarisers**
Por,-P.-T.; Kraan,-W.-H.; Rekveldt,-M.-Th.
Nuclear-Instruments-&-Methods-in-Physics-Research,-Section-A- Accelerators,-Spec- trometers,-Detectors-and-Associated-Equipment. 1 Feb. 1994; 339(3): 550-5

62 **An experimental study of the magnetic behaviour of particulate dispersions. I. Chromium dioxide**
Mayo,-P.-I.; O'Grady,-K.; Sollis,-P.; Bissell,-P.-R.; Gilson,-R.-G.; Chantrell,-R.-W.; Balkenende,-A.-R.; Rekveldt,-M.-Th.; Kraan,-W.; Por,-P.-T.
Journal-of-Magnetism-and-Magnetic-Materials. Nov. 1993; 128(1-2): 191-203

63 **Domain wall effects in neutron depolarisation in Co-Cr films**
Kraan,-W.-H.; Rekveldt,-M.-Th.; de-Haan,-P.; Lodder,-J.-C.
Journal-of-Magnetism-and-Magnetic-Materials. March 1993; 120(1-3): 372-4

64 **Adiabatic rotators for 3-D neutron polarisation analysis**
Kraan,-W.-H.; Rekveldt,-M.-T.; Por,-P.-T.
Nuclear-Instruments-&-Methods-in-Physics-Research,-Section-A- Accelerators,-Spec- trometers,-Detectors-and-Associated-Equipment. Jan. 1991; A300(1): 35-42

65 **Testing a multilayer mirror system in use for polarised neutrons**
De-Haan,-V.-O.; Kraan,-W.-H.; Van-Well,-A.-A.
Nuclear-Instruments-&-Methods-in-Physics-Research,-Section-A- Accelerators,-Spec- trometers,-Detectors-and-Associated-Equipment. 1 April 1990; A289(1-2): 17-29

66 **Magnetic correlations in alumite studied by neutron depolarisation**
Kraan,-W.-H.; Rekveldt,-M.-T.
IEEE-Transactions-on-Magnetics. Jan. 1990; 26(1): 219-21

67 **Neutron Larmor precession method for transmission experiments**
Kraan,-W.-H.; van-Tricht,-J.-B.; Rekveldt,-M.-T.
Physica-B. Jan.-Feb. 1989; 156-157: 657-9

68 **Neutron depolarisation in alumite in remanent states after in-plane and perpendicular magnetisation**
Kraan,-W.-H.; Rekveldt,-M.-T.
Journal-de-Physique-Colloque. Dec. 1988; 49(C-8) pt. 3: 1985-6

69 **Stripe domains in magnetised Co-Cr films measured by neutron depolarisation**
Kraan,-W.-H.; Rekveldt,-M.-T.; Bernards,-J.-P.-C.; Luitjens,-S.-B.
Journal-de-Physique-Colloque. Dec. 1988; 49(C-8) pt. 3: 1981-2

70 **SANS experiments on thin CoCr films with perpendicular domain structure**
Rekveldt,-M.-T.; Zeyen,-C.-M.-E.; Lodder,-J.-C.; Kraan,-W.-H.
Journal-of-Magnetism-and-Magnetic-Materials. Jan. 1989; 78(1): 110-17

71 **Neutron Larmor precession transmission experiments**
Kraan,-W.-H.; Van-Tricht,-J.-B.; Rekveldt,-M.-T.
Nuclear-Instruments-&-Methods-in-Physics-Research,-Section-A- Accelerators,-Spec- trometers,-Detectors-and-Associated-Equipment. 1 April 1989; A276(3): 521-8

72 **Neutron depolarisation in magnetic alumite disks for perpendicular recording**
Kraan,-W.-H.; Rekveldt,-M.-T.; Umahara,-Y.; Tokushima,-T.
IEEE-Transactions-on-Magnetics. March 1988; 24(2) pt. 2: 1793-5

73 **Neutron Larmor precession and energy analysis**
Rekveldt,-M.-T.; Kraan,-W.-H.
Nuclear-Instruments-&-Methods-in-Physics-Research,-Section-B- Beam-Interactions-with-Materials-and-Atoms. Aug. 1987; B28(1): 117-22

74 **Domains in CoCr investigated by neutron depolarization**
Kraan,-W.-H.; Rekveldt,-M.-T.; Hemmes,-K.; Lodder,-J.-C.
IEEE-Transactions-on-Magnetics. Jan. 1987; MAG-23(1): 65-7

75 **Neutron depolarisation in CoCr layers to study the perpendicular magnetic domain structure**
Kraan,-W.-H.; Rekveldt,-M.-Th.; Hemmes,-K.; Lodder,-J.-C.
Physica-B-&-C. Jan.-Feb. 1986; 136B(1-3): 440-2

76 **Neutron depolarisation in individual magnetic domains and domain walls in an Fe(Si) single crystal**
Kraan,-W.-H.; van-Loef,-J.-J.; Rekveldt,-M.-Th.; Ungemach,-V.
Journal-of-Physics-C-Solid-State-Physics. 30 March 1985; 18(9): 1941-53

77 **The magnetic domain structure of CoCr layers studied by neutron depolarisation**
Hemmes,-K.; Lodder,-J.-C.; Rekveldt,-M.-Th.; Kraan,-W.-H.
Journal-of-Physics-D-Applied-Physics. 14 Oct. 1984; 17(10): L157-62

78 **Curved neutron mirror system as an improved polariser**
Rekveldt,-M.-Th.; Kraan,-W.-H.
Physica-B-&-C. May 1983; 120B(1-3): 81-5

79 **Neutron depolarisation in zigzag folded 90 degrees walls in silicon iron**
Kraan,-W.-H.; VanLoef,-J.-J.; Rekveldt,-M.-Th.; Ungemach,-V.
Journal-of-Physics-C-Solid-State-Physics. 30 Aug. 1983; 16(24): 4901-16

80 **Three dimensional neutron polarization analysis in the study of ferromagnetic domain structures**
Rekveldt,-M.-Th.; Kraan,-W.-H.; van-Loef,-J.-J.
Journal-de-Physique-Colloque. Dec. 1982; 43(C-7): 63

81 **Neutron depolarization and Faraday rotation in the domains of YI(Ga) garnet**
Kraan,-W.-H.; Rekveldt,-M.-Th.; Van-Loef,-J.-J.
Journal-of-Magnetism-and-Magnetic-Materials. July 1980; 21(1): 51-63

82 **Domain structure of YI(Ga) garnet studied by neutron depolarization and Faraday rotation**
Kraan,-W.-H.; Rekveldt,-M.-Th.; van-Loef,-J.-J.
Journal-of-Magnetism-and-Magnetic-Materials. Jan.-March 1980; 15-18 pt. 3: 1501-2

83 **Static and dynamic neutron depolarization studies of ferromagnetic domain structures**

Rekveldt,-M.-Th.; Van-Schaik,-F.-J.; Kraan,-W.-H.
Nukleonika-. 1979; 24(7-8): 809-23

84 **Calculation of neutron depolarization in a uniaxial ferromagnet**
Kraan,-W.-H.; Rekveldt,-M.-Th.
Journal-of-Magnetism-and-Magnetic-Materials. May 1978; 8(2): 168-74

85 **Analysis of the magnetic domain structure of electrodeposited nickel studied by neutron depolarization**
Kraan,-W.-H.; Rekveldt,-M.-Th.
Journal-of-Magnetism-and-Magnetic-Materials. June-July 1977; 5(3): 24

86 **Magnetic domain structure of electro-deposited nickel studied by neutron depolarization**
Kraan,-W.-H.; Rekveldt,-M.-Th.
Physica-B-&-C. Jan.-March 1977; 86-88B pt. 3: 1341-2

87 **Magnetic domain structures studied by neutron depolarization**
Kraan,-W.-H.; Rekveldt,-M.-Th.; Van-Loef,-J.-J.
Proceedings-of-the-Conference-on-Neutron-Scattering. 1976: 720-1

88 **A superconducting interference grating**
De-Waele,-A.–Th.–A.-M.; Kraan,-W.-H.; de-Bruyn-Ouboter,-R.
Physica-A. 1968; 40(2): 302-8
RT: Journal-Paper

89 **Relationship between current, voltage and magnetic field for a superconductiong double-point-contact diode placed in center of a coaxial cavity**
de-Bruyn-Ouboter,-R.; Kraan,-W.-H.; DeWaele,-A.–Th.–A.–M.; Omar,-H.–M.
Physica-PY 1967; 35(2): 335

90 **On existence of a corrugated surface representing relationship between current, voltage and magnetic field for weakly connected superconductors**
Omar,-H.–M.; Kraan,-W.-H.; DeWaele,-A.–Th.–A.–M.; de-Bruyn-Ouboter,-R.;
Physica 1967 34(4): 525

91 **On D.C. Voltage across a double point contact between 2 superconductors at zero applied DC current in situations in which junction is in resistive region due to circulating current of flux quantization**
DeWaele,-A.–Th.–A.–M.; Kraan,-W.H.; de-Bruyn-Ouboter,-R.; Taconis,-K.-W.
Physica 1967 37(1): 114

The author was born 26 August 1944. During the second half of his study experimental physics at RU-Leiden he worked in the group, at the time headed by Prof.dr. K.W. Taconis devoted to superconductivity and superfluid Helium at Kamerlingh Onnes Laboratory, Leiden. His subject was in the field of weak contacts (”Josephson junctions”) between superconducting bodies. He passed the ”doctoraalexamen” terminating this study on 15 April 1969.
After military service he became a member of the group ”Stralingsfysica” (nowadays called Neutronenphysica en Mössbauerspectrometrie), then headed by Prof. dr. J.J. van Loef. It was his duty to develop a setup for application of long-wavelength polarized neutrons, under supervision of Dr. M.Th. Rekveldt. After initial realization of this setup he studied magnetic domain structures by neutron depolarization in electro deposited films, single crystals of Fe_3Si, CoCr films and alumites for perpendicular recording, magnetic liquids and multilayers for neutron polarization.
Throughout the past 3 decades he has been permanently involved in improving this setup and extending the use of polarized neutrons. Part of this work is covered by this thesis.
The author worked as a guest scientist in Germany (Physikalisch-Technische Bundesanstalt, Braunschweig, 1991) and Russia (Petersburg Nuclear Physics Institute, Gatchina, 1994, 1997, 2000, 2001, 2002) in these fields.